NASA Conference Publication 3176

FIBER-TEX 1991

The Fifth Conference on Advanced Engineering Fibers and Textile Structures for Composites

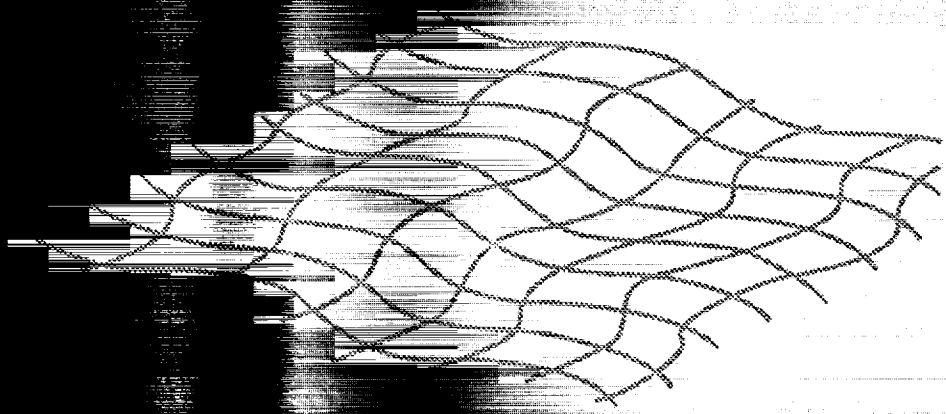

Proceedings of a conference held in
Raleigh, North Carolina
October 15–17, 1991

NASA

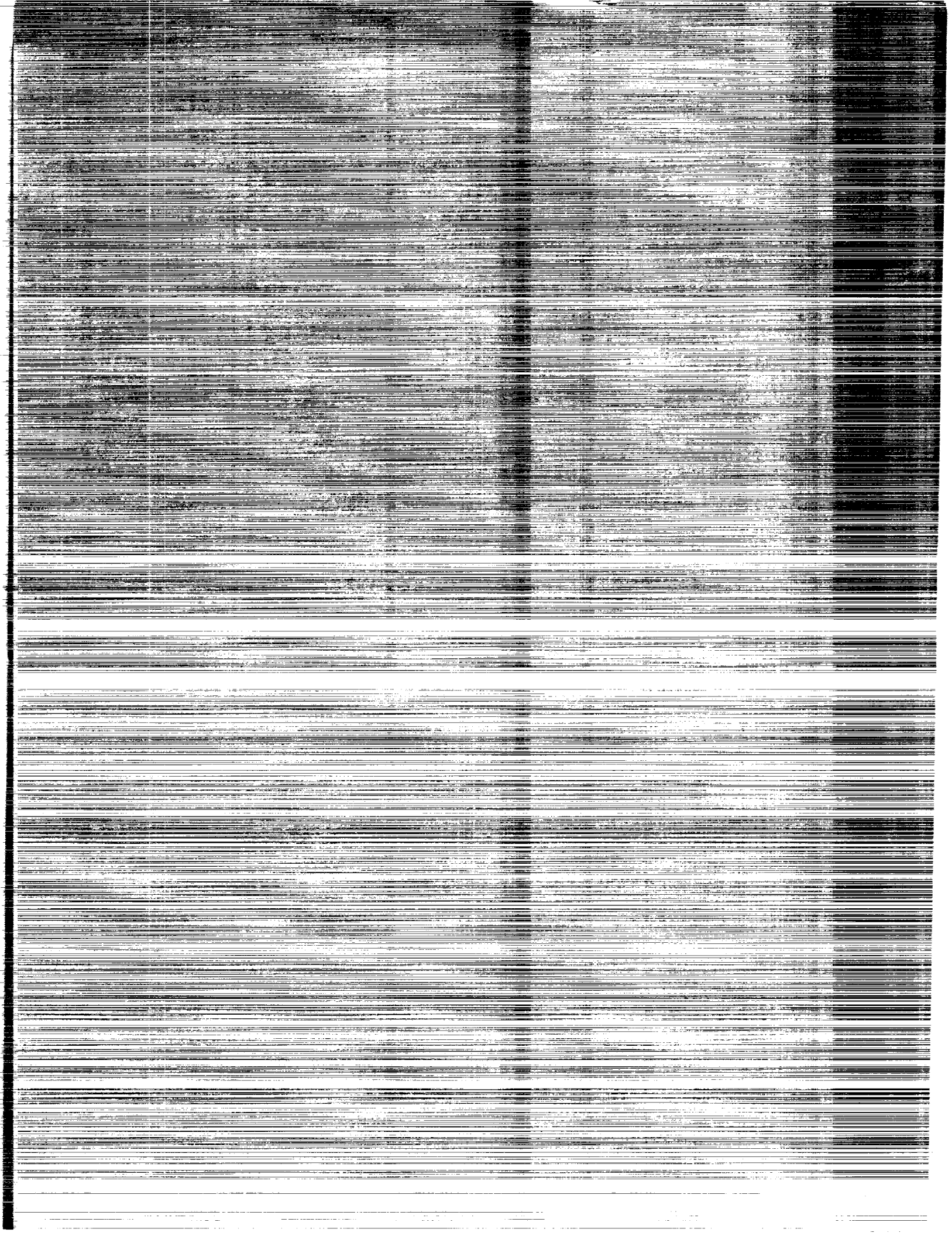

NASA Conference Publication 3176

FIBER-TEX 1991

The Fifth Conference on Advanced Engineering Fibers and Textile Structures for Composites

Edited by
John D. Buckley
NASA Langley Research Center
Hampton, Virginia

Proceedings of a conference sponsored by the National Aeronautics and Space Administration, Washington, D.C., the Department of Defense, Washington, D.C., North Carolina State University, Raleigh, North Carolina, Clemson University, Clemson, South Carolina, and Drexel University, Philadelphia, Pennsylvania, and held in Raleigh, North Carolina
October 15–17, 1991

NASA
National Aeronautics and Space Administration
Office of Management
Scientific and Technical Information Program
1992

PREFACE

The *FIBER-TEX 1991* proceedings contain the papers jointly sponsored by the National Aeronautics and Space Administration, the Center for Advanced Engineering Fibers at Clemson University, the Department of Defense, the North Carolina State University, and Drexel University. The conference was held in Raleigh, North Carolina on October 15–17, 1991 to create a forum to encourage an interrelationship of the various disciplines involved in the fabrication of materials, the types of equipment, and the processes used in the production of advanced composite structures. Topics discussed were Reinforcing Fibers, Matrix Materials, Mechanics of Woven Materials, Structural Fabric Production, Pultrusion and Composite Processes, and Structures and Applications.

Certain materials and processes are identified in this publication in order to adequately specify procedures. In no case does such identification imply recommendation or endorsement by the government, nor does it imply that the materials or processes are the only or best ones available for the purpose.

John D. Buckley
NASA Langley Research Center

CONTENTS

An Evaluation of Composites Fabricated from Powder Epoxy Towpreg

J. Timothy Hartness and Tim Greene

BASF Structural Materials

Abstract

BASF has developed a unique process for applying powdered resin systems to continuous reinforcement fibers in order to produce flexible towpreg material. Evaluation of three powder epoxy resins by BASF using this towpregging process is in progress under NASA contract NASI-18834. Shell RSS-1952, Dow CET-3, and 3M PR500 powder epoxy systems have been successfully towpregged with G30-500 6K carbon fiber. Both neat resin and basic unidirectional composite properties have been developed to compare performance. Cure cycles for each system have also been developed for repeatable fabrication of high-quality composite laminates. Evaluations of the powder towpreg material for use in textiles processes such as weaving and braiding are underway. Traditional 8-harness weaving has been successfully performed with one system (PR500/G30-500) to date, with some basic composite properties generated. Ongoing work will demonstrate scaleup of the towpregging process for higher throughput, as well as evaluation of the powder towpreg material in advanced preforming processes such as 3-D braiding and weaving.

POWDER EPOXY TOWPREG DEVELOPMENT

- NASA Contract/Materials Characterization
- Primary Focus Subsonic Applications (180°F Service)
- Evaluate Mechanical Performance
- Evaluate Use in Textiles Preforming
- Evaluate Manufacturing/Processing Methods

ADVANTAGES OF "DRY" MATERIAL FORMS

- Conformability
- Textile Yarn Form/Textile Technology Applications
- No Refrigeration Required

POWDER EPOXY TOW ADVANTAGES

- Predetermined Fiber Volume
- "Predetermined" Chemistry
- Good Fiber/Resin Distribution
- No Solvents
- Room Temperature Storage

CANDIDATE POWDER EPOXY SYSTEMS

- PR-500 (3M)
- RSS-1952 (SHELL CHEMICAL)
- CET-3 (DOW CHEMICAL)

PHYSICAL PROPERTIES, NEAT RESIN

		PR-500 (3M)	RSS-1952 (SHELL)	CET-3P (DOW)
Tg (DSC, °C/°F)		205/401	219/426	164/327
TENSILE	STRENGTH (KSI)	8.3		13.0
	MODULUS (KSI)	507		410
	ELONGATION (%)	1.9		5.0
FLEXURAL	STRENGTH (KSI)	18.4	16.9	21.0
	MODULUS (KSI)	504	426	450
	STRAIN (%)	4.2	5.1	7.0
DENSITY (gm/cc)		1.25	1.15	1.27
MOISTURE ABSORPTION (% WT.)		1.56	1.1	1.35

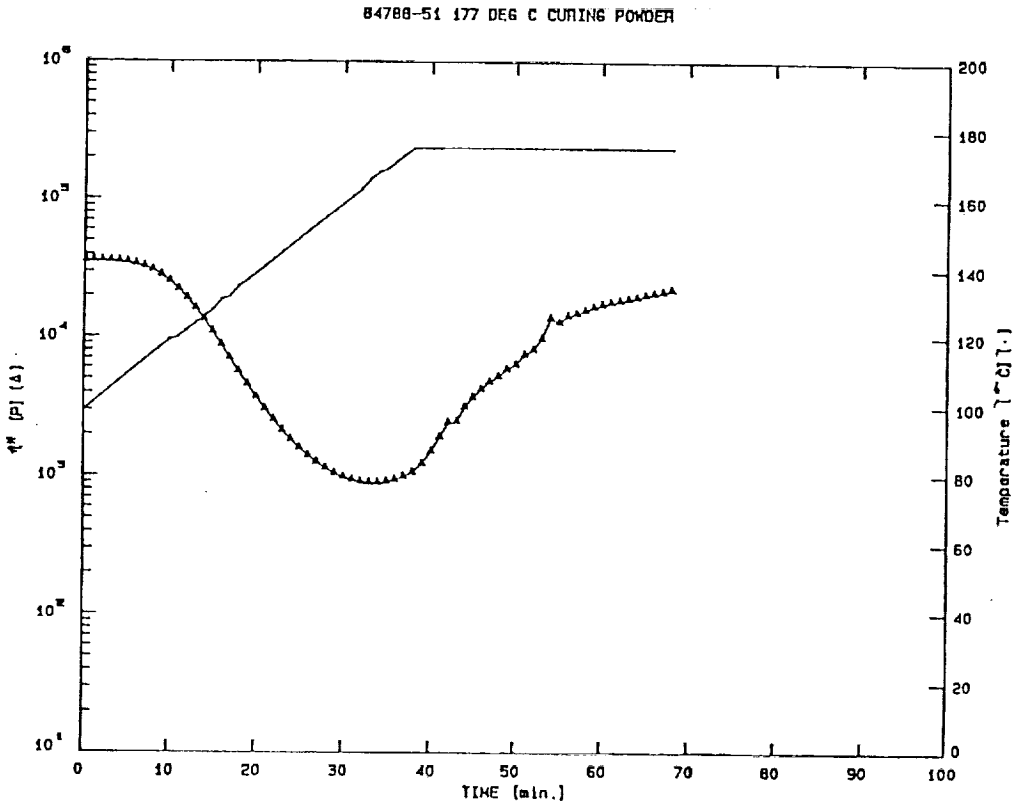

PR-500 Powder, Viscosity Sweep

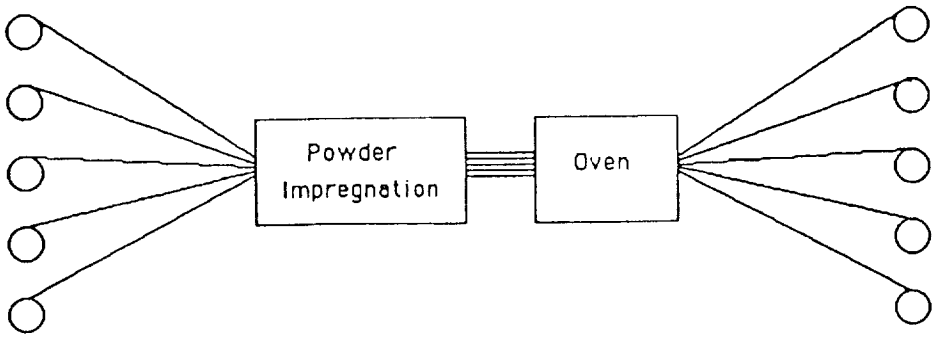

Schematic, Powder Coating Process

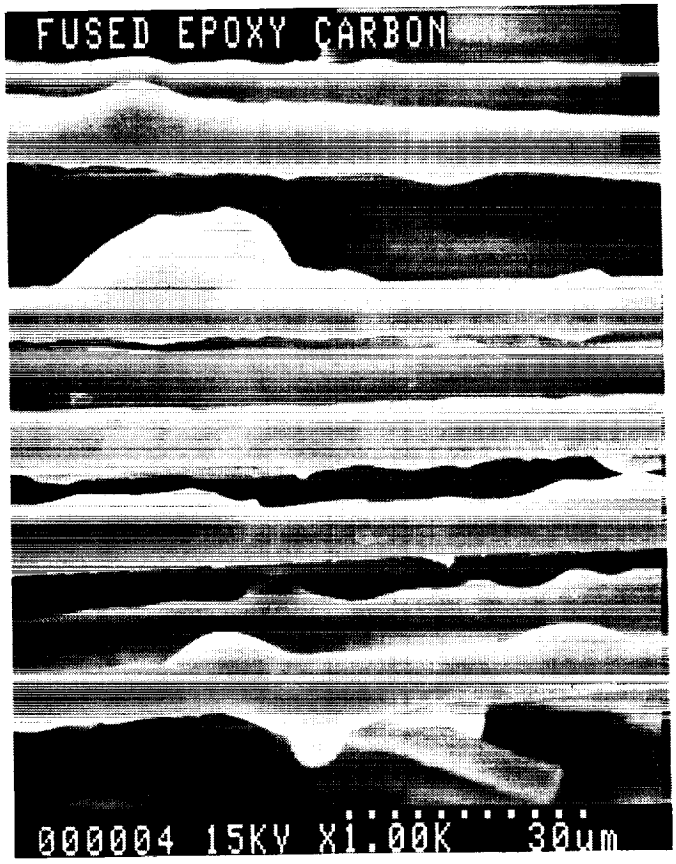

Powder Coated Tow, 1000X

CURE CYCLE, FUSED TOWPREG

PR-500 (3M): 350°F/2 hours

RSS-1952 (Shell): 300°F/2 hours, ramp to 400°F/4 hours

CET-3P (Dow): 300°F/4 hours; 400°F/4 hour post-cure

COMPOSITE PROPERTIES, UNIDIRECTIONAL TOW

	PR-500/G30-500	RSS-1952/G30-500
FIBER VOLUME	55%	63%
0° 3 PT. FLEXURE (RT, 32-1)		
STRENGTH (KSI)	242	320
MODULUS (MSI)	16	19
0° 4 PT. SHEAR (RT, 16-1)		
STRENGTH (KSI)	12.2	10.0
90° 3 PT. FLEXURE (RT)		
STRENGTH (KSI)	11.0	9.0
MODULUS (MSI)	1.2	1.18

PHYSICAL PROPERTIES, 8-HARNESS FABRIC

RESIN: PR-500 (3M)

FIBER VOLUME: 56%

3 PT. FLEXURE (RT, 32-1)

STRENGTH (KSI)	102.0
MODULUS (MSI)	7.1

4 PT. SHEAR (RT, 16-1)

STRENGTH (KSI)	6.0

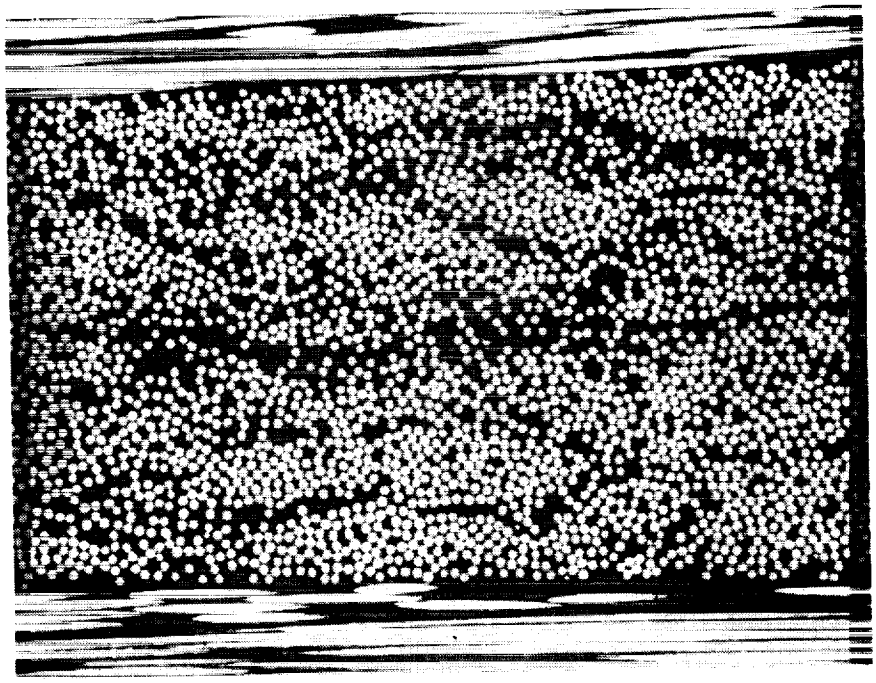

Photomicrograph, Cured 8 Harness Laminate

CONCLUSIONS/ACCOMPLISHMENTS

- Fused Towpreg Approach Is Viable With Powder Epoxy
- 5-Ends Successfully Demonstrated
- Fused Epoxy Tow Is Weaveable Using Standard Techniques
- Good Fiber/Resin Distribution and Wet-Out Demonstrated
- Initial Unidirectional and 8-Harness Data Generated

FUTURE PLANS

- Generate RSS-1952 and CET-3 8-Harness Fabric Data
- Complete RT and Hot/Wet Mechanical Testing
- Determine Processing Window
- Verify Preforming Feasibility (2-D and 3-D)
- Develop De-bulking and Part-Manufacturing Methods

CONCLUSIONS/ACCOMPLISHMENTS

- Fused Towpreg Approach Is Viable With Powder Epoxy
- 5-Ends Successfully Demonstrated
- Fused Epoxy Tow Is Weaveable Using Standard Techniques
- Good Fiber/Resin Distribution and Wet-Out Demonstrated
- Initial Unidirectional and 8-Harness Data Generated

FUTURE PLANS

- Generate RSS-1952 and CET-3 8-Harness Fabric Data
- Complete RT and Hot/Wet Mechanical Testing
- Determine Processing Window
- Verify Preforming Feasibility (2-D and 3-D)
- Develop De-bulking and Part-Manufacturing Methods

ADVANCED STITCHING TECHNOLOGY

Frank L. Scardino
IFAI Professor of Industrial Fabrics
Philadelphia College of Textiles and Science
School House Lane and Henry Avenue
Philadelphia, Pennsylvania

INTRODUCTION

In the design of textile composites, the selection of materials and constructional techniques must be matched with product performance, productivity, and cost requirements. Constructional techniques may vary from slow and expensive, hand laid-up batch manufacturing (one unit at a time) to very quick and cost effective continuous pull-through processing. No single textile material, resin system, textile assemblage, or constructional technique can be considered optimal for all applications.

A classification of various textile composite systems is given in Table I. In general, the chopped fiber system (Type I) is not suitable for structural composite applications because of fiber discontinuity, uncontrolled fiber orientation and a lack of fiber integration or entanglement. Linear filament yarn systems (Type II) are quite acceptable for structural components which are exposed to simple tension in their applications. To qualify for more general use as

structural components, filament yarn systems must be multi-directionally positioned. With the most sophisticated filament winding and laying techniques, however, the Type II systems have limited potential for general load-bearing applications because of a lack of filament integration or entanglement, which means vulnerability to splitting and delamination among filament layers.

TABLE I. TEXTILE COMPOSITE SYSTEMS

Type	Reinforcement System	Textile Construction	Fiber Length	Fiber Orientation	Fiber Entanglement
I	Suspended	Chopped Fiber	Discontinuous	Uncontrolled	None
II	Linear	Filament Yarn	Continuous	Linear	None
III	Laminar	Simple Fabric	Continuous	Planar	Planar
IV	Integrated	Advanced Fabric	Continuous	3-D	3-D

The laminar systems (Type III) represented by a variety of simple fabrics (woven, knitted, braided and nonwoven) are especially suitable for load-bearing panels in flat form and for beams in a rolled up or wound form. The main features of simple fabric systems are fiber continuity, planar fiber orientation and planar fiber entanglement or integration, in general. The major vulnerability of simple fabric laminate systems is delamination between layers of the fabrics which tends to be more critical in flat panels than in rolled up tubular or rectangular configurations.

The totally integrated, advanced fabric systems (Type IV) are thought to be the most reliable for general load-bearing applications because of fiber continuity and because of controlled multiaxial fiber

orientation and entanglement. Consequently, the risk of splitting and delamination is minimized and practically omitted. Type IV systems can be woven, knitted, braided or stitched through with very special equipment.

In general, multiaxial fabrics are classified as Type IV in Table I. A practical advantage of multiaxial fabrics is the elimination of much of the hand lay-up work in composite manufacturing which is so labor intensive and time consuming. Also, multiaxial fabrics are easier to handle because the various yarn orientations are held in a fixed position during manipulation. (1)

MULTIAXIAL FABRIC TECHNOLOGIES

Several alternate technologies are commercially available today for the conversion of yarn into multiaxial constructions for a variety of industrial fabric applications, but particularly for flexible and rigid composites. These multiaxial fabric technologies include adhesive bonding, triaxial weaving, triaxial braiding, weft insertion warp knitting, bias ply stitch bonding and bias warp knitting. Each multiaxial fabric technology has unique attributes and limitations, and accordingly, will find a place in the industrial fabric market on a cost/performance/availability/processability/machineability/join-ability/maintainability basis.

Adhesively-bonded multiaxial systems are easily produced by combining several layers of yarn or fabric at various angles (including skewed WIWK fabrics, bias woven, etc.). While the productivity is

attractive, adhesive bonding does not provide resistance to delamination or to crack propagation. Another major limitation of adhesively bonded yarn and fabric systems is a lack of through-the-thickness strength. Adhesively-bonded constructions are classified as Type II if made directly from yarn or Type III if made by combining layers of fabric. By contrast, all of the following multiaxial fabric systems are classified as Type IV.

In triaxial weaving technology, three systems of yarns are interlaced at sixty degree angles (2,3). With two warps and one filling, the resulting orientation is $+30^{\circ}/-30^{\circ}/90^{\circ}$. While triaxial weaving technology has been developed for quite some time, triaxial woven fabric is commercially available in limited styles from Sakase Textile Company in Japan.

Triaxial braids incorporate one longitudinal yarn system with two helical or diagonal yarn systems. Consequently, the resulting yarn orientation can vary from $0^{\circ}/+30^{\circ}/-30^{\circ}$ to $0^{\circ}/+60^{\circ}/-60^{\circ}$, depending upon processing variables. Triaxial braids are particularly well suited for tubular applications.(4)

Weft insertion warp knit (WIWK) technology is well developed and established for a variety of industrial fabric applications. Biaxial WIWK fabrics are made by knitting 0° and 90° straight-laid yarn systems together. It is possible to produce quasi-quadraxial WIWK fabrics by adding two additional laid-in yarn systems in a counter zig-zag fashion in the machine direction, wherein each yarn continues for up to two inches in the $+45^{\circ}$ or -45° direction before reversing its path.(5,6)

Several companies are capable of producing quasi-quadraxial WIWK fabrics on LIBA or Mayer WIWK machines.

Multiaxial stitch bonded fabric preforms can be made by stitching together several layers of yarn at various angles or plies of skewed fabric. The stitching processes provides through-the-thickness strength and integrity. Stitching can be performed efficiently and with high productivity on any suitable multi-needle process capable of through-the-thickness penetration including sewing machines, Mali machines, warp knitting stitch-through machines, etc. The major advantages of multiaxial stitched-through fabric preforms are high density, control of yarn orientation in each layer, and the integration of the yarn/fabric layers by stitching. The major disadvantage is the impaling and localized dislocation of yarn during stitching which leads to reduced strength and to poor structural consistency.(7)

Several companies are presently involved in multiaxial stitch-through technology including Hexcel in Seguin, Texas; Bean Fiberglass Company in Jaffrey, New Hampshire; Brunswick Technologies in Brunswick, Maine; Bay Mills in Ontario, Canada; Chomarat in France; and others in Europe; each of whom has devised their own unique multiaxial orientation system. Commercial stitch-through machines without bias orientation capability are available from LIBA, Karl Mayer and Textima. Also, LIBA is presently marketing a machine called Copcentra-Multiaxial which coordinates multiaxial orientation with stitching through on a weft insertion warp knit type of machine. Multiaxial stitch-through fabrics are available in several plies of yarn systems oriented in the

warp, weft and bias directions. Light nonwoven webs can be added, as a ply, if desired, and fabric widths of four to eight feet are possible.

All of the laid-in yarns are linear, are in a specific plane, and are continuous between fabric edges. Obviously, multiaxial stitch-through fabrics can be engineered for specific directional properties. Currently, most fabrics are composed of high modulus laid-in tow/yarn systems with a fine polyester stitching yarn system. Fabric constructions of the various ply orientations can be made up to approximately 1/4-inch thickness. Multiaxial stitch-through fabric weights vary according to construction but are often in the range between 12 and 48 ounces per square yard.

Multiaxial warp knit fabric technology has been developed recently by the Karl Mayer Textile Machine Company in West Germany. The process is officially known as multiaxial magazine weft insertion and informally referred to as the bias machine. As an alternate to multiaxial stitch-through technology, the Mayer bias machine precisely knits rather than punches the stitching yarn through the various layers of laid-in yarns. Consequently, no yarns are impaled and the texture is quite uniform throughout the fabric, leading to higher translation efficiencies. The major design limitation of the Mayer bias machine is a maximum of four yarn layers (0°, 90°, $+45^{\circ}$, -45°) plus a fiber web, if desired. Also, fabrics made from the Mayer bias machine tend to be somewhat more voluminous than comparable stitch-through multiaxial fabrics, which provides for easier resin penetration but slightly lower fiber volume fractions, potentially.(6) Milliken is the only company

in the U.S. with a Mayer bias machine.(8) Nine other Mayer bias machines are in operation in Europe.

MULTIAXIAL FABRIC BEHAVIOR

The behavior of various fabric constructions under uniaxial stress in the machine (0°), crosswise (90°) and bias ($\pm 45^{\circ}$) directions are illustrated in Figures 1, 2, and 3, respectively. In-plane shear resistance is parallel to the direction indicated in each figure. With the variety of fabric constructional forms available, it is possible to have textile composite preforms behave according to any position desired on the performance maps illustrated in figures 1 through 3, in general.(9)

When made from high modulus or fully drawn yarns, most multiaxial fabric constructions tend to have excellent dimensional stability and outstanding in-plane shear resistance in all directions (machine, crosswise, and bias) compared with regular woven, knitted, and braided constructions. Normally, dimensional stability and conformability are mutually exclusive. However, when made from partially oriented yarns (POY), multiaxial fabric constructions can be designed for directional conformability during 3-D draw-molding, 3-D draw-stamping or 3-D draw-wrapping with excellent omni-directional dimensional stability and shear resistance in the final 3-D configuration.

In many composite applications, isotropy (for performance) and porosity (for ease of resin impregnation) are quite important in composition preforms. A performance map plotting in-plane isotropy versus porosity for a variety of fabric constructional forms is

illustrated in Figure 4. It can be readily seen that warp knitting technology (regular, weft insertion, stitched-through and multiaxial) offers the greatest range of design possibilities.

EXPLORATIONS IN STITCHING TECHNOLOGY

A number of multiaxial stitch-through samples have been made from a variety of high modulus yarns in recent years by hand orienting and stitching to simulate machine-made constructions. Typically, $0^{\circ}/-45^{\circ}/+45^{\circ}/90^{\circ}$ orientations have been made in 4, 8, 12, and 16 layers on tension frames of various dimensions and chain stitched at 2 or 3 wales per inch simulating a machine stitch-through operation. Yarn impaling/filament damage during hand stitching remains a problem especially with high density multiaxial orientations.

Most of the hand-made multiaxial stitch-through samples have been made with chain stitching in the 0° (simulated machine) direction as straight and as uniformly as possible. Such an approach is appropriate for making large, thick, dense multiaxial preforms for planar applications requiring substantial, through-the-thickness strength and in-plane shear resistance. Currently, irregular stitching patterns with various stitching materials in various paths and angles are being explored in order to improve the conformability of large, thick, dense multiaxial stitch-through samples in adapting to non-planar applications.

In the analysis of 3-D textile composites, Norris Dow showed clearly that improvements in a given property are usually accomplished

at the sacrifice of some other properties(10). He concluded that there is no magic configuration. Just as trade-offs are required to minimize the penalties for enhanced through-the-thickness properties, trade-offs are also required to minimize the penalties for enhanced conformability. Net shape textile preforms have received a great deal of attention in recent years, and rightly so. Perhaps advanced stitching technology will make as great an impact on net shape textile preforms in the near future as it has on planar multiaxial preforms in the recent past.

REFERENCES

1. Scardino, F.L.
An Introduction to Textile Structural Composites for Primary and Secondary Load Bearing Applications
Philadelphia College of Textiles and Science
Philadelphia, Pennsylvania, January 1983, 28p.

2. Scardino, F.L. and Ko, F.K.
Triaxial Woven Fabrics. Part I: Behavior Under Tensile, Shear, and Burst Deformation
Textile Research Journal 51: February, 1981, p.80

3. Scardino, F.L.
The Doweave Story ... Marketing Strategy Versus Technical Capability ... A Case Study in the Management of Textile Technology
Philadelphia College of Textiles and Science
Philadelphia, Pennsylvania, April, 1981, 54p.

4. Ko, F.K.
Braiding
Section 8BB, Engineered Materials Handbook, Vol. 1, Composites
ASM International, 1987

5. Ko, F.K., et al
Development of Multi-Bar Weft Insertion Warp Knit Fabrics for Industrial Applications
ASME Paper No. 90 - TEXT - 7, October, 1980

6. Pastore, C.M.; Whyte, D.W.; Soebruto, H.; and Ko, F.K.
Design and Analysis of Multiaxial Warp Knit Fabrics for Composites
Journal of Industrial Fabrics 5: No. 1, Summer, 1986, p.4

7. Ko, F.K.; Fang, P.; and Pastore, C.M.
Multilayer Multi-dimensional Warp Knit Fabrics for Industrial Applications
Journal of Industrial Fabrics 4: No. 2, 1985, p.4

8. Milliken Multiaxial Structure Receives the Techtextil Prize for Innovation
Kettenwirk-Praxis 3/91, page E31
Obertshausen, Germany

9. Scardino, F.L.
Introduction to Textile Structures and Behaviors
Chapter One, Textile Structural Composites
Elsevier Science Publishers B.V.
Amsterdam, The Netherlands 1989, p.1-26

10. Dow, N.F.
Analysis of 3-D Composites
2nd Textile Structural Composites Symposium
Drexel University, Philadelphia, Pennsylvania, February, 1987

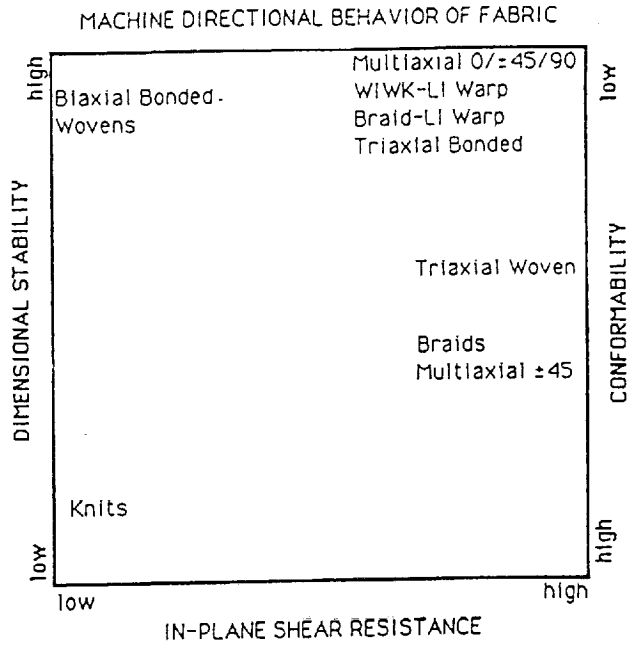

Figure 1. Behavior of Various Fabric Structural Forms Under Uniaxial Stress in the Machine (0°) Direction

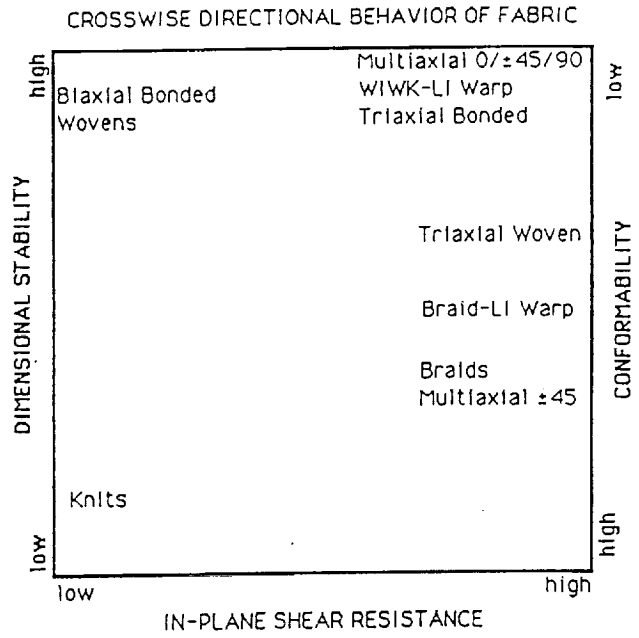

Figure 2. Behavior of Various Fabric Structural Forms Under Uniaxial Stress in the Crosswise (90°) Direction

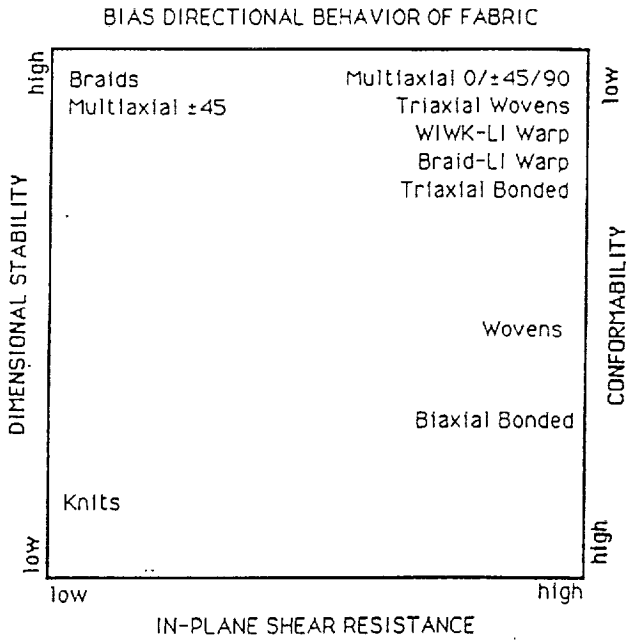

Figure 3. Behavior of Various Fabric Structural Forms Under Uniaxial Stress in the Bias (45° or -45°) Direction

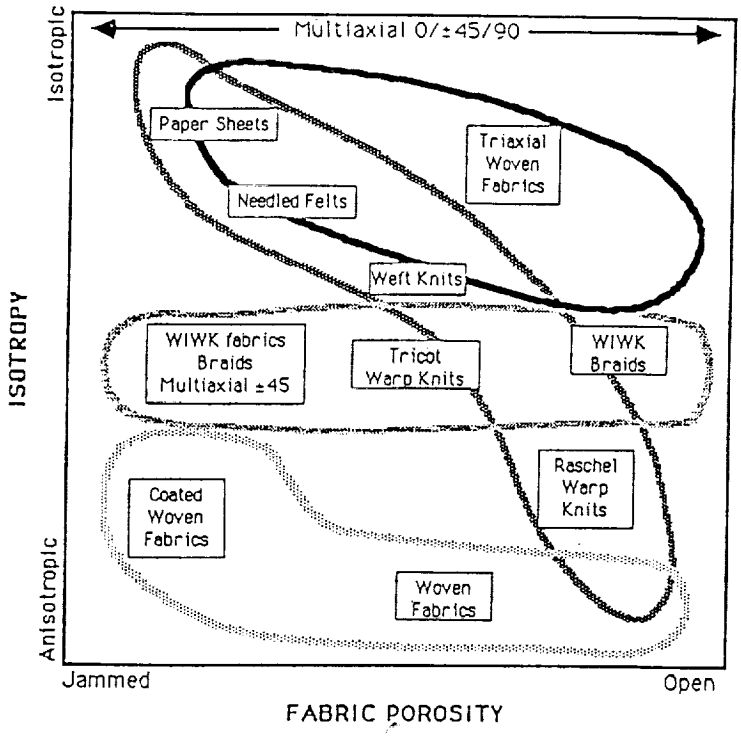

Figure 4. In-Plane Isotropy Versus Porosity for a Variety of Fabric Constructional Forms

N93-14747

Flow Behavior in Liquid Molding

D. Hunston, F. Phelan, and R. Parnas
National Institute of Standards and Technology
Polymers Division
Gaithersburg, MD

ABSTRACT

The liquid molding (LM) process for manufacturing polymer composites with structural properties has the potential to significantly lower fabrication costs and increase production rates. LM includes both resin transfer molding and structural reaction injection molding. To achieve this potential, however, the underlying science base must be improved to facilitate effective process optimization and implementation of on-line process control. The National Institute of Standards and Technology (NIST) has a major program in LM that includes materials characterization, process simulation models, on-line process monitoring and control, and the fabrication of test specimens. The results of this program are applied to real parts through cooperative projects with industry. The key feature in the effort is a comprehensive and integrated approach to the processing science aspects of LM. This paper briefly outlines the NIST program and uses several examples to illustrate the work.

INTRODUCTION

Polymer based composite materials have much to offer in a wide range of products, particularly in structural applications. Despite the advantages, however, composites have realized only a small fraction of their potential. The most important barrier to their expanded use is the inability to make them rapidly, reliably, and cost effectively. Rejection rates in manufacturing are often too high, and the labor intensive manufacturing methods now used are slow and costly. The solution to this problem is the implementation of more effective processing methods and the development of the scientific understanding necessary to optimize their use.

The process known as liquid molding (LM) has great potential in this regard. LM includes both resin transfer molding (RTM) and structural reaction injection molding (SRIM), which is a high speed cousin to RTM. LM combines some of the speed advantages of simple injection molding with the ability to make the high performance parts associated with continuous fiber reinforcement. Flexibility in the type, amount, and orientation of the reinforcement in every section of the mold enables the generation of very complex parts. Moreover, since the resin viscosity is low, the parts can be quite large and three dimensional.

Because of these potential advantages, LM is the leading candidate for the fabrication of structural composite parts in the automotive industry. Likewise, the drive for more cost effective

manufacturing has caused a variety of other industries including aerospace and marine to consider LM. Effective utilization of this processing method, however, requires developments in both preform fabrication and the technology required for process optimization and on-line process control. Because this technique has such great potential, the National Institute of Standards and Technology (NIST) has initiated a major program to address the scientific issues associated with process optimization and control. This paper will give a general overview of the NIST program and then illustrate the work with two examples from the program.

NIST PROGRAM OVERVIEW

The LM program at NIST has four tasks which are summarized in Table I. Each will be briefly discussed in the material that follows.

Table I:
NIST Program on Liquid Molding

- Materials Characterization
  - Permeability
  - Thermal and Cure Behavior
- Process Simulation
  - Macroscopic Models
  - Microscopic Models
- Process Monitoring / Control
  - Flow Behavior
  - Thermal and Cure Monitoring
- Sample Preparation and Application to Parts

Materials Characterization

The first task focuses on characterization of the material properties associated with processing, i.e. preform permeability, thermal conductivity, and cure behavior. Preform permeability measures the resistance offered by the preform to the flow of a resin. Since the reinforcement can have very different resistances to flow in different directions, the permeability, **K**, is a tensor quantity. This means a variety of measurements both in the plane and through the thickness of the preform material must be conducted to evaluate **K**. The resistance to flow is also very sensitive to the fiber volume fraction so this dependence must be determined. The most direct procedure to measure permeability is unidirectional flow experiments, and a variety of special molds have been developed at NIST to minimize edge effects and facilitate measurements at a variety of fiber volume fractions. For those cases where the part of interest has a shell-like

structure which permits the use of two dimensional flow models, it may be adequate to determine only the in-plane components of the permeability, and this significantly simplifies the characterization.

This task also has the goal of developing the technology to predict the permeability from a knowledge of preform microstructure and fiber surface treatment. This would be a very significant advance because the preform could then be designed to optimize both performance and processibility. Although this technology is well beyond current capabilities, it is an important long range objective. An example of research in this area is given later in this paper.

The measurement of thermal and cure properties for the materials involved relies heavily on the process monitoring facilities established at NIST over the last five years. The objective in developing these facilities was to take advantage of NIST's position as an outstanding measurement laboratory by assembling a wide range of process measurement techniques including virtually all the commonly used methods. Table II lists the ten different techniques that have been adapted to process monitoring in this program. This capability permits the examination of the chemical and physical changes that occur during processing at size scales ranging from individual chemical bonds where the chemistry occurs up to bulk properties such as viscosity and viscoelasticity. By applying these techniques both individually, and in combinations, a detailed picture of the changes can be achieved.

Table II: PROCESS MONITORING TECHNIQUES

Size Scale		
Chemical Bond	Molecules	Bulk
Optical Spectroscopy Calorimetry	Conductance Dielectric Spectroscopy Fluorescence Spectroscopy Chromatography SANS[1]	Ultrasonics Dynamic Mechanical Viscosity
Measurement Methods		

[1]Small Angle Neutron Scattering

Process Simulation

The second task in the NIST program is the development of process simulation models. The models fall into two somewhat arbitrary categories, macroscopic and microscopic. The macroscopic models employ the so called volume averaging approach. This approach focuses on volume elements that are large enough so that variations in local features such as the arrangement of individual fibers in space, interactions between fluid and fibers, etc. average out and thus only the average properties need to be considered. Such treatments are generally quite

good for analyzing macroscopic events such as mold filling.

The macroscopic models are less useful, however, for predicting other important events like void formation since these events depend on local features. To deal with this, microscopic models are needed. Such models include some or all of the local features. In principle, it is possible to simulate the entire part at this level of detail, but the computational time required is prohibitive. As a result, events dependent on local features are simulated by first using macroscopic models of the part to predict boundary conditions on the local area and then simulating this area using a microscopic model.

To analyze complex geometries, the process simulation models are applied using finite element methods. In the NIST research effort, a variety of mold filling programs have been developed (1). The simplest is a 2D program, which is appropriate for flat, thin structures. The most general is a fully 3D program which is used for complex parts with thick sections. Bridging the gap between these is what is called a 2.5D model. This is for flow in shell-like structures in which locally there is always a plane with a thickness dimension that is small compared to the dimensions in the local plane. In these parts, it is assumed that there is no flow in the thickness direction, and thus, the flow is treated as two dimensional even though the structure is three dimensional. Both the 2D and 2.5D programs have significant computational speed advantages relative to the fully three dimensional program, which is the primary advantage of their use. The 2.5D and 3D simulations both account for the effect of gravity on the flow.

Process simulations must analyze many factors including resin flow, heat transfer, chemical reactions, etc., as well as the interactions between these factors. Chemical reactions, for example, generate heat which must be considered in the heat transfer relationships. In certain cases, it is possible to separate some of these factors and thereby simplify the modeling. Often, the mold filling may be completed before the chemical reactions produce significant effects. When possible, the use of such simplifications can significantly accelerate the analysis.

Process Monitoring / Control

The third task in the NIST program involves on-line process monitoring. The purpose is to develop this technology and then use it to address two areas. First, the experiments seek to test and refine the process simulation models. Second, the technology for on-line process control is explored for those situations where it is appropriate. For testing the simulation models, the first step is an examination of flow behavior in mold filling. The principle tool is flow visualization experiments. One drawback of this approach, however, is that visualization which is performed with molds having one or more clear sides provides information only about what is happening at the surface. Consequently, sensors such as fiber optic probes are being developed to measure flow front position inside the preform. Such sensors may also have the potential to measure flow velocity and pressure if properly optimized for LM experiments. The area of cure monitoring is also an important part of the program. Cure monitoring has been a major focus of NIST's research for some time. A detailed examination of the monitoring techniques listed in Table II was conducted to identify those that have the potential for on-line measurement. One result of this effort was a recent report (2) which provides an assessment of the state-of-the-art

process monitoring sensors for polymer composites. The preparation of this report was greatly facilitated by the fact that NIST had direct experience with all of the techniques involved. This capability will now be exploited through application to liquid molding.

Sample Preparation and Application to Parts

The final task involves the fabrication of samples for testing in another NIST program which considers the performance and durability of polymer composites. In addition, this task is applying the developments in the LM program to the study of real parts through cooperative efforts with industry. The best example is a program between NIST and the Automotive Composites Consortium (ACC). The ACC is a joint effort between Ford, Chrysler, and General Motors and was formed to conduct precompetitive research that promotes the use of composites for structural applications in automobiles. The ACC is demonstrating the results of their research by fabricating a series of parts. The first part chosen was the front end structure of the Ford Escort, and the fabrication method of choice was SRIM.

NIST is cooperating with the ACC by conducting process simulations to help optimize the fabrication of this part. In addition, the permeabilities for the reinforcement materials used in the part are being measured at NIST. The ACC benefits by the development of the technology to optimize part design and manufacturing. NIST benefits by having the opportunity to test research results with application to a real part. The initial process simulation focuses on mold filling and uses a 2.5-dimensional model with gravity since the part is a shell-like structure. The complexity of the reinforcement, however, may make it necessary to employ a fully three dimensional flow model eventually. To better visualize the mold filling, a computer animation program has been developed. It allows examination of the mold filling from any angle and permits halting the flow temporarily at any point for closer examination of the details of the filling pattern. Important events such as the closing off of an unfilled area and the formation of knit lines can be seen and studied much more easily with the animation than with the normal output from process simulations.

EXAMPLES FROM THE NIST PROGRAM

To illustrate the NIST program, two examples will be briefly outlined. More details on these particular studies can be found in references 3 and 4. The first example looks at the prediction of permeability and illustrates the use of microscopic flow models and how they can help to examine the effects on flow behavior of localized features such as the distribution of fibers in space. The second example examines two techniques that are commonly used to measure permeability and compares the results. This work illustrates the research in both materials characterization and flow visualization.

Permeability Prediction

Macroscopic models for fluid flow in LM are usually based on Darcy's law

$$\langle \boldsymbol{v} \rangle = -\frac{\boldsymbol{K}\cdot\nabla\langle P\rangle}{\mu} \qquad (1)$$

where <v> and <P> are the volume averaged velocity and pressure, respectively, **K** is the permeability of the porous medium, and μ is the viscosity. These models are the basis for most process simulation programs including those developed at NIST (1). One of the most important factors affecting the agreement between the actual filling of a part and the predictions of such process simulation programs is the accuracy of the permeability data available. At the present time, the best and essentially the only method for determining the permeability is through experimental measurements (3,5-7). While this is satisfactory in the sense that various techniques give consistent results (3), and hence, appear to be reliable, it is also desirable to have available theoretical models which can accomplish this. Such models would not only permit optimization of preform structure but also greatly increase the speed with which LM processes could be implemented and/or modified by eliminating (or reducing) the large number of carefully controlled experiments that are currently required for determining the necessary permeabilities.

A number of theoretical models for predicting permeability as a function of structure in fibrous porous media are available (8-10). The most widely used relation in composite applications is the Carman-Kozeny equation which for fibrous porous media is given by

$$K=\frac{\epsilon^3}{(1-\epsilon)^2}\frac{d^2}{16c_K} \qquad (2)$$

where ϵ is the porosity, d is the diameter of the fibers which make up the media, and c_K is the Kozeny constant which has a theoretical value of 2. While some studies have reported success with this equation (11,12), generally such success is over a limited porosity range with a value of the Kozeny constant much different from its theoretical value (13).* Such limited success is somewhat typical. Therefore, at this time, there is not available a general relation which describes the permeability of fibrous porous media over the entire range of porosities that are of interest.

In order to aid the development of theoretical models for permeability, various numerical studies have been undertaken with microscopic models (14-17*). In such studies, flow in ideal periodic arrays of cylinders (or some other appropriate structure) is modeled, from which predictions for permeability as a function of structure are calculated. Corresponding experiments on systems which closely resemble the idealized arrangements have also been conducted. A review of the relevant experimental and numerical results for fiber porous media has recently been completed (13). An interesting result for the case of axial flow through unidirectionally aligned fiber beds is that experimental measurements (11,18) consistently yield higher permeability values than those predicted by simulation (15). The same result holds true for the case of transverse flow (13). Thus, there is difficulty in matching experimental results not only with theoretical relations such as Carman-Kozeny but also with detailed simulation.

One possible reason for this discrepancy between simulation and experiment is that the materials used in LM preforms are heterogeneous in the sense that the network of fiber bundles

*personal communication,

(tows) which make up the global porous medium are themselves porous. Thus, in actual materials, there is flow not only around but through the tows. The effect of this heterogeneous structure on unsteady flow transients, void formation and ultimate properties has recently been discussed (19,20) and shown to be quite important. Therefore, it seems reasonable to investigate the effect of this property on the permeability as well.

The numerical study of the microscopic flow in fibrous porous media is complicated by the fact that this problem involves both open regions (the space between tows) and porous media (the tows themselves). The flow in the open media can be modeled using the Navier-Stokes equation. The flow in the porous media might be modeled using Darcy's law, but with this approach it is not possible to properly handle the interface between the two regions because the order of Darcy's equation does not allow for the proper specification of boundary conditions (i.e., continuity of velocity and stress) at interfaces. The approach used in this study to achieve the correct degree of continuity is to model the flow in the porous region using the Brinkman (21,22) form of the volume averaged momentum equation (denoted hereafter as BVAME) which is given by

$$\mu\nabla^2\langle \boldsymbol{v}\rangle - \mu\boldsymbol{K}^{-1}\cdot\langle \boldsymbol{v}\rangle = \nabla\langle P\rangle \qquad (3)$$

It is interesting to note that if only the first term on the left were present, the result would be mathematically equivalent to Stokes equation while if only the second term on the left were present, the relationship would be identical to Darcy's law. The most important feature of Brinkman's equations, however, is the presence of second order terms. When this relationship is used to describe the flow in the porous region, the second order terms make it possible to satisfy the boundary conditions at the interface with the open region where Stokes law is used to describe the flow. A variety of problems involving heterogeneous media have been successfully treated using this equation (23,24). While more general expressions than Eq. (3) are available (11,15,25,26) Eq. (3) represents the simplest and most easily applied form.

Simulation

The BVAME was used to develop a microscopic model for flow to elucidate the effect that tow permeability had on the overall permeability in fibrous porous mediums. The axial flow in a periodic, square array of cylinders acting under the influence of a constant pressure gradient of value -G was simulated for the case of both solid and porous cylinders. The computational domain for these geometries is depicted in Figure 1. The problem was scaled using the cylinder diameter, d, as the characteristic length, and a characteristic velocity of d^2G/μ. The relevant component of Eq. (3) is then

$$\frac{\partial^2 U}{\partial X^2} + \frac{\partial^2 U}{\partial Y^2} - \frac{a}{K^*}U = -1 \qquad (4)$$

where X, Y, U, and K^* are the dimensionless coordinates, velocity, and permeability, and a is a computational parameter equal to 1 in porous media, and 0 in open media. Solutions to this set of equations using the appropriate boundary conditions were generated using a Galerkin finite element scheme. Details of the boundary conditions and numerical formulation are discussed in

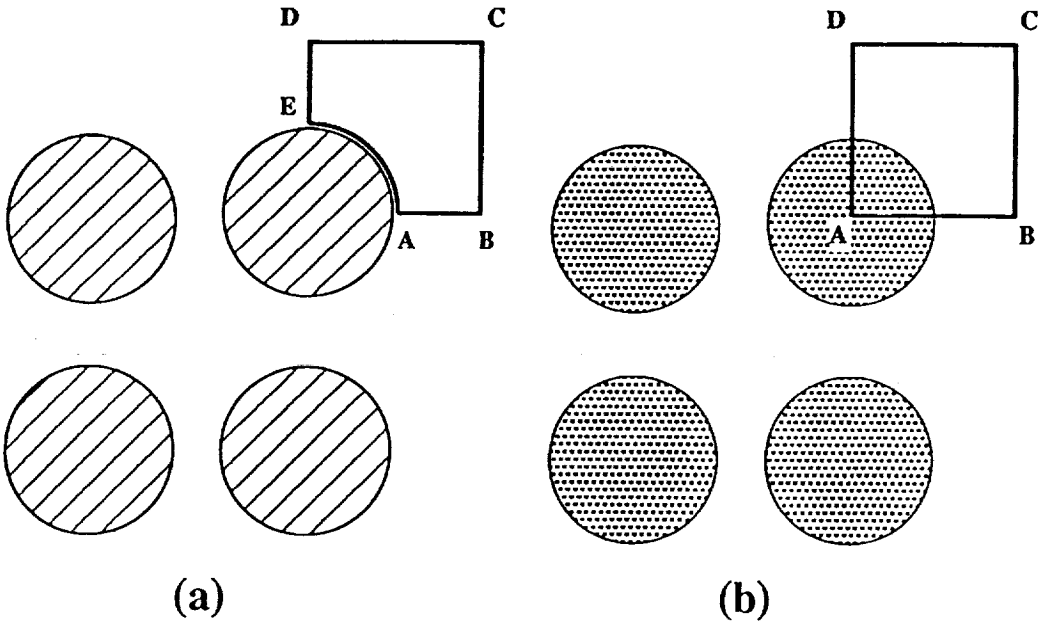

Figure 1: Model for flow simulation for (a) solid and (b) porous cylinders. The unit cell is indicated by the marked area.

detail elsewhere (4).

Calculations were performed for the case of solid cylinders first to verify the numerical scheme by comparing with other calculations, and also, to provide a reference point for looking at porous cylinder results. Figure 2 summarizes the computations by showing the dimensionless effective permeability (i.e., K/d^2) as a function of the porosity. Although not shown in the Figure, the results from the calculations performed here agree quite well with the computations by Sparrow and Loeffler (27). For the sake of comparison, the predictions of the Carman-Kozeny equation and experimental data of Gutowski et al. (11) are also plotted. The Carman-Kozeny results match the numerical calculations only at intermediate to low porosities, and deviate strongly at the extremes. This is similar to what is generally found when comparing Carman-Kozeny to experimental data for systems with solid fillers (13). The most significant observation from the Figure, however, is that the experimentally determined values of dimensionless permeability with porous tows are much higher than any of the numerically calculated and theoretical curves for solid cylinders.

Calculations for porous cylinders were performed with cylinder permeabilities of 0.1, 0.01, 0.001, and 0.0002. Iso-velocity contours (at the same contour values) for solid and permeable cylinders at a cylinder spacing corresponding to an overall porosity of 0.65 are compared in Figure 3 for the case of a cylinder permeability equal to 0.001. The Figure shows that the effect of the cylinder permeability is to shift the contour values inward towards the axis of the cylinder. This shifting results in an increase in the overall flow rate throughout the system.

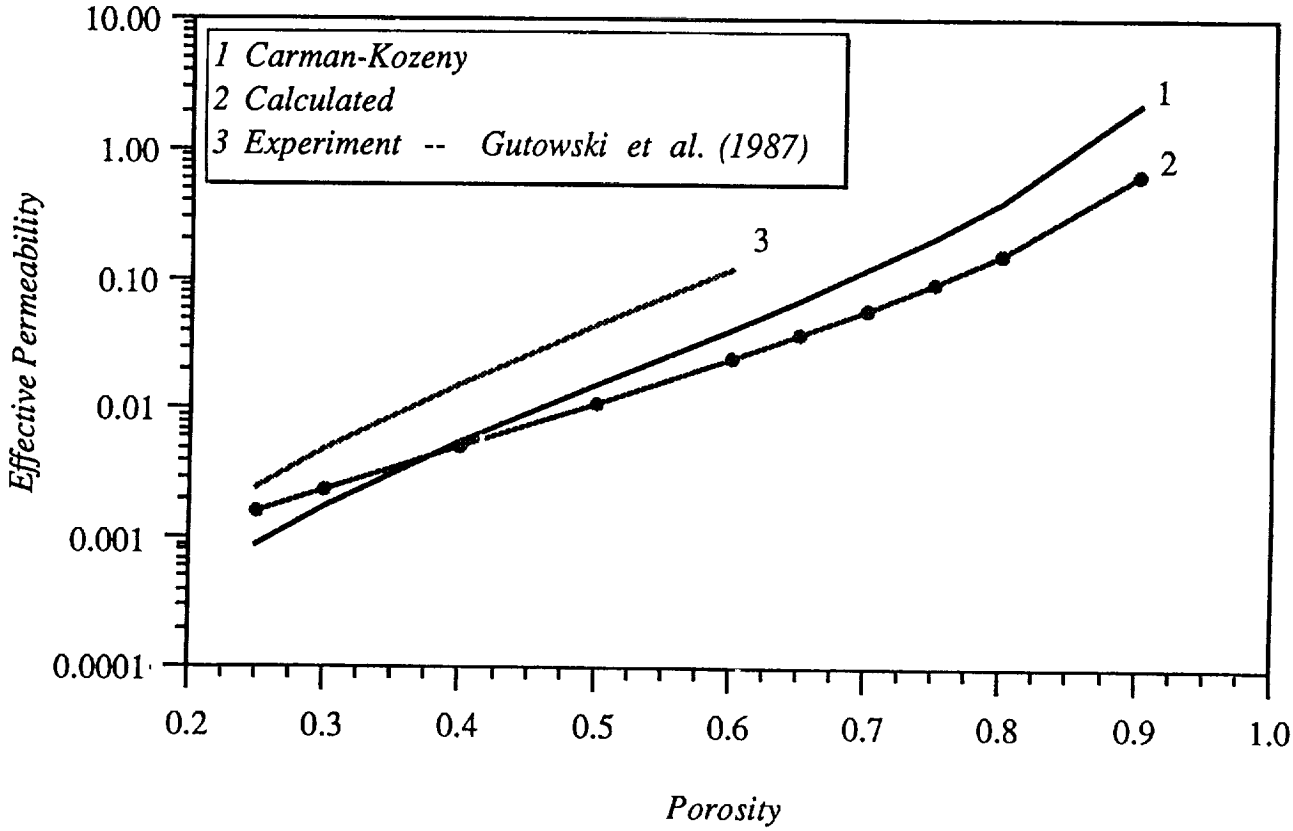

Figure 2: A comparison of the calculated and experimental values for effective permeability as a function of overall porosity.

Axial Flow, Iso-Velocity Contours

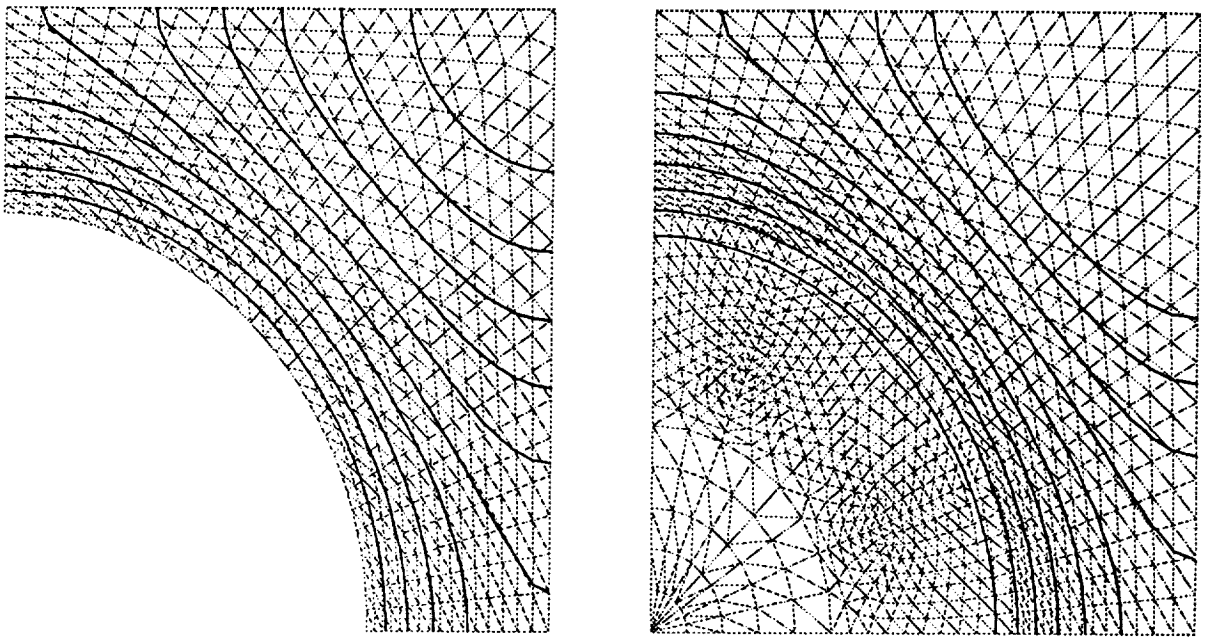

(a) Solid (b) Porous

Porosity = 65%

Figure 3: Iso-velocity contours for axial flow through periodic, square arrays of (a) solid and (b) porous cylinders. There are ten equally spaced contours. The maximum velocity for both cases occurs at the upper right-hand corner. The permeability of the porous cylinder is 0.001.

To further quantify this, the ratio of the flow rate in the open media portion of the porous cylinder flow to the flow rate for the solid cylinder flow, as a function of inner cylinder permeability, was computed for cylinder spacings corresponding to porosities of 0.9 and 0.65. This is shown in Figure 4. As was expected from inspection of the velocity contours, the results show that there is a significant flow rate enhancement due to cylinder permeability. The level of enhancement properly converges towards zero as the inner cylinder permeability decreases. Perhaps the most interesting feature of Figure 4 is that it shows that the flow rate enhancement due to the permeability of the cylinder becomes more important as the cylinder volume fraction increases. Thus, even at a cylinder permeability of 0.0002, the flow enhancement is still over 13% (see Table III).

When examining these results, it is important to note that although there is flow through

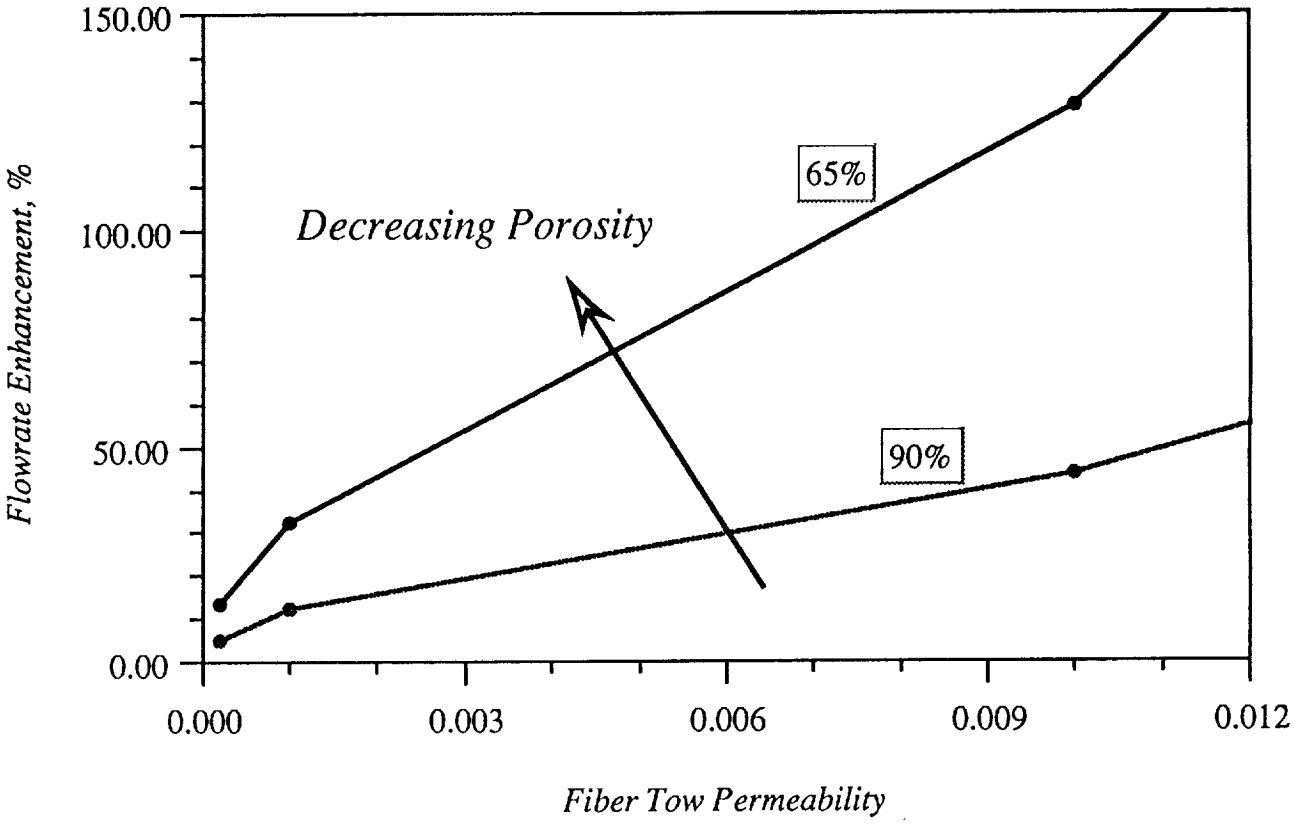

Figure 4: The percentage increase in the flow rate outside the porous cylinder with respect to the case of solid cylinders as a function of tow permeability. The effect becomes more pronounced as the overall porosity decreases.

the porous cylinders, this flow is quite small, and in fact, almost negligible compared to the overall flow rate. The real mechanism for the flow increase is the change in boundary conditions at the cylinder surface which shifts all of the flow contours in Figure 3 toward the center of the porous cylinders relative to the case for solid cylinders. This causes an increase in velocity throughout the entire flow field. Note particularly the increase in the size of the cross-sectional area at the highest flow velocity (upper right corner in Figure 3). Since the flow rate is the integral of the velocity taken over the entire flow domain, the overall change in this quantity is quite substantial.

Table III: Flow Rate Enhancement vs Fiber Tow Permeability

Fiber Tow Permeability	Flow Rate Enhancement (%)	
	Porosity = 0.90	Porosity = 0.65
0.1	225.0	749.6
0.01	43.7	128.8
0.001	12.1	32.7
0.0002	5.1	13.6

Summary

The calculations presented here indicate that the heterogeneous nature of the LM preform material can have a significant effect on the permeability. The calculations predict that the flow rate is substantially higher for porous cylinders than for solid cylinders at equal cylinder spacing and that this increase becomes more pronounced as fiber volume fraction increases. This is consistent with results in the literature where experimentally determined values of permeability in such model networks are generally found to be higher than their theoretical counterparts (13). The results here show that in such situations, the permeability of the tows provides a potential mechanism for flow rate enhancement, and hence, an increased permeability. At this time, calculation of an effective permeability for the overall medium for the case of porous cylinders has not been attempted. This will be done in the future, but requires intra-tow permeability vs. porosity data which is not presently available. Nevertheless, the results obtained here suggest that in order to develop theoretical relationships for permeability as a function of structure in fibrous porous media, it is important to take into account the intra-tow properties of the media.

Permeability Determination

The second example from the NIST program concerns the measurement of permeabilities.

Although all components of the permeability tensor can be important, the discussion here will focus on the in-plane components. There are two techniques commonly used to measure the in-plane permeabilities of preform materials. The first involves unidirectional flow while the second focuses on radial flow. As part of a major effort on permeability characterization, the NIST program is working in cooperation with General Electric's Central Research and Development Laboratory to conduct a detailed comparison of results from the two methods. This tests both the experiments and the flow model used to compare the results. In addition, the data are being examined in terms of the structure of the preform material in an effort to understand the observed behavior. The initial experiments involved measurements on three woven glass reinforcements: J.P. Stevens 8-Harness satin, and Carolina Narrow Fabrics 8-Harness satin and Crowfoot weaves.

Characterization of the in-plane permeability requires the determination of three parameters: the two principle permeabilities, K_{11} and K_{22}, and the principal angle, θ, i.e the angle between the warp direction of the preform material and the direction of the larger of the two principal permeabilities. Moreover, the values obtained for the permeabilities are different for measurements of flow into a dry preform and for flow into a preform completely saturated with the fluid. Although explanations for this difference have been offered (19), experimental measurements for both are still required for a complete characterization.

One-Dimensional Flow Experiments

The one-dimensional flow experiments were conducted in a mold with a 152.5 mm x 152.5 mm (6 in. x 6 in.) sample section where the thickness of the test specimen could be adjusted between 3.175 mm and 12.7 mm (0.125 in. and 0.5 in.) (see Figure 5a). The top of the mold was 12.7 mm (0.5 in.) thick plexiglass to permit observation of the flow front, and the flatness of the plexiglass surface was checked during the experiments to detect and prevent problems due to pressure driven deflection. Fluid was forced through the mold from a pressure-pot, and the flow was measured as it entered the mold with a calibrated rotameter and was also monitored at the mold exit with volumetric measurements. Pressures at the mold inlet were measured by transducers that were mounted at two positions on the back face of the mold located at the lower boundary of the reinforcement sample.

The results from the one-dimensional flow experiments were accumulated by measuring, at preset pressure drops, the flow of corn syrup/water solutions through the woven glass fabric, compressed to 12.7 mm (0.5 in.) thickness and previously saturated with the test fluid. As the pressure drop was increased, the flow rate increased linearly (see Figure 6), as expected, for the Newtonian test fluid. Assuming Darcy's law to be valid, the effective permeability of the preform in the flow direction was obtained from the slope of the flow-pressure curve. The linear relationship of the flow and pressure drop qualitatively indicates that pressure induced bending

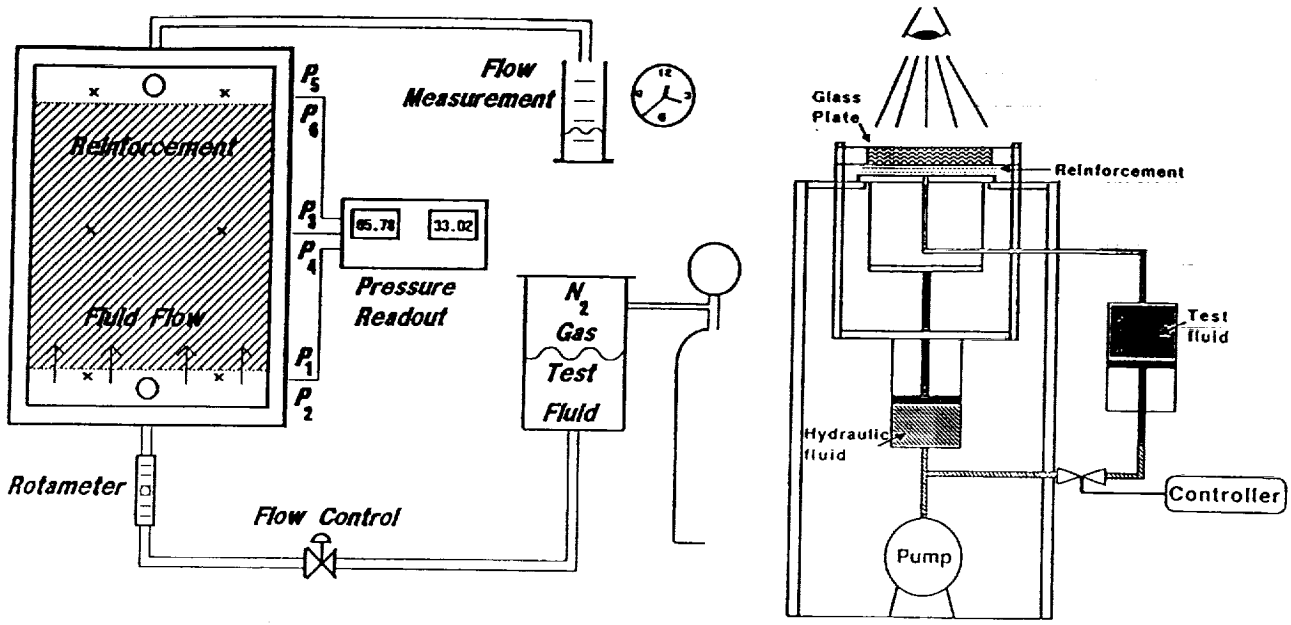

Figure 5: Schematic diagrams of the experimental equipment: (a) one-dimensional flow equipment and (b) radial flow equipment.

of the upper plexiglass plate did not occur. This provides a very accurate way to determine permeability in saturated flow. Since the top of the mold is plexiglass, experiments can also be performed to measure the progression of the flow front into a dry preform. Thus, although the experiments here focused on saturated flow, the permeabilities for both saturated and unsaturated flow can be obtained with this technique.

Radial Flow Experiments

The radial flow experiments were conducted at General Electric's Central Research Laboratory using the apparatus shown in Figure 5b (3). A radial planar flow was achieved by injecting the fluid through a central 1.524 mm (0.060 in.) diameter gate into a 203.2 mm x 203.2 mm (8 in. x 8 in.) region between two parallel plates containing the reinforcement. Each layer of reinforcement had a 4.762 mm (0.1875 in.) diameter hole centered over the gate to permit the fluid to penetrate evenly through the thickness of the sample. A 25.4 mm (1.0 in.) thick upper glass plate permitted visual observation of the flow. A central hydraulic system supplied both the pressure to clamp the reinforcement sample and pump the test fluid from a separate injection cylinder.

After an initial transient, the flow front maintained a shape and orientation that appeared qualitatively unchanged as it grew. Traces of the flow front were made manually, with a typical example shown in Figure 7 for the J.P. Stevens 8-Harness satin weave fabric. Although relatively crude, this presentation technique illustrates important general features of the flow front. The shape of the flow fronts were analyzed by digitizing the traces. For a preform that

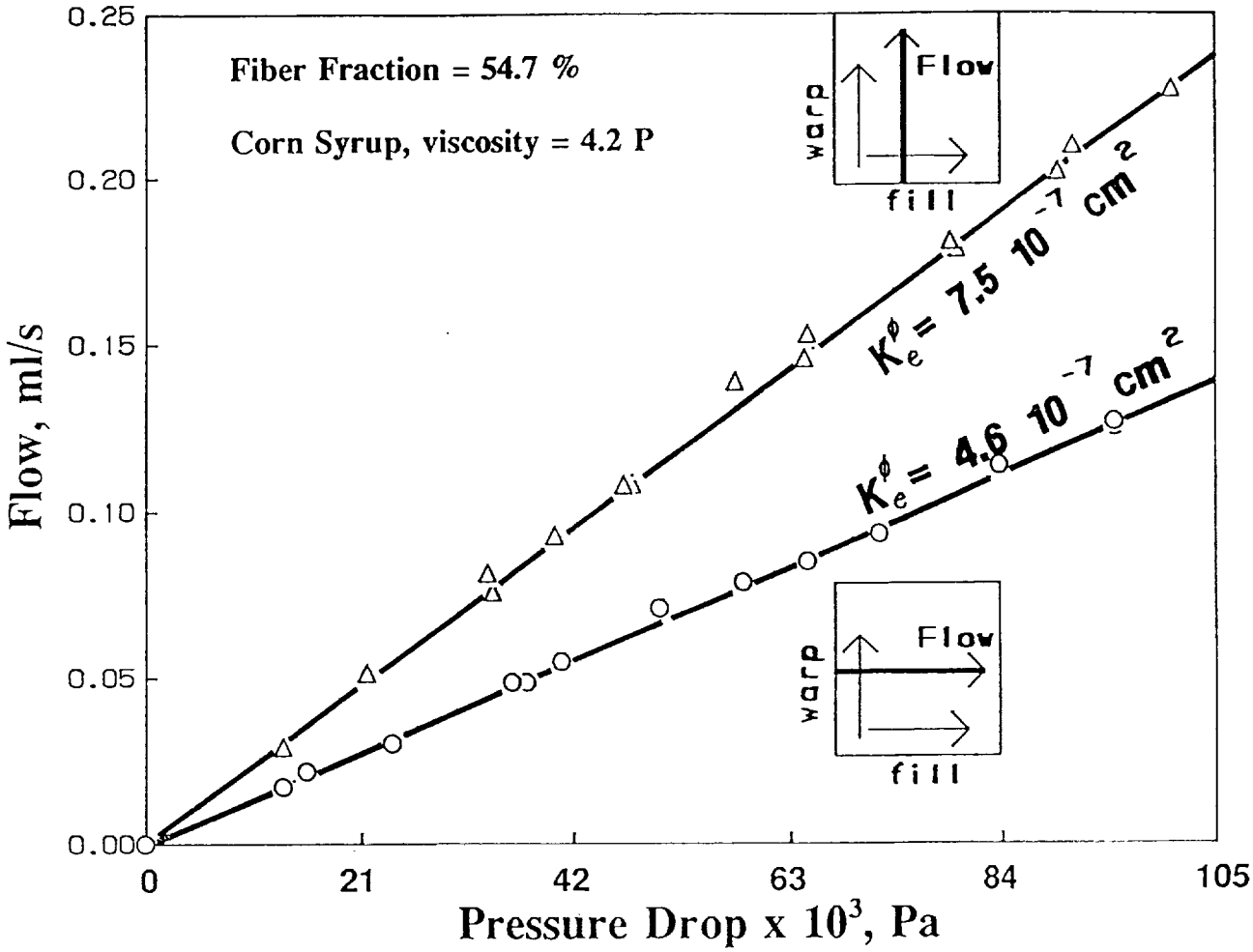

Figure 6: Typical results from a one-dimensional flow experiment showing flow vs. pressure drop for two fabric orientations.

is isotropic in the plane, a circular pattern would be expected. If the permeability in the plane is anisotropic but orthotopic, an elliptical shape should fit the data. For the materials examined here, the flow front was indeed elliptical in shape, and this confirms orthotopic behavior for the high volume fractions tested. The direction of the principal axis of the ellipse relative to the warp fibers in the preform provides a measure of the principal angle, while the square of the ratio of the major to minor axis lengths in the ellipse is equal to the anisotropy which is the ratio of the two principal permeabilities, K_{22}/K_{11}.

As can be seen, the determination of the principal angle and the anisotropy in the radial flow experiment is quite easy. Although it is also possible to determine the quantitative values of the permeabilities, this is more difficult. Moreover, the experiments described above measured

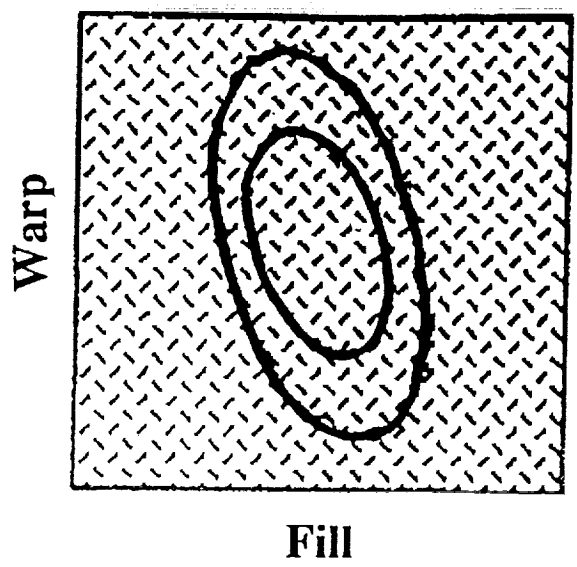

Figure 7: The elliptical flow fronts observed in J.P. Stevens 8-Harness satin fabric.

unsaturated flow properties. Although permeability measurements for saturated flow are possible in the radial flow experiments, they are considerably more difficult. Consequently, the work here focused only on the determination of the principal angle and anisotropy for unsaturated flows and compared the results with values for these parameters obtained from saturated, unidirectional flow experiments.

Comparison of Results

To compare the one-dimensional flow results with the radial flow results, it was necessary to calculate the principal permeabilities and the principal angle from the unidirectional flow experiments. By using a two-dimensional version of Darcy's Law, the effective permeability, K_e^{ϕ}, in a direction which is at an angle, ϕ, relative to the warp direction in the preform can be written in terms of the principal permeabilities and the principal angle.

$$K_e^{\phi} = K_{11}\cos^2(\phi-\theta)\bullet$$

$$\left[(1+\frac{K_{22}}{K_{11}}\tan^2(\phi-\theta)) - \frac{(K_{22}/K_{11}-1)^2}{\frac{K_{22}/K_{11}}{\tan^2(\phi-\theta)}+1}\right] \qquad (5)$$

Since this equation involves three unknowns, measurements at a minimum of three different orientations must be made. To improve reliability, four orientations were tested in this work. The results of measurements conducted at two orientations are shown in Figure 6. That figure indicates that the permeability is anisotropic which agrees with the radial flow experiments. From the four experiments on each material, the values for the principal permeabilities and the principal angles were calculated for the three materials tested. The results are given in Table IV along with the data obtained in the radial flow experiments. Additional details of the analysis are given in reference 3.

The consistency of the radial flow experiments performed at GE and the one-dimensional flow experiments conducted at NIST is illustrated in Table IV. Even though two different laboratories conducted the experiments, the agreement is quite good. As the experimental techniques are further refined, it will be important to see if the agreement gets even better.

Table IV: Comparison of 1-D and Radial Flow Experiments

Material	Laboratory	Principle Angle	K_{22}/K_{11}
J.P. Stevens 8-H satin	GE	12	0.64
	NIST	13	0.72
Carolina Narrow Fabric 8-H satin	GE	-17	0.77
	NIST	-15	0.73
Carolina Narrow Fabric Crowfoot	GE	3	0.69
	NIST	4	0.61

It is interesting to note that the principal direction of the permeability is not coincident with either the warp or fill yarn directions. An hypothesis for this behavior has been developed based upon a closer examination of the structure of the woven fabrics. The crossing of the fiber tows creates a series of valleys in a woven material known as the crimp. Figure 8 illustrates this structure for the J.P. Stevens 8-Harness satin fabric, and the Carolina Narrow 8-Harness and Crowfoot fabrics used in the experiments reported above. The close proximity of neighboring crossing points creates a nearly continuous trough that may act as a conduit of low resistance to flow.

Note that the orientation of the illustrated crimps in Figure 8 match the orientation of the principal axes of permeability observed in both the radial and one-dimensional flow experiments with the two 8-Harness satin weave fabrics. A secondary, nonorthogonal crimp direction does not appear to influence the flow because the tow crossing points are not on adjacent tows. However, a crimp direction in the Crowfoot weave could not be identified for comparison with the principal axis of permeability in that material. An additional unresolved point in this discussion is that the major crimp directions on opposite sides of the fabrics are not oriented identically, creating a complex interface between fabric layers which must be explored further.

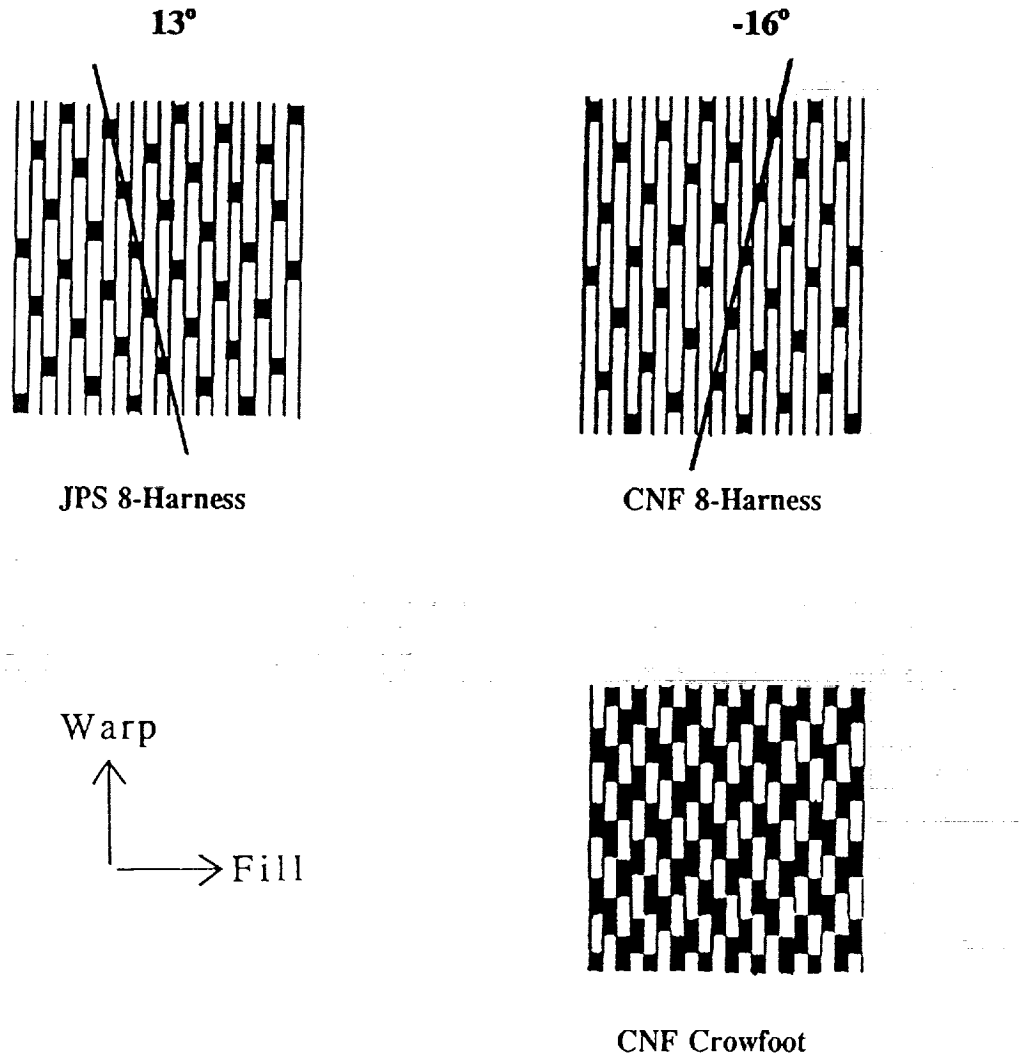

Figure 8: Structure of woven fabrics showing crimp directions. The angle between the crimp direction and the warp fiber direction is indicated. Note that a crimp direction is not apparent in the Crowfoot weave.

The data developed in this project represent a first step in exploring not only the test methods for permeability measurement but also the models used to analyze the data. Constitutive models, such as Darcy's Law, have largely been used without detailed verification. The limited results obtained so far not only indicate that the unidirectional flow and radial flow experiments are consistent but also support the use of Darcy's Law in flow simulations. Since the radial flow experiments quickly provide a measure of flow anisotropy and principal orientation while the one-dimensional flow experiments easily yield quantitative measurements of the permeability, the results also suggest that the two experiments could be used in combination to simplify the characterization of preform materials.

CONCLUSIONS

The program described here seeks to advance the scientific basis for liquid molding through a coordinated effort involving four tasks: (1) characterization of the material properties associated with processing, (2) development of process simulation models at both the macroscopic and microscopic levels, (3) application of on-line measurement techniques to test and refine the simulation models and to explore the technology for on-line process control, and (4) production of test samples and the application of the technology developed in the program to real parts through cooperative interactions with industry. Such a comprehensive and interdisciplinary approach offers the best hope for achieving the full potential of the liquid molding process.

REFERENCES

1. F. R. Phelan Jr., "Liquid Molding: Computer Simulation," p. 36 in "Polymers, Technical Activities 1991," NISTIR-4696, February 13, 1992.

2. D. Hunston, W. McDonough, B. Fanconi, F. Mopsik, F. Wang, F. Phelan, and M. Chiang, "Assessment of the State-of-the-Art for Process Monitoring Sensors for Polymer Composites," U.S. Department of Commerce, NISTIR-4514, June 1, 1991.

3. A. J. Salem, and R. S. Parnas, "Presented at the ASC 6th Technical Conference on Composites," (1991).

4. F. R. Phelan Jr., "Advanced Composite Materials: New Developments and Applications, Proceedings of the 7th Annual ASM/ESD Advanced Composites Conference," 175, ASM International, (May 1991).

5. K. L. Adams, and L. Rebenfeld, Textile Research Journal, 57, 647-654, (November 1987).

6. K. L. Adams, B. Miller, and L. Rebenfeld, Polymer Engineering and Science, 26(20), 1434-1441, (November 1986).

7. C. A. Fracchia, "Numerical Simulation of Resin Transfer Mold Filling," M.S. Thesis, University of Illinois at Urbana-Champaign, (January 1990).

8. R. Gauvin, and M. Chibani, SAMPE Quarterly, 21(5), 52-58, (1990).

9. R. K. Young, S. P. McCarthy, J. P. Fanucci, S. C. Nolet, and C. Koppernaes, SAMPE Quarterly, 22(3), 16-22, (April 1991).

10. R. M. Koerner, J. A. Bove, and J. P. Martin, Geotextiles and Geomembranes, 1, 57-73, (1984).

11. T. G. Gutowski, T. Morigaki, and Z. Cai, Composite Materials, 21, 172-188, (1987).

12. R. C. Lam, and J. L. Kardos, "Proceedings of the Society of Plastics Engineers 48th Annual Technical Conference (Antec '89)," 1408-1412, (May 1989).

13. L. Skartis, J. L. Kardos, and B. Khomani, Materials Research Laboratory and Department of Chemical Engineering, Washington University, St. Louis, MO, 1991.

14. A. S. Sangani, and A. Acrivos, Int. J. Multiphase Flow, 8, 193-206, (1982).

15. R. E. Larson, and J. J. L. Higdon, J. Fluid Mech., 166, 449-472, (1986).

16. R. E. Larson, and J. J. L. Higdon, J. Fluid Mech., 178, 119-1362, (1987).

17. L. Skartis, J. L. Kardos, and B. Khomani, Materials Research Laboratory and Department of Chemical Engineering, Washington University, St. Louis, MO, 1991b.

18. R. R. Sullivan, J. App. Phys., 13, 725, (1942).

19. R. S. Parnas, and F. R. Phelan Jr., SAMPE Quarterly, 22(2), 53-60, (1991).

20. N. Patel, and L. J. Lee, "Proceedings of the Society of Plastics Engineers 49th Annual Technical Conference (Antec '91)," 1985-1990, (May 1991).

21. J. C. Slattery, "Momentum, Energy and Mass Transfer in Continua," Robert E. Kreiger Publishing Company, Huntington, New York, 2nd Edition, Huntington, New York, (1981).

22. H. C. Brinkman, App. Sci. Res., A1, 27, (1947).

23. M. N. Kaddioui, and D. Sigli, Applied Scientific Research, 47, 23-44, (1990).

24. R. Parnas, and Y. Cohen, Chem. Eng. Comm., 53, 3-22, (1987).

25. P. G. Saffman, Stud. Appl. Maths., 50, 93-101, (1971).

26. J. Koplick, H. Levine and A. Zee, Phys. Fluids, 26(10), 2864-2870, (1983).

27. E. M. Sparrow, and A. L. Loeffler Jr., AIChE Journal, 5(3), 325, (1959).

N93-14748

ADVANCES IN 3-DIMENSIONAL BRAIDING

Cirrelia Thaxton, Rona Reid, and Aly El-Shiekh
Mars Mission Research Center
College of Textiles
North Carolina State University
Raleigh, NC

ABSTRACT

This paper encompasses an overview of the history of 3-D Braiding and an in-depth survey of the most recent, technological advances in machine design and implementation. Its purpose is to review the major efforts of university and industry research and development into the successful machining of this textile process.

INTRODUCTION

The technology of 3-D Braiding epitomizes the evolution of ancient art and custom into the science of engineering a new, innovative textile process. Unlike other textile techniques like weaving and knitting, 3-D Braiding involves the continuous intertwining of two or more yarn groups in a bias direction, and the structure formed possesses remarkable structural integrity, high damage tolerance, torsional stability and characteristic handling ease [16]*. As this technology expands from university research to industrial manufacturing and development, careful investigation into the design and automation of successful braiding machines is imperative. Furthermore, the future growth of this technology depends on the ability of investigators to improve upon and modify processing parameters while reducing any process limitations. Accordingly, this paper addresses current advances in the area of 3-D braiding machines, focusing on the three main design areas: machine bed configuration, carrier design, and beat-up mechanisms. These three components are instrumental to the overall feasibility of a design for a modern 3-D braiding apparatus.

* (References 1–24 are cited in the text)

HISTORY

The origin of 3-D braiding can be traced to knot-tying, which is one of the oldest technologies known to man [17]. Since the beginning of time, man has ritualistically twisted and plaited hair for convenience, adornment and customs. This decorative styling of the hair developed into the practice of intertwining grass and natural fibers to form ropes and ornate embellishments in artwork and clothing design. In the ancient Orient, skilled artisans crafted intricate braids called Kara Kumi for ornamental purposes [21]. During the 17th century, English sailors devised spool braiders that formed braids for practical rather than artistic use. The spool braider or sinnet made braids that served a useful purpose as durable ropes [21]. The formation of braids for scientific rather than artistic means underwent a slow evolution until the mid-twentieth century.

During the next phase of development of braiding as an advanced technology, the practice of braiding was no longer considered only a crafting art. In the 1940's, W. T. Harburger authored a paper on the engineering structure of braids [17]. His paper addressed geometric factors relating to the concept of braiding. In the next decade, D. Brunnschweiler discussed the configuration, geometry, and tensile properties of tubular braids [17]. In the 1960's a plethora of new concepts involving the mechanisms of the 3-D braiding process evolved. An informative book by W. A. Douglas dealing with braiding machinery and processing parameters became a cornerstone for the growing technology [17]. Comprehensive patents by Bluck and General Electric established 3-D braiding as a technical process in the field of science and engineering. Emerging from this period of growth and innovation were two fundamental classifications for the braiding process, four-step and two step. Both classifications share two distinct machine types, regular and circular [13]. The former produced braids having right-angled corners, whereas the latter produced round cross-sectional shaped braids. In 1965, General Electric Reentry Systems Divisions invented the Omniweave braiding process for the production of multidirectional braids for aerospace composites. The 4-step machine incorporated sequential, discrete carrier motion as opposed to continuous motion [17]. GE claimed that the Omniweave would vary fiber orientation while braiding stiff, brittle fibers without delamination failure [13]. In 1969 the Bluck patent on "High-Speed Bias Weaving" detailed a

circular 4-step braiding machine for the production of hollow braids [13]. On the machine spools sitting beneath the braiding plane supplied yarns. During the process, these yarns moved through a network of holes in a guide nest which circumrotated the machine. This process was faster than its predecessors; however, entanglement of feeding yarns due to guide nest movement was a major limitation [13]. Consequently, the braided product had a fixed length and yarn delivery was intermittent.

In 1973 Maistre patented the first automated 3-D braiding machine. He promoted the new braiding process as SCOUDID, an acronym for Structure Composite Unidirectionelle Indelaminable (undelaminable, unidirectional composite structure) [13]. A regular-type, 4-step braiding machine, the SCOUDID had the capability to braid over 3200 yarns in simultaneous fashion. The yarn supply rose vertically and did not traverse the cross-section of the braid. The braided products had fixed lengths and two layers of yarn with adjoining edges [13].

In 1982, Florentine developed a versatile braiding machine for the production of complex-shaped 3-D preforms having integrated structural geometry and varying lengths. The Magnaweave, his 4-step regular braiding machine had a system comprised of 4 x 2 motion due to row/column shifts actuated by pneumatic cylinders, and manufactured braids possessing "SCOUDID" texture geometry [13]. Also, a combing or compacting movement followed an orthogonal shedding mechanism providing a high degree of freedom in material orientation control [9]. The Magnaweave had a counterpart, the Magnaswirl. This counterpart was a circular braider producing braids with circular cross-sections by three distinct motions: (1) ring or angular, (2) spoke or radial and (3) vertical or combing [16]. The design of the machine consisted of radial rows where carriers sat and a base track for tangential motion of arcuate members. The partial occupancy of the radially positioned rows by carriers produced tight braided structures [13].

Contributing further to the evolution of the 3-D braiding process was the invention of Through - the - Thickness$^{t\,m}$ technology by Atlantic Research Corporation (ARC), which is considered in industry to be the leading authority on 3-D or Through -the - Thickness Braiding. The circular braider manufactured had concentric grooved rings and carriers capable of alternate row and column position shifts. During the process of Through - the - Thickness^{tm} braiding, a technique for manufacturing 3-D seamless patterns by continuous intertwining of fibers, the carriers situated on

the machine bed moved simultaneously [6]. The process was a major advancement exhibiting a novel textile technology of arranging fibers in irregular geometries for arbitrary thickness [8]. The braided products of this process had varying lengths, composite material toughness, and adequate delamination resistance.

As the present decade approaches the 22nd century, the advance of 3-D Braiding is inevitable. The current trend is toward computer-aided design and manufacture of the braiding process. Ko and his associates devised a computer simulation of the 4-step 3-D braiding procedure [17]. This system screened braid geometries for their respective cross-sections. Then, Brown and Harman used computer aided design to simulate the operation of a braiding machine and to trace the resulting yarn paths of the braid [18]. Developing areas of machine design and exploring multidirectional braiding techniques for near-net shapes of preforms through the extensive use of CAD/CAM technology are the future of composite engineering.

MACHINE BED DESIGN

The machine bed, a major component of any 3-D braiding apparatus, supports the precise movement of fiber-carrying devices (carriers or braiders). Accordingly, the purpose of the machine bed is to facilitate and expedite carrier placement along predetermined paths within the braiding plane. In recent years many configurations for machine beds of regular, circular, and variations of both types have been designed and tested.

The 3-D braiding group at North Carolina State University's (NCSU) College of Textiles designed and constructed a 2-step regular braiding machine. Its machine bed warrants attention due to its potential as a marketable advance. Consisting of an assembly of unit tiles made of aluminum plates embedded with orthogonal T-grooves, the 2-step braider utilizes a dual arrangement (Figure 1) [18]. The first prototype exhibited machine arrangement one, having machine sides parallel and perpendicular to slots. The prototype consisted of four (4) tiles. Each unit tile has dimensions of 12" x 12" x 1" and a distance of 3" between grooves (Figure 2) [19]. Each tile has a hole for axial insertion from spools underneath the braiding plane. Next, for the second arrangement, which reduces machine space, machine sides are parallel and perpendicular to the preform sides, being at 45° angles to the slots.

The actuation system embodies an array of stiffened timing gear-belts that push the carriers. While inside the machine bed grooves, the belt behaves like a "rigid rod" [18]. The flexible joint action occurs once the belt emerges from the groove and drops under its own weight. Also, the driving system utilizes stepping motors [20]. Four of the eight stepping motors drive the timing gears to control carrier stroke. The other four motors transport the driving units carriages across the perimeter of the machine bed.

The 2-step regular machine incorporates a computer terminal and controller as its control system. Utilizing a special motor control language, the braiding programs are written. The programs are transmitted to the CPU of the controller, while the APPCOR IMC-8 controller guides the action of the eight stepping motors (Figures 3 & 4) [19].

This prototype has many advantages. First, it can be easily manufactured and expanded as a result of its tile assembly construction of the machine bed. Second, the machine cost can be reduced because only eight stepping motors are needed regardless of machine size. Lastly, the mechanism of a horizontal rod driven by two air cylinders over the machine bed acts as a convergence device which eliminates the "over jamming" effect [18].

An emerging technology is in the area of multi-ply braiding. This concept involves the formation of braid with more than 2 layers (plies). Brown and Ratliff of ARC invented a technique to move the machine bed that was comprised of a sequenced braider motion for the multi-ply technology [7]. Patented in 1986, this method includes a machine bed configuration of a row/column carrier arrangement. When an intermediate row moves to block the motion of a column, a tamping force causes the column to shift to one side of the selected row [7]. This sequence of action makes carrier alignment in columns simpler.

This braiding innovation claims the following advantages: (1) machine jams are eliminated, (2) unjammed operation of a multi-ply braiding system is achievable and (3) lower cost, low tolerance multi-ply braiders may be used [7].

For circular braiders, row movement is caused by the shift of concentric rings. Column (radial) movement occurs when discreet carriers are shifted. A difficulty in machining of circular braiders arises due to the expense of producing properly fitting concentric rings [15]. Often, a circular braider is quite large, requiring ample space. Also jamming can occur when a large number of carriers shift radially.

Consequently an easily expandable 2-step braiding machine in circular form having no concentric rings was next designed and built by El-Shiekh and his colleagues at NCSU. The machine bed has 12 tiles arranged together to form a circular configuration (Figures 5 and 6) [13]. Each tile, made of aluminum, consists of axial tubes, magnets, stoppers, and braiding carriers. The yarn supply for the axials passes from a point above the plane of braiding down through the axial tubes where they are suspended by weights. The spooled carriers maintain a supply of up to fifteen feet of yarn.

On the machine bed a magnet attracts the carriers against yarn tensions. The action of the stoppers halts carrier movement maintaining adequate yarn tension. The bed has 48 slots in clockwise direction. Every slot is formed in the shape of an inverted "T" shape, which facilitates the in and out movement of the carriers [13]. Elimination of the jamming effect is a major advantage of this assembly. The carrier arrangement determines the required preform shape.

An ARC circular braiding machine was patented in 1988 by Richard Brown. The apparatus bed consists of a plurality of interchangeable rings having the same diameter (Figure 7) [4]. The rings are situated side by side in an axial arrangement. These ring members hold carriers that move axially and rotate about the central axis of the machine. During the braiding process, the Brown apparatus intertwines yarn by shifting adjacent carrier rows in opposing directions while spinning adjacent ring members in opposite directions. Notably, an actuating mechanism causes the ring rotation and propels the carrier rows in axial fashion to form the braid. This mechanism comprises a "manually or power driven actuator" that is connected to the rings through gears [4]. The actuation system for the carriers is composed of "slidable" rods or pistons which are situated at opposite carrier-row ends. These pistons may be driven pneumatically or mechanically.

The cylindrically designed circular braiding machine is a noteworthy advancement due to the following distinctions [4]:

(1) ring members have same dimensions for ease in constructing the machine bed
(2) ring members are both expandable and interchangeable
(3) the machine requires little space and
(4) the machine can produce axi-symmetric and cartesian braids.

ARC also patented a continuous circular braider comprised of a multitude of "flexible annular" members or belts. These belts support the carriers and are arranged in side by side fashion, axially

aligned [10]. The belts glide circumferentially relative to a central axis. The carriers, mounted on the belts move as well. An actuation device drives the belts and carrier rows along axial routes intertwining the fiber into a braided structure [10]. During the braiding process, the motion of adjacent carrier rows in opposing axial directions and the movement of adjacent belts in opposite circumferential directions initiate braid formation.

On this apparatus the mechanism of actuation consists of sensors mounted on the belts which activate engaging slots found on a sector-by-sector basis. After belt shifting occurs this actuating mechanism allows the sector positioning of sensors [10]. Next shoes, sliding mechanisms, are exchanged with belts in that one sector. This sequence of sensor positioning and shoe sliding repeats for each sector until the original sector is reached.

The Culp patent makes the following progressive claims [10]:

(1) a multitude of belts are arranged axially to support carriers for axial motion,
(2) the machine track supports and guides the belts along a circular path
(3) a group of carrier rows are situated on the belts
(4) an actuation device moves the belts circumferentially and carrier rows axially.

In 1989 Spain of Airfoil Textron Incorporated (ATI) patented a regular, 3-D braiding apparatus with a machine bed designed for the integration of braider and axial yarns. The machine surface consists of a grooved X-Y grid equipped with axial guides for the yarn supply lying beneath the grid on creels [23]. Inside the grooves sit the carriers whose movement is controlled by means of solenoids or fluid cylinders at opposing ends for each column and row (Figure 8) [23].

This patented design is noteworthy due to its inclusion of an innovative technique of fugitive (non-permanent) braider or carrier yarn removal following braiding. This procedure facilitates matrix impregnation, spacing control between non-fugitive (permanent) braider yarns and engineering of preform physical and mechanical properties [23]. In another embodiment of the machine bed for this design both axials and braiders are permanent, creating a resultant structure with improved mechanical properties [23]. Therefore, the Spain apparatus varies machine configurations in order to diversify the design potential for the resultant braided products.

In 1990 Ivsan and his associates of ATI patented a braiding apparatus having a cylindrical surface unlike flat, planar machine beds. This cylindrical or quadratic carrier surface serves to minimize the distance between carriers and the convergence point of the

forming braid (Figure 9) [15]. At opposite ends of the quadratic surface lie actuators of hydraulic or pneumatic form, which propel the carriers along support members or curved tracks comprising the bed [15]. The support members move sequentially as carriers transit adjacent tracks. A series of tubes on the tracks guide 'axial stuffer fiber strands' in a radial fashion [15].

The basic structure of the machine bed also includes stationary, independent base members that house spindles and guide rods [15]. In contrast to carrier movement the cylindrical bed does not allow independent axial movement relative to the support members [15]. The axial direction of motion forms a circular arc with respect to corresponding support members. The shifting of carrier paths across adjacent support members causes the intertwining of carrier and axial yarns to maintain proper yarn tensioning and convergence of the braid.

Fabrication of a multi-layer interlocked braided preform requires a machine bed which unlike track and column machines does not limit the insertion of 0^{o} orientation yarns. This process is faster, allowing complex carrier systems movement and reducing the mechanical efficiency necessary to automate the process [3]. During the multi-layer interlock braiding process, carrier movement is both smooth and continuous. David Brookstein of Albany International Research Corporation (AIRC) commented,"the primary structural characteristics of multi-layer interlock braids are the nature of interconnectivity of adjacent laminae" [2]. The resultant braid consists of yarn that traverses from an original braided layer to an adjacent layer and back to the original layer.

AIRC has manufactured a multi-layer interlocking tubular braiding machine, equipped with five layered machine configuration. Each layer has the capability of braiding 48 yarns. A network of counter rotating horn gears propels the carriers along diagonal paths moving the yarns layer to layer of the preform [2]. The machine provides for up to 48 axials per layer. Thus, 480 yarns may be simultaneously braided. Another system developed by the AIRC group was designed to manufacture braided preforms of varying shapes. Cross-sections in the form of C, I, J, L, X,and Z are possible to construct on the system. The proposed system consists of a group of 4 x 2 track and gear modules [2]. These modules have "extra-modular" interlock positions which can be assembled to produce a given shape. The braided product of this system differs from the product of either the 4-step or 2-step process due to the yarn configuration patterns [2]. For instance, the yarns in one exterior layer of the interlocked structure need not pass through the adjacent

layer. Also, in contrast to the 2-step process, no axial yarns are needed for structural integrity [2].

CARRIER DESIGN

All 3-D braiding machines need sufficient yarn supplies delivered from movable housings, called carriers, which follow predetermined paths forming viable braided structures. Since the notion of moving a large yarn supply is problematical, the manufacture of small, compact and efficient carrier assemblies is crucial. Small carrier assemblies transit machine beds quickly and precisely. Yet, on flat, planar machine beds, due to their change of distance at the convergence point of the braid, these assemblies must retract yarn to prevent yarn slackening [13]. Thus the mechanism of the carrier serves to maintain a properly tensioned yarn, to allow feeding or retraction of the yarns (if necessary), and to direct the movement of yarn paths during the braiding process.

In 1987, William Heine of ARC filed a patent on an apparatus equipped with a main fiber spool which sat atop the fiber carrier [14]. The yarn follows a path from the main supply around a guide and through an aperture positioned within a take-up spool. The rotational axis of the main spool is perpendicular to the rotational axis of the take-up spool. This take-up spool is equipped with a tensioning device in the form of a spring assembly [14]. The carrier can be equipped with wheels for ease of movement.

Fulfilling the need for a carrier assembly that is compact, reliable and easily constructed, the Heine carrier also employs an adequate tensioning mechanism that has horizontal orientation above the yarn supply. This mechanism consists of a ratchet within the take-up spool that releases a pretensioned spring giving rotational force for the desired fiber tension [14]. While the braiding progresses, the take-up spool rewinds slack in the yarn preventing sagging. Also, constructed of a suitable material like metal or plastic, the carrier is economical.

The major claims of the patent provided a basis for future research and invention in the area of carrier design (Figure 10) [14]:

(1) an elongated housing with an open end
(2) a cap member mounted on the open end of the housing which is removable and
(3) a take-up spool rotatably held on the cap member with perpendicular rotation to the axis of rotation of the supply spool.

The design is suitable for use on a multi-ply braiding machine which uses a matrix array of carriers undergoing alternate track and column shifts.

At the 3-D braiding laboratory of North Carolina State University, College of Textiles, El-Shiekh and his associates devised a suitable carrier device for the 2-step braiding process [20]. For the 2-step process, which requires an expansive yarn supply, the group designed and built a prototype having a large rewinding length. The prototype meets the requirements for successful carrier design by having continuous yarn supply and adequate tension level [18].

The NCSU carrier assembly had several notable features. First it is driven by a mechanical motor which feeds yarn, rewinds yarn and tensions the yarn (Figure 11) [20]. The action of the compact carrier is economical, furnishing a continual yarn supply with predetermined tension. The carrier made of steel has a rewinding length of fifteen feet [18]. The reliability of the carrier action compounded by its simplicity enhances the marketability of this prototype.

In 1990 Brown of ARC patented a fiber spool apparatus having a rewinding capability of smaller proportions as compared to the NCSU carrier assembly. Equipped with a motor housing, which consists of a coiled spring, axle and supply spool, the compact device advances yarn to the braiding apparatus (Figure 12) [5]. The carrier also has a tensioning mechanism similar to the NCSU design operation to adjust and maintain suitable levels of strand tension during braiding.

A fully automated braider equipped with well-tensioned carriers for the 2-step process was suggested by Du and his associates at the University of Delaware. The braider and its carriers not only fulfill the process requirements of effective speed, but also are cost effective. The system comprises "motorized" carriers mounted on a reformable track [11]. The system regulates carrier position at the start of each cycle (2-Step) due to the varying distance moved by each carrier. Each carrier assembly has a "fixed parking station" [11]. The carriers move from these stations simultaneously traversing in two steps and stopping at their next respective station.

The motorized carriers have the following components: (1) a small DC motor with gear head, (2) driving traction, (3) a bobbin holder permitting yarn retraction by an electronic tensioning device, (4) power contact - brushes and (5) an off/on control microswitch [11]. Thus, the Du motorized carrier system utilizes electronic and

mechanical devices that insure the precise carrier movement needed for the 2-Step process.

Yokoyama and his colleagues at Kyoto Institute of Technology, Japan, devised a computer-controlled system for driving the motion of carriers on a 3-D braiding machine. The system facilitates the change of the carrier track configuration [24]. Also, the system creates and modifies the carrier track for certain braid specifications.

This robot driven system is a noteworthy advancement. A robot answers optical sensors that cause the system to follow a guide-tape track plan [24]. A computer program dictates the relationship between carrier motion and yarn path. All processing parameters for carrier motion are programmed through the computer. The automated (self-driven) simulation controls both the carrier speeds and track positions for the construction of particular braids [24]. Also the computer simulates the product being formed by the carrier movement while activating the self-driven system.

The aforementioned ATI cylindrical braiding apparatus advanced not only the design of the machine bed, but served to reduce the complexity of carrier design. Its inventors realized that it is "desirable to minimize the difference between distances from a carrier member to the consolidation point..." [15]. The carrier members consist of T-shaped, platform bases for ease of sliding. The platform of the base has a spindle with a yarn supply. This platform includes a guide tube that carries yarn from a supply spool. No tensioning and retraction mechanism is needed due to the side by side carrier arrangement on the cylindrical machine bed. Next, for the manufacture of an axially reinforced braid, Spain and Bailey also designed carriers including "free-wheeling pulley assemblies" [15]. These assemblies mounted on support rods include a yarn supply and connect to a bias movable pulley along the guide rod axis.

BEAT-UP MECHANISMS

A necessary element for the production of 3-D braided preforms is the convergence of the structure to prevent fiber entanglement and to produce a uniform structure. With cartesian or 4-step braided structures, the convergence of the structure is obtained by the use of a beat-up or combing action. In most cases this beat-up action is performed manually, using rods, or by hand. Manual beat-up is not only labor intensive, but is slow and manufactures inconsistent products. In an effort to improve the

quality of the preforms, researchers are automating the beat-up process.

One of the earliest beat-up mechanisms is found in Florentine's MAGNAWEAVE process. In MAGNAWEAVE braiding, a combing action follows the intertwining of the yarns, controlling the orientation and density of the material [12].

In 1990, Ashton and Patterson of ARC developed a beat-up mechanism for multi-ply braiders. Monofilaments are mounted on one side of the braider with a rigid connection at one end and a flexible connection (such as a spring) at the other (Figure 13) [1]. Pusher arms take the lines to a central point between the fibers. At this point, gripper arms come in and grip or engage the lines, pulling them through to the other side of the braider. The gripper arms travel down support posts, bringing the interlacings down to the point of convergence [1]. The motion of the pusher and gripper arms can be controlled by hydraulic piston and cylinder devices.

At NCSU, El-Shiekh and his graduate students have developed a robotic arm to replace the beat-up motion usually performed manually. Utilizing a computer, a controller, two stepping motors, and a series of guide rods, a mechanical arm is used to bring the interlacings of fibers to the convergence point of the structure [18]. The beat up arm, after entering the area between carrier columns, swings up toward the convergence point while the beat-up unit travels parallel to the braider bed. This beat-up action is repeated for a designated number of positions along the braider bed. By positioning the beat-up arm between the carriers and moving the arm up and across the braider bed simultaneously, the contact between the fibers and the beat-up arm is minimized, thus reducing fiber damage due to the beat-up process [18]. In addition, the mechanized beat-up action produces a repeatable, uniform structure.

BIBLIOGRAPHY

1. Ashton, Clint H. and Gerald A. Patterson, "Combing Apparatus for Braiding Machine," U. S. Patent 4,898,067, 1990.

2. Brookstein, David S., "A Comparison of Multilayer Interlocked Braided Composites with other 3-D Braided Composites," 36th International SAMPE Symposium, Vol. 36, Book 1, April 15-18. 1991, pp. 141-150.

3. Brookstein, David S., "Interlocked Fiber Architecture: Braided and Woven," 35th SAMPE International Symposium, Vol. 36, Book 1, April 2-5, 1990, pp. 746-756.

4. Brown, Richard T., "Braiding Apparatus," U. S. Patent 4,753,150, 1988.

5. Brown, Richard T., "Fiber Spool Apparatus," U. S. Patent 4,903,574, 1990.

6. Brown, Richard T., "Through-the-Thickness Braiding Technology," 30th National SAMPE Symposium, March 19-21, 1985, pp. 1509-1518.

7. Brown, Richard T. and Eric Ratliff, "Method of Sequenced Braider Motion for Multi-ply Braiding Apparatus," U. S. Patent 4,621,560

8. Brown, Richard T. and Mabel E. Harman, "Advanced Textile Braiding Techniques," Advances in High Performance Composite Technology Conference, Clemson University.

9. Christianson, Carla, "3-D Fabrics Enhance End Product Performance," Industrial Fabric Products Review, January 1984, pp. 50-52.

10. Culp, Carl H., Steven M. Hastings and Richard T. Brown , "Braiding Apparatus," U. S. Patent 4,934,240, 1990.

11. Du, Guang-Wu et al, "Analysis and Automation of Two-Step Braiding," NASA Conference Publication 3038, Fiber-Tex 1988, Greenville, SC, Sept. 13-15.

12. Florentine, Robert A., "Magnaweave Automation: Status of 3D Braiding Manufacturing Technology," NASA Fiber-Tex 1988, Sept. 13-15, 1988.

13. Hammad, Mohamed A., "Staple Fiber Spinning Technology-3D Braiding," PH. D. Thesis, Alexandria University, Egypt, June 1991.

14. Heine, William M., "Fiber Spool Apparatus," U. S. Patent 4,700,607, 1987.

15. Ivsan, Thomas J. et al, "Apparatus and Method for Braiding Fiber Strands," U. S. Patent 4,922798, 1990.

16. Klein, Allen J., "Braids and Knits: Reinforcement in Multi-directions," Advanced Composites, Sept./Oct. 1987, pp. 36-48.

17. Ko, Frank, "Braiding," Composites: Engineered Materials Handbook, Vol. 1, ASM International, 1987,pp. 519-528.

18. Li, Wei, "On the Structural Mechanics of 3D Braided Preforms for Composites," PH. D. Thesis, NCSU, Raleigh, NC, March 1990.

19. Li, Wei and Aly El-Shiekh, "The Effect of Processes and Processing Parameters on 3D Braided Preforms for Composites," SAMPE Quarterly, pp. 22-28.

20. Li, Wei et al, "Automation and Design Limitations of 3D Braiding Process," NASA Fiber-Tex 1989, 3rd Conference on Advanced Engineering Fibers and Textile Structures for Composites, Greenville, SC, Oct. 30-Nov. 1, 1989, pp. 115-140.

21. Pastore, Christopher, "Processing Science Model for Three Dimensional Braiding," PH. D. Thesis, Drexel University, Philadelphia, PA, March 1988.

22. Popper, Peter, "Braiding," Encyclopedia of Composites, VCH Publishers, September 1988.

23. Spain, Raymond G. "Method of Making Composite Articles," U. S. Patent 4,885,973, 1989.

24. Yokoyama, A. et al, "A New Braiding Process--Robotised Braiding Mechanism," Materials and Processing--Move into the 90's, 10th International SAMPE European Chapter Conference, July 11-13, 1989.

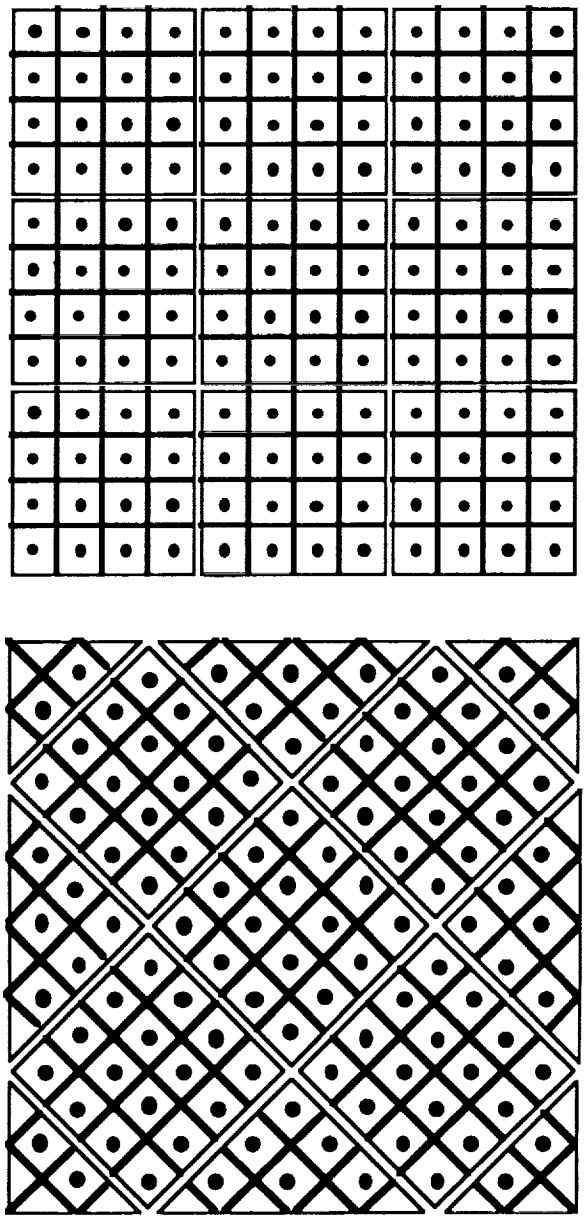

FIGURE 1: TWO ASSEMBLY ARRANGEMENTS FOR THE 2-STEP MACHINE BED

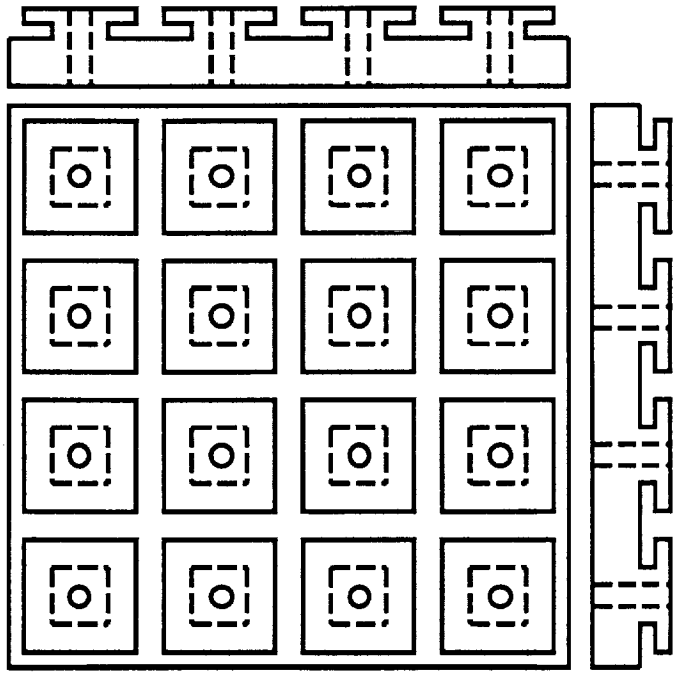

FIGURE 2: UNIT TILE OF THE 2-STEP MACHINE BED

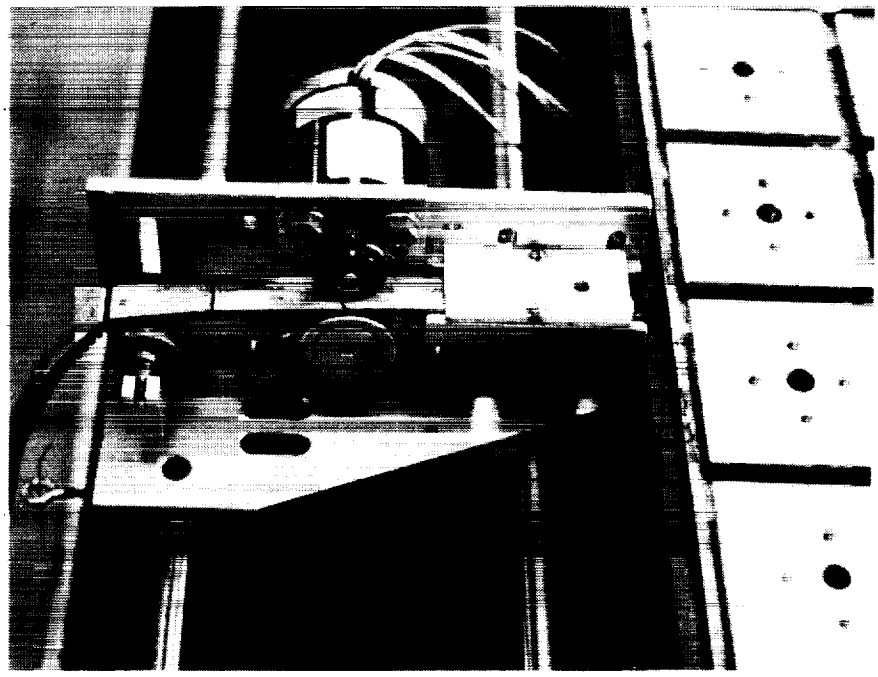

FIGURE 3: DRIVING UNIT OF THE 2-STEP MACHINE

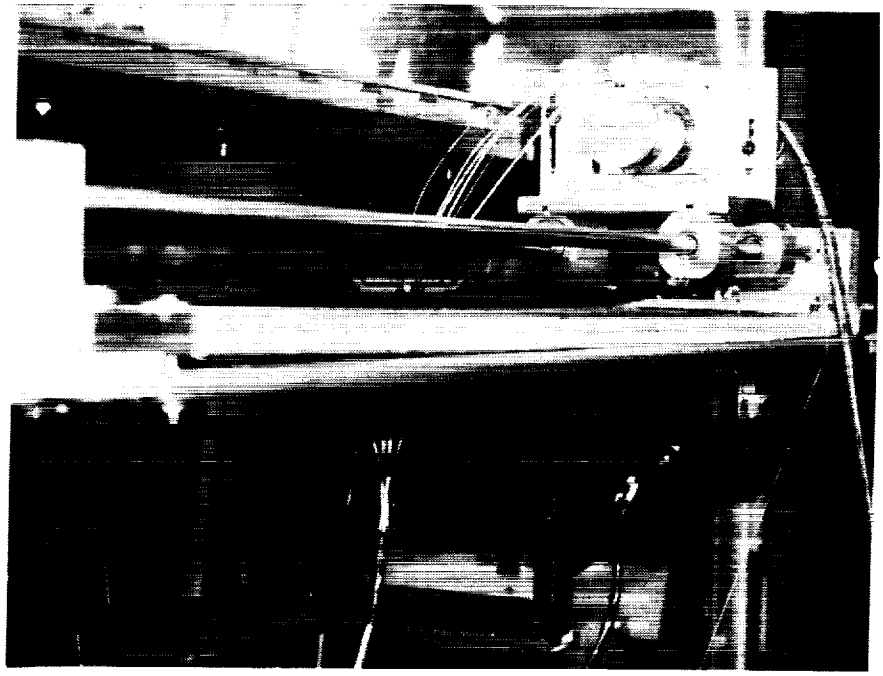

FIGURE 4: TRANSPORTATION SYSTEM FOR DRIVING UNIT IN THE 2-STEP MACHINE

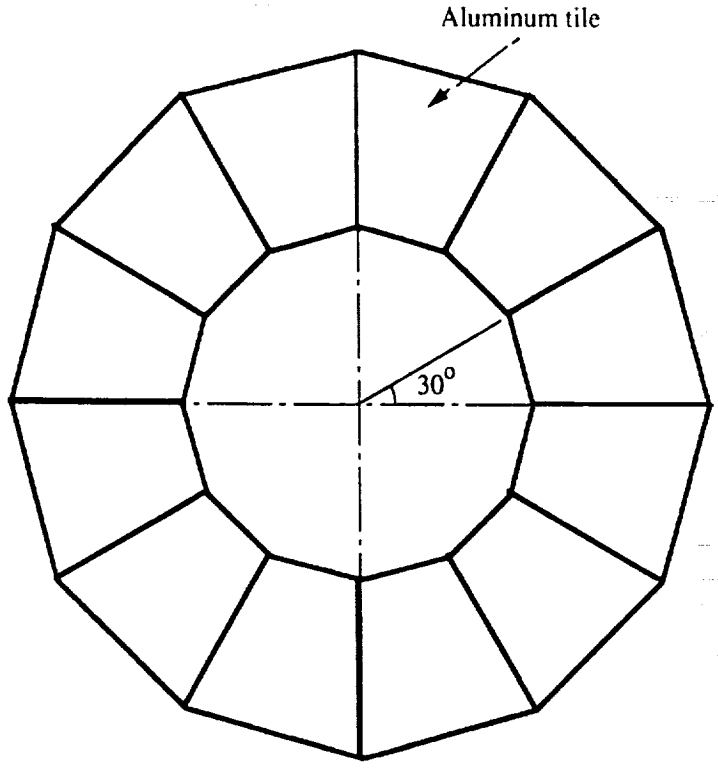

FIGURE 5: CIRCULAR CONFIGURATION OF 2-STEP MACHINE BED

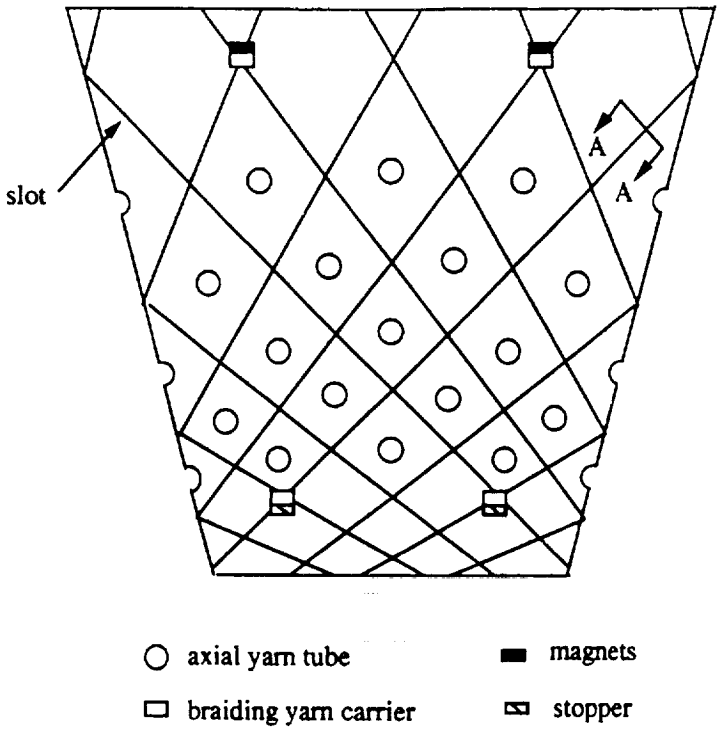

FIGURE 6: A UNIT TILE OF THE 2-STEP CIRCULAR MACHINE BED

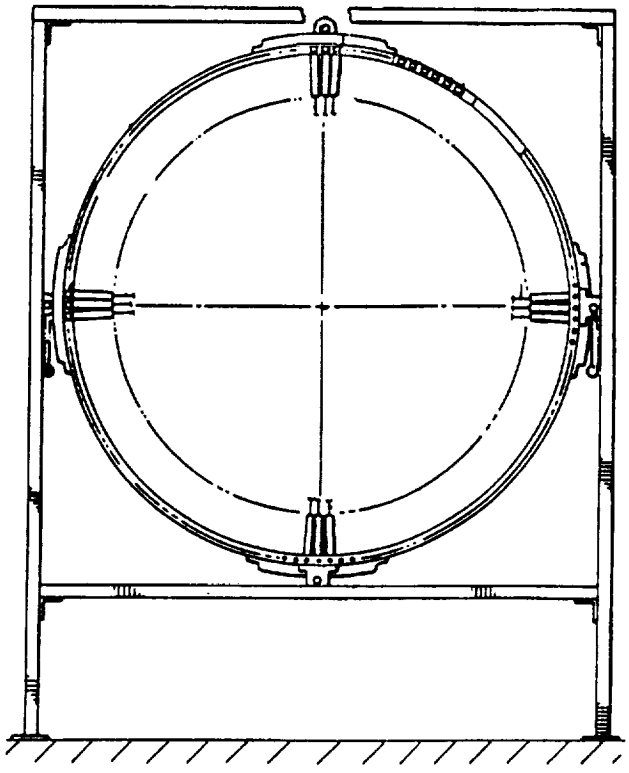

FIGURE 7: ARC CIRCULAR BRAIDING MACHINE

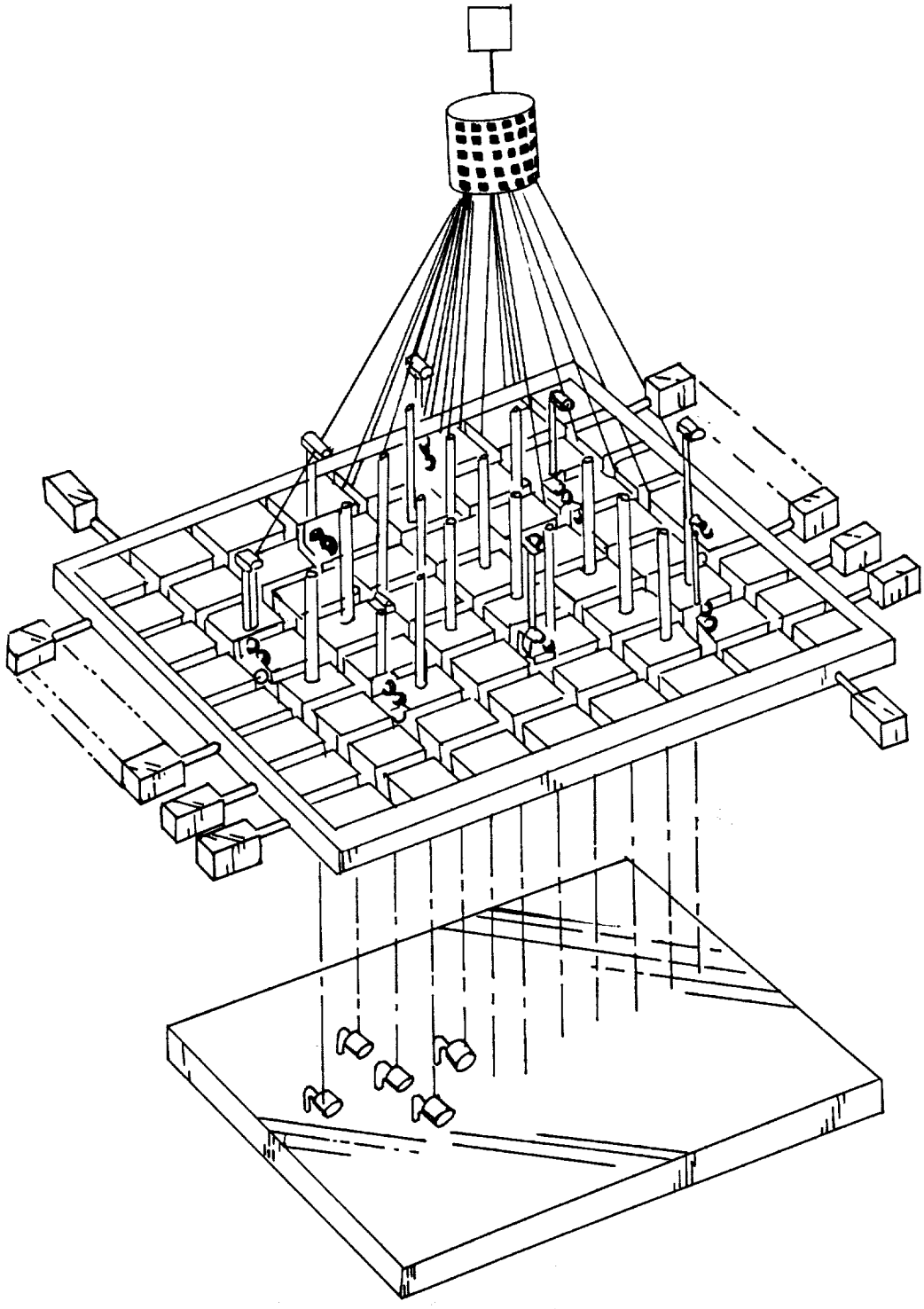

FIGURE 8: ATI 3-D BRAIDING APPARATUS

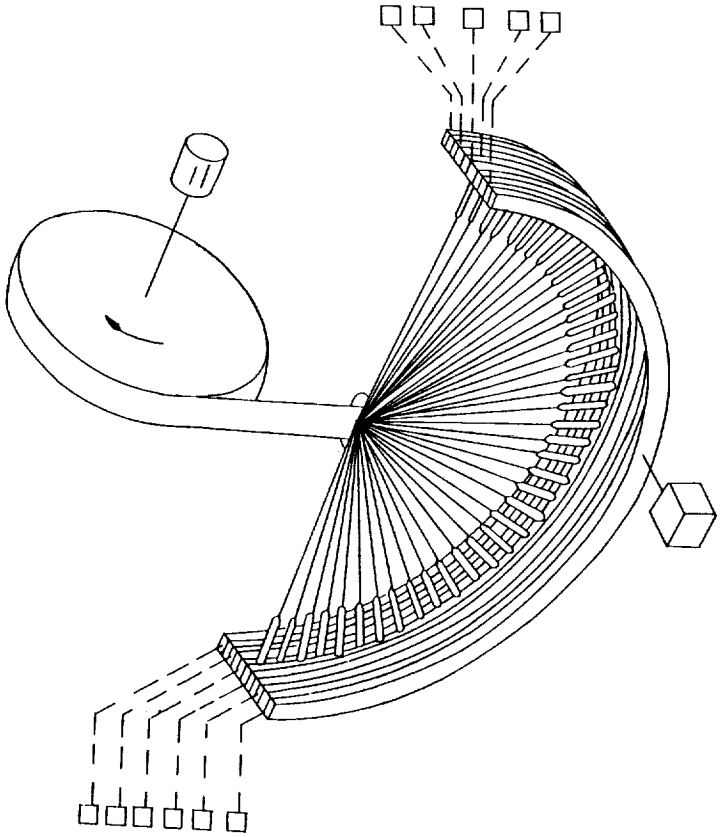

FIGURE 9: ATI CYLINDRICAL BRAIDING MACHINE

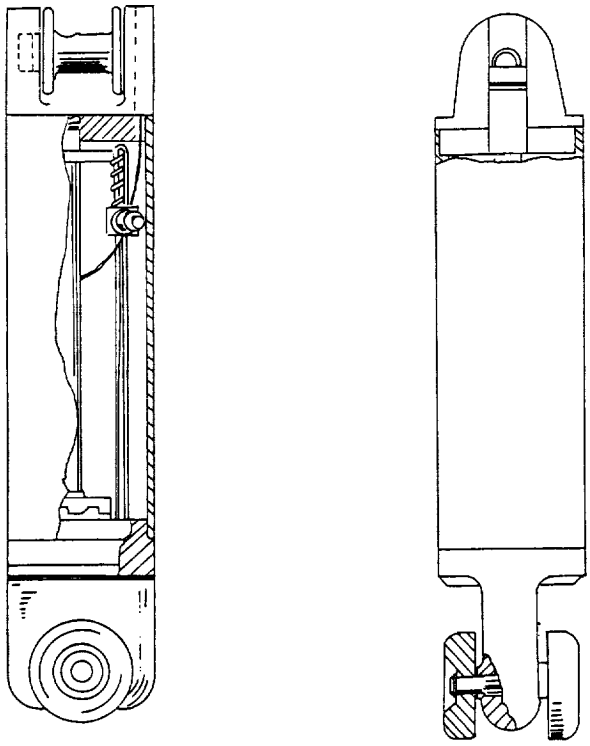

FIGURE 10: ARC CARRIER

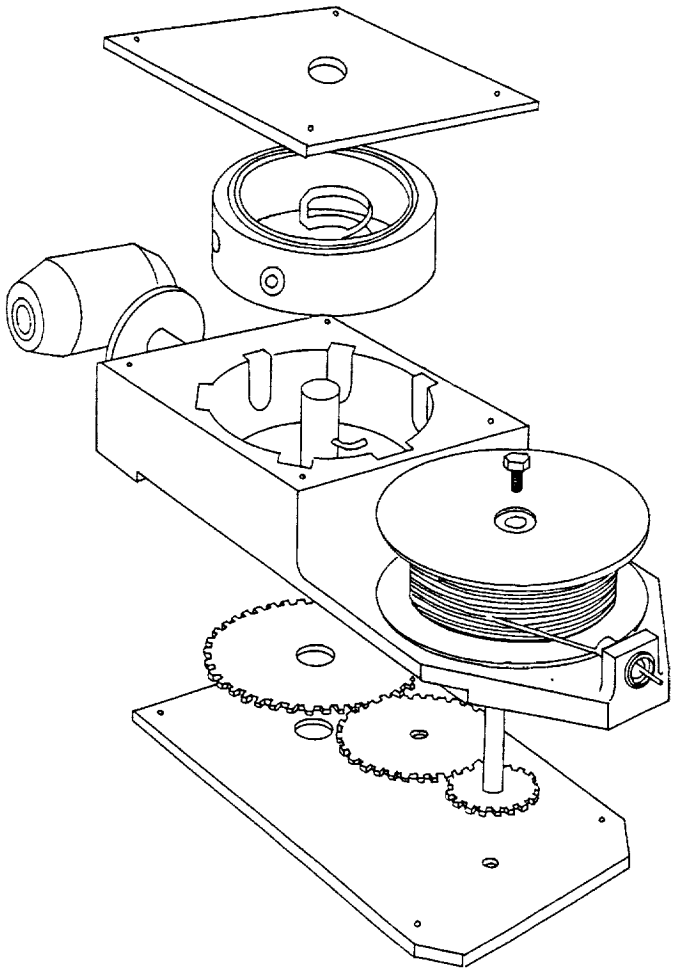

FIGURE 11: NCSU CARRIER ASSEMBLY

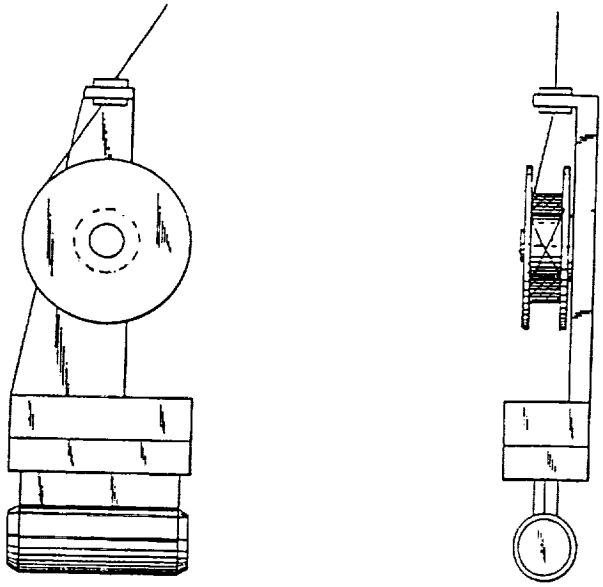

FIGURE 12: ARC CARRIER

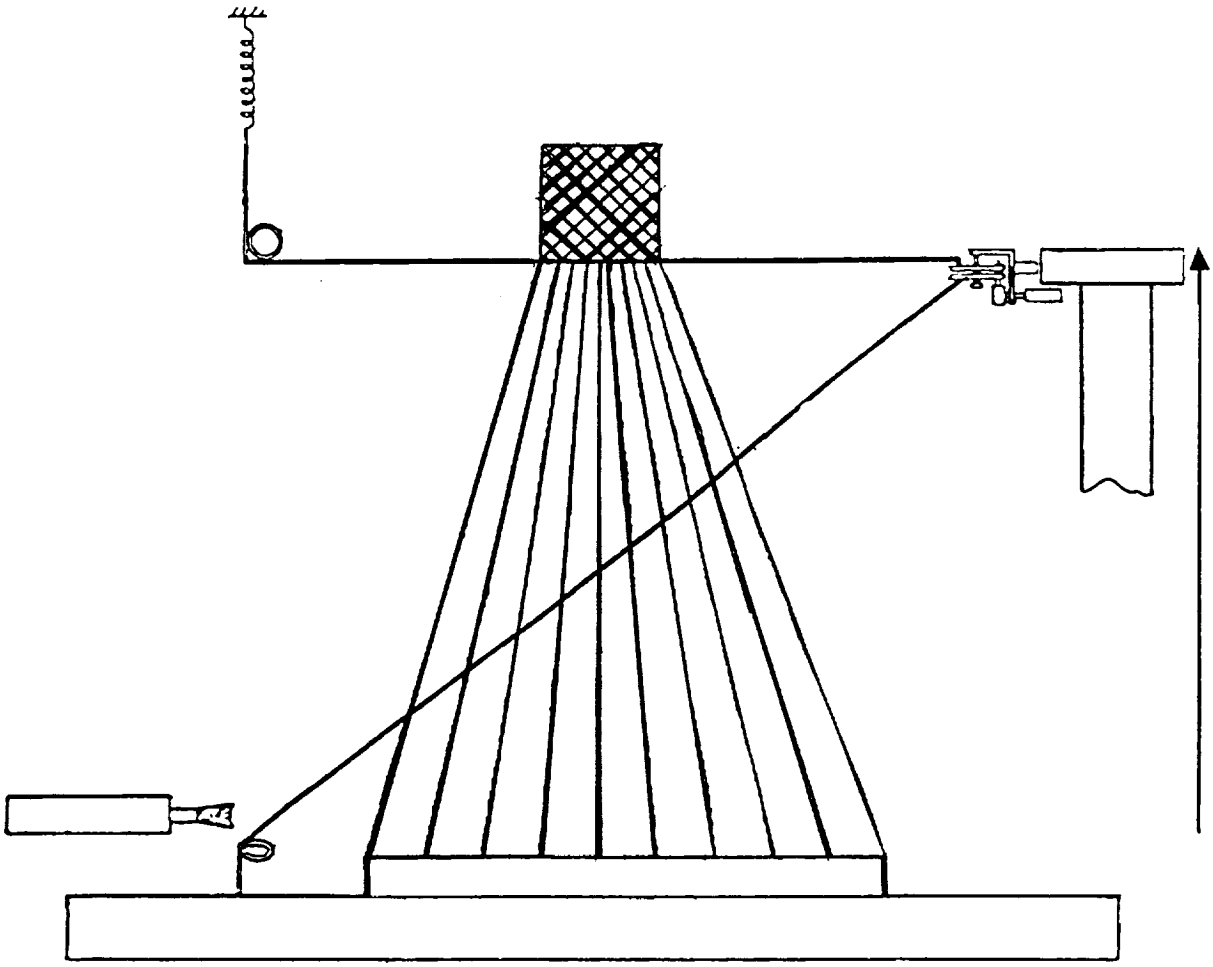

FIGURE 13: ARC BEAT-UP MECHANISM
FOR A MULTI-PLY BRAIDER

DEVELOPMENT OF GENERALIZED 3-D BRAIDING MACHINES FOR COMPOSITE PREFORMS

Cecil O. Huey, Jr.
Department of Mechanical Engineering
Clemson University

Gary L. Farley
NASA Langley Research Center

ABSTRACT

The development of prototype braiding machines for the production of generalized braid patterns is described. Mechanical operating principles and control strategies are presented for two prototype machines which have been fabricated and evaluated. Both machines represent advances over current fabrication techniques for composite materials by enabling nearly ideal control of fiber orientations within preform structures. They permit optimum design of parts that might be subjected to complex loads or that have complex forms. Further, they overcome both the lack of general control of produced fiber architectures and the complexity of other weaving processes that have been proposed for the same purpose. One prototype, the Farley braider, consists of an array of turntables that can be made to oscillate in 90 degree steps. Yarn ends are transported about the surface formed by the turntables by motorized tractors which are controlled through an optical link with the turntables and powered through electrical contact with the turntables. The necessary relative motions are produced by a series of linear tractor moves combined with a series of turntable rotations. As the tractors move about, they weave the yarn ends into the desired pattern. The second device, the shuttle plate braider, consists of a braiding surface formed by an array of stationary square sections, each separated from its neighbors by a gap. A plate beneath this surface is caused to reciprocate in two perpendicular directions, first in one direction and then in the other. This movement is made possible by openings in the plate that clear short columns supporting the surface segments. Yarn ends are moved about the surface and interwoven by shuttles which engage the reciprocating plate as needed to yield the desired movements. Power and control signals are transmitted to the shuttles through electrical contact with the braiding surface. The shuttle plate is a passively driven prime mover that supplies the power to move all shuttles and the shuttles are simple devices that employ only a solenoid to engage the shuttle plate on command. Each shuttle is assigned a unique identity and is controlled independently. When compared to each other, the Farley braider is felt to have the advantage of speed and the shuttle plate braider, the advantage of simplicity.

INTRODUCTION.

The work reported here was part of a study of the potential for practical 3-D braiding machines having the ability to generate any prescribed relative motions of the braiding yarns. [1-8] Such a braider would afford complete freedom in defining braid structures and would facilitate the design of high-performance composite components. An ideal braider would possess only the mechanical com-

plexity needed to control the braiding pattern, yet be capable of producing generally variable patterns. Most 3-D braiding schemes either achieve simplicity by limiting flexibility or seek flexibility at the expense of complexity. For example, most braiders yield structures having characteristics inherently linked to the process and that cannot be changed, and they therefore have no flexibility at all. Examples are: conventional 2-D mechanical braiders [2,6,7], the Florentine Magnaweave scheme [3,4], and the two-step braider [2,6,7], all of which produce braid patterns that are intrinsic to the process. On the other hand, methods such as the **AYPEX** [8] procedure and the Bluck [1] and Fakuta [5] processes possess the necessary flexibility but suffer from complexity in their implementation. This complexity becomes overwhelming when the processes are scaled up to produce large sections with full flexibility. Even when the size of the product is modest, the flexibility required to produce a variety of structures requires a great deal of redundant capacity.

Two different approaches were examined in detail as part of this study and small prototypes were built. The first machine was based on an idea developed prior to the start of the study by one of the authors (Farley) and is referred to here as the Farley braider. The other was originated during the course of the study and is referred to as the shuttle plate braider. Four general requirements were set initially and were principal influences on the detailed design of the prototypes. These were as follows:

- A completely general braiding capability was to be attained which would permit any particular yarn end to be moved from any position on the braiding surface to any other position by any prescribed path.
- The mechanical construction and control requirements had to be practically feasible in machines of large size.
- A large number of non-braiding, axial yarns were to be accommodated.
- The physical dimensions of the braiding surface were to be minimized, ideally no greater than needed to allow the use of yarn packages of one inch diameter.

THE FARLEY BRAIDER

The braiding surface of the Farley braider consists of an array of turntables that can be made to oscillate in 90° steps. Yarn ends are transported about the surface by motorized tractors which are controlled through an optical link with the turntables and powered through electrical contact with the turntables. The tractors are guided by track segments mounted on the turntables and are propelled by small motors driving through a gear train against a rack incorporated into the track segments. The necessary relative motions are produced by a series of linear tractor moves combined with a series of turntable rotations. With the turntables oriented in one direction, the track segments become aligned and form a continuous path in one direction for the tractors. When oriented in the other direction (rotated 90°), the track segments again form a continuous path but in a direction perpendicular to the first orientation. A proper combination of turntable rotations accompanied by

appropriate tractor moves along the paths formed by the track segments weaves the yarn ends into the desired pattern. Stationary axial yarns, if needed, would pass through the braider surface in the space between the turntables. The basic concept is illustrated in Figure 1.

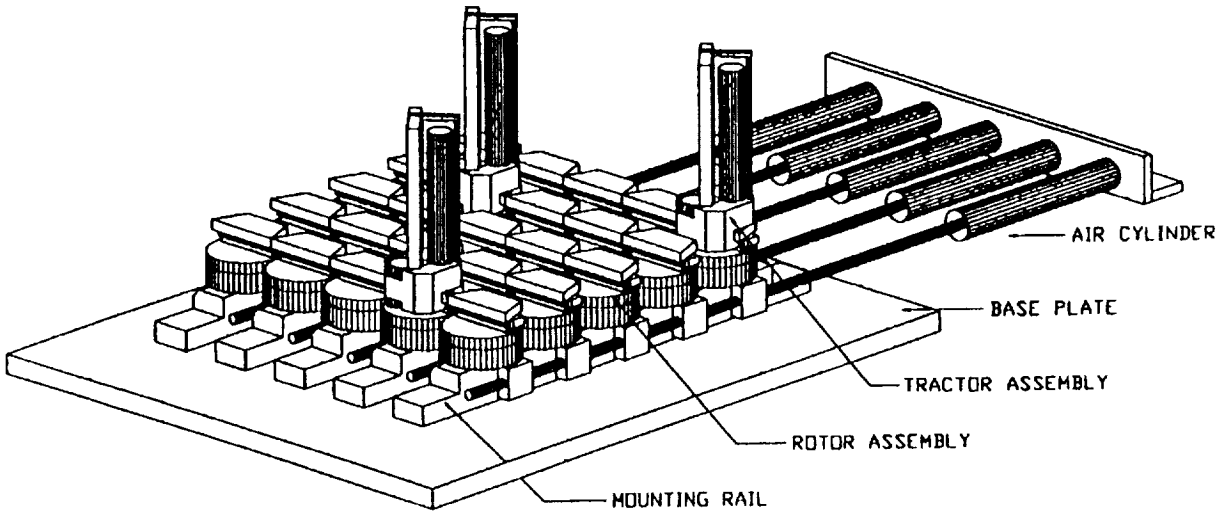

Figure 1-- Prototype Farley Braider Showing Basic Components of the System

As originally conceived, the Farley braider would consist of a large array of independently controlled rotating turntables. Such independent control of the turntables is desirable but would require an immense number of actively controlled devices when implemented on a practical scale. Consequently, in the prototypes, and likely in a practical implementation, the turntables were made to operate in unison and were actuated by a single actively controlled prime mover. The switching action of the turntable array is controlled by a computer with each rotation occurring after a complete set of tractor moves along a given axis. For example, with the turntables set in the X-axis, the tractors are moved as necessary in the X-direction. After each tractor reaches its current destination, the turntables are switched to the Y-axis. The next set of moves of the tractors, all in the Y-direction, then take place. The turntables are then returned to the X-axis orientation, and another set of tractor moves occurs. The switching back and forth of the turntables continues in this alternating manner until the entire braiding program has been executed.

Each of the tractors incorporates an electronic control circuit and a small d.c. motor and gear train. Power is conveyed to the tractors through contact with electrically isolated conductors incorporated into the turntables. Control signals are transmitted by frequency modulated optical signals through emitter-detector pairs mounted in the turntables and in the tractors. Signals are

directed to specific turntables in the array. Directional start signals are transmitted to the locations occupied by the tractors. Stop signals are erected at the destinations of the tractors. The tractors, once set in motion, continue in motion until they encounter the stop signals. When all tractors have completed moving, the turntables are commanded to rotate a quarter-turn to align with the opposite coordinate axis. In the current prototype, this rotation is accomplished via solenoid controlled valves and pneumatic cylinders. After the rotation has occurred, the next set of instructions is sent to the tractors and the appropriate moves are accomplished as before. The sequence of operations continues, alternating between tractor moves and turntable rotations, until the desired braided shape is completed.

THE SHUTTLE PLATE BRAIDER

The shuttle plate braider consists of a braiding surface formed by an array of stationary square sections, each separated from its neighbors by a gap (Figure 2). A flat plate beneath this surface is caused to reciprocate in two perpendicular directions, first in one direction and then in the other. This movement is made possible by openings in the plate that clear short columns supporting the surface segments. Yarn ends are moved about the surface and interwoven by shuttles which engage the reciprocating plate as needed to yield the desired movements. An operating sequence is illustrated schematically in Figure 3.

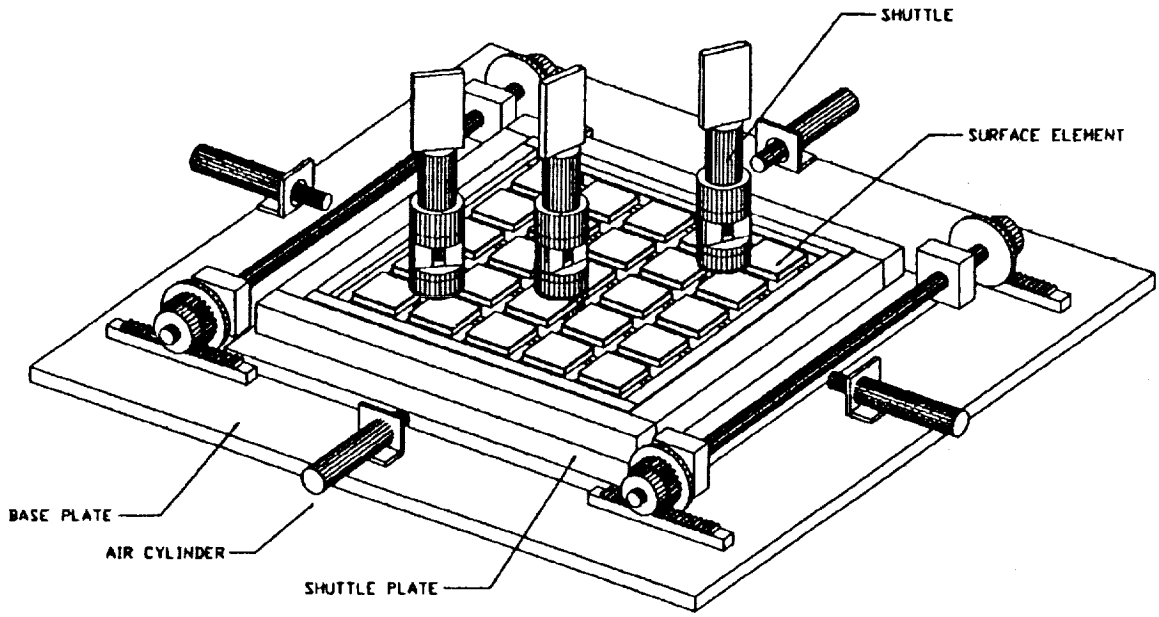

Figure 2-- Prototype Shuttle Plate Braider

In the current version, both power and control signals are transmitted to the shuttles through electrical contact with the braiding surface. The shuttle plate is a passively driven prime mover that

supplies the power to move all shuttles. The shuttles themselves are very simple devices that employ

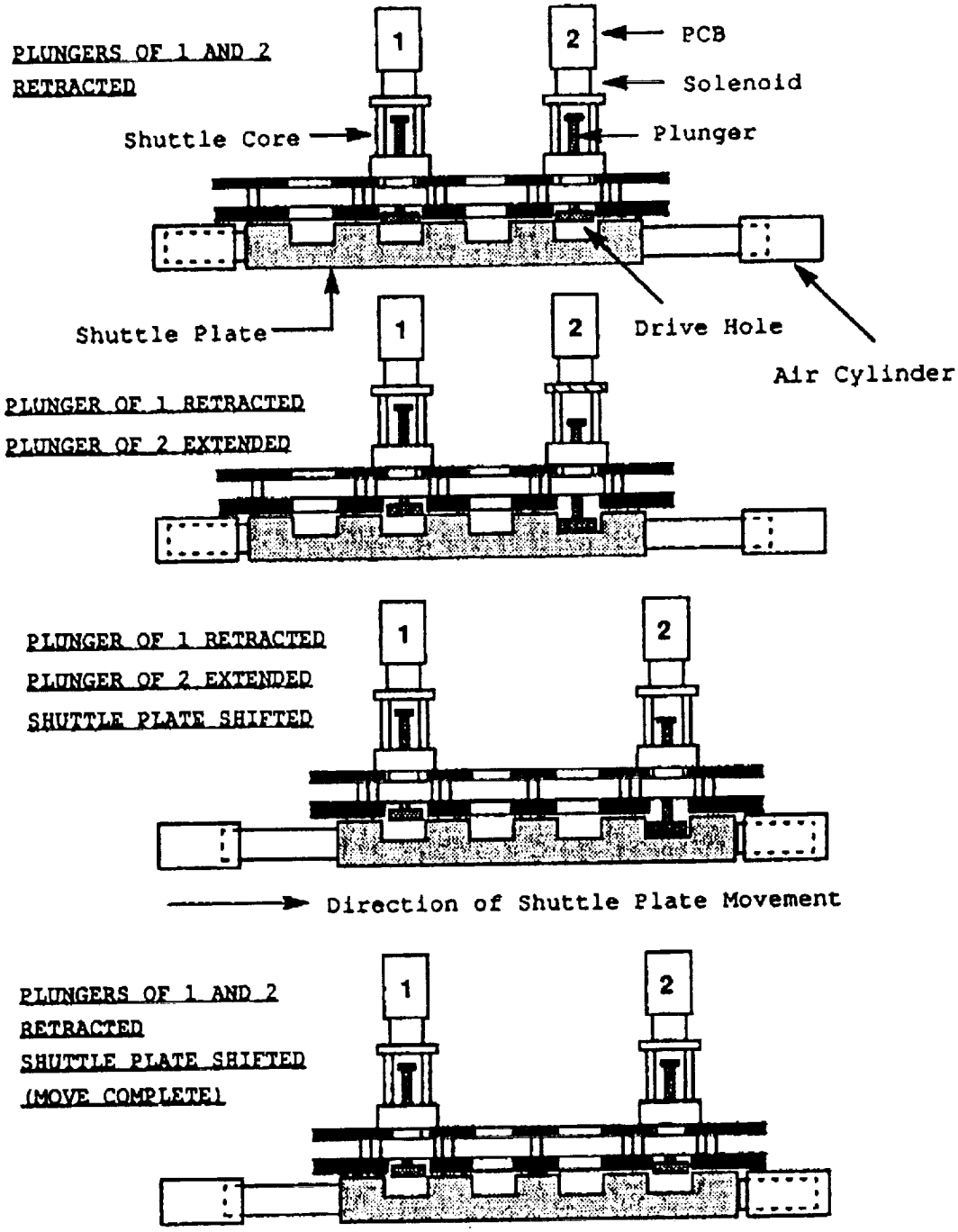

Figure 3-- Schematic Representation of Shuttle Plate Operating Sequence.

only solenoids to extend a plunger that engages the shuttle plate on command. Each shuttle is assigned a unique identity and is controlled independently by directing commands to particular addresses.

The shuttle plate approach was originated after identifying two additional attributes likely to be found in an ideal braiding machine. These attributes were as follows:

- The braiding action should require the minimum of actively and independently controlled devices required be reduced to an absolute minimum. Assuming simultaneous and independent control of all braiding yarns, this minimum would equal the number of braiding yarn ends.

- Actively controlled actions should be mechanically uncomplicated.

The shuttle plate device possesses both of these attributes. The move commands are transmitted directly to the shuttles and the controlled action is a simple on/off command to actuate a solenoid. Such simplicity is in stark contrast to other methods that require control of actuators, direction control devices, and the like at each point on a braiding surface that could be occupied by a yarn end. For example, the Bluck [1] and Fakuta [5] braiders and the **AYPEX** [8] process, as originally proposed, require an x-y grid of actuators, all independently controlled and quite complicated in their function. A 100*100 braiding grid would require ten thousand such actuators, even when only a few hundred or perhaps a few dozen yarn ends are being controlled. With the shuttle plate approach, the size of the braiding grid has no effect on the number of required controlled devices.

It is possible to make the shuttle plate itself a completely passive device by driving it alternately in one direction, then the other at a constant frequency. However, the braiding process can be sped up by independently driving the plate in the two axes in a fashion tocontrolled eliminate wasted moves when possible. Such control adds one element to the number of controlled devices and promises substantial speed increases for certain braid patterns.

THE PROTOTYPE MACHINES

Both braiding approaches have been reduced to practice in the form of small devices consisting of a 5*5 braiding grid with three shuttles. Both work well. However, the greater mechanical complexity of the Farley braider rendered it much more temperamental and difficult to make reliable. The shuttle plate braider works with hardly a hitch. The prototypes are shown in the photographs of Figures 4-6.

COMPARISON OF THE TWO APPROACHES

The two braiders discussed both accomplish generalized braiding, both in theory and as reduced to practice, in that they are both capable of moving any yarn end from any endpoint to any other endpoint by any path specified by the programmer. To the investigators' knowledge, this has not been practically achieved before.

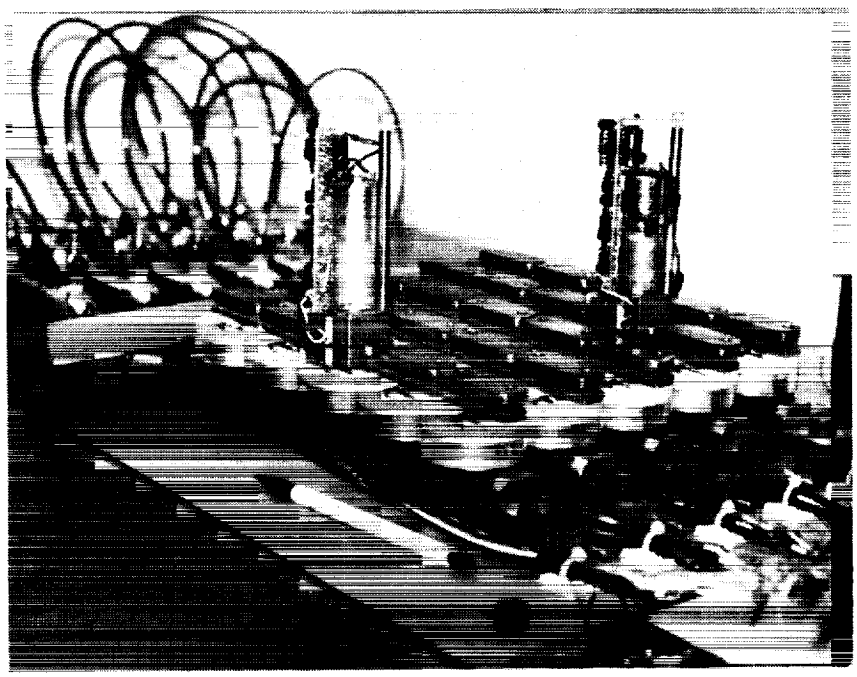

Figure 4-- Photograph of Prototype Farley Braider Showing Two Yarn Carriers and with Track Segments Oriented along the X-Axis

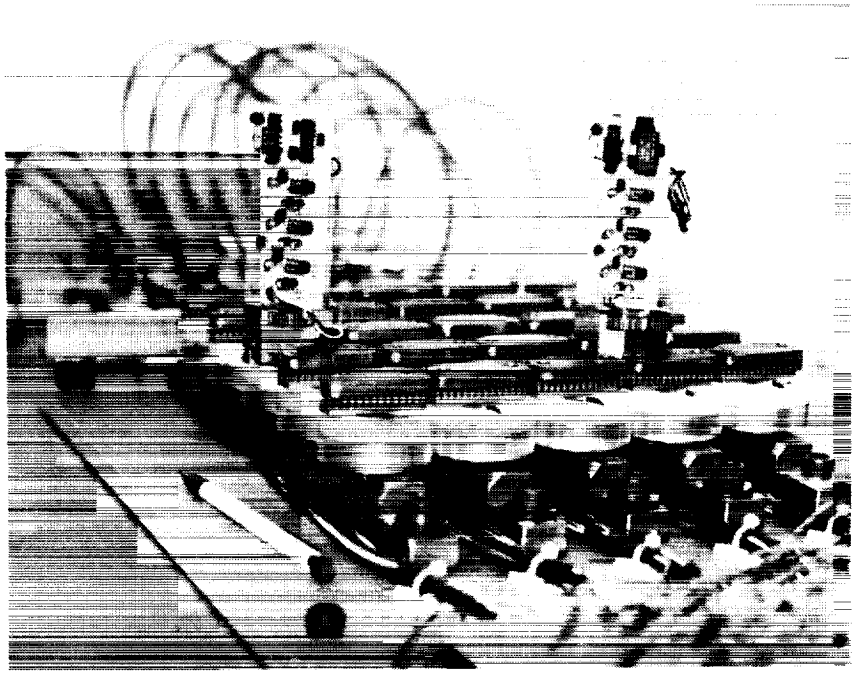

Figure 5-- Photograph of Prototype Farley Braider with Track Segments Rotated to Align with the Y-Axis

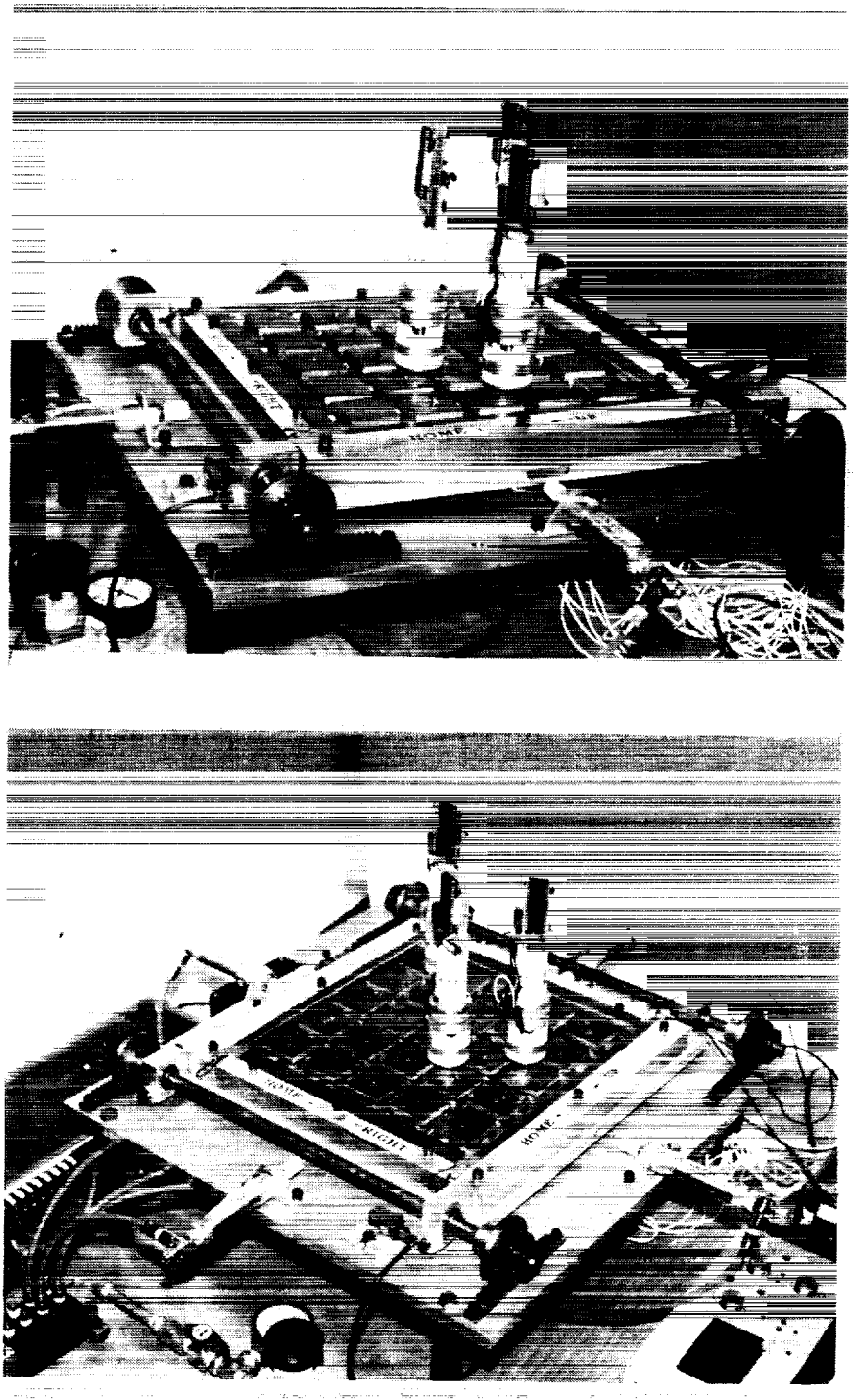

Figure 6 Photographs Showing Prototype shuttle plate Braider

Comparing the two braiders against each other, as opposed to comparing against other braiding techniques, the following advantages and disadvantages have been determined through operation of the two prototypes in the laboratory. The shuttle plate braider is a very simple design

from a mechanical viewpoint, and its control requirements are as simple as they can be made, since all that is required are simple on/off commands. Further, all the power needed to move the shuttles is derived from the shuttle plate, and thus little power is needed for the shuttles themselves. The modified Farley braider does not have this simplicity, but it does have the advantage of speed for braiding patterns which require numerous long moves of the yarn carriers. In addition, while at any given time all the yarn carriers of the modified Farley braider must move along a given axis, some can be moving in the forward direction while others are moving in the reverse direction. Of course, this speed advantage diminishes as the average move length of a yarn end becomes shorter in complex patterns.

For the Farley braider the timing and synchronization of moves between yarn carriers become an issue of concern, especially as the number of carriers increases. This concern could force the use of more complicated devices, such as stepper motors, and neighbor proximity detectors. The shuttle plate braider does not have this timing difficulty, since all shuttle moves are automatically synchronized by the driving plate.

Although both braiders transmit power to the yarn carriers via the braiding surface, the need for such power is significantly different in kind. The shuttle plate braider needs power on the surface to engage the solenoid in each shuttle. As currently implemented, this power is held continually to maintain engagement. If several solenoids are activated at the same time, this would require high currents on the surface. However, there are numerous ways to overcome this difficulty in a scaled up version of the shuttle plate braider. These include such options as using mechanical latching and momentary currents to engage the latch. For the Farley braider, the motors must be powered continually. Thus the current, of necessity, must increase as the number of moving yarn carriers increases. There is no simple solution to this dilemma. Finally, as the size of the braiders is scaled up to practical applications, addition difference would be evident. The shuttle plate braider scales up readily, since the control problem remains the same no matter the size of the braider. The Farley braider might more easily be implemented on an upwardly curved surface. Use of such a surface would reduce the size of the braiding surface needed to control braid angles. However, such an approach would complicate the design significantly. For example, the turntables of the modified Farley braider would have to be of unequal size or rotate through unequal angles, depending upon location on the curved surface. Finally, set up and operation of the shuttle plate braider is much easier and more reliable, as discovered in operations to date.

SUMMARY

A successful attempt to develop and implement generalized, three dimensional braiding has been accomplished and two practical schemes for implementation have been designed, built, and tested. Both schemes, as implemented, produce the motions necessary to generate any desired braiding pattern. Each scheme has its advantages and disadvantages. However, the shuttle plate braider offers the greater immediate promise because of its mechanical simplicity and ease of control, especially when scaled up to practical dimensions.

BIBLIOGRAPHY

1. Bluck, Raymond M., "High Speed Bias Weaving and Braiding," US Patent 3,426,804, Feb 11, 1969.

2. Du, Guang-Wu et al, "Analysis and Automation of Two-Step Braiding," presented at Fiber-Tex '88 Conference, Sept 1988.

3. Florentine, R. L., "Apparatus for Weaving a Three-Dimensional Article," US Patent 4,312,261, Jan 26, 1982.

4. Florentine, R.L., "Magnaweave Process - From Fundamentals to Applications," Textile Research Journal, pp 620-623, Oct 1983.

5. Fukuta, et al, "Method for Formation of Three Dimensional Woven Fabric and Apparatus Therefor," US Patent 4,615,256, Oct 7, 1986 .

6. McConnell, R. and Popper, P., "Complex Shaped Braided Structures," US Patent 4,719,837, Jan 19, 1988

7. Popper, P. and McConnell, R., "A New 3D Braid for Integrated Parts Manufacture and Improved Delamination Resistance - The 2-Step Process," 32nd International SAMPE Symposium, Apr 1987

8 Weller, Richard D., "AYPEX: A New Method of Composite Reinforced Braiding," 3-D Composite Materials, pp 229-249, NASA Conference Publication 2420, Nov 1985

N93-14750

INDUSTRIAL APPLICATIONS OF MULTIAXIAL WARP KNIT COMPOSITES

James R. Kaufmann

Hoechst Celanese Corporation
Technical Fibers Division
P.O. Box 32414
Charlotte, NC 28232

Over the past few years, Multiaxial Warp Knit (MWK) fabrics have made significant inroads into the industrial composites arena. This paper will examine the use of MWK fabrics in industrial composite applications (1-10). Although the focus will be on current applications of MWK fabrics in composites, this paper will also discuss the physical properties, advantages and disadvantages of MWK fabrics. The author will also offer possibilities for the future of MWK fabrics in the industrial composites arena.

According to a Frost and Sullivan study, the demand for high performance composite materials in the USA should more than triple between 1987 and 1992 (3). A yearly growth rate of high performance composite materials for this same period has been forecast to be at least 25%. Others predict that the worldwide market for composite materials, currently at $2 billion, will grow to $20 billion by the year 2000 (8). One of the biggest reasons for this projected growth is the ever-expanding use of composite structures in industrial applications.

Advanced composite structures, high strength materials combined with a resin system, are being used in the most diverse sectors of the industrial arena. One fabric that is playing an increasingly

important role in this arena is the Multiaxial Warp Knit (MWK). MWK fabrics are ideally suited for this type of end use because of their flexibility and engineerability. MWK fabrics, produced in a one-step process, have properties similar to those of quasi-isotropic layup structures. Besides good handleability, MWK fabric preforms are extremely conformable.

This paper will examine the use of MWK fabrics in industrial composite applications. The focus will be on the MWK fabric itself, and why it is being used as a preform in industrial composites. Current end use applications for the MWK fabric composites will be discussed and possibilities for the future of MWK fabrics in the industrial composites arena will also be offered.

What Is An MWK Fabric Composite

The basic principle of fabric composites is to combine the singular properties of more than one substrate and/or medium to create a single structure that performs much better than any of the individual components. An advanced composite is based on the same principle as using steel reinforced concrete to build a bridge, or straw and mud to make a brick for building a fireplace. In advanced composite structures, reinforcing fibers or fabrics are embedded in resin systems such as epoxy or other binders. Multiaxial warp knitting is a means of manufacturing stable reinforcing fabrics from fibers such as graphite, glass, Kevlar, ceramic, or other textile fibers which have the ability to resist stress and strain from any direction.

MWK fabrics are unique structures which are produced by warp knitting techniques. With these techniques, straight ends of parallel and uncrimped yarns are inlaid into the knitted structure at virtually any desirable angle. Because of the versatility of this process, fabric characteristics can be engineered into the structure to give the ideal combination of mechanical properties at a favorable production cost. This produces MWK fabrics, with the combined advantages of design flexibility, performance, productivity and availability, and the potential to become a major fabric preform for industrial composites.

An industrial composite can be defined as any composite structure that is not being used as a household good such as kitchen utensils, furniture, clothing, jewelry, and/or sporting goods.

THE MWK FABRIC

MWK fabrics generally possess up to four different load bearing yarn systems arranged so that each can take on stress and strain in virtually all directions. Since these load bearing yarns lie straight in the fabric, with no crimp, the physical parameters of the individual yarn system are fully utilized.

From a structural geometry viewpoint (see Figure 1), MWK fabrics consist of warp (0 degrees), weft (90 degrees), and bias (+/- various degrees) yarns that are stitched together during the warp knitting process by a fifth yarn system through the thickness of the fabric structure (4). The warp and weft yarns stabilize the fabric in the machine and cross machine directions while the diagonally arranged or biased yarns absorb tension from any required angle. The fifth yarn precisely binds together all of the load bearing yarn systems. The bias or diagonal yarns in the fabric can be inlaid at any angle along the plane of the machine direction, the most common of which is +/- 45 degrees. It should be noted that all four load bearing yarn systems do not have to be used in a MWK fabric construction. Also, different yarn types and counts can be used in each of the yarn systems. MWK fabrics allow the designer freedom of choice in the arrangement of load bearing yarns in the structure. This provides the fabric designer with a tremendous amount of design flexibility.

Unlike the crimp inserted into the yarn in woven fabrics during weaving, the load bearing yarn in MWK fabrics lies straight and parallel to other yarns in its yarn system. This characteristic of MWK fabrics allows for the yarn properties to be more fully utilized in withstanding in-plane forces. Fabric design is made easier because the designer can more accurately calculate the tensile load of a MWK fabric with a much higher degree of confidence than had been previously attainable with woven fabrics. Testing is still required to verify the estimates, but the starting points can be calculated instead of guessed at. In addition to design flexibility, isotropic stress and strain resistance, excellent tear resistance, and improved conformability to complex shapes are also characteristics of the MWK family of fabrics.

MWK fabrics are capable of withstanding stresses and strains in an optimum fashion. This is due largely to the parallel and straight arrangement of the load bearing yarns in the MWK fabric. Because the load bearing yarns lie straight in the fabric, their tensile properties are fully utilized and are able to absorb tension without the elasticity that occurs when the yarns are crimped or in a wavelike form, such as in a woven fabric. Because of the arrangement of the yarn systems at various angles (see Figure 1), the MWK fabric is able to withstand shear forces from various angles (7). This isotropic ability is particularly important in many of the advanced composite structures and a primary reason for the use of MWK fabrics.

Due to the parallel nature of the load bearing yarns in the MWK fabric, excellent tear propagation resistance is achieved. If a tear were to occur in the MWK, the yarn layers would shift slightly under the force of the tear and bunch together. The inherent movement of the load bearing yarns and the diagonal element would act to reinforce the area and prevent further tearing (7). This resistance to tear propagation becomes increasingly important when a MWK structure is damaged while in use (such as in a sail, inflatable

structure, or aircraft skin). The damage is minimized by the resistance to further tearing (2).

Because the yarn systems are not interwoven, but rather lie directly on top of each other and are held together by the fifth yarn system, conformability of the fabric is greatly improved. This allows the MWK fabric preforms to conform to many complex geometrical shapes and still maximize the translation of fiber mechanical properties to the composite structure. The conformability of the uncured MWK fabric also provides good shape retention during the laying up and curing process.

By combining a web or nonwoven fabric (usually nylon, polyester or fiberglass) to the MWK fabric during the knitting process, it is possible to control many other physical aspects of the fabric structure. Both the MWK fabric and the web can demonstrate their specific advantages. Because the web is fed into the knitting machine during production of the MWK fabric, it is linked to the load bearing yarns by the stitch yarn, rather than being rigidly bonded. This allows for a certain amount of give to the MWK and web structure.

Adding a web to the MWK structure allows the designer even greater design flexibility. Addition of a web can further control the strength and elongation of the MWK fabric, and at the same time provide variations of fabric cover and density, water and air permeability, stiffness, thickness, initial tear resistance, increased tear propagation resistance, and yarn slippage resistance; all of which can be tailored by the designer to meet the end use requirements of the MWK fabric. The web also provides greater stability of the yarn layers during the further processing stages of creating an industrial composite. It has been shown that the addition of a web to the MWK preform increases the flow of resin during the resinating process in making the advanced composite structure. This results in better processing times and lower production costs (5).

Few, if any other fabric production techniques, offer such a wide range of properties with such versatility in relation to type and count as MWK fabrics. Although a comprehensive data base is not yet available for MWK fabrics due to their relatively recent introduction into the industrial composites arena, several studies have been done and are being carried out to assess their potential (6). The obvious properties that MWK fabric composites offer the industrial composites arena are their incredible design flexibility, isotropic stress and strain resistance, tear propagation resistance, and conformability (9).

End Use Applications of Industrial Composites Using MWK Fabrics

Because the MWK fabrics are relatively new to the industrial composites arena, the number of recognizable end use applications is

relatively small when compared to those of traditional woven fabrics. But when given the head start that woven fabrics have had, some several hundred years, the progress made by MWK fabrics in the industrial composites arena is nothing less than phenomenal.

The majority of current end uses for industrial composites made from MWK fabrics can be separated into two different industries, marine and aerospace. Probably 65 percent of all MWK fabrics currently made are used in marine composite applications, while another 20 percent are used in the aerospace industry. The remaining 15 percent encompass all of the varied end use applications being evaluated with MWK fabric composites. Table I divides many of the current end uses into the three categories.

MWK fabrics are becoming the fabric preform of choice in the marine industry, especially in yachts, sailboats, and high speed racing boats. The MWK fabric composite is generally used in these vessels for the hulls, deck superstructures and substructures, and motor bays.

Because of the isotropic properties of the MWK fabric structure, boat designers are finding that they can use less MWK fabric in the composite structure and still maintain, or often improve upon, the structural integrity and torsional stiffness of the boat. This also means that boat hulls made of MWK fabric composites can withstand greater stresses and strains with less overall weight. Less overall weight obviously requires less energy to power the boat, which translates into fuel savings and/or faster boats. The improved structural integrity makes the boat safer at higher speeds.

MWK fabric composites are being used in most of the fastest ocean going racing boats and yachts because of their increased stability and weight savings. The hulls and masts of several of the sailboats used in the America's Cup competition were made of MWK fabric composites because of the performance edge experienced by using these composite structures. Partially as a result of using MWK fabric composite structures, speed boats and racing boats are achieving speeds previously thought to be unreachable with any degree of safety.

Another example of improved performance as a result of using MWK composite structures in marine applications was seen in a new generation of racing shells used by some of the top rowing teams in the country. The shells (long narrow row boats, usually powered by 8 rowers) were found to give a greater translation of power into speed because of the improved torsional stiffness. This allowed energy to be translated more directly into speed rather than being absorbed by the shell when flexing.

MWK fabrics are also being looked at for applications in sails. In this case, however, the composite structure is the MWK fabric combined with a plastic film, usually through laminating. Because of the lack of crimp in the yarn in the MWK composite structure, the force of the wind is immediately translated into power and not

absorbed at all by the crimp deformation associated with woven fabric structures.

Fabric composites of all types are being used in the marine industry because of their inherent resistance to corrosion. This saves on the manufacturing cost because expensive metal treatments and repeated paintings are not needed to protect the craft from the corrosive nature of salt water.

In the aerospace industry, which includes the military, aerospace and commercial aircraft industries, MWK fabric composites are being used more and more. Relatively speaking, they are being used in this industry for many of the same reasons as in the marine industry, namely reduced weight, and increased strength and integrity. Because of the flexibility and tailorability of mechanical and physical properties, MWK fabric composites can be customized for the application and specific properties can be emphasized to suit the particular need.

Currently, there are very few aircraft that use MWK fabric composites in critical structures such as the fuselage or wings. Most current applications center around the skin of the aircraft. Other areas of use are in the top and side tail units, fuselage paneling, leading edges on side rudders, and engine paneling. MWK fabric composites are also being evaluated for rotor blades, outer skin, and ballistic protection for helicopters. It is thought that the use of MWK composites is also being evaluated in the new military plane/helicopter, the V-22 Osprey, and the all-composite Beech Starship business plane (8).

The lower weight achieved through the use of MWK composite structures means that less fuel is consumed by the aircraft, which translates into significant energy savings for the user. Also, because of the improved structural integrity offered by the MWK fabric composite, it is believed that safety is enhanced.

Other various applications for MWK fabric composites can be found in the industrial composites arena. In Europe, MWK fabric composites are being used for flooring in sports halls where the combination of multi-directional force distribution and excellent tear resistance are beneficial. The MWK fabric composite also helps to improve the sound damping characteristics of the flooring. MWK fabrics coated with rubber are also being used in the industrial roofing industry.

The Future of MWK Fabric Composites In Industrial Applications

The main obstacle in gaining acceptance for MWK fabric composites in the industrial composites arena has been the lack of confidence derived from inexperience and a lack of sustained performance data for MWK composites. With the advent of time, these obstacles will undoubtedly be overcome and MWK fabric composite usage will dramatically increase (1).

Numerous end use possibilities exist for MWK fabric composites. They can not only be used to replace traditional materials, but also to improve the performance of many new industrial composites which seem to have reached their performance limit. MWK fabric composites can be used to replace traditional structural materials such as concrete, wood, and steel, thus creating new possibilities in various industries and end uses.

The advantages of using MWK fabrics in composite structures are clearly the flexibility and freedom of choice in the desired properties in all directions which can be matched to individual needs. As a result, MWK fabric composites are uniquely suited to a wide range of industrial applications.

MWK fabric composites incorporating a nonwoven structure are ideally suited for many high strength geotextile applications, where isotropic strength, resistance to tear and tear propagation, good water permeability, low creep, and good fabric/soil interaction are required.

With the flexibility of fiber placement and potentially high productivity, MWK fabric composites are ideally suited for many structural load bearing applications in the automotive and aerospace industries. MWK fabrics, because of their structural makeup, have good flexibility which allows them to be formed during molding into virtually any desired shape. The through thickness reinforcement provided by the stitching process helps to reduce the possibility of delamination of layers in the composite structure.

Numerous applications for MWK fabric composites also include protective helmets and armored protection of vehicles, buildings, and people. Various drive belts, V-belts, fan belts, and conveyor belts will benefit from the availability of diagonal load bearing yarns in the composite structure. Inflatable rafts, cushions, balloons, and fuel cells are ideal applications due to the MWK fabric composite's isotropic strength and tear resistance.

There are probably hundreds or even thousands of other areas that could benefit via the use of MWK fabric composites. The flexibility of the MWK fabric system provides endless potential end use applications. All that is needed is for the designers and engineers of the world to dare to improve upon what they already have and open their minds to the future.

Conclusions

The MWK process offers limitless possibilities for the formation of new fabric preforms for the composites industry. By varying the angle of the load bearing yarn systems, and the type and count of yarn used, the strength in any fabric direction can be tailored to the requirement, rather than the requirement being tailored to the fabric available. Because of the complete versatility of the MWK fabric, design flexibility is virtually limitless.

MWK fabric composites offer many never before realized advantages to the industrial composites arena, giving the designer flexibility that he or she has never before had. The ability to design a composite structure with the load bearing systems aligned precisely where they are needed provides opportunities to make better, more cost efficient structures.

The use of MWK fabric composites in many of the areas mentioned earlier shows that their development is worthwhile. New end uses are being developed daily and in many cases MWK fabric composite structures are being used to replace expensive, heavier or technically inferior constructions produced from other materials. Many times these replacements are converted directly into cost savings. Also, with each new application, comes more experience and an addition to that ever-expanding data base, which so many engineers and designers require. All that is needed is for them to open their minds and give MWK fabric composites a try.

Acknowledgements

The author wishes to thank the people at Karl Mayer Textile Machine Corporation and Advanced Textiles, Inc. for their help and support in supplying much of the information used for this paper. Their assistance was greatly appreciated. The author would also like to thank his employer Hoechst Celanese for allowing him the time and facilities to produce this paper.

References

1. Allbee, Nancy, "Tapping the Market for Industrial Applications," Advanced Composites Magazine, July/August, 1989, pp. 49-52.
2. "Excellent Tear Propagation Resistance Properties of Bi- and Multi-Axial Structures," Kettenwirk Praxis, February, 1989, p. 65.
3. "Industrial Textiles With High Growth Rates," Kettenwirk Praxis, February, 1989, p. 45.
4. Ko, F., "Multiaxial Warp Knit Composites: Structure, Properties, and Analysis," International Man-Made Fibres Congress, September, 1986.
5. "Multiaxial Structures With Web Inserts and Diagonal Yarns in Alternate Directions," Kettenwirk Praxis, March, 1988, pp. 5-10.
6. Raz, S., "Bi-Axial and Multi-Axial Warp Knitting Technology," Kettenwirk Praxis, March, 1987, pp. 11-16.
7. Raz, S., "The Karl Mayer Guide to Technical Textiles," Special Supplement to Kettenwirk Praxis, January/February, 1989, pp. 60-94.
8. Slutsker, Gary, "Don't Screw It, Glue It," Forbes Magazine, November 28, 1988, pp. 234-239.

9. Technical Bulletin, Mayer Textile Machine Corporation, 7102 Sherwin Extraordinary Strength Properties Achieved Through Multi-Axial Magazine-Weft Insertion."
10. Technical Bulletin, Mayer Textile Machine Corporation, 7102 Sherwin Road, Greensboro, N.C. 27410, "RS-2-DS."

Table I. Listing of MWK Composite Applications by Category

INDUSTRY	MARINE	AEROSPACE	OTHER
Estimated % of MWK Fabric Composite Market	65%	20%	15%
Applica-tions	-hulls -decks superstructure substructure -support beams -motor bays -sails -racing shells	-aircraft skin -tail units -fuselage paneling -leading edges on wings and rudders -engine paneling -rotor blades -ballistic protection	-flooring -geotextiles -wall panels -automotive applications -protective helmets -industrial belting -inflatables

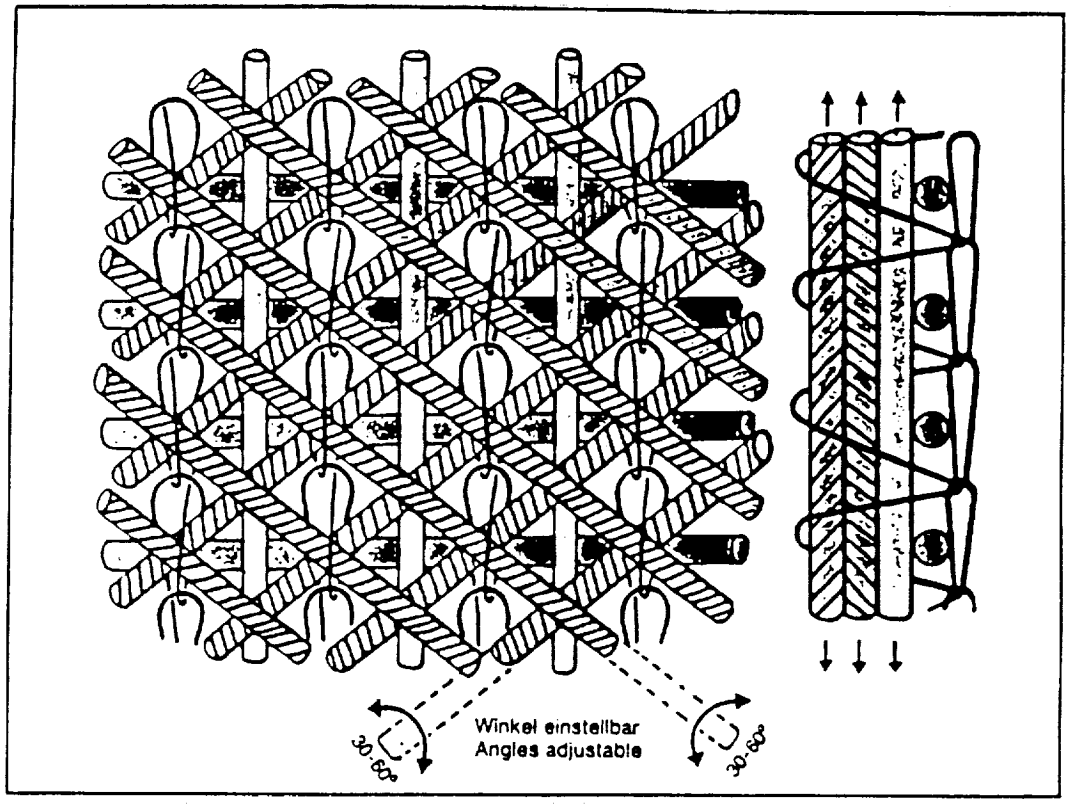

Figure 1: Structural Representation of MWK Fabric (10)

Properties of Textile Grade Ceramic Fibers

Eric Pudnos

Dow Corning Corporation

Abstract

The availability of textile grade ceramic fibers has sparked great interest for applications in composite reinforcement and high temperature insulation. This paper summarizes the properties of various small diameter textile grade ceramic fibers currently available. Room temperature mechanical and electrical properties of the fibers are discussed for three cases: ambient conditions, after heat aging in argon, and after heat aging in wet air. Dow Corning (R) HPZ Ceramic Fiber, a silicon nitride type fiber, is shown to have improved retention of mechanical and electrical properties above 1200C.

Introduction

The utility of ceramic fibers for reinforcement of ceramic matrix composites (CMC) is well established. The extensive research on a variety of composite systems is worldwide in scope and has produced some outstanding high temperature composite materials. The high strength and excellent toughness of these systems is a direct result of the mechanical properties of the reinforcing fibers. Commercially available fibers such as Ceramic Grade (CG) Nicalon (R) fiber, Nextel (R) 480, and SCS-6 offer a composite fabricator a range of desirable properties to work with. It is also well recognized that in many of these systems, the reinforcing fiber is a limitation due to thermal decomposition and/or loss of mechanical properties at the elevated temperatures that are encountered during composite fabrication or end-use conditions.

The purpose of this paper is to review the properties of some commercial fiber materials and compare these to a new fiber recently introduced by Dow Corning. The paper will be broken down into two sections: first, some general information about HPZ fiber, and then some more specific mechanical and electrical properties of various textile grade ceramic fibers. This discussion will be limited to the class of small diameter, textile grade ceramic fibers generally considered to be most desirable for CMC reinforcement. The data presented is limited to direct fiber tests and is not composite data. The author feels that these comparisons are useful for initial evaluation of fiber properties and material selection. We also recognize that such comparisons do not predict composite performance. Ongoing studies of fiber-matrix compatibility and fiber interfaces are necessary to fully determine performance of composites.

General Information about HPZ Ceramic Fiber

HPZ Ceramic Fiber is made via a polymer precursor route. This unique, amorphous silicon nitride-type fiber has been developed as part of a DARPA/Air Force contract. The processing chemistry and characterization of this material have been the subject of several publications and will not be covered here. Silane monomers manufactured by Dow Corning (Figure I) are reacted to form a preceramic polymer which is then extruded through a spinnerette at temperatures ranging from 100-300C. The resulting uncured polymer fiber

(green fiber) is then cured to a fully crosslinked, non-melting form. The cured fiber is then pyrolyzed to yield the ceramic fiber. During pyrolysis, various flue gases (CO, CH_4, SiO, etc.) are given off.

HPZ was officially introduced to the marketplace at the SAMPE show in April. It is available in developmental quantities and has a useful balance of mechanical and electrical properties. Typical properties are shown in Table I. The filament diameter has an oval cross-section that is calculated by taking the geometric average of the major and minor axes. As a developmental product, properties typically quoted cover a range of values. As you can see from Figure II, over the last two years we have been able to almost double the average tensile strength of the fiber through a series of process and procedural improvements. While no guarantees are made with regard to continuing this rate of improvement, suffice it to say that we are constantly working on improving fiber properties and that the values achieved today may be improved upon in the future.

Figure III is a typical range of tensile strength values from one particular lot of HPZ fiber. Each data point represents an individual filament tensile test (recall that HPZ is currently supplied in 500 filament tows). The range of values falls between a low of over 200 ksi to a high of about 650 ksi with an average tensile strength of 417 ksi. Such a spread of values is typical for ceramic fibers and other relatively brittle ceramic material.

As we'll see in the following section, HPZ maintains a large percentage of its mechanical and electrical properties at elevated temperatures. It has been proven elsewhere that this behavior can be attributed to the stability of the Si-N-C chemistry and that the oxygen in the fiber primarily resides near the surface of the fiber. A composition depth profile (Figure IV) produced with a scanning Auger microscope reveals that at the surface there is roughly 37% oxygen and 40% carbon, but at a depth of less than 700 nanometers, these concentrations have dropped to 5% and 12% respectively.

HPZ Ceramic Fiber is available in both 100g and 250g spools. The 250g spool contains nearly 1.5 miles of continuous tow (Figure V). The fiber is also available in several weave styles (8HS and Plain weave). Weavers who have handled HPZ for us have remarked that the fiber handles at least as well as mid-modulus carbon fibers. The fiber is supplied with a PVA sizing that can be removed by either a double hot water wash, or a 30 minute/600C/air exposure. Both of these methods will effectively remove the sizing without any effect on the mechanical or electrical properties.

As a class, non-oxide fibers such as HPZ have a higher strength than oxide fibers. Since non-oxide fibers typically have a lower density, they are considerably stronger than oxide fibers on a specific strength basis. Figure VI illustrates this nicely. The small circled area shows the range of properties currently possible with laboratory prepared HPZ. The excellent combination of specific strength and modulus of T-300 carbon fiber (as an example of carbon fibers) is shown by its location in the upper right quadrant of the chart. Clearly, we would like to improve the properties of ceramic

fibers to equal the room temperature properties of the graphite fibers, and have the properties retained at very high temperatures in air.

Room Temperature Properties

Table II illustrates the mechanical and electrical properties of several textile grade ceramic fibers considered in this paper. Structural and compositional information is presented in Table III. Of the fibers in this list, only Dow Corning (R) HPZ Ceramic Fiber is likely to be new to this audience. The reader should note that unless otherwise specified, fiber tensile data is for single filament testing at 1" length, tensile modulus values are calculated using machine compliance corrections, and that electrical measurements are made at 10 Ghz (x-band) at room temperature.

Obviously, it is the elevated temperature performance of ceramic fibers that is critical for the majority of applications where they are considered for use. Although some workers only consider oxidizing conditions to be of interest, we felt that inert, non-oxidizing conditions are useful since they represent conditions encountered during some composite fabrication processes and some use conditions (For example, the interior of a fully dense CMC may contain a very low partial pressure of oxygen). A two hour, 1400C flowing argon heat soak became a somewhat standard test condition during early studies within our program. This condition was initially chosen because Nicalon fiber was almost completely destroyed by such treatment. As shown in Figure VII, both Nicalon and Tyranno almost totally lose their reinforcing properties after such a thermal treatment. These studies, as well as work by others, show that this is a result of massive decomposition that occurs with loss of CO and SiO. As is also reported elsewhere, the oxide fibers generally weaken somewhat due to grain growth. In the case of HPZ fiber, it has been determined that the chemistry and the amorphous structure are very stable at 1400C. However the strength of the fiber is sensitive to minute levels of impurities. Recently we have tested a number of samples that retain fully 100% strength and maintain >300 ksi after a 2 hour soak at 1400C. No other fiber tested has shown such excellent inert atmosphere stability.

Similar argon agings have been carried out at lower temperatures. Generally, these studies show trends that are consistent with studies reported in the literature. Figure VIII shows the large weight losses that occur with Nicalon and Tyranno as CO evolves at higher temperatures. Note however, that the High Volume Resistivity (HVR) Nicalon fiber does remain reasonably stable for 65 hours at 1100C. As expected, the more stable chemistry of Nextel fiber shows only the weight loss associated with organic sizing present on the tows. Similarly, HPZ fiber shows the sizing burnoff and finally the loss of some surface oxygen at 1300C.

The electrical properties of the fibers essentially reflect the changes in bulk chemistry occurring. Figures IX and X show that the dielectric behavior of Nicalon and Tyranno change significantly as the chemistry changes due to loss of CO. In sharp contrast, HPZ and Nextel are electrically very stable as a result of the much more stable chemistry of these fibers.

Since certain applications require that fibers are exposed to air at elevated temperatures, it is important to examine heat aging under oxidizing

conditions. We selected 100 hours at 1000C as a representative condition. Flowing wet air (humidified at RT) was selected for its aggressiveness. In the study illustrated in Figure XI, we found that SiC-type fibers CG Nicalon, HVR Nicalon, and Tyranno lost strength in sequence as expected based on our findings in the inert atmosphere. Thus, the retained strength was (in order) CG Nicalon, HVR Nicalon and Tyranno. Once again, the titanium present in Tyranno did not aid stability under these conditions. Another surprise was the significant strength loss of the oxide fibers under oxidizing conditions. Apparently, some grain growth occurs even at 1000C in air causing a strength loss. Of the commercial fibers, only CG Nicalon retains >200 ksi strength.

Although it was expected that a silicon nitride fiber such as HPZ would show good oxidative stability, the results were still somewhat surprising. Within the normal error of the tensile test, no change in strength was observed during this experiment. Other work at Dow Corning at 1100C has also shown excellent strength retention for periods up to at least 15 hours.

As illustrated by the data, HPZ ceramic fiber strength is unaffected by a 100 hour oxidative treatment. Multiple batches and repeat runs show no loss of strength although some evidence of surface oxidation is observed. At higher temperatures, for instance, this surface oxidation can lead to fusion of the individual filaments within the tow bundle. Such fusion creates a very brittle, weak tow when treated at room temperature. Paul Sawko (NASA Ames) has studied fiber tow oxidation over a range of temperatures as illustrated in Figure XII. This data was generated by tensile testing fiber tows at room temperature after a 2 hour soak in air. This data nicely shows that while only HPZ fiber retains strength well in 1200C heat soaks, the strength reduction caused by fiber fusion does degrade strength at higher temperatures. Thus, in tow form, the usable temperature of HPZ fiber in free air appears to be 100-200C higher than for other non-oxide materials, but is still limited to about 1200-1300C. Note that the HPZ sample used in this experiment was from the earlier stages of our program. The denier here is only 400, while today's fiber has 1000 d. Also the starting fiber strength is about 200 ksi, and current values are around 400 ksi. Newer material would start at about 8 kg/denier and be expected to follow the same trend.

Although room temperature tests after heat soaks can be useful in judging the performance of a fiber, actual properties at various temperatures are necessary to effectively design composites for high temperature use. Workers at Penn State University have developed equipment and procedures for elevated temperature tensile testing of single filaments in air. One uniqueness of this technique is the capability for testing at greater than 1400C. Figure XIII shows the results of one test series. As reported previously, the oxide based fibers are generally lower strength at room temperature and maintain strength reasonably well to about 800C. Above 800C the strength degrades rapidly until at 1200C there is sufficient deformation to prevent testing at higher temperatures. In contrast, non-oxide fibers are considerably stronger at room temperature and generally maintain strength well up to about 1200C in fast fracture tests of this type. Above 1200C, Tyranno fiber loses strength rapidly, presumably due to its high oxygen content, while only Nicalon and HPZ hold useable strength levels at 1400C. Even at 1450C, the HPZ fiber has greater than 100 ksi strength. Elevated temperature modulus data (Figure XIV)

generally parallels the same behavior, although here the excellent stability of HPZ's microstructure and fiber chemistry is even more apparent as evidenced by the superior modulus retention.

Conclusions

1) Non-oxide fibers have good room temperature strength and modulus, generally much higher than for oxide fibers.

2) CG Nicalon and HPZ are the only fibers to retain useable tensile strength and modulus above 1300C.

3) HPZ fiber exhibits good retention of mechanical properties after oxidation at 1000C for 100 hours. This is the only material showing no strength loss under such conditions.

4) The handling properties of HPZ are similar to mid-modulus carbon fibers.

DOW CORNING® HPZ CERAMIC FIBER

Typical Properties

• Composition (Wt. %)	Si	57%
	N	28%
	C	10%
	O	5%
• Amorphous Structure		
• Diameter	10-12 microns	
• Tensile Strength	420 ksi (2.9 GPa)	
• Tensile Modulus	28 Msi (193 GPa)	
• Density	2.4 g/cc	
• DK	6.1	
• LF	0.06	
• Heat Capacity	0.68 J/g C	
• Coeff. of Thermal Ex (20-1100°C)	4.1 ppm/C	

Table I : HPZ Ceramic Fiber - Typical Properties

FIBER PROPERTIES

Fiber	Diameter	Tensile Strength	Modulus	DK	LF
CG NICALON	15	400	28-30	9.5	1.0
HVR NICALON	15	350	26-28	6.4	0.05
LVR NICALON	15	425	26-28	>20	>10
C-Coated NICALON	15	425	28-30	-	-
TYRANNO	8	450	22	7.8	1.0
HPZ	10-12	420	28-32	6.1	0.06
NEXTEL 480	8-10	220	30-32	6.4	0.05

Table II : Comparable Fiber Properties

FIBER CHARACTERISTICS

Fiber	Composition	Density (g/cc)	Structure
CG NICALON™	Si-C-O	2.55	nanocrystalline SiC/ amorphous
HVR NICALON	Si-C-O	2.35	
LVR NICALON	Si-C-O	2.35	
C-Coated NICALON	Si-C-O	2.55	
TYRANNO®	Si-O-C-Ti	2.40	amorphous
HPZ	Si-N-C-O	2.40	amorphous
NEXTEL® 480	$Al_2O_3/SiO_2/B_2O_3$	3.10	crystalline, mullite

Table III : Fiber Characteristics

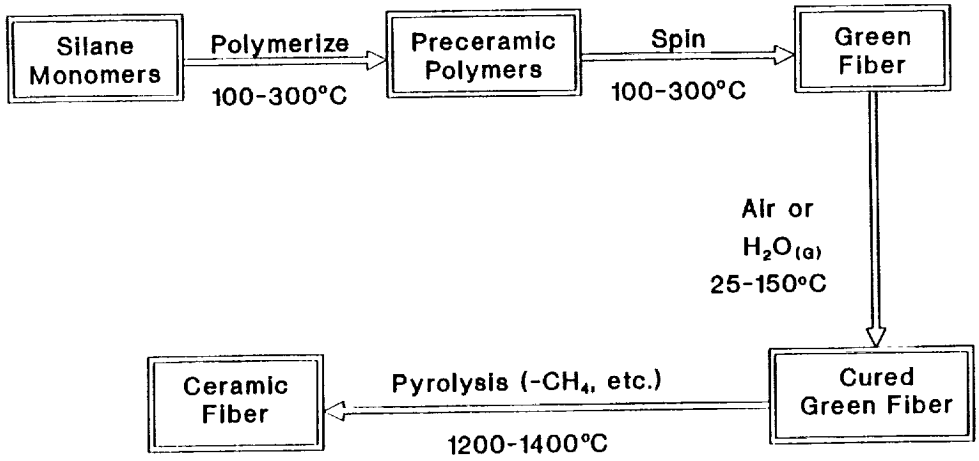

Figure I : Process Schematic - Polymer Precursor Route

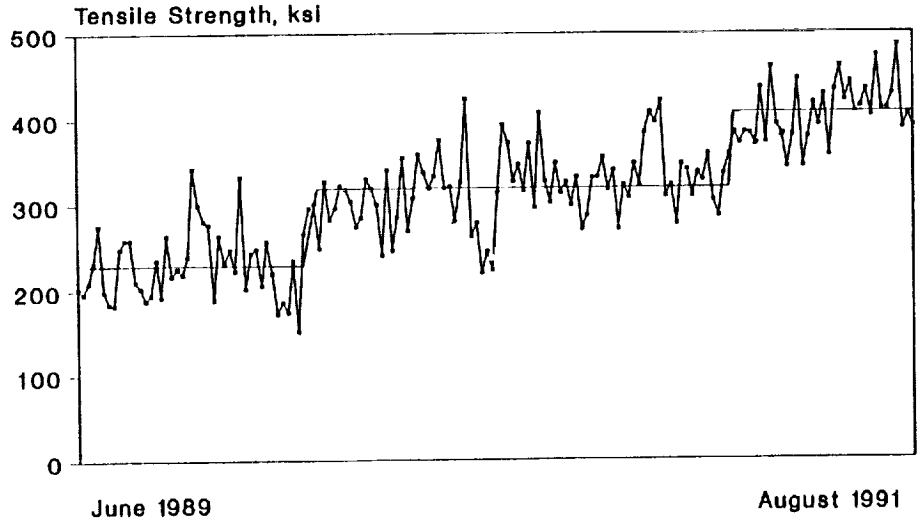

Figure II : HPZ Ceramic Fiber - Tensile Improvements

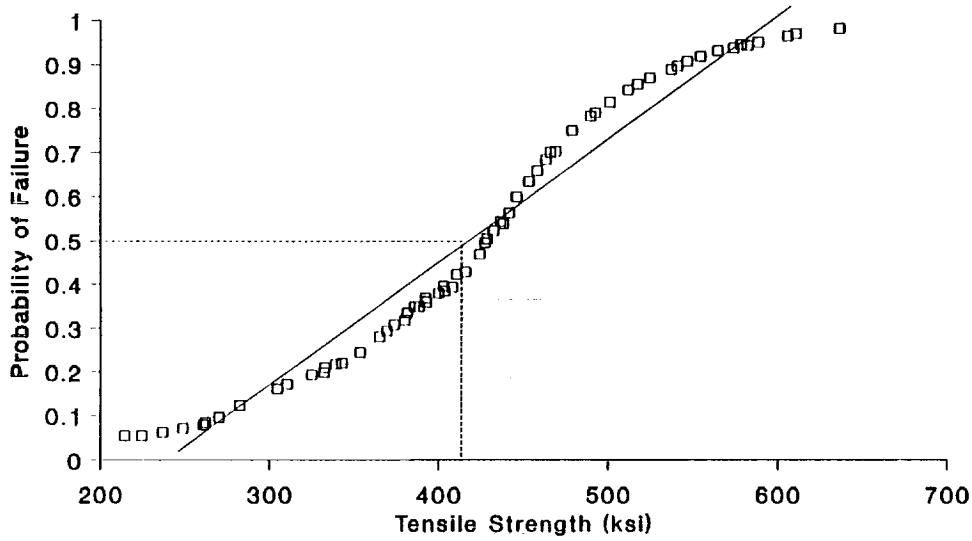

Figure III : Failure Probabilities

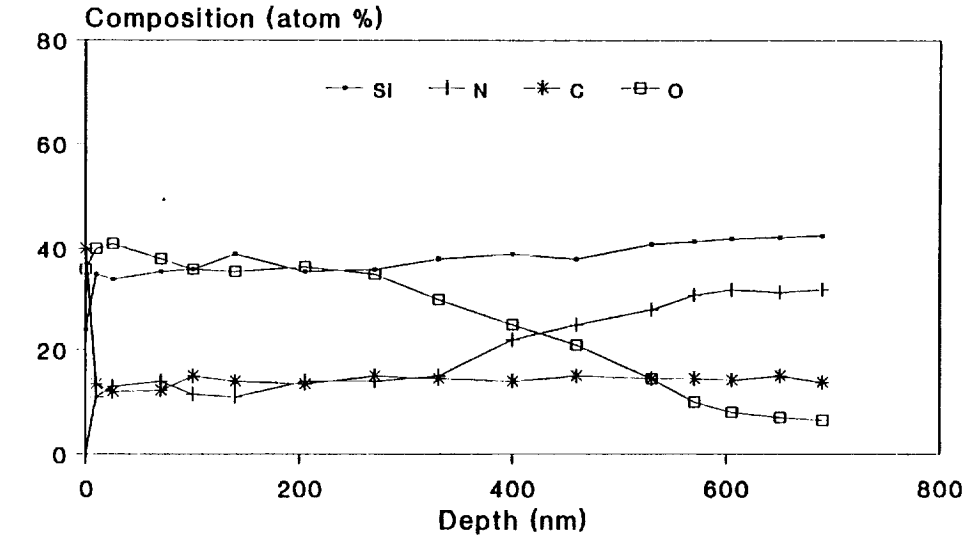

Data from A. Zangvil, U. Illinois

Figure IV : Compositional Depth Profile

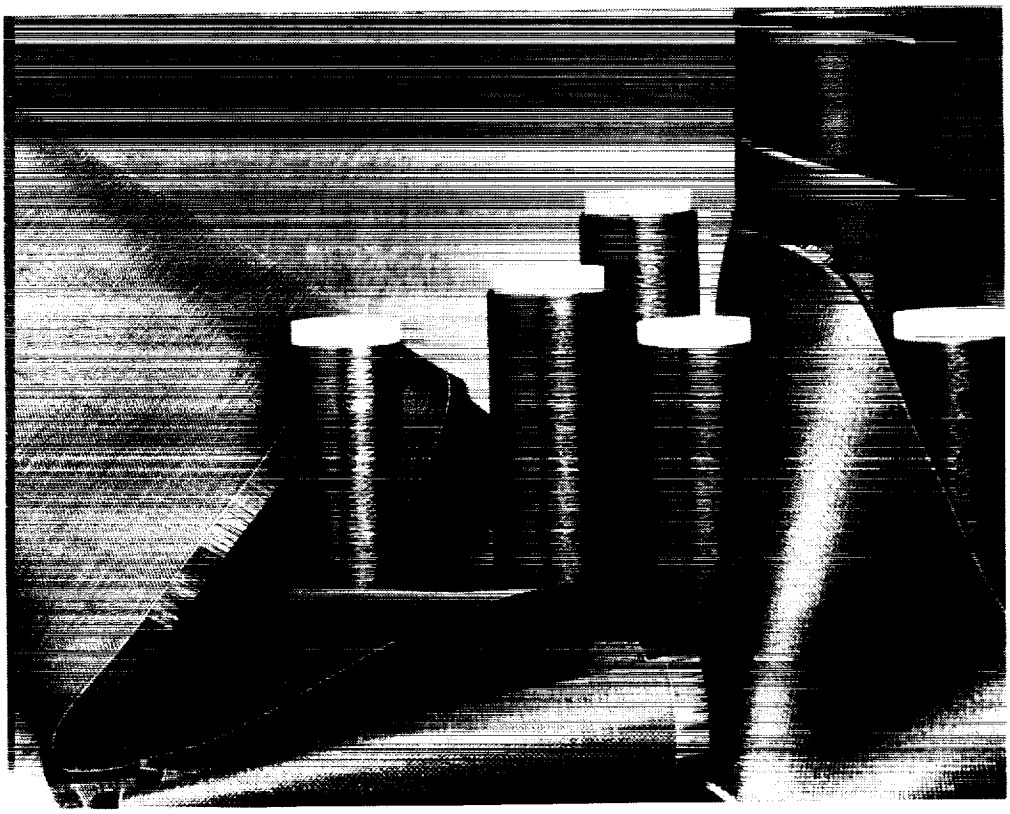

Figure V : HPZ spools and woven cloth

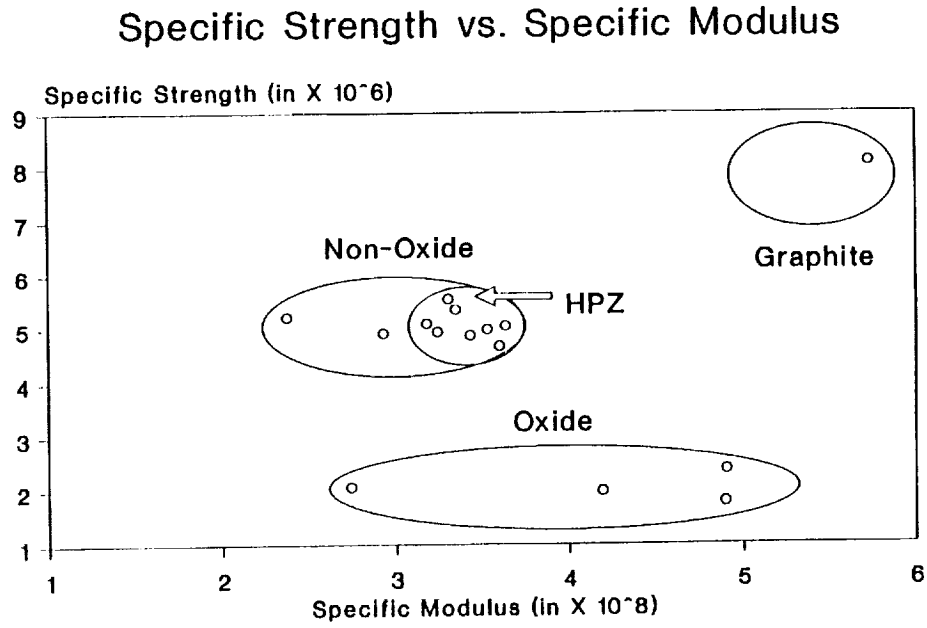

Figure VI : Continuous Fiber Comparisons

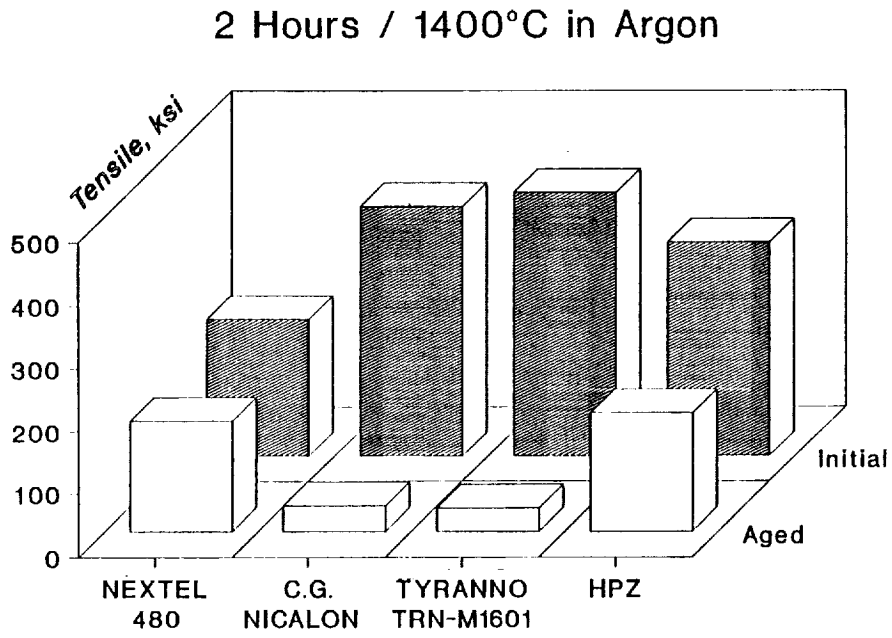

Figure VII : Inert Aging Comparisons

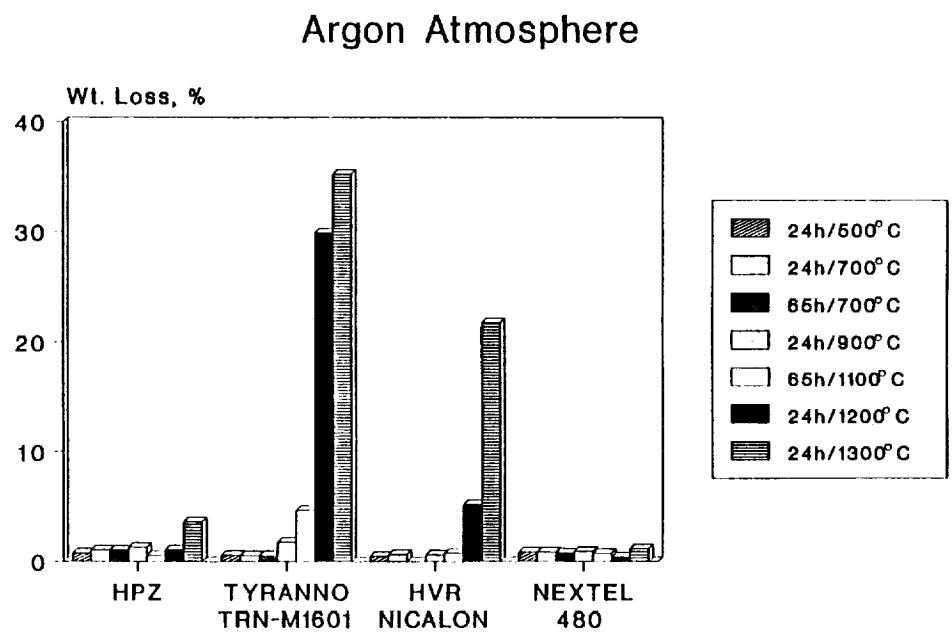

Figure VIII: Aging Effect on Fiber Weight

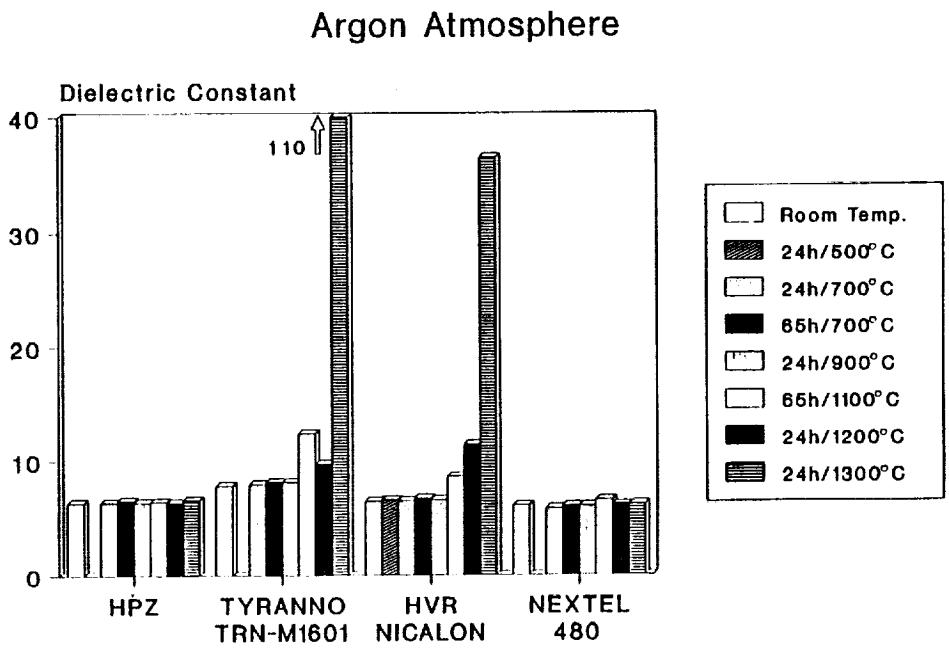

Figure IX : Aging Effect on Fiber DK

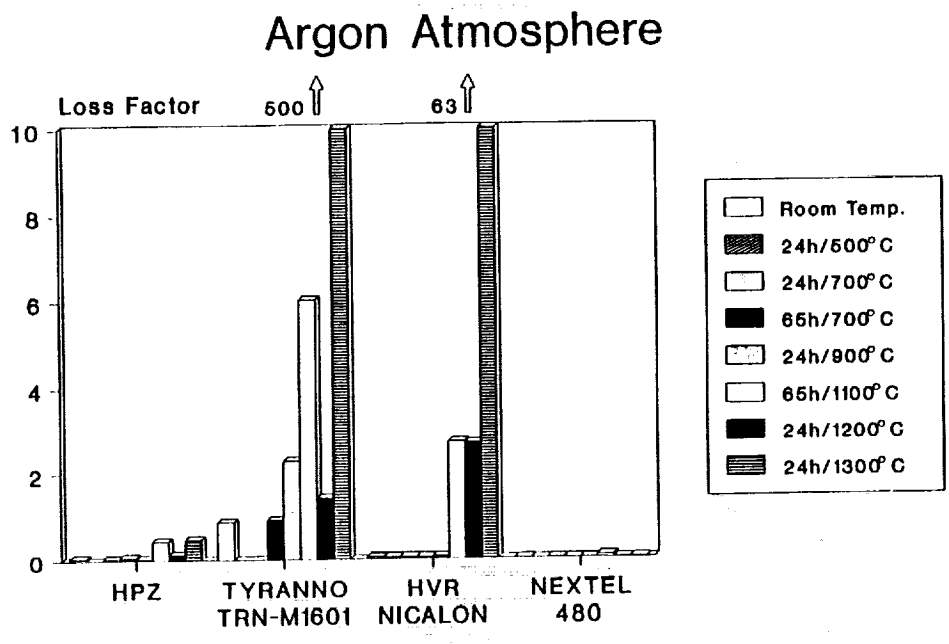

Figure X : Aging Effect on Fiber LF

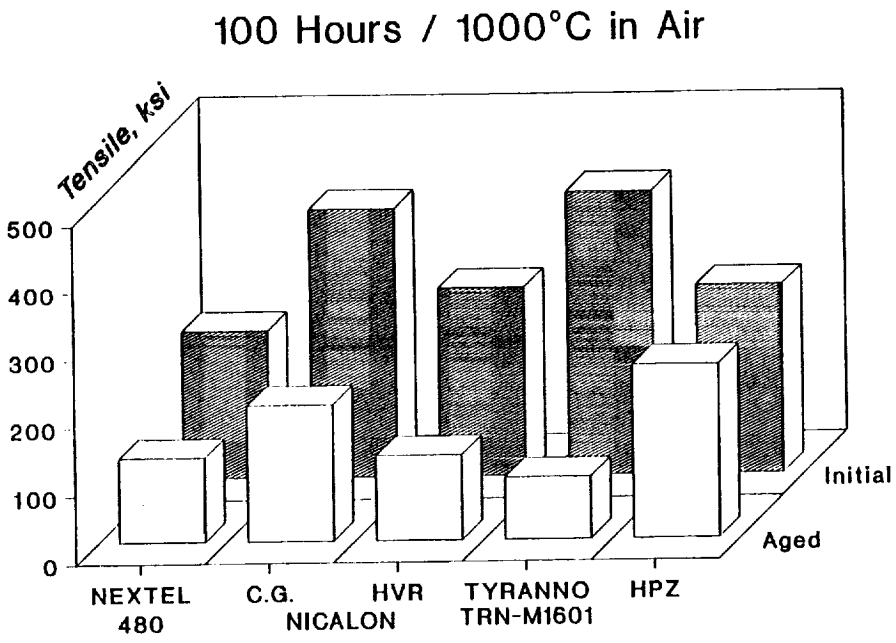

Figure XI : Fiber Oxidation Results

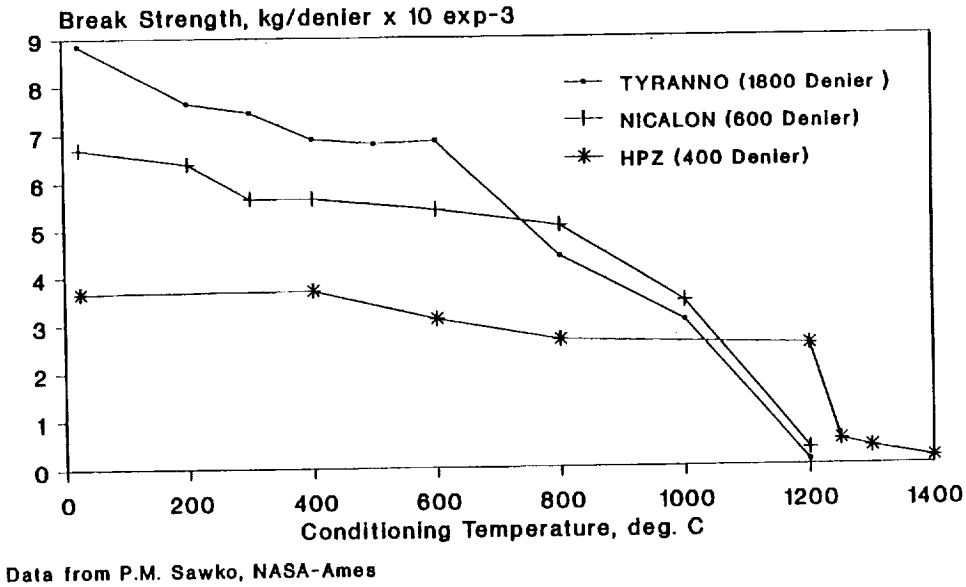

Data from P.M. Sawko, NASA-Ames

Figure XII : Effect of Conditioning Temperature on Break Strength

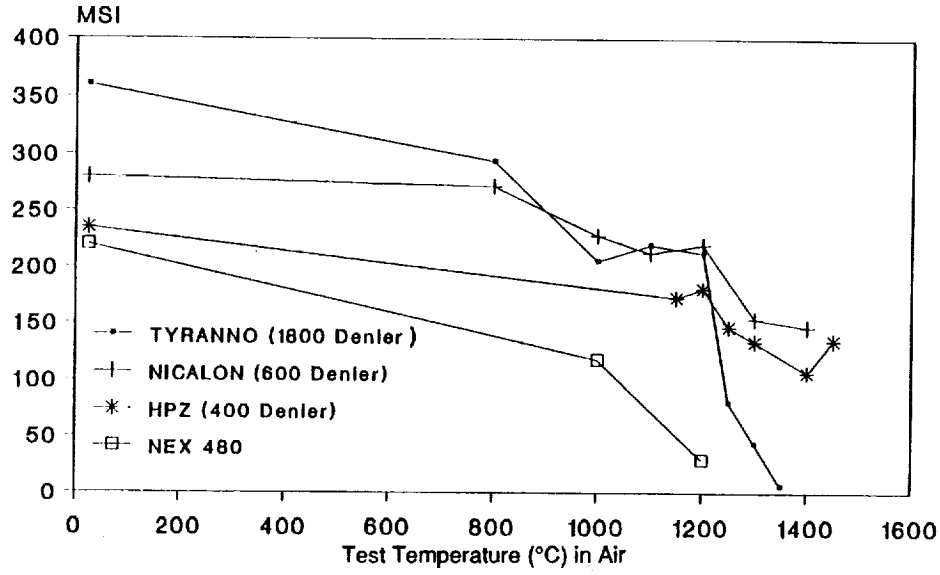

Data from R. Tressler, Penn State

Figure XIII: Fiber Tensile Strength - At Temperature In Air

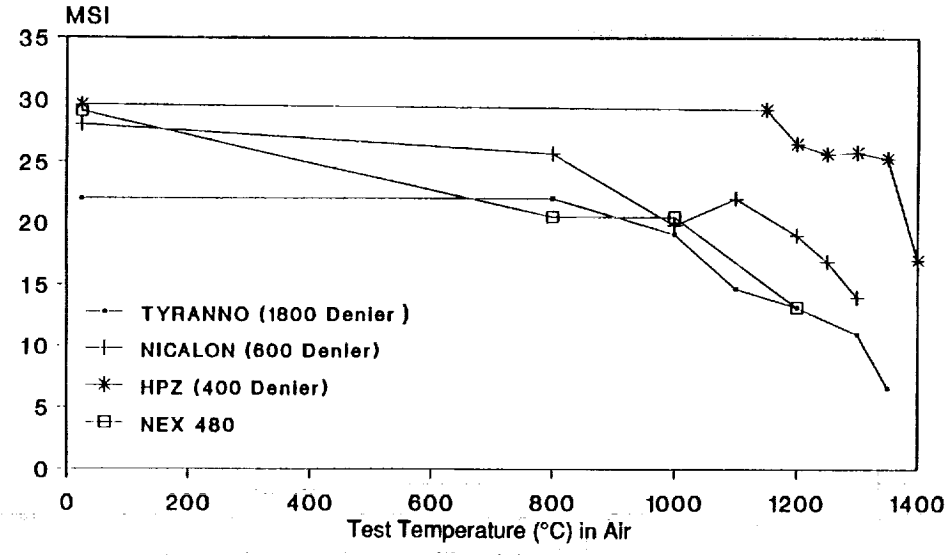

Data from R. Tressler, Penn State

Figure XIV : Fiber Tensile Modulus - At Temperature In Air

THE OPTIMAL FIBER VOLUME FRACTION AND FIBER-MATRIX PROPERTY COMPATIBILITY IN FIBER REINFORCED COMPOSITES

Ning Pan
Division of Textiles and Clothing
University of California
Davis, CA

Abstract

Although the question of minimum or critical fiber volume fraction beyond which a composite can then be strengthened due to addition of fibers has been dealt with by several investigators for both continuous and short fiber composites, a study of maximum or optimal fiber volume fraction at which the composite reaches its highest strength has not been reported yet. The present analysis has investigated this issue for short fiber case based on the well-known shear lag (the elastic stress transfer) theory as the first step. Using the relationships obtained, the minimum spacing between fibers is determined upon which the maximum fiber volume fraction can be calculated, depending on the fiber packing forms within the composites. The effects on the value of this maximum fiber volume fraction due to such factors as fiber and matrix properties, fiber aspect ratio and fiber packing forms are discussed. Furthermore, combined with the previous analysis on the minimum fiber volume fraction, this maximum fiber volume fraction can be used to examine the property compatibility of fiber and matrix in forming a composite. This is deemed to be useful for composite design. Finally some examples are provided to illustrate the results[1–14].

1 INTRODUCTION

Adding fibers to strengthen materials is a technique which has been used since ancient times. It is applied mainly to materials which are much weaker in tension than in compression so that by adding fibers into them the superior tensile property of fibers can be fully utilized and stronger new materials are obtained.

Yet it is understandable that if very few fibers are added to a matrix, the material is weakened rather than strengthened. Therefore there must be a minimum critical fiber volume fraction V_{min}, only exceeding that with which the fiber reinforcing function can be realized. There have been several studies which addressed this problem and derived the specific values of V_{min} for various cases and under different conditions [1,8,11]. On the other hand, however, as the fiber amount in the system is being increased, the tensile strength of the

composite will increase to a certain point where, upon further increasing of fiber amount, the bonding between the fibers and the matrix will start to deteriorate as the fibers become too close to each other. As a result, for a short-fiber composite, the tensile strength of the composite will decline due to the bond failure of the system caused by the excessive fibers. Therefore there will be a maximum value of fiber volume fraction as well, that being the upper limit of fiber amount allowable in the system for reinforcement.

There have been no reported studies on this issue as far as the present author is aware. This may be due mainly to the fact that, in most cases, the fiber amount which can be incorporated into a matrix system is limited by the processing technology [4] so that technically it may be difficult for the fiber volume fraction to reach this maximum allowable value. Hence the maximum fiber volume problem may not be as significant as the minimum one for practical applications. Nevertheless, study on this issue is still desirable partly due to its theoretical significance, and more importantly, because the investigation of this issue as presented in this article cannot only provide the maximum value of fiber volume fraction, but also determines the property compatibility of various fiber and matrix materials for a composite so as to guide the design procedures in achieving the optimum composite strength and full material usage.

The present study deals with this problem based on a shear strength criterion between fibers within the composite. The effects of fiber length and fiber misalignment are also investigated.

2 THE MINIMUM ALLOWABLE SPACING BETWEEN FIBERS IN A SHORT FIBER COMPOSITE

It has been a well known mechanism that when a fiber composite is under a uniaxial tension, the axial displacements in the fiber and in the matrix will be different because of the differences in tensile properties of these two components. As a result, shear strains will be created on all planes parallel to the axes of the fibers. The shear strain and the resulting shear stress are the primary means by which load is transferred to fibers (for a short fiber composite), or distributed between and supported by the two components of composites. It is through this interaction between fibers and matrix that a fiber reinforcing function is realized. There have been several theories trying to explain this fiber-matrix interaction. The first one was entirely based on the elastic mechanism by Cox [3] in 1952, and is now referred to as the shear lag theory, and another similar version was later proposed by Rosen [12]. Since then, a number of new theories were suggested such as the slip theory [7] to account for matrix plasticity at the fiber surface near the fiber ends, applicable to well-bonded reinforced metals, and the theory of frictional sliding [7] to reinforced polymers and ceramics. However for the present study, the model of the elastic stress transfer will be used as the main theoretical basis. It will be shown that, although this theory basically only explains the behavior of composites at low stress, it still provides adequate information in determining the maximum fiber volume fraction for design purposes. Furthermore the analysis will surely be helpful in the attempt to look into the case of the inelastic interaction as well.

Assumptions made in this analysis include :

1. Since the elastic model is used here, conclusions from the present analysis are valid only if the original assumptions associated with this model hold.
2. The composite consists of many short fibers each with constant length l, circular cross-section area A_f of uniform radius r and tensile modulus E_f.
3. All fibers are distributed uniformly along the length of the composite so that the fiber area fractions on all the cross sections of the composite are identical.
4. Both fibers and matrix behave elastically, and the interface transfers the stress between fibers and matrix without yielding or slipping.
5. Fiber ends are all normal so that the shape effect of fiber end on the stress transfer [6] is excluded in this analysis.
6. Furthermore, the fiber-fiber interaction within the composite and the effect of matrix property change as a result of the fiber interfering with dislocation motion in the matrix are also ignored.

We take the mean fiber center to center spacing normal to their length to be $2R$ (see Figure 1). Assume the composite as a whole is subject to a strain ϵ_c which will cause a strain ϵ_f in a fiber. If P is the load in the fiber at a distance x from the fiber end, then according to Cox [3], the distribution of tensile stress in this arbitrary fiber is

$$\sigma = \frac{P}{A_f} = E_f \epsilon_f [1 - \frac{\cosh \beta(\frac{l}{2} - x)}{\cosh \beta \frac{l}{2}}] \tag{1}$$

where

$$\beta = \frac{1}{r}\sqrt{\frac{G_m}{E_f}(\frac{2}{\ln(R/r)})} \tag{2}$$

and G_m is the shear modulus of the matrix. Note that $\sigma = 0$ at $x = 0$, and l.

The maximum stress occurs at the middle of position $x = l/2$ where

$$\sigma_{max} = E_f \epsilon_f [1 - \frac{1}{\cosh \beta \frac{l}{2}}] \tag{3}$$

It can be seen from Equation 3 that, in order to fully make use of the tensile strength of the fibers, i.e. to make $\sigma_{max} = \sigma_{bf}$, the fiber-fiber spacing R is the key factor for given fiber strain, and fiber and matrix properties.

If τ is the shear stress in the direction of the fiber axis, on planes parallel to this axis, then at the fiber surface we have

$$\frac{dP}{dx} = -2\pi r \tau \tag{4}$$

Equation 1 and 4 give the expression for the shear stress distribution

$$\tau = E_f \epsilon_f \sqrt{\frac{G_m}{2E_f \ln(R/r)}} \frac{\sinh \beta(\frac{l}{2} - x)}{\cosh \beta \frac{l}{2}} \tag{5}$$

The maximum value of τ occurs at the fiber ends, i.e. at $x = 0$ and l,

$$\tau_{max} = E_f \epsilon_f \sqrt{\frac{G_m}{2E_f \ln(R/r)}} \tanh \beta \frac{l}{2} \tag{6}$$

and it is zero at the middle of the fiber. Both of these stress distributions are shown in Figure 2. The ratio of the maximum value of shear stress to the maximum tensile stress in the fiber is

$$\frac{\tau_{max}}{\sigma_{max}} = \sqrt{\frac{G_m}{2E_f \ln(R/r)}} \coth \beta \frac{l}{4} \tag{7}$$

This ratio is of great importance as it represents fiber and matrix properties as well as fiber spacing R within the matrix. The validity of equations 1 - 7 has been verified by several experimental studies [6,7].

In reinforcing the composite to its maximum tensile strength, the tensile strength of fibers has to be utilized to the fullest. In other words, a stress equal to the tensile breaking stress of the fibers σ_{bf} must be reached at the middle of a fiber,i.e. $\sigma_{max} = \sigma_{bf}$. So the above equation can be rearranged as

$$\tau_{max} = \sigma_{bf} \sqrt{\frac{G_m}{2E_f \ln(R/r)}} \coth \beta \frac{l}{4} \tag{8}$$

This equation gives the relationship between fiber spacing R (or the spacing ratio R/r) and the maximum value of shear stress. When the spacing between fibers R decreases, the value of τ_{max} will increase as shown by Figure 3. The minimum spacing R_{min} is thus determined when τ_{max} has been increased to such a large value that it reaches the shear strength of the matrix adjacent to the interface or the shear strength of the fiber/matrix interface, whichever is less, designated as τ_s. Because of the elastic assumption where the matrix can not deform plastically, this will cause either the fiber /matrix interface or the matrix to fail in shear.

Furthermore replacing τ_{max} by τ_s and rearranging Equation 8 give the final relationship between the minimum spacing ratio R_{min}/r and the strength ratio $\frac{\sigma_{bf}}{\tau_s}$, the fiber aspect ratio $\frac{l}{r}$ as well as the modulus ratio $\frac{G_m}{E_f}$

$$\ln(R_{min}/r) = (\frac{\sigma_{bf}}{\tau_s} \coth \beta \frac{l}{4})^2 \frac{G_m}{2E_f} = \frac{\sigma_{bf}}{\tau_s} \coth[\frac{1}{4} \frac{l}{r} \sqrt{\frac{G_m}{E_f} \frac{2}{\ln(R_{min}/r)}}]^2 \frac{G_m}{2E_f} \tag{9}$$

This is a transcendental equation for R_{min}/r, and its solution can only be calculated numerically.

However if the fiber length is relatively long so that $\coth \beta \frac{l}{4} \rightarrow 1$, we have an explicit relationship between the fiber spacing ratio and the fiber-matrix properties

$$\ln(R_{min}/r) = (\frac{\sigma_f}{\tau_s})^2 \frac{G_m}{2E_f} \tag{10}$$

or

$$R_{min}/r = e^{(\frac{\sigma_f}{\tau_s})^2 \frac{G_m}{2E_f}} \tag{11}$$

In this analysis, the effect of stress transfer across the fiber ends is neglected which will cause an extra load on both the fiber and the matrix in this region. However this effect is considered insignificant [11] as long as the fiber aspect ratio $l/r > 10$. Also the influence of stress concentration across the fiber ends, which will lead to a greater shear stress [8] and will affect the slip behavior of the fiber ends, is ignored.

In addition, in the present analysis, fiber and the matrix are assumed to be completely elastic. This is of course an ideal case, and only valid in practice to brittle materials. For some cases where plastic deformation of the matrix does exist, the conclusion drawn from this study will be a conservative one and certain modification may be needed, since the plastic deformation of the matrix will alleviate the shear stress. However a different model of the spacing/stress relationship is desirable for a matrix which is significantly plastic and flows under loading, or for structures where the effect of frictional sliding between fiber and matrix during the stress transfer is not negligible.

3 THE MAXIMUM FIBER VOLUME FRACTION IN COMPOSITES

As indicated above since there is a minimum spacing R_{min}/r between fibers within a composite below which the structure will collapse due to shear failure, correspondingly this minimum spacing will define an upper limit of fiber amount which is allowed to be incorporated into a given matrix. The composite will reach its highest strength at this maximum fiber volume fraction V_{max}, as there will be a maximum amount of fibers in the composite and each is fully utilized. In other words, this maximum fiber volume fraction is also the optimal value for maximizing the composite tensile strength. Obviously the specific value of V_{max} is dependent on the forms of fiber arrangement within a composite as well. Moreover, for the short fiber case where fiber ends don't meet, the maximum fiber volume fraction also varies with the distance between fiber ends. Let us assume this distance between the ends of two fibers is $2\delta_f$ as shown in Figure 4(a).

The following are the two cases most often encountered in a composite [11].

3.1 Hexagonally Packed Fibers

The fiber arrangement of this type is schematically shown in Figure 1-(c). Suppose there are totally N fibers within the composite. According to the definition of fiber volume fraction of a composite, we have

$$V_f = \frac{V_{fiber}}{V_{total}} \tag{12}$$

Considering the hexagonal area enclosed by the dotted line in Figure 1-(c), the maximum fiber volume fraction in this case is

$$V_{fmh} = \frac{3\pi r^2 l}{\frac{3\sqrt{3}}{2}(2R_{min})^2(l+2\delta_f)} = \frac{\pi}{2\sqrt{3}}(\frac{r}{R_{min}})^2(\frac{1}{1+2\delta_f/l}) \tag{13}$$

When all fibers are packed so densely that they are actually contacting each other in full with fiber ends also connected, that is

$$R_{min} = r, \qquad \delta_f = 0 \tag{14}$$

the maximum fiber volume fraction becomes

$$V_{fmh} = \frac{\pi}{2\sqrt{3}} \tag{15}$$

Also for the case when the fiber length is so long as $l >> \delta_f$ that the fiber end effect can be neglected

$$V_{fmh} = \frac{\pi}{2\sqrt{3}}(\frac{r}{R_{min}})^2 \tag{16}$$

Because of this direct relationship between the maximum fiber volume fraction and the minimum fiber spacing, it is equivalent in the later analysis to refer to either of them.

3.2 Square-Packed Fibers

The fiber arrangement in this case is shown in Figure 1-(d) and we will have

$$V_{fms} = \frac{\pi r^2 l}{(2R_{min})^2(l + 2\delta_f)} = \frac{\pi}{4}(\frac{r}{R_{min}})^2(\frac{1}{1 + 2\delta_f/l}) \tag{17}$$

For the longer fiber case we have

$$V_{fms} = \frac{\pi}{4}(\frac{r}{R_{min}})^2 \tag{18}$$

In the extreme case when fibers are closely packed to each other so that $R_{min} = r$, there will be

$$V_{fms} = \frac{\pi}{4} \tag{19}$$

In either of two packing forms, the value of maximum fiber volume fraction monotonically increases as the fiber spacing decreases. The relationship of or difference between the maximum fiber volume fractions of these two packing forms is given by

$$\frac{V_{fms}}{V_{fmh}} = \frac{\sqrt{3}}{2} \tag{20}$$

That is, the maximum possible fiber volume fraction for square-packed fibers is less than that of a hexagonally Packed case. Again because of this direct relationship between the two fiber packing forms, for briefness, only the Square-Packed form is used in the following analysis.

Note that when there is fiber misalignment existing in the composite, the fiber arrangement may not be as regular as the two examples shown here. Consequently the value of the actual maximum fiber volume fraction may be lower than the present results.

4 THE MINIMUM FIBER VOLUME FRACTION IN COMPOSITES

In the next paragraph, ϵ_{bf}, ϵ_{bm} and ϵ_{ym} represent the fiber breaking strain, the matrix breaking strain and the matrix yield strain. Although there may be three cases [11]

1. $\epsilon_{bf} < \epsilon_{ym}$,
2. $\epsilon_{ym} < \epsilon_{bf} < \epsilon_{bm}$,
3. $\epsilon_{bm} < \epsilon_{bf}$.

existing in composite, each of which will lead to different failure behavior of the composite, usually the breaking strain of the fiber ϵ_{bf} is less than the yield strain of the matrix ϵ_{ym} so that only the first case is considered here. The treatments of two other cases, however, are in principle the same.

If the variations of fiber tensile properties are ignored, according to the Law of Mixture, the breaking strength of the composite σ_{bc} is of the contributions from both fibers and the matrix, and can be expressed as [1]

$$\sigma_{bc} = \sigma_{fm}(1 - V_f) + \eta_l \eta_\theta \sigma_{bf} V_f, \qquad V_f > V_{min} \tag{21}$$

where σ_{bf} is the breaking strength of the fiber, and σ_{fm} is the stress on the matrix at the breaking tensile strain of the fiber. The factors η_l and η_θ account for the effects of limited fiber length for the short fiber case, and of fiber misalignment, and are often called the length efficiency and fiber orientation efficiency factors. V_{min} is the minimum value of the fiber volume fraction which must be exceeded if the strength of the composite is to be given by the Law of Mixture. The value of V_{min} can be determined analytically, according to Kelly [8],as shown below.

If the amount of fiber added into the composite is very small, it will actually weaken the composite so that the strength of the composite becomes

$$\sigma_{bc} = \sigma_{bm}(1 - V_f) \tag{22}$$

where σ_{bm} is the breaking strength of the matrix.

Inserting this relation into Equation 21 gives:

$$\sigma_{bm}(1 - V_f) = \sigma_{fm}(1 - V_f) + \eta_l \eta_\theta \sigma_{bf} V_f \tag{23}$$

The minimum fiber volume fraction can be derived from this equation,i.e.

$$V_{min} = \frac{\sigma_{bm} - \sigma_{fm}}{\eta_l \eta_\theta \sigma_{bf} + \sigma_{bm} - \sigma_{fm}} \tag{24}$$

For a continuous fiber composite where all fibers are aligned in the loading direction, there will be

$$\eta_l = 1, \eta_\theta = 1$$

and

$$V_{min} = \frac{\sigma_{bm} - \sigma_{fm}}{\sigma_{bf} + \sigma_{bm} - \sigma_{fm}} \tag{25}$$

5 DETERMINATION OF THE FIBER LENGTH EFFICIENCY FACTOR

It has been claimed [9] that in the post-cracking stage the combined efficiency factors due to both length and orientation can not be simply calculated as the product of the length efficiency factor and the orientation efficiency factor because the orientation efficiency factor is also a function of the fiber length in the case of short fibers. For the elastic model of pre-cracking stage as in the present case however, these two factors can be considered to be independent of each other and therefore can be determined separately.

The length efficiency factor, specifying the effect of a definite length of fibers in a short fiber composite, has two expressions, depending on the stress interaction mechanisms [9]. For the inelastic case, the most common version of this fiber length efficiency factor is expressed in terms of critical fiber length [1,8, 9]. For the elastic case, it can be easily determined based on the tensile stress distribution. From Equation 1, the average tensile stress over the length of this short fiber can be calculated as

$$\bar{\sigma_{fl}} = E_f \epsilon_f [1 - \frac{\tanh \beta \frac{l}{2}}{\beta \frac{l}{2}}] \tag{26}$$

While for continuous fibers, there is

$$\bar{\sigma_{fl}} = \sigma_{fl} = E_f \epsilon_f \tag{27}$$

Therefore the fiber length efficiency factor can be defined as

$$\eta_l = 1 - \frac{\tanh \beta \frac{l}{2}}{\beta \frac{l}{2}} \tag{28}$$

When $l \to \infty$, $\eta_l = 1$.

This expression shows that, compared to the continuous fibers, the tensile stress on a short fiber is discounted by a factor η_l due to limited fiber length.

It is easy to prove that when $l \to 0$, $\eta_l = 0$.

6 DETERMINATION OF FIBER ORIENTATION EFFICIENCY FACTOR

In most published studies where the effect of fiber misalignment was considered, fibers were assumed either all aligned in the same direction at a fixed angle with respect to the axis of the composite loading direction[1,8,11], i.e., there is no variation or spread existing in

fiber orientations, or distributed totally in random [3, 9]. Although it is usually desirable to orient the fibers to enhance stiffness and strength properties, in short-fiber composites, it is normally very difficult, if not impossible, to achieve perfect alignment or completely random distribution of short fibers. The orientation distributions of fibers in a composite are determined by the processing conditions. Partial fiber alignment is typical in injection and transfer moulded composites while planar partial random orientation is typical in sheet moulding compounds [2]. Therefore for most cases, variation of fiber orientation distribution has to be included in the study. There have been several reports [2,5,13,14] dealing with fiber orientation spreading. A more explicit form of the expression of this fiber orientation efficiency factor is obtained in the present study.

6.1 Form of Fiber Orientation Density Function

Since it is impractical to deal with fibers of different orientations individually, a statistical approach is usually a better, or the only, alternative. To do this, a known form of the function to describe the fiber orientation probability density is the premise.

Two cases of the fiber orientation distribution are of practical importance [2]. In the case of injection moulded objects, fiber orientation distribution is independent of the base angle ϕ if the direction of flow is along the $x_3(z)$ axis. In sheet moulding compounds it is reasonable to assume that the short fibers all lie within a plane and the problem is reduced to a two-dimensional one. In either case, by properly arranging the coordinate system, the fiber orientation density function can be expressed as

$$\Omega(\theta) = \begin{cases} \frac{1}{\alpha} & 0 \leq \theta \leq \alpha \\ 0 & \alpha \leq \theta < \pi/2 \end{cases}$$

where θ is the polar angle of a fiber with respect to the x_3 axis (the loading direction), and α is the limit of θ.

6.2 Relationship Between Strains of Composite, Matrix and Fiber

Assume the composite as a whole is subject to a strain ϵ_c which will cause strain ϵ_f in the fiber and ϵ_m in the matrix. It has been widely accepted that the elastic stress transfer mechanism is dominant at the pre-cracking stage and therefore the longitudinal displacements of the fiber and matrix interface are considered geometrically compatible. In other words, the matrix strain will be the same as the composite strain before cracking. The fiber strain however is dependent on the fiber orientation with respect to the loading direction.

There are several approaches in finding the relationship between the composite strain and fiber strain, such as the tensor transformation method[10] and the affine deformation model [5]. However a few simple differentiation operations as shown below can also derive the same result.

Let us consider a cylinder of matrix material with height H and radius R_c. Inside the matrix there is a fiber with length l and orientation θ (see Figure 4-(b)). We have a relationship between the three variables

$$l^2 = R_c^2 + H^2 \tag{29}$$

Differentiating both sides gives

$$2ldl = 2R_c dR_c + 2HdH \tag{30}$$

It can be further expressed as

$$\frac{dl}{l} = \frac{R_c^2}{l^2}\frac{dR_c}{R_c} + \frac{H^2}{l^2}\frac{dH}{H} \tag{31}$$

Bringing

$$\frac{dH}{H} = \epsilon_c \tag{32}$$

and

$$\frac{dR_c}{R_c} = -\nu_m \epsilon_c \tag{33}$$

into it yields

$$\epsilon_f = \frac{dl}{l} = \epsilon_c(\cos^2\theta - \nu_m \sin^2\theta) \tag{34}$$

where ν_m represents the matrix Poisson's ratio. Note that, similar to previous analyses [5, 8], the effect of the fiber Poisson's ratio has been excluded in equation 33. Equation 34 has been found to be consistent with both the experimental data and the results based on other more sophisticated analytical analysis [5]. However, since the change of the fiber orientation during composite deformation is neglected in the above analysis, it is preferable to apply equation 34 to the small strain case.

6.3 The Result of Fiber Orientation Efficiency Factor

Once we have the relationship between fiber strain and the overall composite strain, the average strain on an arbitrary fiber due to its misalignment can then be calculated as

$$\bar{\epsilon_f} = \int_0^{\alpha} \epsilon_c(\cos^2\theta - \nu_m \sin^2\theta)\Omega(\theta)d\theta \tag{35}$$

Bringing the distribution function into the above equation gives

$$\bar{\epsilon_f} = \frac{\epsilon_c}{4\alpha}[2\alpha(1-\nu_m) + (1+\nu_m)\sin 2\alpha] \tag{36}$$

The overall average tensile stress on this fiber thus becomes

$$\bar{\sigma_f} = \eta_l E_f \bar{\epsilon_f} = \eta_l E_f \frac{\epsilon_c}{4\alpha}[2\alpha(1-\nu_m) + (1+\nu_m)\sin 2\alpha] \tag{37}$$

Furthermore because of fiber misalignment, the contribution of this fiber toward the composite strength will be discounted according to the equation in [9]

$$[\sigma_{fc}] = [T][\sigma_f] \tag{38}$$

where $[T]$ is the transformation matrix

$$[T] = \begin{bmatrix} \cos^2\alpha & \sin^2\alpha & -2\sin\alpha\cos\alpha \\ \sin^2\alpha & \cos^2\alpha & 2\sin\alpha\cos\alpha \\ \sin\alpha\cos\alpha & -\sin\alpha\cos\alpha & \cos^2\alpha - \sin^2\alpha \end{bmatrix} \tag{39}$$

and $[\sigma_f]$ and $[\sigma_{fc}]$ are the actual fiber stress tensor and the fiber stress tensor in the orthogonal directions with respect to loading direction. For the present uniaxially loading case, the above equation reduces to

$$\sigma_{fc} = \bar{\sigma_f}\cos^2\theta - 2\bar{\tau_f}\sin\theta\cos\theta \tag{40}$$

It can be easily proven from Equation 5 that

$$\bar{\tau_f} = 0 \tag{41}$$

So we have

$$\sigma_{fc} = \bar{\sigma_f}\cos^2\theta \tag{42}$$

The average value of this stress with respect to fiber orientation is

$$\bar{\sigma_{fc}} = \int_0^\alpha \bar{\sigma_f}\cos^2\theta\Omega(\theta)d\theta = \eta_l E_f \epsilon_c \frac{1}{16\alpha^2}[2\alpha(1-\nu_m) + (1+\nu_m)\sin 2\alpha](2\alpha + \sin 2\alpha) \tag{43}$$

The fiber orientation efficiency factor is thus derived as

$$\eta_\theta = \frac{1}{16\alpha^2}[2\alpha(1-\nu_m) + (1+\nu_m)\sin 2\alpha](2\alpha + \sin 2\alpha) \tag{44}$$

It can be proved that when $\alpha \to 0$, $\eta_\theta = 1$. The minimum value of $\eta_\theta = \frac{(1-\nu_m)}{4}$ is achieved when $\alpha \to \pi/2$

7 THE PROPERTY COMPATIBILITY OF FIBER AND MATRIX IN COMPOSITES

Now that we have determined the maximum allowable fiber volume fraction and the minimum necessary fiber volume fraction, we can use these two values to examine the fiber-matrix property compatibility.

Obviously, for composite design with any possible combinations of fiber and matrix, the criterion

$$V_{max} \geq V_{min} \tag{45}$$

has to be satisfied. As these two values are determined by the properties of the fiber and matrix as well as the spacing between fibers, Equation 45 actually provides the interrelationships between all these parameters in a composite, and can hence be used to study the fiber-matrix property compatibility and to select proper materials for a composite.

The easier way of using this equation is to study the boundaries enclosed by the maximum and the minimum fiber volume fraction curves for a given property. Some examples will be shown in the next section.

8 CALCULATION AND DISCUSSION

First of all, since we have had all the equations describing the relationships between the composite structural parameters and the fiber and matrix properties, a parametric study becomes possible to show the effects of these properties on a composite structure. The data used for calculation are listed in Table 1. For generality, the ratios of fiber matrix properties are used wherever possible. When the effect of a specific parameter in Table 1 is investigated over the given range, other parameters will take the typical values provided. The results are illustrated in Figures 5 - 12.

Table I. The Fiber Matrix Properties Used for Calculation

Item	Range	Typical
Strength Ratio $\frac{\sigma_{bf}}{\tau_s}$	1.5 - 5.0 [7]	2.4
Modulus Ratio $\frac{G_m}{E_f}$	0.02 - 0.3 [7]	0.03
Fiber Aspect Ratio $\frac{l}{r}$	5 - 200 [assumed]	60
Fiber Breaking Strength σ_{bf}	4 - 20 Gpa [9]	8 Gpa
Matrix Stress Difference $\sigma_{bm} - \sigma_{fm}$	0.2 - 4.0 Gpa [assumed]	2 Gpa
Fiber Orientation Range α	$0 - \frac{\pi}{3}$	$\frac{\pi}{6}$
Matrix Poisson's Ratio ν_m	0.2 - 0.5 [assumed]	0.3
Fiber End spacing Length ratio $\frac{\delta_f}{l}$	0.0008 - 0.05 [assumed]	0.003

Figure 5 shows the effect of the Strength Ratio $\frac{\sigma_{bf}}{\tau_s}$ on the values of V_{max}. As the strength ratio increases, meaning stronger fibers are used, or a weaker bonding shear strength between the matrix and fibers, V_{max} is decreasing, a greater spacing between fibers is required in order to maintain a stable structure. Note that fiber length does not have significant effect on the result.

The effect of the modulus ratio $\frac{G_m}{E_f}$ on the V_{max} value is illustrated in Figure 6. It is also a monotonically decreasing relationship. This means that a matrix with higher shear modulus or a less tough fiber will result in a smaller V_{max} value, or allow greater spacing between fibers. In other words, fewer fibers will be needed in the structure. Again there is no noticeable difference for different fiber length cases.

Figure 7 and 8 show the relationships between the fiber length efficiency factor η_l and the fiber aspect ratio $\frac{l}{r}$, and between the fiber orientation range α and the fiber orientation efficiency factor η_θ respectively. As shown in the results, increasing the fiber aspect ratio (a longer or thinner fiber) will raise the fiber length efficiency factor, and a wider spread (a greater α value) of fiber orientation will lower the fiber orientation efficiency factor.

Figures 9 and 10 on the other hand indicate the effects of the matrix Poisson's ratio ν_m and the fiber orientation range α on the value of minimum fiber volume fraction V_{min}. When α becomes larger, the value of V_{min} will increase as shown in Figure 10, indicating that the fiber reinforcing function is hampered due to fiber misalignment so that more fibers are needed. A similar trend is found between ν_m and V_{min} in Figure 9 except that the relationship appears to be linear.

The curves in Figures 11 and 12 can be used to test the property compatibility between the fibers and matrix. First of all, Figure 11 shows the effects of the modulus ratio on the values of V_{max} (the same curve as the short fiber case in Figure 6) and V_{min}. Unlike V_{max},

V_{min} decreases very slightly when $\frac{G_m}{E_f}$ is increasing. Based on Equation 45, only those fiber and matrix types whose $\frac{G_m}{E_f}$ values are greater than the critical $\frac{G_m}{E_f}$ value are compatible for being selected to form a properly functioning composite. Likewise in Figure 12, first, the effects of $\frac{l}{r}$ on both volume fraction values V_{max} and V_{min} can be seen, showing different trends but both gradually approaching its own asymptote as $\frac{l}{r}$ increases. On the other hand, as shown in the figure, there is a critical $\frac{l}{r}$ value above which a feasible structure can then be made.

9 CONCLUSIONS

The stress transfer between matrix and fibers in a composite is not only determined by the intrinsic properties of fiber and matrix, but also affected by the geometric parameters of fiber arrangement within the matrix such as the spacing between fibers and the orientation of fibers.Consequently the shear strength of the interface between fibers and the matrix can be used as a criterion to determine the spacing between fibers in a composite.

For a composite made of given fiber and matrix materials, there is an optimal spacing between fibers at which the fiber tensile strength will be fully exploited. Moreover this optimal spacing is also the minimum allowable spacing between fibers below which the structure will start to disintegrate under loading before the fiber tensile failure. This minimum spacing then defines a maximum fiber volume fraction allowable for a composite.

The maximum fiber volume fraction combined with the minimum fiber volume fraction studied previously can be used for composite design. Both volume fractions are found dependent on such parameters as fiber modulus E_f, fiber tensile strength σ_{bf}, fiber aspect ratio $\frac{l}{r}$ and fiber orientation range α, the matrix properties as Poisson's Ratio ν_m, shear modulus G_m, and the bonding shear strength τ_s between fiber and matrix, as shown in this study. Consequently, these two values of fiber volume fraction V_{max} and V_{min} can be applied to define the boundaries in determining the property compatibility of various combinations of fiber and matrix types for a particular application so as to optimize the result of composite design.

10 REFERENCES

1. Bentur, A. and Mindess, S., "Fiber Reinforced Cementitious Composites", Elsevier Applied Science, New York (1990)

2. Chou, T. W. and Nomura, S., Fiber Orientation Effects on the Thermoplastic Properties of Short-Fiber Composites, Fiber Science and Technology, 14, 279 (1980-81)

3. Cox, H.L., The Elasticity and Strength of Paper and Other Fibrous Materials, British Journal of Applied Physics, 3, 72 (1952)

4. Curtis, P.T., Bader, M.G. and Bailey, J.E., The Stress and Strength of a Polyamide Thermoplastic Reinforced with Glass and Carbon Fibers, Journal of Materials Science, 13, 377 (1978)

5. Fan, C. F. and Hsu, S., Effects of Fiber Orientation on the Stress Distribution in Model Composites, Journal of Polymer Science: Part B: Polymer Physics, 27, 2605 (1989)

6. Fan, C. F. and Hsu, S., A Spectroscopic Analysis of the Stress Distribution along the Reinforcement Fibers in Model Composites: End Effects, Macromolecules, 22, 1474 (1989)

7. Kelly, A and Davies, G.J., The Principles of the Fiber Reinforcement of Metals, Metallurgical Reviews, 10, 1 (1965)

8. Kelly, A. and MacMillan, N.H., "Strong Solids", 3rd ed.,Clarendon Press, Oxford (1986)

9. Laws, V., The Efficiency of Fibrous Reinforcement of Brittle Matrices, J. Phys. D; Appl. Phys., 4, 1737 (1971)

10. Malvern, L.E., "Introduction to the Mechanics of A Continuous Medium", Prentice-Hill, Englewood Cliffs, NJ (1969)

11. Piggott, M.R., "Load Bearing Fiber Composites", Pergamon Press, New York, (1980)

12. Rosen,B.W., Mechanics of Composite Strengthening, in "Fiber Composite Materials", American Society for Metals, pp.37 (1965)

13. Takao, Y., Chou, T.W. and Taya, M., Effective Longitudinal Young's Modulus of Misoriented Short Fiber Composites, Transactions of the ASME, 49, 536 (1982)

14. Taya, N. and Chou, T. W., Prediction of the Stress-Strain Curve of a Short-Fiber Reinforced Thermoplastic, Journal of Materials Science 17, 2801 (1982)

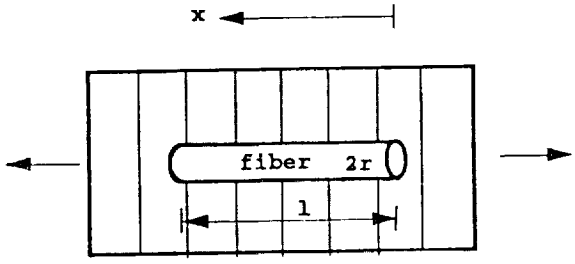

(a) Before loading

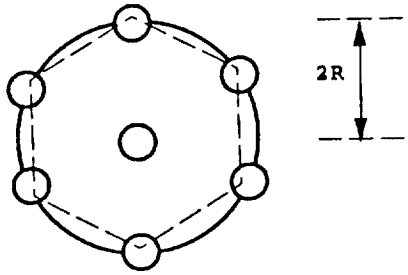

(c) Fiber with nearest hexagonally packed neighbours

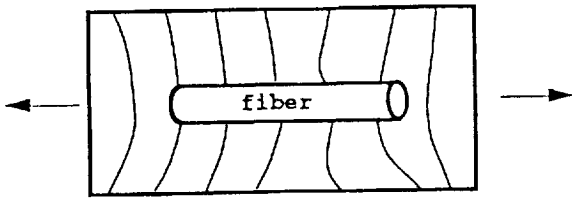

(b) After loading

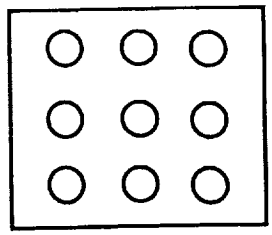

(d) Fiber with nearest square-packed neighbours

Figure 1 Fiber embedded in a matrix and the fiber packing forms

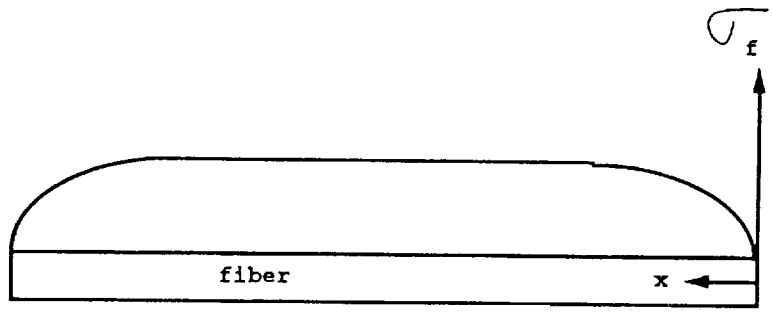

(a) The tensile stress distribution

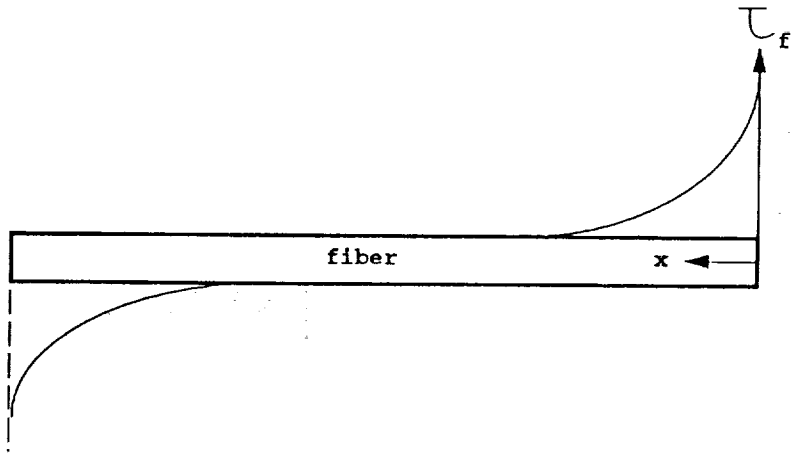

(b) The shear stress distribution

Figure 2 Elastic Stress Distribution in the Fiber

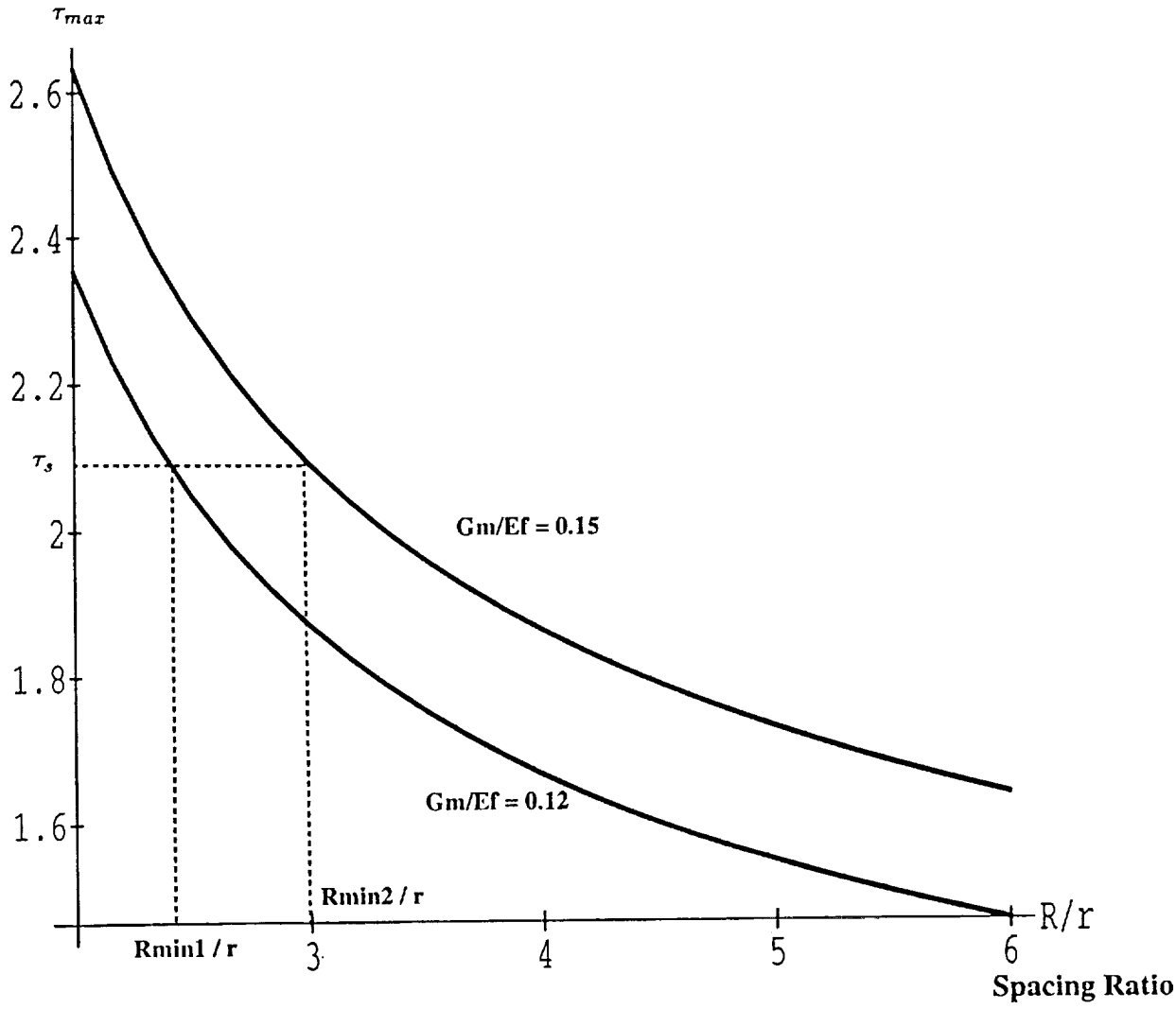

Figure 3 Maximum Shear Stress vs. Spacing Ratio

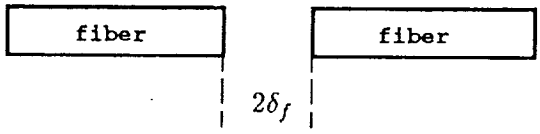

(a) Distance between fiber ends

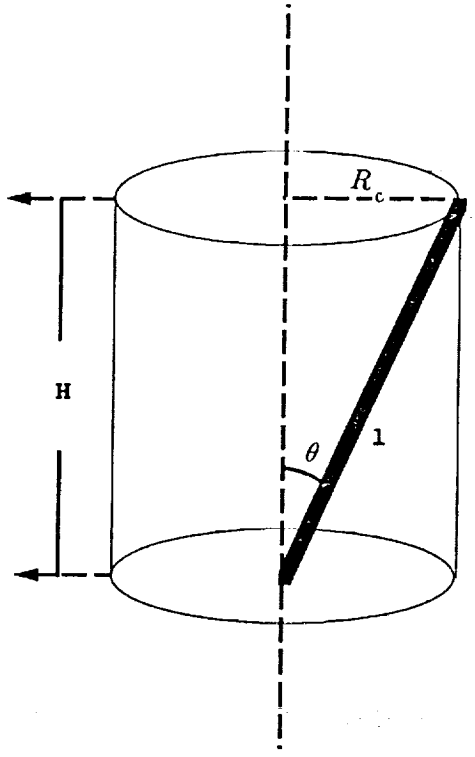

(b) A fiber in the matrix

Figure 4 Geometric Relationships between Fiber and Matrix

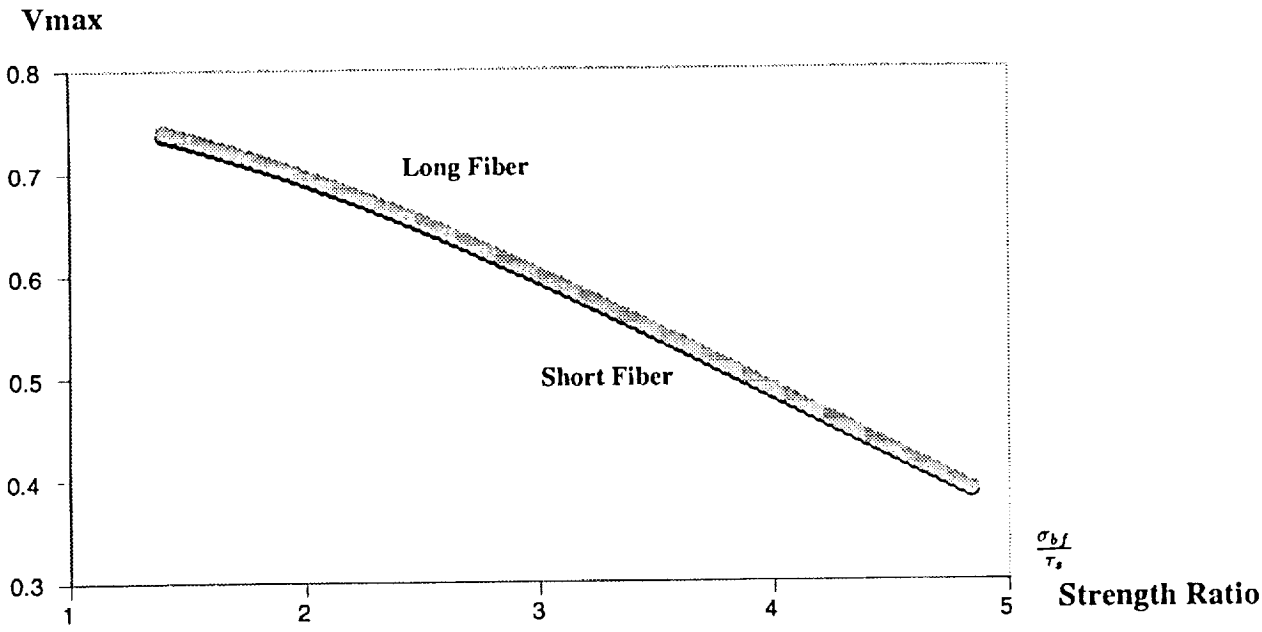

Figure 5 Maximum Volume Fraction vs. Strength Ratio

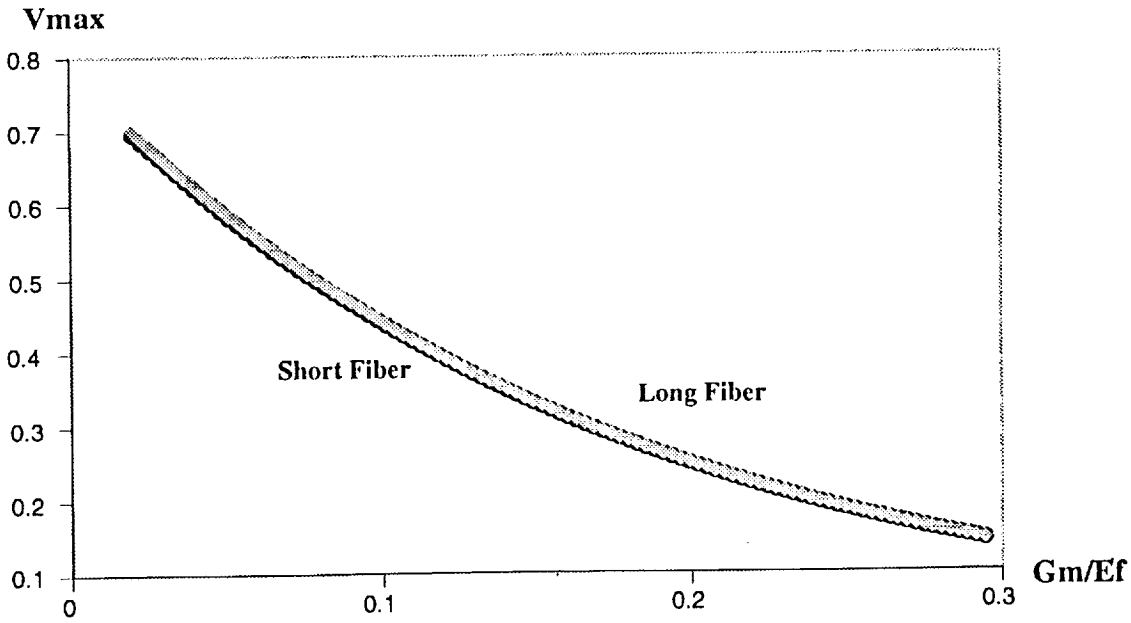

Figure 6 Fiber Volume Fraction vs. Gm/Ef

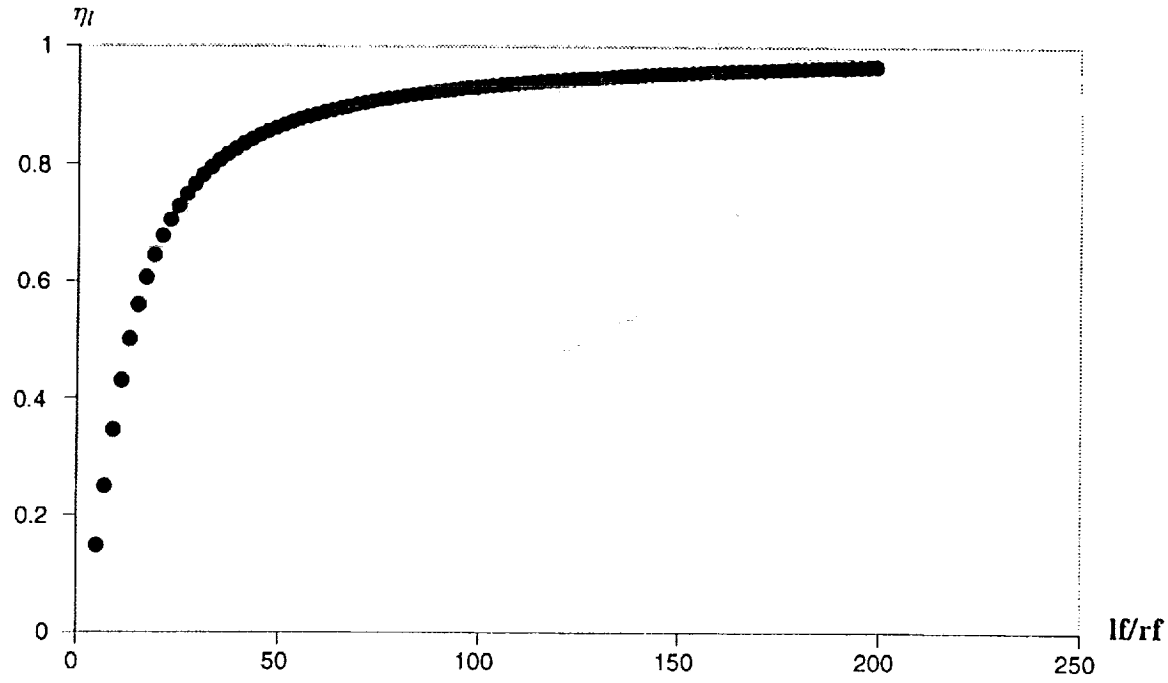

Figure 7 Length Efficiency Factor vs. lf/rf

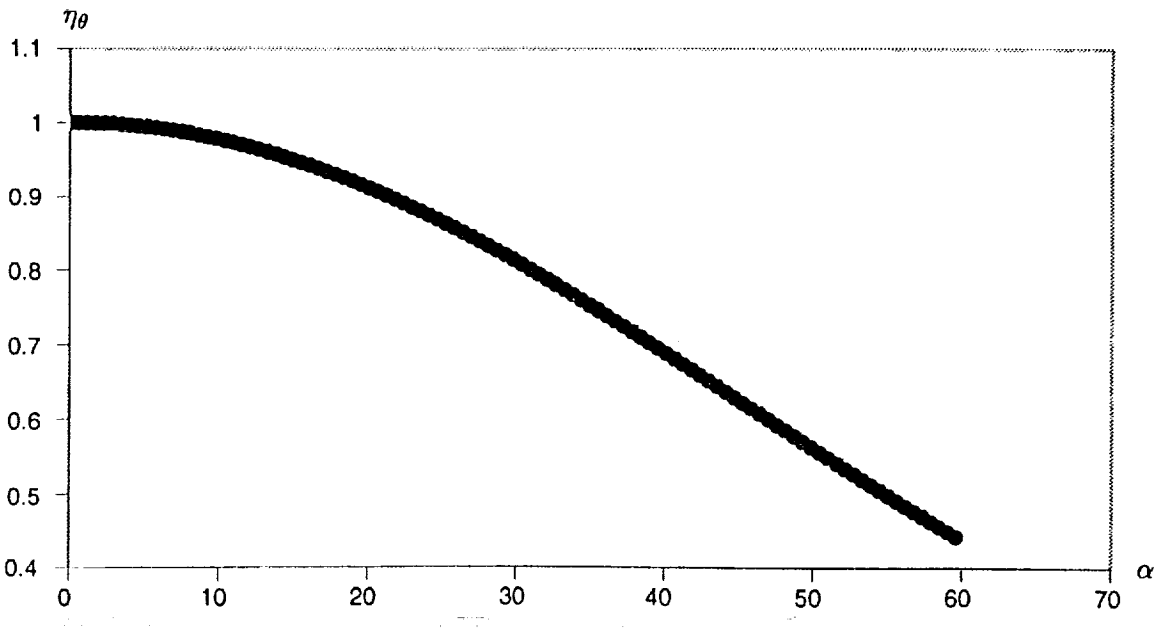

Figure 8 Relationship between Orientation Range and Efficiency Factor

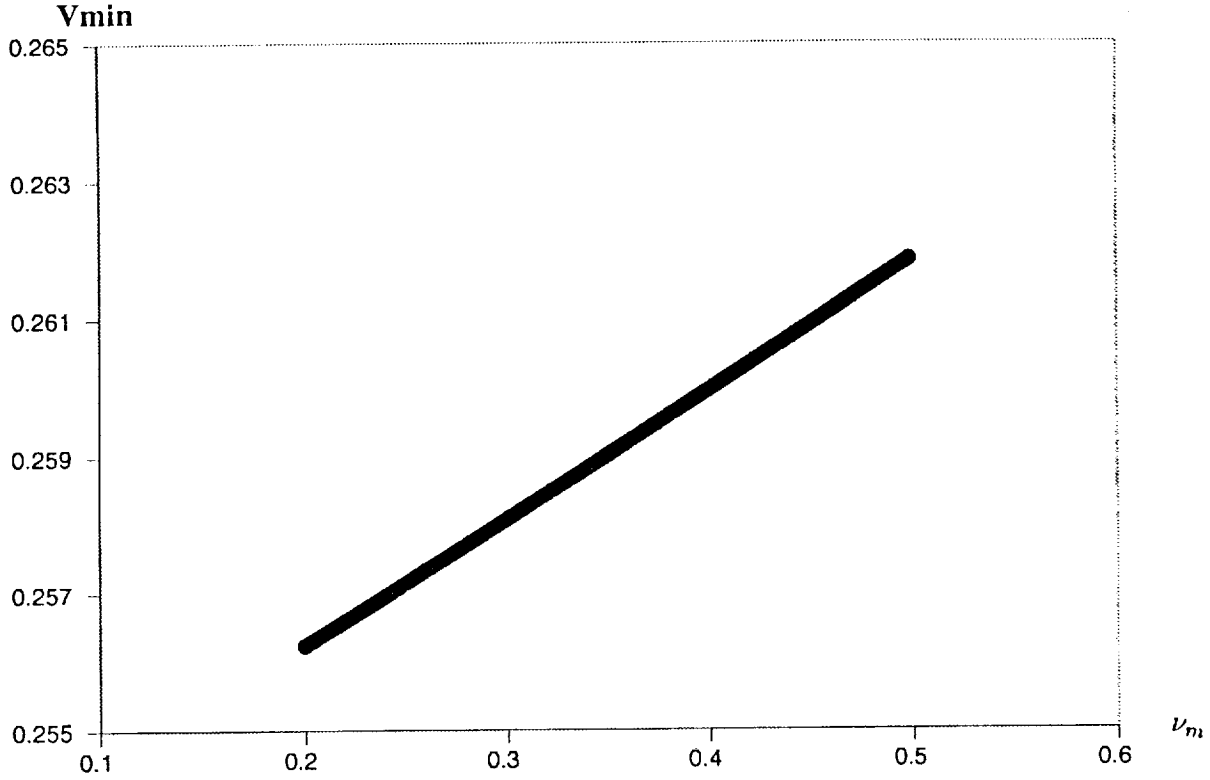

Figure 9 Matrix Poisson's Ratio vs. Vfmin

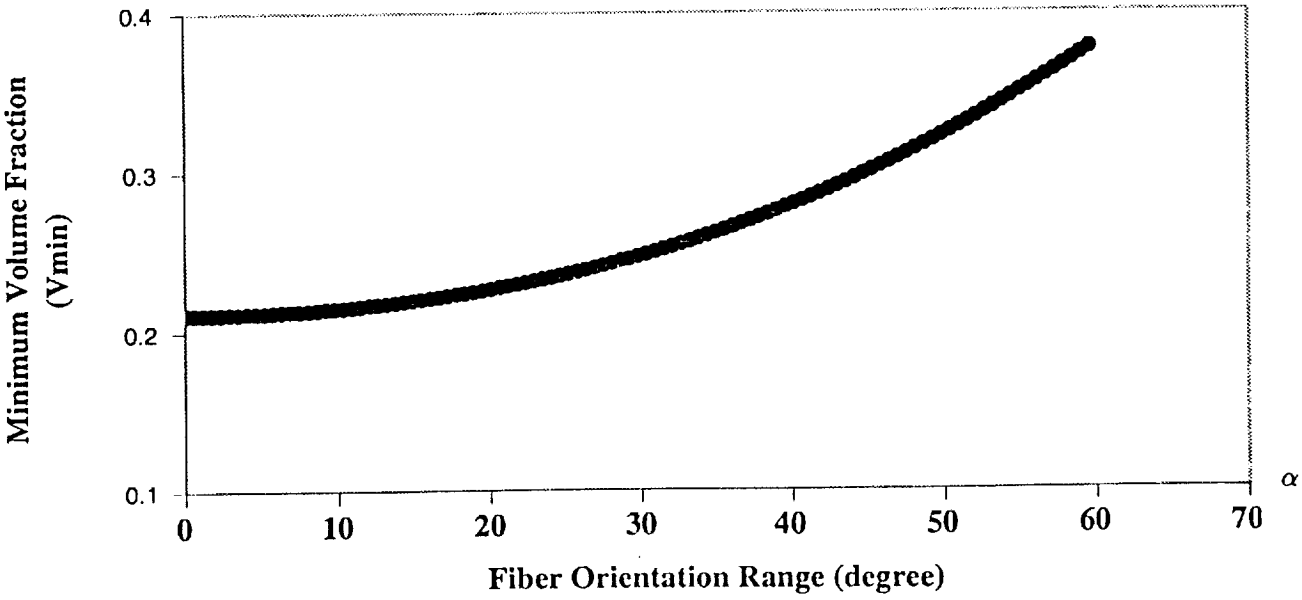

Figure 10 Vmin vs. Fiber Orientation

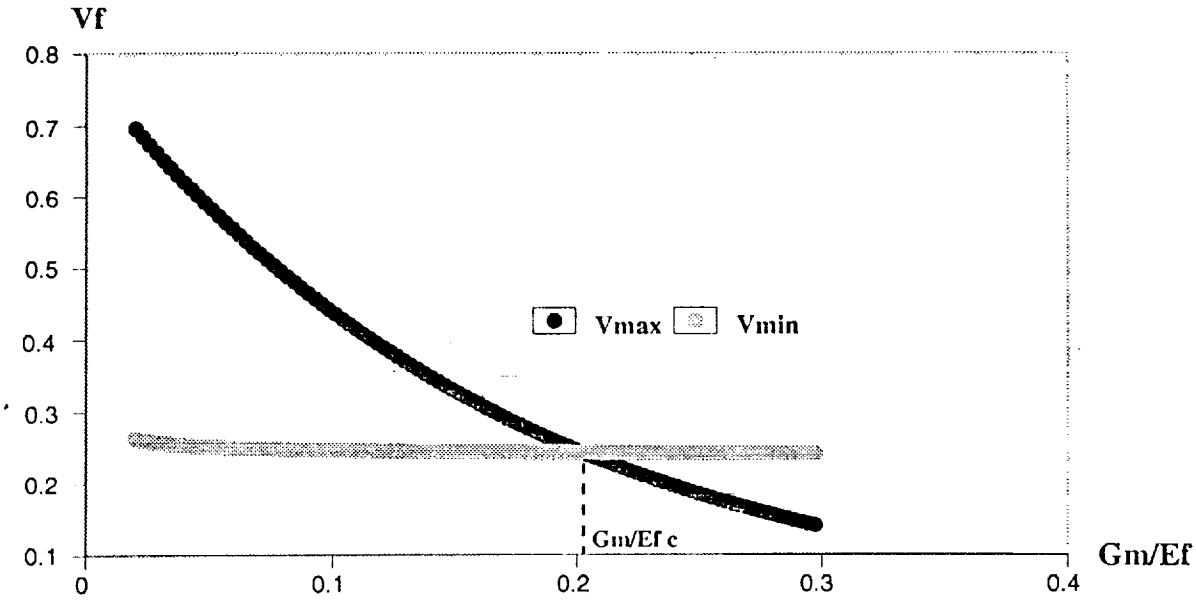

Figure 11 Effects of the Modulus Ratio on Volume Fractions and the The Property Compatibility Boundary Defined

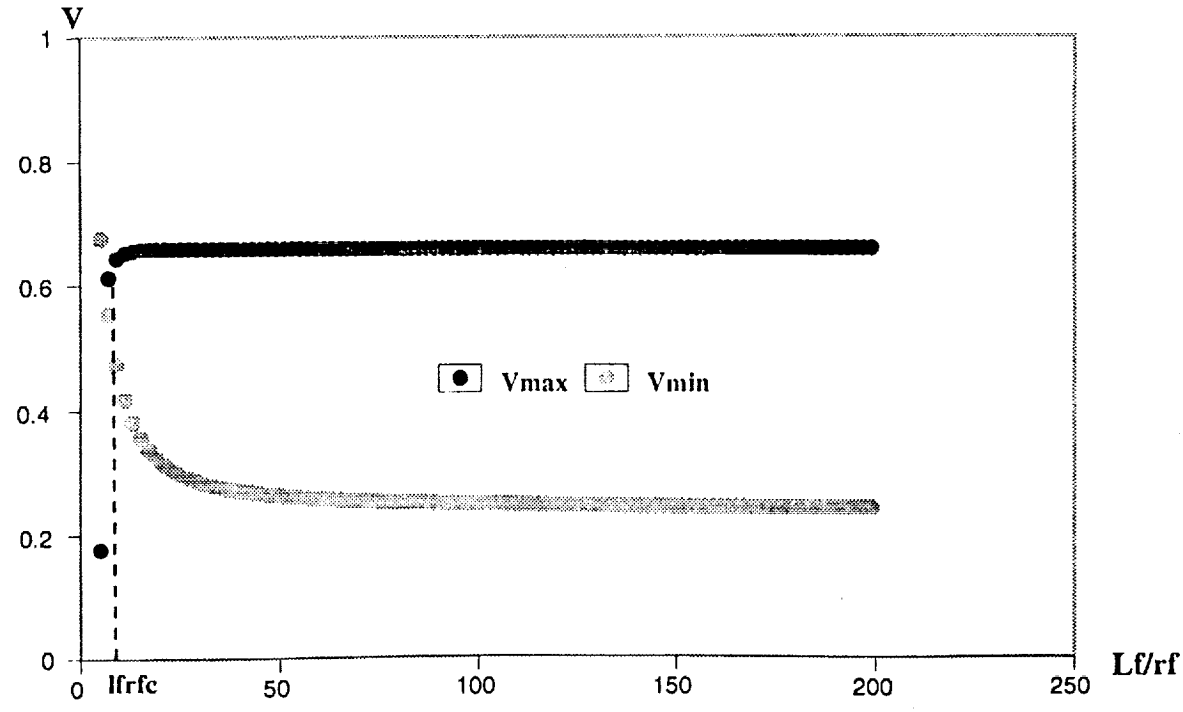

Figure 12 Critical Fiber Aspect Ratio

MECHANICAL RESPONSE OF COMPOSITE MATERIALS WITH THROUGH-THE-THICKNESS REINFORCEMENT

Gary L. Farley
U.S. Army Aerostructures Directorate
NASA Langley Research Center

Larry C. Dickinson
Lockheed Engineering and Sciences Company
NASA Langley Research Center

ABSTRACT

An experimental investigation was conducted to identify the key geometrical parameters and quantify their influence on the mechanical response of through-the-thickness (TTT) reinforced composite materials. Composite laminates with TTT reinforcement fibers were fabricated using different TTT reinforcement materials and reinforcement methods and laminates were also fabricated of similar construction but without TTT reinforcement fibers. Coupon specimens were machined from these laminates and were destructively tested.

Through-the-thickness (TTT) reinforcement yarns enhance damage tolerance and improve interlaminar strength. Thick-layer composites with TTT reinforcement yarns have equal or superior mechanical properties to thin-layer composites without TTT reinforcement yarns. A significant potential exists for fabrication cost reduction by using thick-layer composites with TTT reinforcement yarns. Removal of the surface loop of the TTT reinforcement improves compression strength. Stitching provides somewhat higher mechanical properties than integral weaving.

OBJECTIVE AND APPROACH

The objectives of the present investigation, as presented in Fig. 1, are to identify the key geometrical parameters that influence the mechanical response of through-the-thickness (TTT) reinforced composite materials and, where possible, to quantify the influence of these key parameters on the mechanical response. The approach used to identify and quantify the effects of key geometrical parameters was based upon observations and destructive testing of coupon specimens, respectively. Composite laminates with TTT reinforcement fibers were fabricated using different TTT reinforcement materials and reinforcement methods. These laminates were microscopically examined to identify potential geometrical features that influence mechanical response. Coupon specimens were machined from these laminates and were destructively tested. Test results were compared with test results from materials of similar construction but without TTT reinforcement fibers.

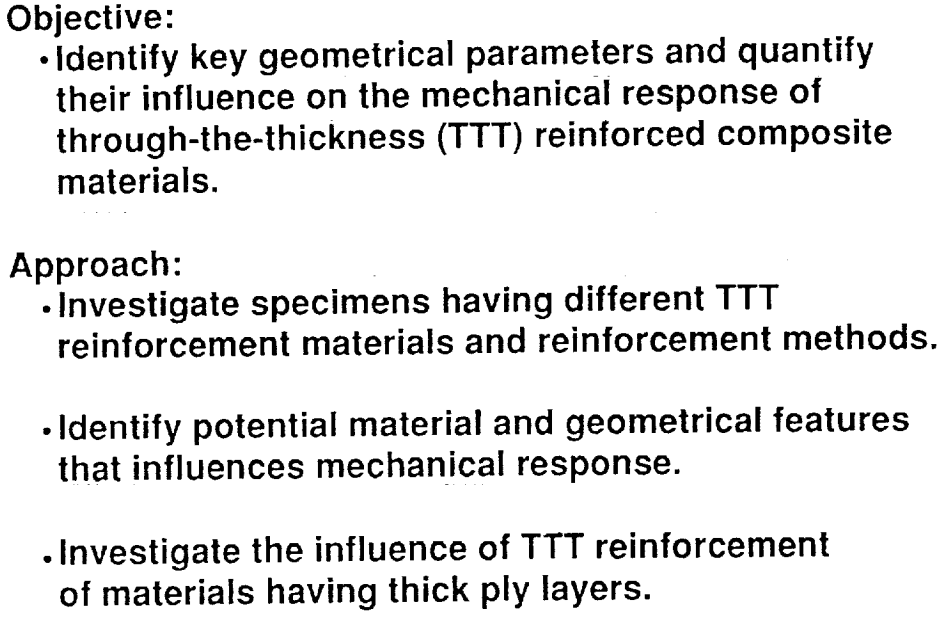

Figure 1

FEATURES OF TTT REINFORCEMENT THAT INFLUENCE MECHANICAL RESPONSE

There are four geometrical features of TTT reinforced composite materials that significantly influences their mechanical response, as shown in Fig. 2. These geometrical features are resin rich regions, in-plane fiber waviness, surface loop of continuous TTT reinforcement fibers and breakage of in-plane fibers.

- Resin rich regions
- In-plane fiber waviness
- Surface loop of continuous through-the-thickness reinforcement
- Breakage of in-plane fibers

Figure 2

PHOTOMICROGRAPHS OF STITCHED AND INTEGRALLY WOVEN COMPOSITE MATERIAL

The resin rich regions identified in Fig. 3 were created by the inclusion of TTT reinforcement fibers. The stitch yarn creates a small inclusion around each TTT reinforcement penetration. The TTT reinforcement fibers of the integrally woven material create resin channels because the integrally woven TTT reinforcement fibers separate adjacent in-plane yarns. It is well understood that changes in fiber volume fraction can change the mechanical properties of composite materials (ref.1). Therefore, it is reasonable to believe that resin rich regions created as an artifact of inserting TTT reinforcement fibers could influence both laminate stiffness and strength.

Fiber waviness in composite laminates has also been identified as a mechanism that can adversely influence compression strength (ref. 2). The vertical portion of the TTT reinforcement fibers creates in-plane fiber waviness of the in-plane reinforcement fibers, as observed in Fig. 3, for both stitched and integrally woven TTT reinforced laminates. The amplitude of the waviness is approximately equal to the diameter of the TTT reinforcement fibers which is generally greater than the fiber waviness found in non-textile composite laminates.

When TTT reinforcement fibers penetrate in-plane yarns, such as in the stitched laminate depicted in Fig. 3, the penetration by the needle and stitching yarn can result in breakage of in-plane fibers. With proper processing the majority of the in-plane fibers at stitch penetration are pushed aside as the needle penetrates the preform. Generally, less than 5 percent of the in-plane fibers at the penetration site are broken (ref.3). No significant breakage of in-plane fibers occurs for integrally woven TTT reinforced materials because the TTT reinforcement does not penetrate the in-plane yarns and hence little or no breakage of in-plane reinforcement fibers occurs in the weaving process.

(Figure 3 appears on the next page.)

PHOTOMICROGRAPHS OF STITCHED AND INTEGRALLY WOVEN COMPOSITE MATERIAL

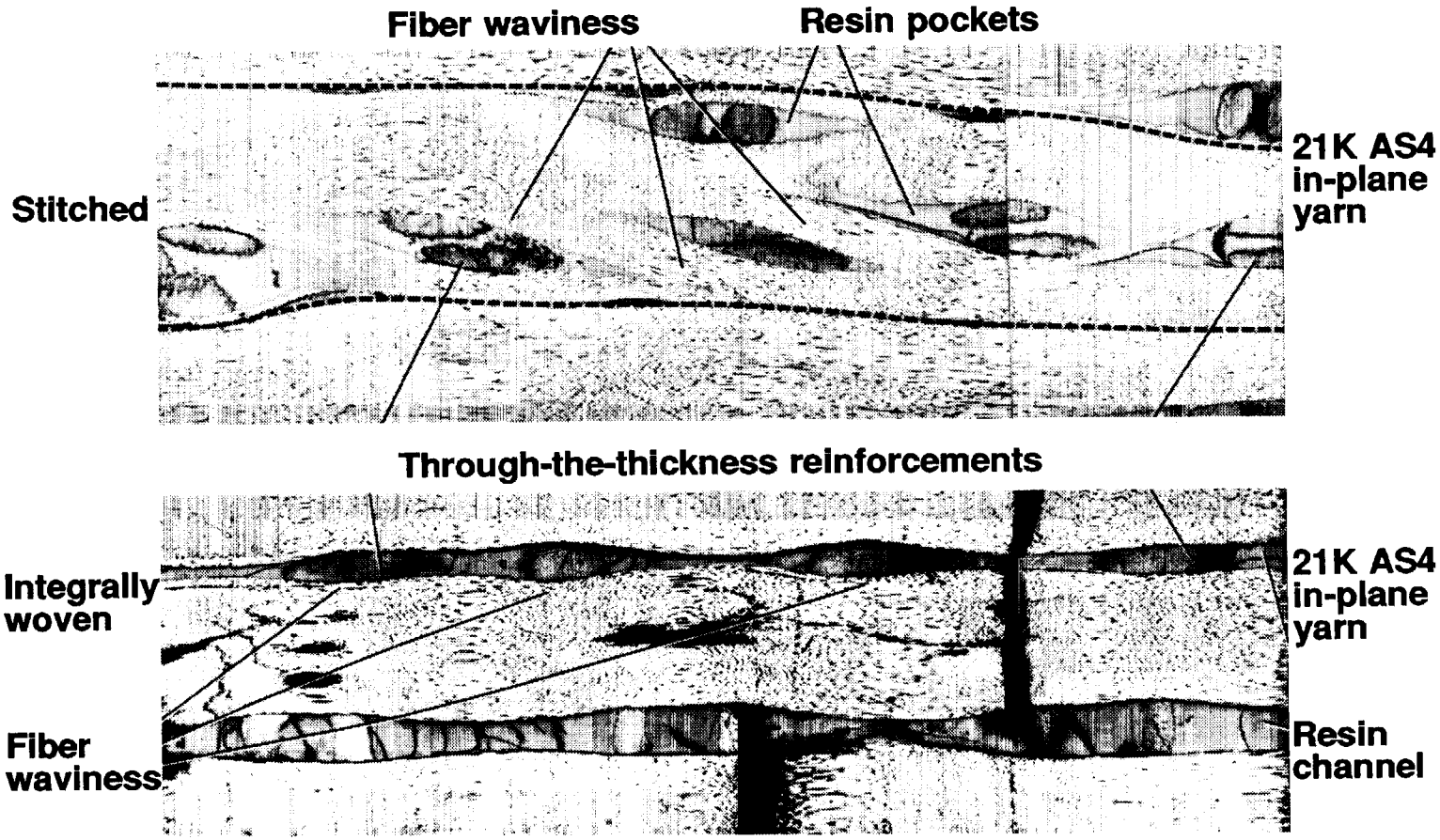

Figure 3

KINKED IN-PLANE SURFACE YARN

Both the stitched and integrally woven materials studied in this investigation use continuous TTT reinforcement fibers. Between successive TTT fiber penetrations, a part of the TTT reinforcement fibers extends across the laminate's surface. The portion of the TTT reinforcement fibers that lies on the surface is referred to as the surface loop, see Fig. 4. When the preform is infiltrated and processed into a composite part, the surface loop of the TTT reinforcement fibers is forced into the surface of the laminate causing a kinking or bending of the laminate's in-plane fibers near the laminate surface. The magnitude of the kinking or bending of the in-plane fibers is a function of the diameter of the surface loop yarn and the compaction pressure used during consolidation. Only the layers of in-plane fibers near the surface of the laminate are influenced by the surface loop. That is, the layers near the center of the laminate are not kinked or bent by the surface loop.

(Figure 4 appears on the next page.)

KINKED IN-PLANE SURFACE YARN

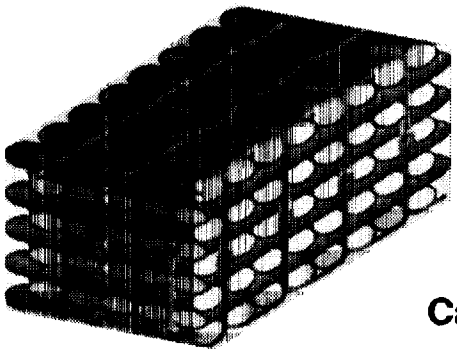

Integrally woven
3-D preform

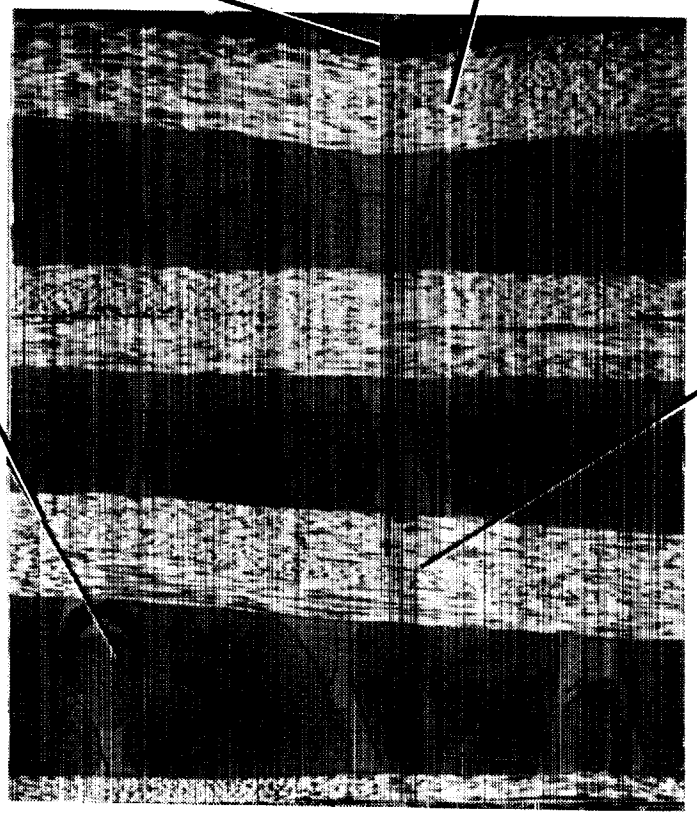

Photomicrograph of laminate cross section

Figure 4

MATERIALS INVESTIGATED

All laminates studied in this investigation were fabricated using Hercules, Inc. AS4 carbon fiber with Hercules, Inc. 3501-6 epoxy resin and were approximately 0.64 cm thick. See Fig. 5. The stacking sequence for all laminates consisted of variations of a 0/90 cross-ply stacking sequence. However, the per ply thickness, stacking sequences, inclusion of TTT reinforcements, TTT reinforcement method and TTT reinforcement material differed between laminates. The 0/90 stacking sequence was chosen so that a direct comparison between materials with stitched and integrally woven TTT reinforcement fibers could be made. Three different laminates were fabricated without TTT reinforcement fibers to quantify the influence of in-plane fiber architecture and TTT reinforcement fibers on the mechanical response. Two of these laminates were fabricated from unidirectional prepreg material. Their stacking sequences are $[(0/90)_2/0/(0/90)_5/0/(0/90)_3/0]_s$ and $[(0_5/90_5)_2/0_3]_s$ and they are referred to herein as the thin-layer and thick-layer material, respectively. The third material without TTT reinforcement, referred to as the uniweave material, was fabricated from a nine layer stack of dry uniweave fabric that was infiltrated and cured to form the composite laminate. This uniweave fabric has approximately 99 percent of its carbon fibers oriented in the fabric's warp direction. The remaining one percent of the fibers are fine denier glass yarns used to hold the carbon warp yarns together. The glass yarns are oriented in the fabric's fill direction. Each layer of the uniweave fabric is approximately equal to five layers of unidirectional prepreg tape material. The uniweave fabric is composed of 21K-filament carbon yarns with a yarn spacing of approximately 5 per cm. The thick-layer and uniweave materials are similar in layer thickness and construction.

All laminates with TTT reinforcement fibers have the same ply orientation as the uniweave material, that is [0/90/0/90/0/90/0/90/0]. Two different types of TTT reinforcement yarn were used, namely carbon and Kevlar yarns. The carbon yarn is a Toray T-900-1000A stitching yarn and the Kevlar yarn is a 1100 denier Kevlar-49 yarn. Both the stitched and integrally woven materials were made with the same number and spacing of TTT reinforcement yarns. The stitched preforms were produced using uniweave fabric. All laminates fabricated with TTT reinforcement fibers were fabricated by stitching or integral weaving. Both stitching and integral weaving are referred to herein as continuous TTT reinforcement processes. Simulated tufted TTT reinforcement was produced by machining the surfaces of stitched or integrally woven laminates to remove the surface loop of the TTT reinforcement fibers. The simulated tufting TTT reinforcement is referred to herein as a discontinuous TTT reinforcement process.

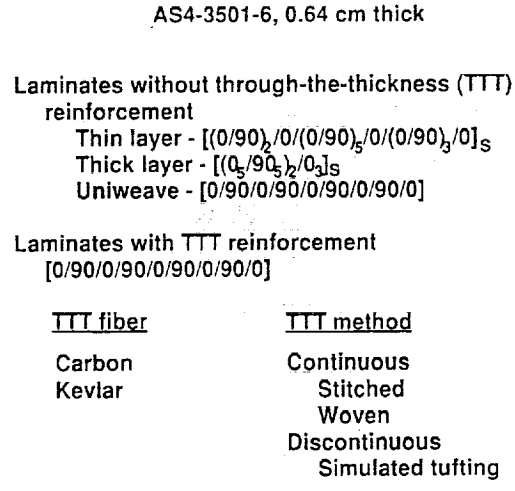

Figure 5

PREFORM ARCHITECTURE

Three different TTT reinforced preform architectures were used in this study, as seen in Fig. 6. The stitched preforms were created by stacking nine layers of uniweave fabric in a 0/90 orientation and the stack was stitched using a modified through-the-thickness lock stitch in orthogonal rows and columns oriented parallel and perpendicular to the 0 degree direction of the preform, respectively. The integrally woven preforms were produced as a single unit on a loom. The in-plane warp and fill yarns were not interwoven. The nine layers of fabric were held together by the TTT reinforcement yarns woven in both the warp and fill directions. The TTT reinforcement yarns were inserted and wrapped around a catcher yarn in the center of the preform and returned to the surface. Therefore, the TTT reinforcement yarn in the integrally woven material was actually composed of two yarns, a yarn originating from the upper surface and one originating from the lower surface. The simulated tufting material was produced by machining away one half of the upper and lower outer surface layers from the stitched and integrally woven cured composite laminates.

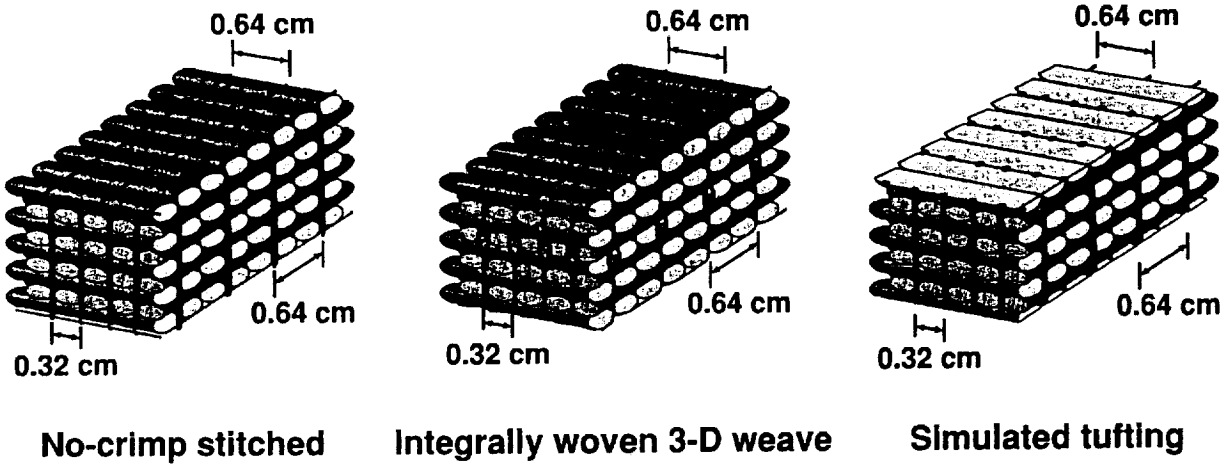

Figure 6

TEST SPECIMENS

Three different test specimens were used to evaluate the mechanical response of the different materials. They were the compression-after-impact (CAI) specimen, the short-block-compression (SBC) specimen and the multi-span-beam (MSB) specimen, as depicted in Fig. 7. The CAI and SBC specimens were machined from laminates such that the direction of the applied load coincided with the 0 degree direction of the laminate stacking sequence. The MSB specimens were machined from laminates such that the 90 degree direction of the laminate stacking sequence was parallel to the length of the specimen.

The CAI specimen was used to evaluate the damage resistance and residual compression strength of a damaged panel. The CAI specimen was 12.7 cm wide by 25.4 cm long. A 0.127-cm-diameter aluminum ball was shot at the center of each CAI specimen with approximately 42J of energy. Back-to-back strain gages were bonded to each CAI specimen. Each CAI specimen was then mounted into a side-supported compression test fixture and statically compressed to failure.

The SBC specimen was used to evaluate the undamaged compression strength of the material. The SBC is 3.81 cm wide by 4.45 cm long. Each specimen was instrumented with back-to-back strain gages. The SBC specimens were mounted in a compression test fixture without side supports and a static compression load was applied until the specimen failed.

The MSB specimens were used to evaluate, in a qualitative manner, the interlaminar strength of the material. The MSB test consists of an upper and lower load introduction structure which makes contact with the specimen at five locations across the width of the specimen. The width of the specimen is 2.54 cm and the length is 12.7 cm. A static compression load is applied to the specimen until failure.

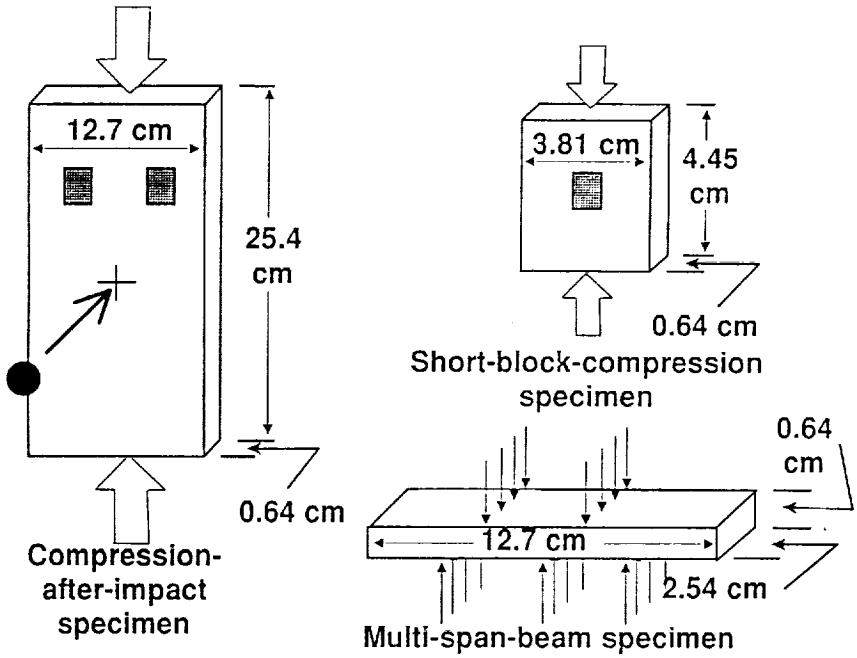

Figure 7

EFFECTS OF TTT REINFORCEMENT ON COMPRESSION STRENGTH

Short-block-compression tests were performed on the thin-layer, thick-layer, uniweave materials as well as the carbon and Kevlar TTT reinforced stitched and integrally woven materials. The highest compression strength was obtained from the thin-layer material followed by the uniweave, thick-layer materials and the materials with TTT reinforcement yarns. See Fig. 8. The difference in strength between the three materials without TTT reinforcement yarns is related to the architecture of the materials. Increasing layer thickness produces a corresponding increase in the magnitude of interlaminar stresses; therefore the thin-layer material should have higher compression strength than the thick-layer material. The thick-layer and uniweave materials have similar layer thickness, however the uniweave had higher strength. This difference in strength is attributed to the glass fill yarn which partially intertwines each warp yarn in the uniweave material and produces some intralaminar reinforcement.

All of the specimens with TTT reinforcement yarns have significantly lower undamaged compression strength than those materials without TTT reinforcement yarns. The stitched material exhibited somewhat higher undamaged compression strength than the integrally woven materials. The strength difference is attributed to the reduced amount of kinking or bending of the in-plane fibers adjacent to the surface loop formed by the needle yarn in the stitched material. The needle yarn used in the stitched material was a small denier yarn which produced less kinking or bending of the in-plane yarns when the preform was processed into a composite part. The type of reinforcement yarn in the TTT reinforced laminates had no influence on compression strength.

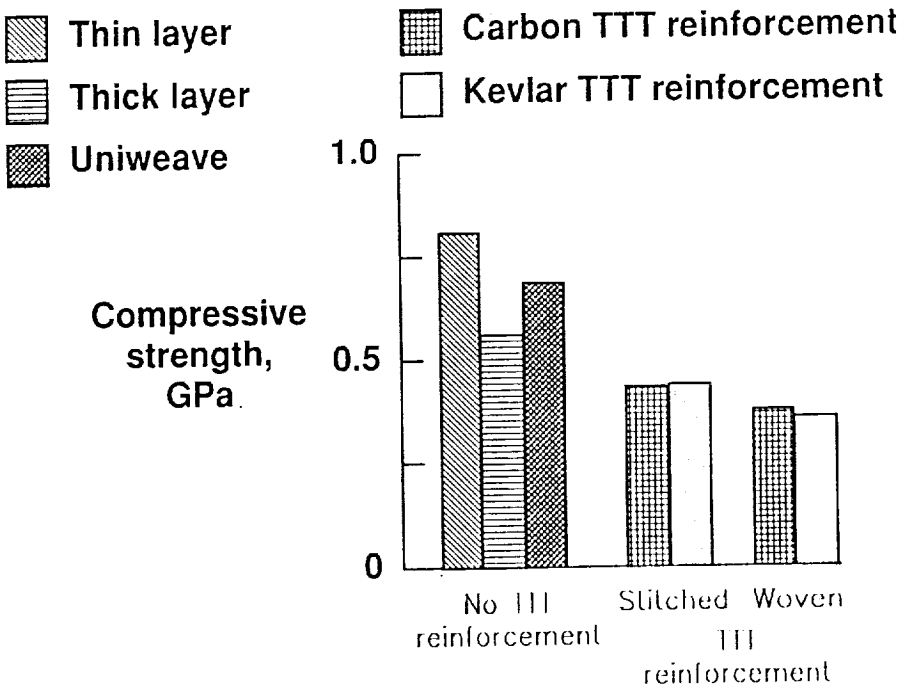

Figure 8

FAILURE MODES OF SHORT-BLOCK-COMPRESSION SPECIMENS

The compression failure mode for the thin-layer, thick-layer and uniweave materials was primarily delamination which precipitated a transverse shear failure, as shown in Fig. 9. This failure mode was caused by interlaminar stresses. All materials with TTT reinforcement yarns exhibited a transverse shear failure mechanism because the TTT reinforcement yarns increase the interlaminar strength of the laminate which suppresses the delamination failure mechanism.

(Figure 9 appears on the next page.)

FAILURE MODES OF SHORT-BLOCK-COMPRESSION SPECIMENS

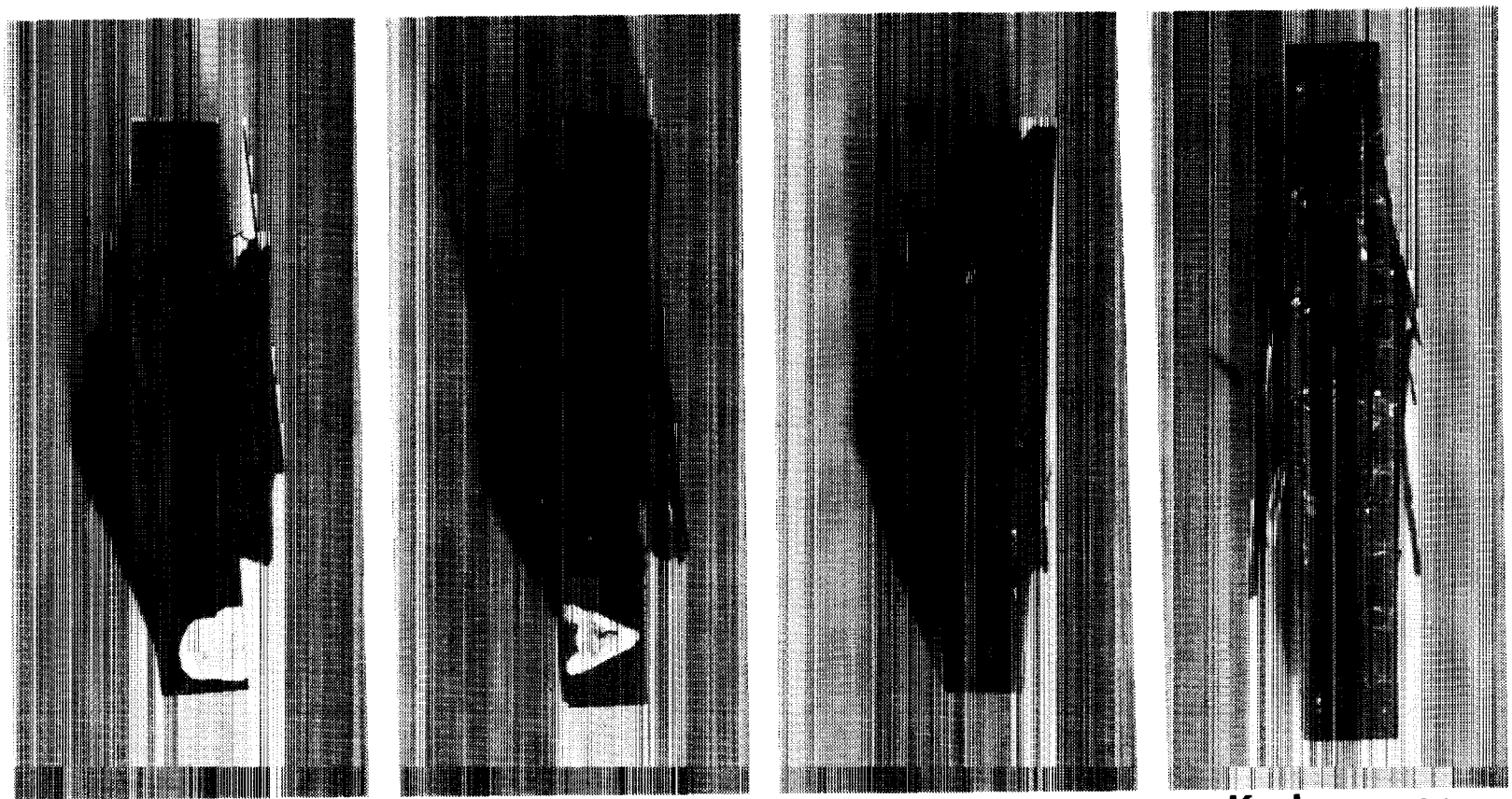

ORIGINAL PAGE
BLACK AND WHITE PHOTOGRAPH

Figure 9

INFLUENCE OF TTT SURFACE LOOP ON COMPRESSION STRENGTH

Short-block-compression tests were conducted on stitched and integrally woven composite laminates. One-half of the specimens had one-half of their surface layers machined away to simulate tufting. The simulated tufted specimens are referred to herein as those "without TTT surface loop". In all cases removal of the TTT reinforcement surface loop and the associated kinked or bent in-plane fibers resulted in higher compression strength. See Fig. 10. Compression strength was based upon the actual cross-sectional area of the specimen, that is the reduced area in the case of machined specimens. The axial-load-carrying capability is primarily due to the 0 degree fibers. Approximately 12 percent of the 0 degree fibers were removed in the machining process because the outer layers were oriented in the 0 degree direction. Since the machining produced a net increase in strength, the 0 degree fibers that were machined away were ineffective in carrying a compressive load.

The stitched material with the TTT surface loop had higher compressive strength than the integrally woven material. However, after the surfaces were machined there was little or no difference in compression strength between the stitched and integrally woven materials. The stitched materials had the surface loop on the bobbin yarn surface created by the carbon or Kevlar TTT reinforcement yarns, whereas the surface loop produced on the needle yarn surface was made with a much smaller denier yarn. The surface loops produced in the integrally woven materials were produced using the same type carbon or Kevlar yarn on the outer surfaces. Therefore, more in-plane fibers in the integrally woven materials were kinked or bent than in the stitched materials, hence the lower compression strength for the integrally woven materials.

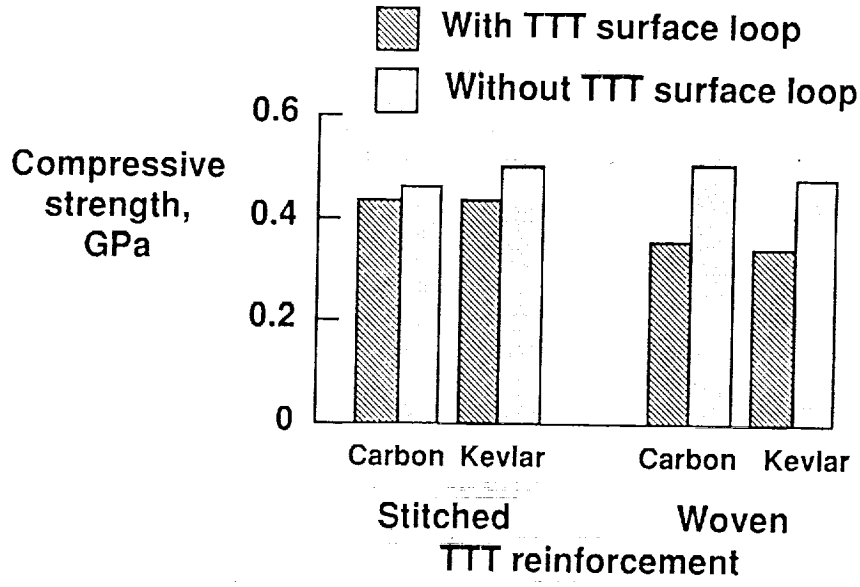

Figure 10

FAILURE MODES OF SBC AND CAI SPECIMENS

The failure modes of SBC and CAI specimens having TTT reinforcement yarns with and without the surface loop of the TTT reinforcement yarn are shown in Fig. 11. Both the unmachined (with surface loop) and machined (without surface loop) specimens have similar transverse shearing failure modes.

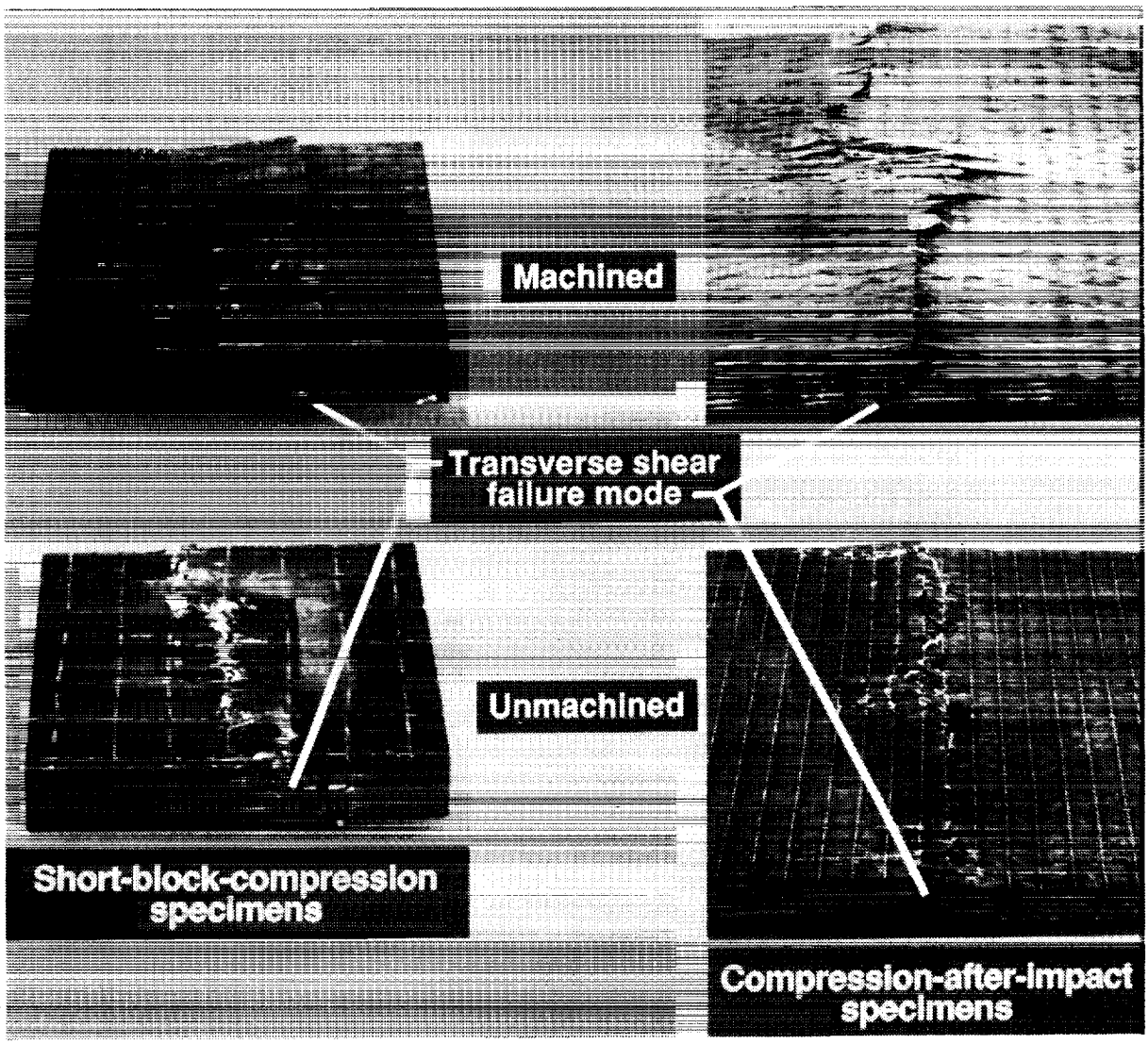

Figure 11

EFFECTS OF TTT REINFORCEMENT
ON COMPRESSION STRENGTH OF IMPACTED PANELS

The materials with TTT reinforcement yarns exhibited nearly twice the CAI strength as materials without TTT reinforcement yarns, as shown in Fig. 12. The typical failure mechanism of the CAI panels is controlled by the interlaminar strength of the material. Inclusion of TTT reinforcement yarns improves the interlaminar normal and shear strengths of the material and produces a higher CAI strength. Stitched materials have slightly higher CAI strengths than the integrally woven materials. This trend is consistent with the undamaged compression strength of these materials. The thin-layer material exhibited higher CAI strength than either the uniweave or the thick-layer materials. The relative magnitude of the CAI strength of materials without TTT reinforcement yarns was consistent with the undamaged compression strength for these materials.

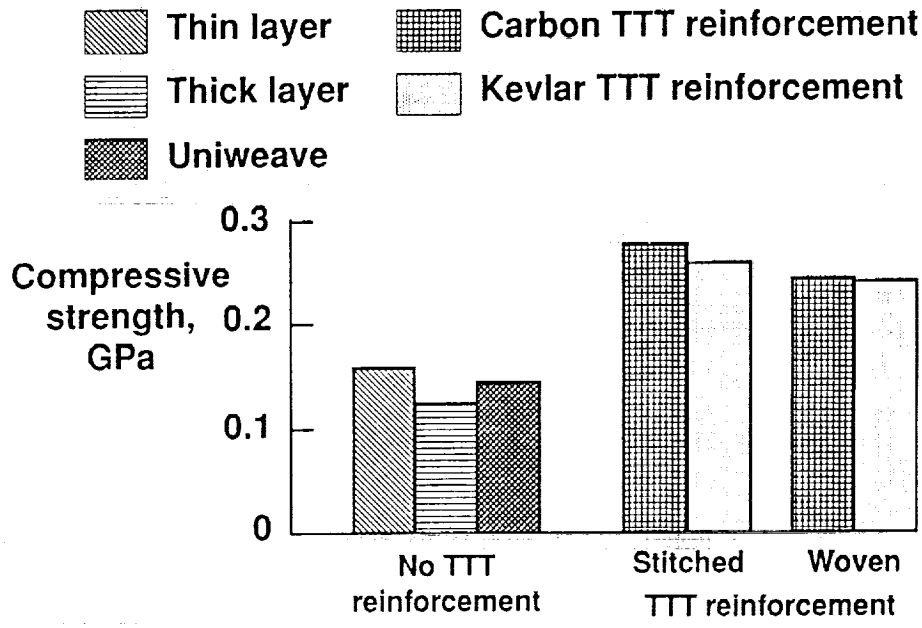

Figure 12

EFFECTS OF TTT SURFACE LOOP
ON COMPRESSION STRENGTH OF IMPACTED PANELS

Neither the CAI strength nor the impact-induced damage area were affected by the removal of the TTT surface loop, as shown in Fig. 13. All panels were impacted at approximately 42J of energy; however the panels with the surface loop removed were 11 percent thinner. It was initially expected that the thinner panel would have a greater damage area due to impact but the results indicate that this was not the case. These results suggest that the surface loop has no positive influence on the CAI strength. Futhermore, the surface loop has no influence on the damage containment because the damage area of the specimens with and without a surface loop was approximately the same.

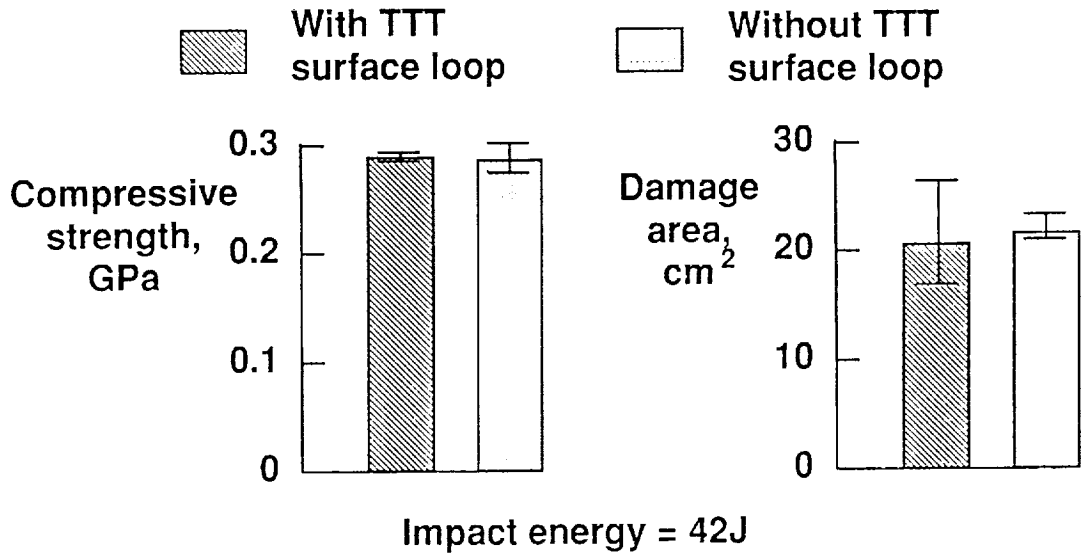

Figure 13

EFFECTS OF TTT REINFORCEMENT ON MULTI-SPAN-BEAM STRENGTH

The MSB strength of the thin-layer material is considerably higher than the MSB strength of either the thick-layer or the uniweave materials as shown in Fig. 14. This ordering of strength is consistent with the compression and CAI strength for these materials without TTT reinforcement yarns because the failure mechanism is induced by interlaminar stresses. However, the MSB strength of the thick-layer material with carbon TTT reinforcement yarns was 60 percent higher than the thick-layer and uniweave materials and was 90 percent of the MSB strength of the thin-layer material. These results suggest that when properly designed, thick-layer material with TTT reinforcement yarns can be used in lieu of thin-layer materials. A significant cost savings (material and processing) can be realized by using thick-layer material with TTT reinforcement yarns.

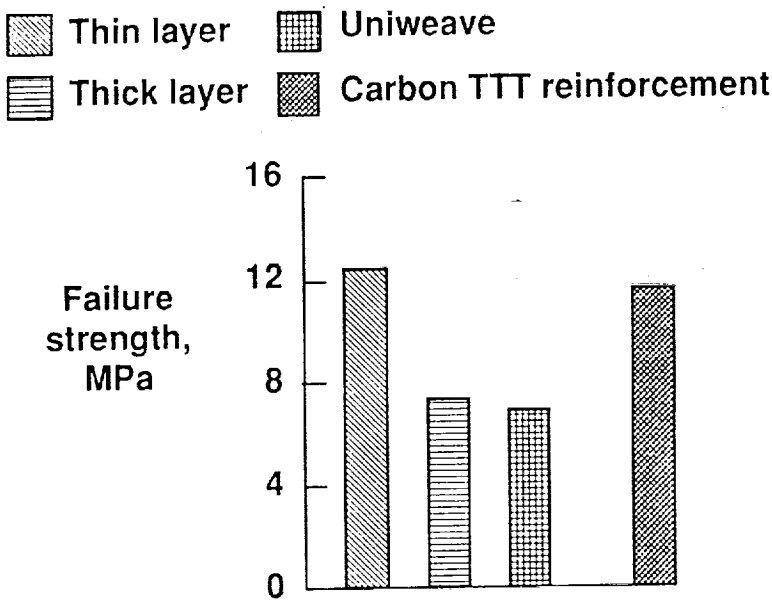

Figure 14

INFLUENCE OF TTT REINFORCEMENT SURFACE LOOP
ON MULTI-SPAN-BEAM STRENGTH

The surface loop had no effect on MSB strength for either type of TTT reinforcement or reinforcement method as seen in Fig. 15. This result is reasonable because the region of high interlaminar shear and the initial failure site are in the center of the laminate. The surface loop influences the mechanical properties of the in-plane fibers along the outer surface of the specimen. Therefore, it is reasonable to expect that the surface loop has no influence on the MSB strength.

The MSB strength of the stitched material is consistently higher than the MSB strength of the integrally woven material. The MSB failures always initiated in the interior of the beam in a 90 degree ply or in one of the resin pockets. The integrally woven materials have larger resin pockets than the stitched material and have TTT yarn loops around a catcher yarn along the specimen's centerline. It is suspected that the larger resin pockets and the presence of the catcher yarns are responsible for the lower MSB strength of the integrally woven materials.

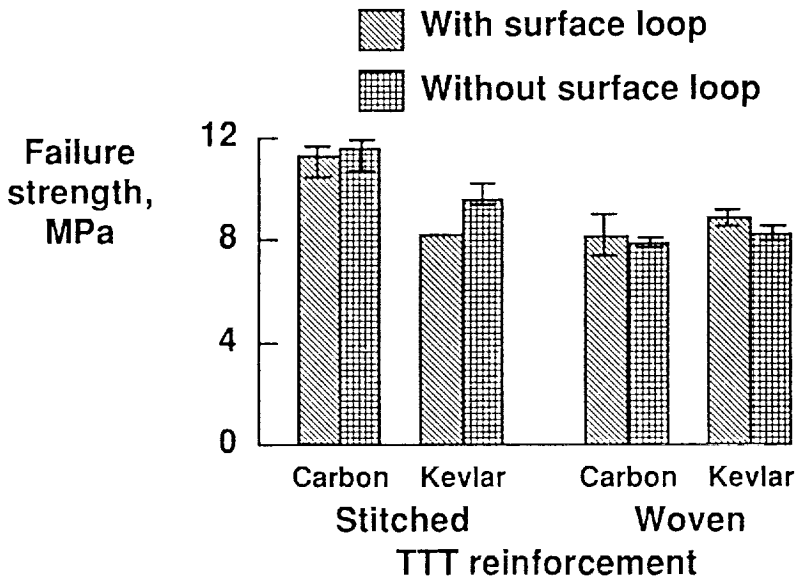

Figure 15

CONCLUDING REMARKS

An experimental investigation was conducted to identify the key geometrical parameters and to quantify their influence on the mechanical response of through-the-thickness (TTT) reinforced composite materials. Composite laminates with TTT reinforcement fibers were fabricated using different TTT reinforcement materials and reinforcement methods. These laminates were microscopically examined to identify potential geometrical features that influence mechanical response. Coupon specimens were machined from these laminates and were tested to failure. Test results were compared with test results from materials of similar construction but without TTT reinforcement fibers. The concluding remarks are summarized in Fig. 16 and discussed further below.

Through-the-thickness reinforcement yarns enhance the damage tolerance and improve interlaminar strength of composite materials. However, TTT reinforcement yarns in composite materials cause a reduction in undamaged compression strength. The reduction of undamaged compression strength due to incorporating TTT reinforcement yarns in composite materials is a result of local resin rich regions, in-plane fiber waviness, surface loop of the TTT reinforcement yarn kinking or bending the in-plane fibers, and breakage of in-plane fibers.

The thick-layer composites studied in this investigation with TTT reinforcement yarns have mechanical properties that are equal to or superior to thin-layer composites without TTT reinforcement. Thick-layer materials can be fabricated from large filament count yarns at a lower cost than with small filament count yarns. Cost of large filament count reinforcement yarns is substantially less than the cost of small filament count reinforcement yarns. Fewer thick layers of material are required to produce a part than are parts produced from thin-layer materials. The reduced number of layers of material reduces part layup cost. Therefore, there is a significant potential cost savings when using thick-layer composites and large filament count yarns.

The stitched materials evaluated in this investigation had different denier yarn for the needle and bobbin yarns. The needle yarn was a smaller denier TTT reinforcement yarn than the bobbin yarn. The smaller denier needle yarn kinked or bent the inplane fiber less than the larger denier bobbin yarn. Since the inplane surface yarns adjacent to the needle yarn are kinked and bent less, then their compression strengths are degraded less. The TTT reinforcement yarns in the integrally woven materials were of the same denier as the larger denier TTT reinforcement yarn in the stitched material. The outer surfaces of the integrally woven laminate were equally influenced by the surface loop of the TTT reinforcement yarns. Therefore, stitched laminates provide somewhat higher mechanical properties than integral weaving.

- Through-the-thickness reinforcement enhances damage tolerance and improves interlaminar strength.
- Thick layer composites with TTT reinforcement have equal or superior mechanical properties to thin layer composites without TTT reinforcement. (Potential exists for fabrication cost reductions.)
- Removal of surface loop improves compression strength.
- Stitching provides somewhat higher mechanical properties than integral weaving.

Figure 16

REFERENCES

1. Jones, R. M. 1975. Mechanics of Composite Materials. New York, NY: McGraw-Hill Book Co.

2. Shuart, M. J., "An Analysis of Shear Failure Mechanisms for Compression-Loaded $[\pm\Theta]_S$ laminates", Journal of Composite Materials, Vol. 23, March 1989.

3. Portanova, M. A., Poe, C. C. and Whitcomb, J. D., "Open Hole and Post-Impact Compression Fatigue of Stitched and Unstitched Carbon/Epoxy Composites", NASA TM 102676, June 1990.

Tensile Properties of Textile Composites

V. Sarma Avva, Robert L. Sadler and Malcolm Lyon

Mars Mission Research Center
Department of Mechanical Engineering
North Carolina A & T State University
Greensboro, NC

Abstract

The importance of textile composite materials in aerospace structural applications has been gaining momentum in recent years. With a view to better understand the suitability of these materials in aerospace applications, an experimental program was undertaken to assess the mechanical properties of these materials. Specifically, the braided textile preforms were infiltrated with suitable polymeric matrices leading to the fabrication of composite test coupons. Evaluation of the tensile properties and the analyses of the results in the form of strength, moduli, Poisson's ratio, etc., for the braided composites are presented. Based on our past experience with the textile coupons, the fabrication techniques have been modified (by incorporating glass microballoons in the matrix and/or by stabilizing the braid angle along the length of the specimen with axial fibers) to achieve enhanced mechanical properties of the textile composites. This paper outlines the *preliminary* experimental results obtained from testing these composites.

Introduction

The advantages in using the engineered laminated composites having high specific strength and specific modulus in the design of payload sensitive spacecraft have been known for some time. As the range of applications using these laminated composites is increasing, other design limiting problems such as the interlaminar strength, material toughness, fabrication and tooling costs need to be addressed critically. By virtue of the inherent geometrical layups of laminated composite structural components, non-uniform stresses in the various layers and directions take place under loads. These stresses in turn induce interlaminar shear and normal stresses at the 'free' boundaries or edges [1] of composite laminates resulting in damage and/or premature failures. While design modifications or techniques can be incorporated to suppress the delaminations, nevertheless newer approaches in developing alternate and cost-effective technologies are needed. As a result, the existing technologies from the textile industry are being explored and developed [2,3] in the design of aerospace composite components.

Many of the textile manufacturing processes such as braiding, knitting, and weaving will reinforce through the "thickness" of the composite structural components, thereby virtually eliminating or minimizing the effect of delaminations as well as giving rise to additional strength, if necessary, between the layers. Further, it's believed that the textile fabrication technologies could contribute to lower costs. As a result, the research and developmental activities in the use of textile technologies for structural composites are gaining momentum in developing multiaxial fabrics, integrally woven structures with stiffeners, and near-net-shape preforms [4,5]. These textiles preforms assume the near net structural shapes after impregnating and curing with suitable matrix with very little, if any, further processing operations. In addition, the textile preforms in their near-net-shape may be dry, prepregged or impregnated with (matrix) powder or commingled with matrix filaments. The latter two techniques by-pass the (liquid) resin transfer molding operation. One of the attractive features in using the net-shape preform technologies is its amenability for automation such as pultrusion, where production quantities justify, thereby maintaining quality control and lowering the cost of fabrication.

Materials, Processing, and Fabrication

The graphite textile preforms were braided with tows of Celion G30-500 (BASF Structural Materials, Inc.) fibers. These fibers measure 7 microns in diameter and have a modulus of 30 Msi. The preforms were braided by a 4-step process where each tow was interlocked with the other tows to form a true 3-D structure. The braid angle was varied between 17 and 30 degrees.

The preforms were fabricated using a vacuum/compression molding consolidation process. The matrix system was comprised of two components-Epon 828 (Shell Chemical Co.) and Jeffamine T-403 (Texaco Chemical Co); 100 parts-by-weight to 42 parts-by-weight, respectively. This resin system was chosen because it had a relatively long pot life and low viscosity which was necessary for this method of molding. The two components were heated separately at 60^0 C for ten minutes to reduce the viscosity which in turn reduces the time required to evacuate the catalyzed resin. The two components were then combined and evacuated for ten minutes after the vacuum pressure reached one Torr. The bottom of the stainless steel mold cavity was completely covered to a depth of about 1/16" with the evacuated resin. The textile preform was then placed into the mold cavity and was covered with the remaining resin, and again evacuated for ten minutes after the vacuum pressure reached one Torr. Once the evacuation process was complete, the plunger was placed in the mold cavity and the mold was placed in a heated press where the excess resin was squeezed out in order to obtain a desired composite thickness. The nominal specimen dimensions are 0.100 x 0.750 x 10 inches. The composites were cured for three hours at 100^0 C. The fiber volume of the specimens was found to vary between 45% and 55%. The tensile coupons were tabbed using 1/8" fiberglass tabs. The tabs were attached with an adhesive film, FM123-5 (American Cyanamid), which required a cure cycle of 90 minutes at 100^0 C and

50 psi. The geometry and dimensions of four different types of braided test specimens are shown in Figure 1.

In an effort to lower the density of the composite specimens, glass microballoons were introduced into the matrix of some of the test coupons. Glass microballoons can be thought of as controlled voids which will displace some of the resin. Thus, the idea was to use controlled voids to reduce the density of the samples without any significant loss in many of the properties. The glass microballoons used in the study had a diameter range from 7 to 70 microns. The resulting density reduction was found to be about 2%. The specimen without microballoons had a density of 1.51 g/cm^3 and with microballoons, it was 1.48 g/cm^3 . The test results indicate that the resin displaced by the glass microballoons (5% by weight) did not significantly affect the tensile strength of the composite specimen. However, a difference in the strain behavior was observed. Further studies are suggested to optimize the strength and density with respect to the percentage of microballoons that can be incorporated in the composite materials.

Experimental Results and Analyses

Numerous factors affect the performance of braided textile composites. It is not uncommon to observe significant variations in the mechanical properties of braided composites. At the laboratory coupon-level fabrication, the quality control of textile composites becomes even more critical if one is assessing the relative merits of these composites for their mechanical properties. Several factors such as the quality of braided preform, stabilizing the braid angle through the molding process, extent of curing, compaction of the preform, maintaining precise fiber volume ratio, size effect, uniform density, location of the specimen cut from a finite length of the preform, complete removal of voids and tiny pockets of trapped air bubbles, uniform distribution of fiber tows and the surrounding matrix throughout the length of the test specimen, symmetry of the composite, dimensional variations in the as-molded specimen, etc., may adversely affect the mechanical properties.

Preliminary experimental data of the tensile properties of four different types of braided composites are shown in Table I. In presenting this initial data, no attempt has yet been made to censor the data based on the factors mentioned in the preceding paragraph that may adversely affect the mechanical properties. Further analyses of the raw data are underway to refine and compare the properties of the four types of specimens with the factors that influence the results in the background.

The objective in introducing the glass microballoons in the composite was to not only lighten the braid but to reduce the formation of resin pockets that may develop at the crossings of large-sized (12k) tows. A cursory examination of the resulting data as shown appears to indicate that the nominal tensile properties were not affected except for the transverse strain. Based on density and fiber volume ratio measurements to be performed shortly, the eval-

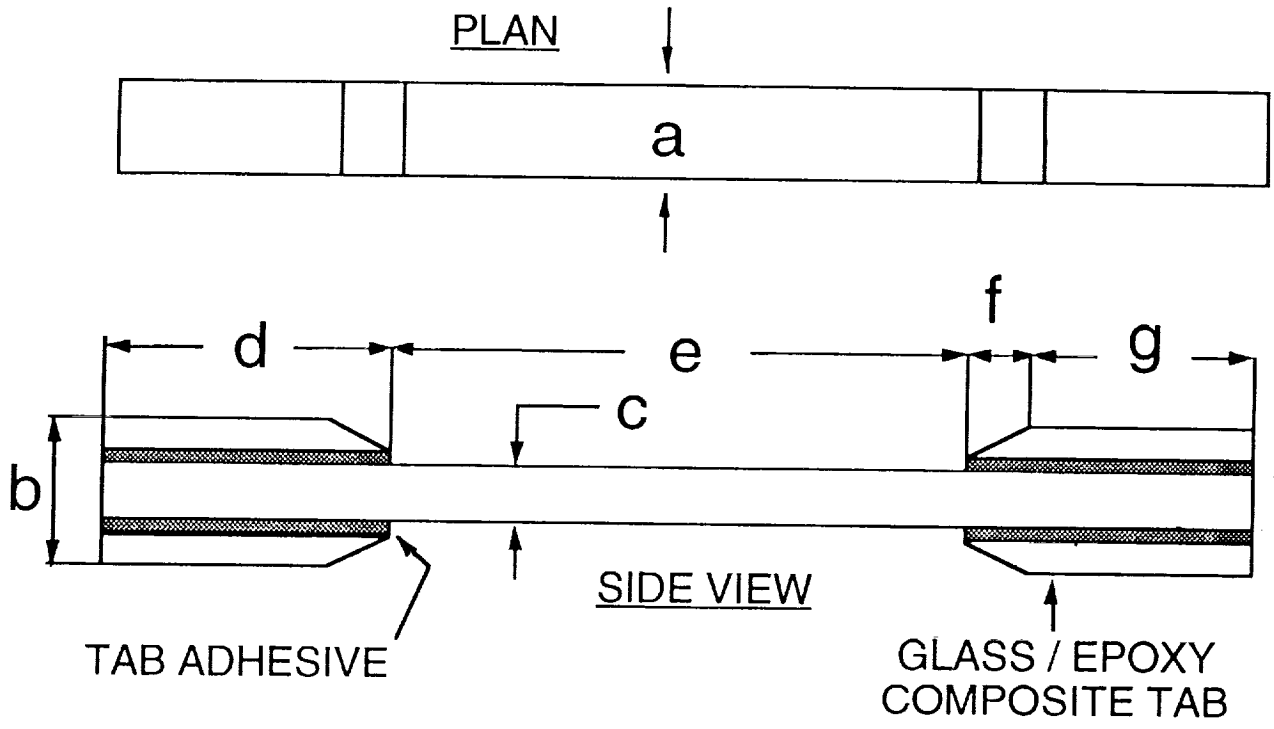

TYPICAL BRAIDED SPECIMEN GEOMETRY

TYPICAL DIMENSIONS OF FOUR TYPES OF SPECIMENS*

	a	b	c	d	e	f	g
Plain braids	0.750	0.352	0.102	2.75	4.5	0.25	2.5
Braids with microballoons	0.753	0.354	0.104	2.75	4.5	0.25	2.5
Braids with axial fibers	0.877	0.354	0.104	2.75	4.5	0.25	2.5
Braids with axial fibers & microballoons	0.878	0.362	0.112	2.75	4.5	0.25	2.5

* All dimensions in inches. Braids with axials have 37% (26 tows out of 70) axial fibers.

Figure 1. Tensile Specimen Geometry and Dimensions

TABLE-I : TENSILE PROPERTIES OF BRAIDS*

	Braid angle (deg)	Load Pmax (kip)	Stress σ_{max} (ksi)	Strain ε_{11max} (%)	Modulus E_{11} (Msi)	Trans.Strain ε_{12} (%)	Poisson's ratio ν_{12}
Plain braids	23/30	13.22 ±1.7	173.5±23	1.47±0.09	11.8	2.31±0.36	1.57
Braids with microballoons	21/30	13.44±2.3	172.1±29	1.52±0.11	11.3	2.69±0.40	1.77
Braids with axial fibers	-	15.81±1.0	179.0±14	1.34±0.07	13.4	1.19±0.27	0.89
Braids with axial fibers & microballoons	-	13.14±2.3	135.3±27	1.26±0.10	10.7	1.39±0.33	1.10

* The experimental data shown here in tabular form is for convenience only. Comparison of data among the various cases shown here is not recommended. Extensive data reduction and detailed analyses are planned for the purpose of comparing the properties on a rational basis. Factors such as braid angle, fiber volume ratio, failure zones, size effect, density, specimen imperfections, if any, etc., are expected to influence the preliminary data shown above.

uation of specific mechanical properties will be conducted. If the succeeding analyses prove to be encouraging, a corollary that needs to be addressed is the percentage of microballoons that could be introduced in a unit volume of the braid resulting in one or more than one designated optimum property or properties. Further, what is the effect of introducing other grades of microballoons as to size and specimen thickness on these properties ?

A nonuniform drift in the braid angle was noticed which may be attributed to the compression molding process. In order to stabilize the braid angle as well as to further improve the mechanical properties of the braids simultaneously, axial fibers(tows) were introduced during the preform fabrication. As expected, preliminary data reveal an improvement in the nominal tensile strength and modulus, and a decrease in the strains. The percentage of axial fibers selected in this study was random. Optimization techniques may be applied to determine the percent of axial fibers that can be embedded in braided specimens.

The experimental results with a matrix containing microballoons and braids containing axials were obtained very recently and are being analyzed critically to understand their significance.

Conclusions

1. Four different types of braided specimens were studied to assess their tensile mechanical properties. Factors that affect the properties are identified for further data reduction and analyses.

2. A preliminary evaluation on the effect of microballoons in the plain braided composites on the mechanical properties is presented. Many of the properties appear to remain unchanged. Further analyses based on density measurements may show an improvement in some of the specific properties.

3. Axial fibers were introduced in the braids to improve the mechanical properties further, and the preliminary results are encouraging.

4. Through these studies, it has become clear that many factors affect the mechanical properties ranging from preform and composite fabrication through testing and rational data reduction.

Acknowledgements

This work is supported by the National Aeronautics and Space Administration through a Grant Number NAGW-1331 to the Mars Mission Research Center at North Carolina State and North Carolina Agricultural and Technical State Universities. Prof. El-Shiekh, a member of the MMRC at NCSU, contributed the braided preforms.

References

1. Simonds, R.A., Stinchcomb, W., and Jones, R.M., "Mechanical Behavior of Braided Composite Materials", *Composite Materials: Testing and Design (Eighth Conference), ASTM STP 972*, J.D. Whitcomb, Ed., American Society for Testing and Materials, Philadelphia, 1988.

2. Ko, F. K., "Tensile Strength and Modulus of a Three-Dimensional Braid Composite", *Composite Materials: Testing and Design (Seventh Conference), ASTM STP 893*, J.M. Whitney, Ed., American Society for Testing and Materials, Philadelphia, 1986.

3. Macander, A.B., Crane, R.M., and Camponeschi, E.T., Jr.,"Fabrication and Mechanical Properties of Multidimensionally (X-D) Braided Composite Materials",*Composite Materials:Testing and Design (Seventh Conference), ASTM STP 893*, J.M. Whitney, Ed., American Society for Testing and Materials, Philadelphia, 1986.

4. Mohamed, M.H., Zhang, Z., and Dickinson, L., "Manufacture of Multi-Layer Woven Preforms", *Advanced Composites & Processing Technology* ; MD-Vol.5, Editors: T.H. Tsiang and R.A.Taylor, The American Society of Mechanical Engineers.

5. El-Shiekh, A.H.M., "The Effect of Processes and Processing Parameters on the Properties of 3-D Composites", *33rd International SAMPE Symposium & Exhibition*, Anaheim, CA., March 7-10, 1988.

MODELING OF EUCLIDEAN BRAIDED FIBER ARCHITECTURES TO OPTIMIZE COMPOSITE PROPERTIES

E. Armstrong-Carroll*, C. Pastore†, and F. K. Ko††

ABSTRACT

Three-dimensional braided fiber reinforcements are a very effective toughening mechanism for composite materials. The integral yarn path inherent to this fiber architecture allows for effective multidirectional dispersion of strain energy and negates delamination problems. In this paper a geometric model of Euclidean braid fiber architectures is presented. This information is used to determine the degree of geometric isotropy in the braids. This information, when combined with candidate material properties, can be used to quickly generate an estimate of the available load-carrying capacity of Euclidean braids at any arbitrary angle.

INTRODUCTION

Three-dimensional braided fiber architectures generate thick fabrics with yarns traveling diagonally through the fabric thickness. The outstanding performance features of these braids are high damage tolerance and delamination resistance. The mechanical properties of these materials are documented in previous works [1, 2].

Correlations between braid fiber architecture and resultant mechanical properties have been made [2]. Further efforts have been made to develop a processing science model of Euclidean braid fiber architectures [3]. The processing model incorporates yarn geometry and other fabrication variables in a geometric cross-sectional slice model. The processing model correlates fabric design inputs parameters with a geometric model in order to more accurately determine the resultant yarn orientations and fabric dimensions.

This paper presents a unit cell model of Euclidean braids in the close-packed condition. The dependence of fiber volume fraction on braid angle is formulated. A geometric isotropy model [4] is applied to the unit cell model. This application generates plots of the distribution of effective fibrous reinforcement in Euclidean braids. These plots provide a quick and effective guideline for selecting the proper braid angle for a specific application.

FABRIC FORMATION PROCESS

Braids are formed by the intertwining of yarns. This intertwining is accomplished by the crossing of yarns on individual yarn carriers. Three-dimensional Euclidean braids are formed in a four-step braiding sequence. In step one columns of yarn carriers are moved up and down relative to each other. In step two tracks of yarn carriers are moved back and forth relative to each other. In step three columns of yarn carriers are moved up and down relative to each other. In step four tracks of yarn carriers are moved back and forth relative to each other. The correspondence between track and column loom movements and yarn movements in forming a fabric are shown in Figure 1.

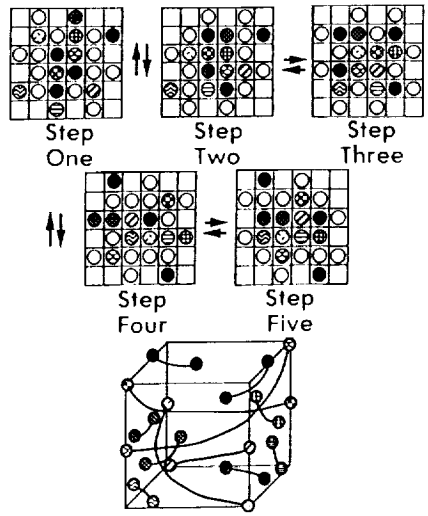

Figure 1. Track/column loom motion used to form an Euclidean braid and the initial unit cell produced by this process

After each set of track and column movements, the yarns are compacted. In this process body diagonal yarn pairs resulting from a track/column movement are compacted against body diagonal pairs arising from the previous track/column motion. The compacting motion intertwines the yarns.

The yarns transverse through the thickness of the fabric in a zig-zag motion as the braiding sequence is repeated. Figures 2 and 3 project the resultant yarn paths into the loom plane for rectangular and circular looms. The three dimensional path of one yarn in a Euclidean braid is depicted in Figure 4. In this figure a discrete lattice is used to locate the yarn in the braid. The presence of this lattice has generated the nomenclature, Euclidean braiding, to describe the track/column braiding process.

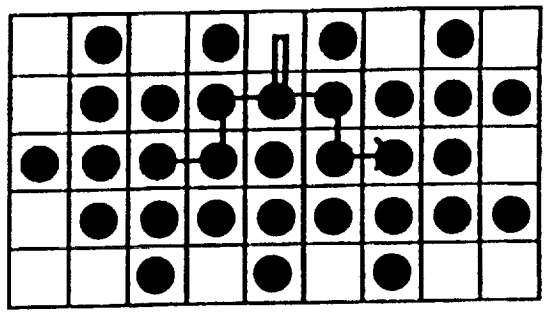

Figure 2. Yarn path projected onto the braiding plane of a rectangular loom [3]

FOOTNOTES:
* Naval Air Development Center, Warminster, PA
† North Carolina State University, Raleigh, NC
†† Drexel University, Philadelphia, PA

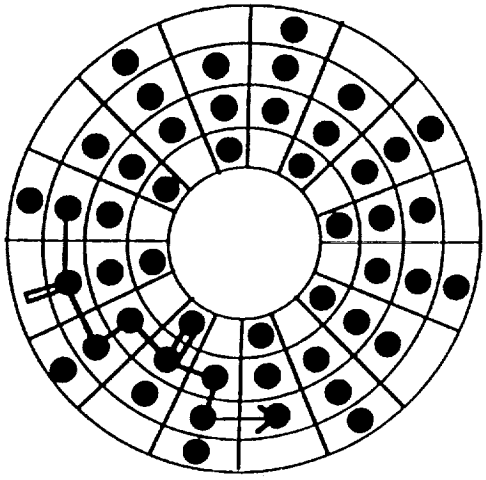

Figure 3. Yarn path projected onto the braiding plane in a circular loom [3]

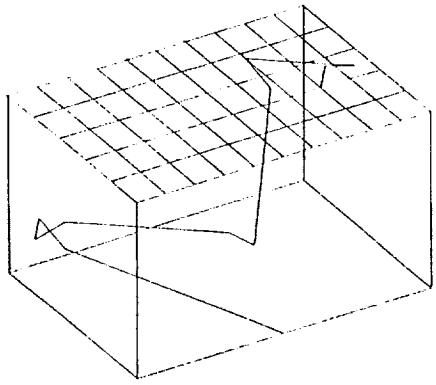

Figure 4. Isolated path of a single yarn in a 3D braided fabric [3]

UNIT CELL MODEL

This model describes the unit cell of a three-dimensional braid when the yarns are close-packed in the xy fabric formation plane. Several simplifying yarn geometry assumptions are made for this model. The yarns are assumed to be incompressible, identical, and circular in cross-section.

The loom and compaction motions involved in the Euclidean braid fabric formation process cause the diagonal movement of the yarns in space. The path of these yarns through a unit volume element is shown in Figure 5. The volume is tetragonal since the yarns possess a circular cross-section and the yarn carriers on the loom are equally spaced in the x and y directions.

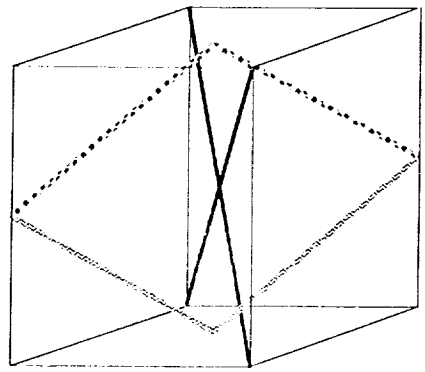

Figure 5. A schematic of yarn paths in an Euclidean braid

Figure 6 is a schematic of through-thickness cross-sections of an Euclidean braid. These cross-sections correspond to the xy planes of the unit cell. The yarns appear elliptical due to the braiding angle. The squares superimposed on the yarns represent the unit cell boundaries in the xy planes. The length of the cell in the x direction is a. The length of the cell in the y direction is b. The unfilled yarns pass through the fringes of the unit cell. The yarns progress through the unit cell as a result of the loom motions. For example, as the columns move, the shaded yarn in the lower left-hand corner of the bottom cell plane zigs halfway up the b length. The subsequent track movement zag and compaction place the shaded yarn in the central region of the unit cell.

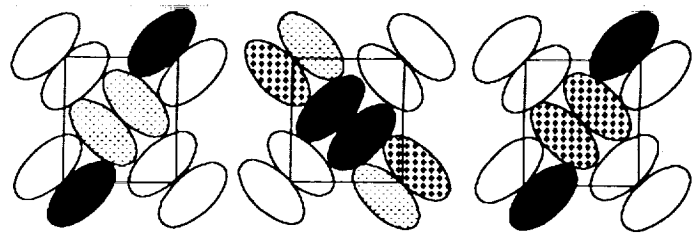

Figure 6. Close-packed through-thickness planes of an Euclidean braid

The lengths of the a and b parameters are equivalent. These lengths are a function of the braid angle and the yarn diameter. Figure 7 defines the braid angle as it appears in the unit cell. The length of the a and b parameters can be defined as:

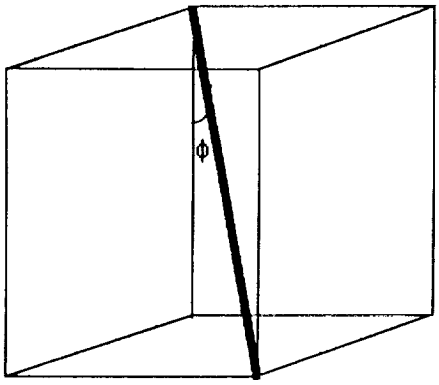

Figure 7. The relationship of the braid angle to the unit cell

$$a = b = (D/\sin\phi) + 2D)/SQRT(2) \quad (1)$$

The height of the unit cell is measured by the parameter c. The length of c can be defined as:

$$c = a\ SQRT(2)/\tan\phi \quad (2)$$

Since there must be enough room in the unit cell for yarns to form the V-shaped and X-shaped cross-overs in the cell, there exists a minimum value for c. This minimum can be defined as:

$$c_{min} = 2D/\sin\phi \quad (3)$$

The volume of the unit cell is the product of these three lengths.

The unit cell contains the six yarns depicted in Figure 5. The sum of the lengths of all these yarns is equivalent to four times the body diagonal length. The volume of yarn in the unit cell is equal to the yarn length times the yarn cross-sectional area. This relationship can be expressed as:

$$V_y = \pi D^2 \sqrt{2a^2 + c^2} \quad (4)$$

The fiber volume fraction in the unit cell is equal to the yarn volume divided by the unit cell volume times the yarn packing factor. The yarn packing factor accounts for interstitial space within the yarn bundle. The value used for this work is 74%. The value results from experimental work performed by C. Pastore at NASA Langley.

MODELING THE EFFECT OF FABRICATION VARIABLES

Since the yarns are close-packed in this model, the fiber volume fraction is solely a function of the braid angle. The effect of varying this angle is plotted in Figure 8. Fiber volume fraction increases with braid angle. The maximum braid angle, 52°, yields a fiber volume fraction of 0.79. The maximum angle corresponds with a minimum in the value of c.

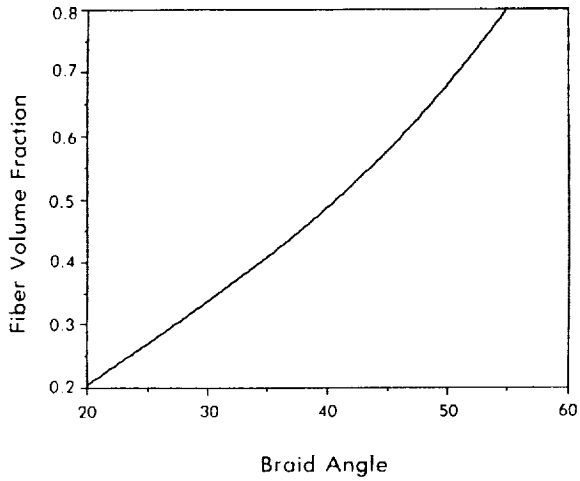

Figure 8. The effect of varying braid angle on fiber volume fraction

DISTRIBUTION OF FIBROUS REINFORCEMENT

A fiber architecture possesses geometric isotropy if the variation in effective fiber volume fraction directly contributing to a loading direction is constant for any angle. The effective fiber volume fraction of a fabric is defined as the fraction of fibers aligned in the proper direction in order for the applied load to be transferred to the fibers. For this model of geometric isotropy the load bearing capacity of a fiber in the transverse direction is assumed to be zero. This capacity is assumed to be one in the longitudinal direction. These assumptions can be applied since the load bearing capacity of a yarn in the transverse direction is many orders of magnitude lower than that in the longitudinal direction.

The unit cell is composed of six yarns which transverse the cell in four distinct yarn orientations. These yarn orientations are orthogonal to each other. The yarn orientations are translated to correspond with 0, 90, 180, and 270 degrees.

The distribution of fibrous reinforcement is described by plotting the effective fiber volume fraction at an arbitrary angle in the xy, xz, and yz planes. The braid angle is projected onto a given plane. Then the effective fiber volume is calculated for any angle in this plane. The fibrous reinforcement distribution function in the xy plane is:

$$V(\vartheta) = 0.25V_f \sin\phi\ (|\cos(\vartheta)| + |\sin(\vartheta)|) \quad (5)$$

The fibrous reinforcement distribution function in the xz and yz planes is:

$$V(\vartheta) = 0.25V_f \cos\phi\ (|\cos(\vartheta)| + |\sin(\vartheta)|) \quad (6)$$

Figure 9 plots fibrous reinforcement distributions in the xy plane for two different braid angles. The xy fabric formation plane corresponds with the through-thickness direction in the finished fabric. Minima in the plot occur at the principal yarn orientation directions. In these directions the other orthogonal yarn pair contributes nothing. Maxima occur 45° from the minima. At this location all yarns are contributing to load-carrying ability. The effective load-carrying ability varies 33% as a function of the arbitrary angle.

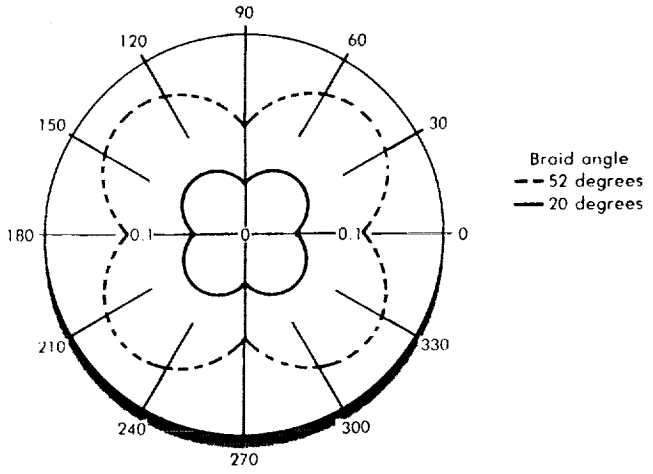

Figure 9. The distribution of fibrous reinforcement in the through-thickness plane

Figure 10 plots fibrous reinforcement distributions in three orthogonal fabric planes for 52° braid angle. Euclidean braid fiber architectures with this maximum braid angle possess the highest amount of through-thickness load carrying ability. As the angle decreases, overall fiber volume decreases and the portion of the fiber volume contributing to through-thickness load-carrying ability decreases.

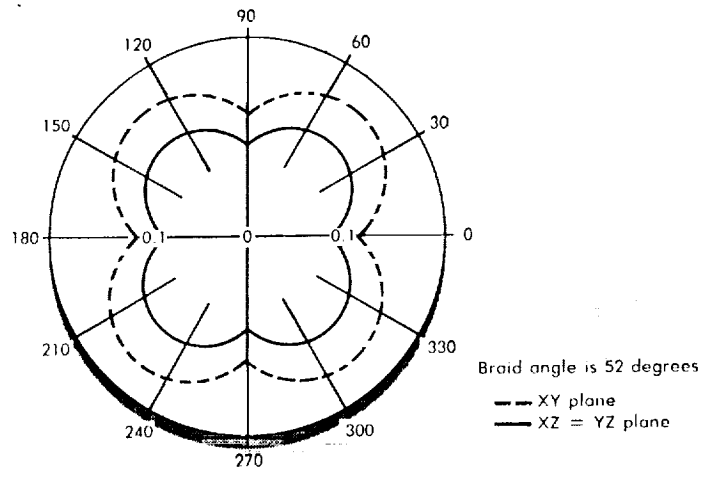

Figure 10. Fibrous reinforcement distribution in the three fabric planes of an Euclidean braid

SUMMARY

Euclidean braid fiber architectures do possess a close-packed fiber plane. With the close-packed condition, fiber volume fraction is solely a function of the braid angle. The fiber volume fraction increases with the braid angle.

The fibrous reinforcement distributions for Euclidean braids closest approach isotropic conditions when the load-carrying ability in each plane is equivalent. Within a plane the fibrous reinforcement distribution is similar to a four-leaf clover. Maxima and minima differences correspond with a 33% difference in load-carrying ability. Due to the degree of isotropy present, no arbitrary angle contributes a large percentage of reinforcement.

In general, geometric isotropy plots are a useful means to determine which fiber architecture is most suited for the desired loading conditions for a particular application.

REFERENCES

1. Ko, F.K., "Three Dimensional Fabrics for Composites", Textile Structural Composites, edited by T.W. Chou and F.K. Ko, pp 129-171, Elsevier Science Publishers, Netherlands, 1989.

2. Whyte, D.W., On the Structure and Properties of 3D Braid Reinforced Composites, PhD Thesis, Drexel University, June 1986.

3. Pastore, C.M., A Processing Science Model for Three Dimensional Braiding, PhD Thesis, Drexel University, 1988.

4. Armstrong-Carroll, E., Classification Systems for Three Dimensional Fiber Architectures, MS Thesis, Drexel University, June 1989.

MICROSTRUCTURE - FAILURE MODE CORRELATIONS IN BRAIDED COMPOSITES

G. J. Filatovs and R. L. Sadler
North Carolina A&T State University, Greensboro, NC
A. El-Shiekh
North Carolina State University, Raleigh, NC

ABSTRACT

Explication of the fracture processes of braided composites is needed for modeling their behavior. Described is a systematic exploration of the relationship between microstructure, loading mode, and micro-failure mechanisms in carbon/epoxy braided composites. The study involved compression, and fracture toughness tests and optical and scanning electron fractography, including dynamic in-situ testing. Principal failure mechanisms of tow sliding, buckling, and unstable crack growth are correlated to microstructural parameters and loading modes; these are used for defining those microstructural conditions which are strength limiting.

INTRODUCTION

The integrated nature of multidimensional braided composites holds promise for overcoming some of the shortcomings of conventional laminate composites, while introducing compromises of their own. While their general behavioral trends are known there are still many knowledge gaps and obstacles to their use. In particular, the high anisotropy and interaction of several structural levels have made selection of representative volume elements and homogenization procedures difficult. At the present, no superior method of modeling and analyzing these materials has emerged.

This paper gives an overview of several projects focused on the deformation and failure of braided materials. The approach is experimental micromechanics-based, relying on testing of small-scale specimens and optical and SEM fractography. There is a prohibitively large number of material and braid geometry combinations to be exhaustively tested; therefore the focus has been on determining the failure sequence and failure controlling microstructural features. The goal is the establishment of a heuristic, rule-based description of the

failure process/microstructural interaction, and of the definition of a mechanical properties unit cell which can be used as a bridge to macro-scale behavior.

MATERIALS AND PROCESSES

The textile preforms were braided with 12K tows of Celion G30-500 (BASF Structural Materials, Inc.) graphite fibers. These fibers measure 7 microns in diameter and have a modulus of 30 Msi. The preforms were braided by a 4-step process in a 3 X 14 design where each of the tows is interlocked with the other tows to form a true 3-D structure. Reference [1] contains a discussion of the 4-step braiding process.

Composites are fabricated from these textile preforms using a vacuum/compression consolidation process. The matrix is comprised of two components, Epon 828 (Shell Chemical Company) and Jeffamine T-403 (Texaco Chemical Company), in a ratio of 100:42 parts-by-weight respectively. After mixing, the catalyzed resin is vacuum degassed for 10 minutes at < 1 Torr. The preform is placed in a mold and submerged in the liquid resin and the evacuation step is repeated. The mold is closed and the composite is press cured for 3 hours at 100 C. A mechanical stop is used to control the thickness of the composite. Typical dimensions for the composite samples are 0.100 X 0.750 X 10.0 inches. More details of the fabrication aspects are given in [2]. The fiber volume fraction was typically 55%.

Composite tubes were also used in these experiments. They were fabricated from a textile preform braided in much the same manner as the flat braid but the machine bed was circular instead of rectangular. The tube preforms were impregnated and consolidated by resin transfer molding (RTM) with Tactic 123 (Dow Chemical Co.) and catalyzed with Millamine 5260 (Milliken Chemical Co.) in a ratio of 100:17 parts-by-weight respectively. This matrix system requires a cure of 1 hour at 70^{o}C followed by 2 hours at 170^{o}C.

STRUCTURAL DESCRIPTION

A structural description of the composite is necessary for any consideration of failure modes. The preform structure has been defined from a textile point of view [1]. Such a description, however, is only partly descriptive of the final component. While computational unit cells have been proposed for braids and weaves [3,4], care must be taken in

extracting them from the actual structure. A different approach will be taken here.

Figures 1a and 1b show the textile preform and the subsequent composite coupon fabricated from it. In this case, a white tracer tow has been added indicating the location of a single tow. Figures 2a and 2b show the top and side views of a single tow extracted from the composite. Based on these, a schematic of the tow location, along with identification of the important microstructural descriptors and the surface/volume mapping can be constructed (Figure 3).

Note that a fiber tow lies on a diagonal-type plane and sinuously spans the thickness of the specimen. This fiber does not exactly match the apparent surface pattern. The true cycle length, or the return of the tow to its starting position may be quite long and depends on the braiding cycle. For the purpose here, it is sufficient to define one cycle as the return to the equivalent point on the diagonal plane. Figure 4 is a further idealization and contains only two representative crossing tows. The diagonal length of this cell is one half the cycle length previously defined.

Figure 4 can be used for creating an efficient representation of the tow structure. Consider a unit cell as commonly defined in x-ray crystallography [5]. This type of unit cell allows the use of Miller Indice notation, which describes directions, planar orientations, and directional relationships in compact form. The X, Y, and Z axes become [100], [010], and [001] respectively. The diagonal plane on which the tows lie are of the form (110), and the crossing points or intersection of the tows are generally on the (111)-type planes. The cell here is, of the the orthorhombic type, and actual cell parameters are established by measurement from the fabricated composite.

TEST RESULTS

Table 1 contains selected test results from small coupons, along with the external load conditions and specimen details. The matrix (neat resin) specimen failed along the expected 45^{o} shear lines. The axial specimens initially failed in shear along the apparent braid angle. SEM fractographs are shown in Figure 5. Internally, the failure was of a mixed mode on the (110) and (111)-type planes. Note the rapid drop in axial strength with the increase of braid angle. The overall trend with fiber volume fraction is shown in Figure 6. In later stages of the failure sequence fiber buckling occurred. For transverse compressive loading, the failure was tows sliding over each other on the (111)-type planes.

The notched specimens were based on ASTM E399 compact fracture toughness specimens [6]. This test was developed for metals but attempts have been made to use it for laminate composites. For braided materials this test appears useful only as a worst-case indicator. If the notch is along the braid direction, the specimen tends to fail in cleavage at values below that of the matrix. The crack front moves in general along the (110)-type planes. For notches perpendicular to the braid direction the failure load is considerably higher but the crack length, area and failure mode are difficult to determine. Figure 6 is an SEM of this case. Considerable additional work is required to remove uncertainties from the testing results.

Tests were also conducted on components. Axial compression of one inch diameter braided tubes and T-sections followed the same trends as the coupons. Figures 7 and 8 are micrographs of these specimens.

The loads and stresses given in Table 1 are those for yielding. There is much post-yield phenomena in these materials, with higher values possible with continued testing, along with increasing damage. At some point the damage becomes catastrophic and the specimen fails.

DISCUSSION

The previous results represent only selective, illustrative data. Our experience with these materials runs to hundreds of samples and a variety of tests, and these will be amplified in other publications. The common trends and generalizations that have emerged will be outlined here.

The dominant descriptive parameter is the braid angle. The differentiation between the apparent and internal braid angles is approximately 3^{0} for most braids, and the surface angle can be used as an approximation in most cases.

In the initial stages of the failure sequence, the tows act as units, giant pseudo-fibers. It is useful to partition the matrix into inter- and intra- tow components. The inter-tow matrix and fibers form the tows which are surrounded by the intra-tow matrix. If the total fiber fraction is V_{total}, and the fiber fraction in the tow is V_{tow}, then the inter-tow matrix fraction is

$$1 - V_{total} / V_{tow} \qquad (1)$$

This assumes the tows are straight.

Most tows are not circular; combined with tow curvature this has the effect that in later stages of failure the individual fibers in a tow do not carry the load evenly and failure occurs by sequential tearing. This is a strength lowering but energy absorbing mechanism.

Fiber-matrix interface debonding is frequently the initiating event in failure, allowing either tow sliding or the formation of cracks at resin-rich areas. It appears that the accumulation and growth of these cracks is encouraged by the resin-rich areas.

There is also a stochastic aspect introduced by structural variability. Most braided materials contain variation in the braiding angle, and this is linked in a complicated way to the local density and fiber volume. The variation in even high quality braids can be as much as 2 degrees. Considering the effect of braid angle on compressive strength given previously, there is bound to be an uncertainty in strength values of components. Further, in components, cracks in tension have a probability of being in the proper orientation for runaway crack growth.

Do these observations point the way to any solutions of the shortcomings? Stronger interfaces are one possibility. To reduce the effects of matrix-rich areas fewer fibers per tow or stress dispersants such as microballoons could be used. But the toughness/energy absorption vs. strength tradeoffs are not fully known, and much work remains in understanding these materials.

As a closure, the question of a mechanical properties unit cell will be considered. Based on the foregoing experimental work, it appears that this could be derived from the unit cell defined previously. This unit cell would reflect the fracture-strength anisotropy, and would contain scaled equivalent volumes of matrix and fiber. These would be corrected to reflect Equation 1, and the interface angles would be based on observed failure processes. Variability can be introduced by considering a distribution of cells. We have used such an approach by assigning failure criteria and using Weibull statistics, and have been able to model some macro failure processes. This work is continuing.

ACKNOWLEDGMENT

The work reported in this paper was supported in part by NASA grant No. NAGW-1331 to the Mars Mission Research Center, and by ONR Research Grant No. NOOO14-K-0682 to the Center for Composite Materials Research, both at N.C. A&T State University, Greensboro, NC.

REFERENCES

1. Wei Li and Aly El-Shiekh, "The Effect Of Processes And Processing Parameters On 3-D Braided Preforms For Composites", SAMPE Quarterly, Vol.19, No. 4, 1988, pp 22-28.

2. Bagher Bagherpour, "Microstructural Aspects Of Failure Modes Of Braided Composite Materials", MS Thesis, N.C. A&T State University, 1991.

3. J. Yang, C. Ma, and T. Chou,"Fiber Inclination Model Of Three-Dimensional Textile Structural Composites", J. Comp. Matl., Vol. 20, 1986, pp 472-483.

4. T. J. Whitney and T-W Chou, "Modeling Of 3-D Angle-Interlock Textile Structural Composites", J. Comp. Matl., Vol. 23, 1989, pp 890-911.

5. B. D. Cullity, "Elements Of X-Ray Diffraction", Addison-Wesley, 1956.

6. ASTM Standards, Section E399-79a.

Table 1 Test Results

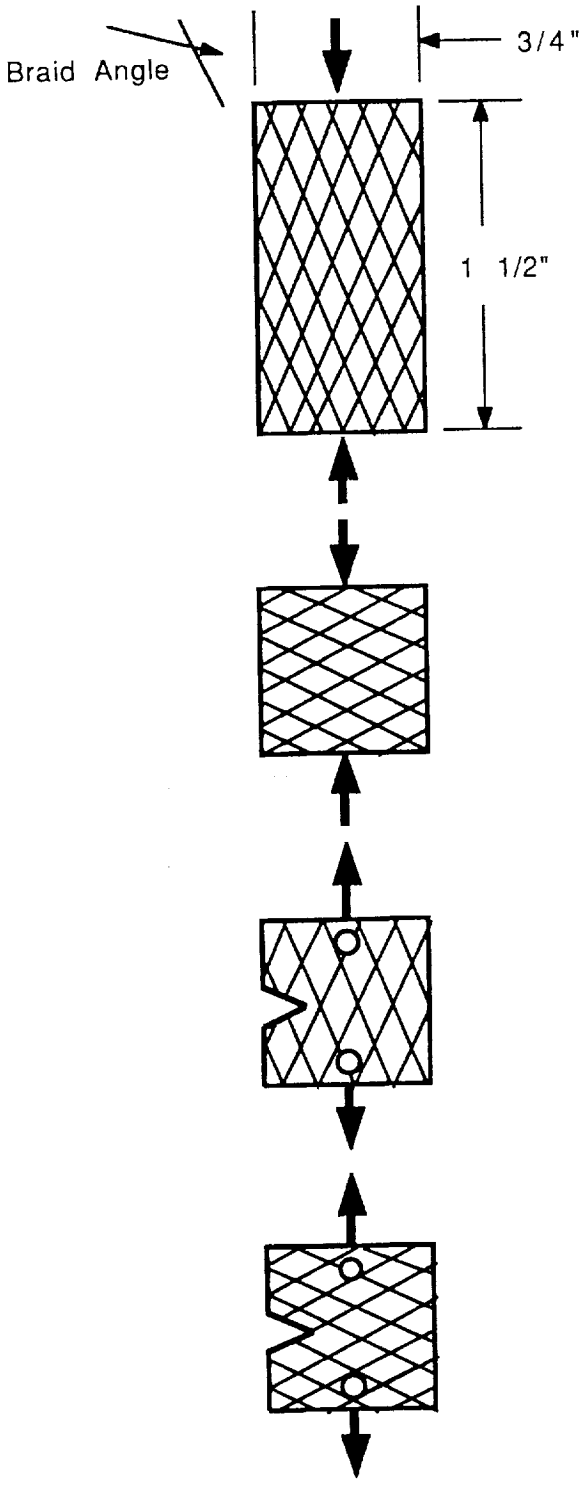

Angle	Axial Yield Stress
3	110,000 psi
13	66,000
18	44,000
23	16,000
Matrix	13,000

Fiber Volume - 55% approx.
Thickness - 0.100 approx.

Angle	Transverse Stress
21	5,000 psi

Angle	Notched Strength
21	140 pounds

Angle	Notched Strength
21	52 pounds
Matrix	60 pounds

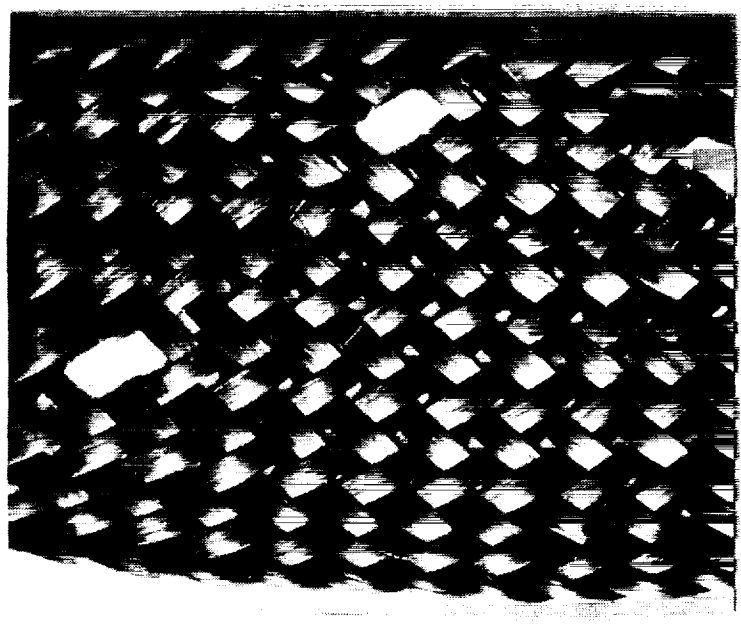

a.

b

Figure 1 a - Braided Textile Preform; b. - Molded Composite. Note the tracer tow. The composite is 3/4 inch wide.

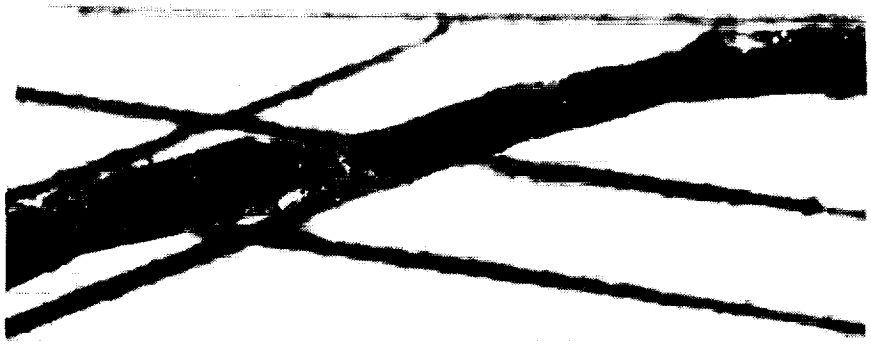

a.

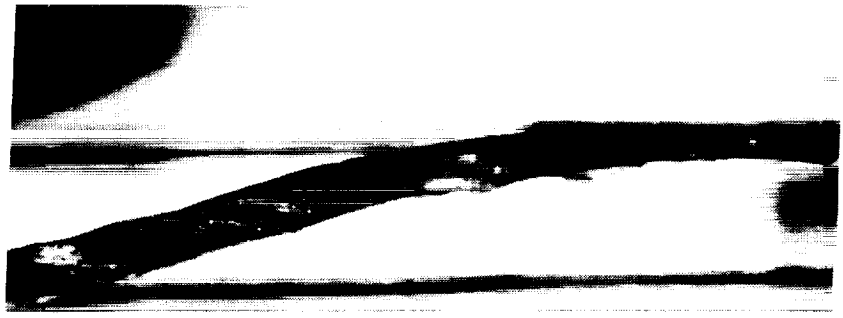

b.

Figure 2. a - Side View of Single Tow. Note the "diamond" where the tow intersects the surface. The lines indicate the apparent braid angle.
b - Top View of Same Tow. Lines indicate the width of the specimen.

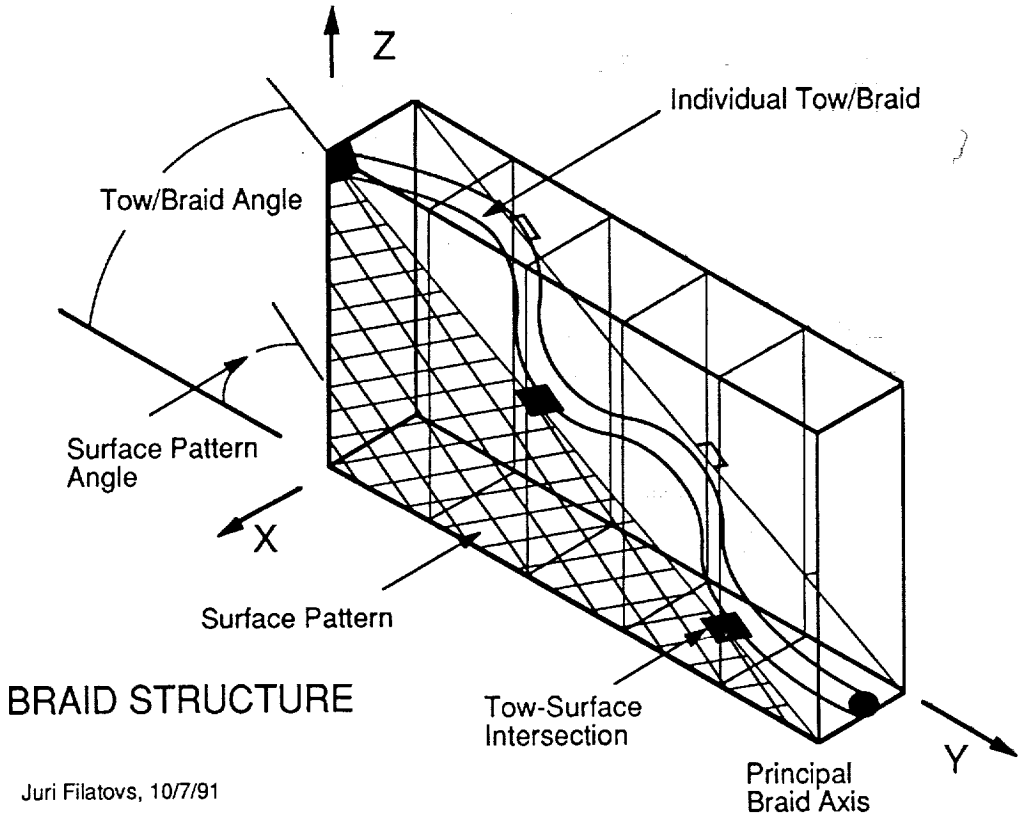

Figure 3. Surface/Volume Mapping of Braid.

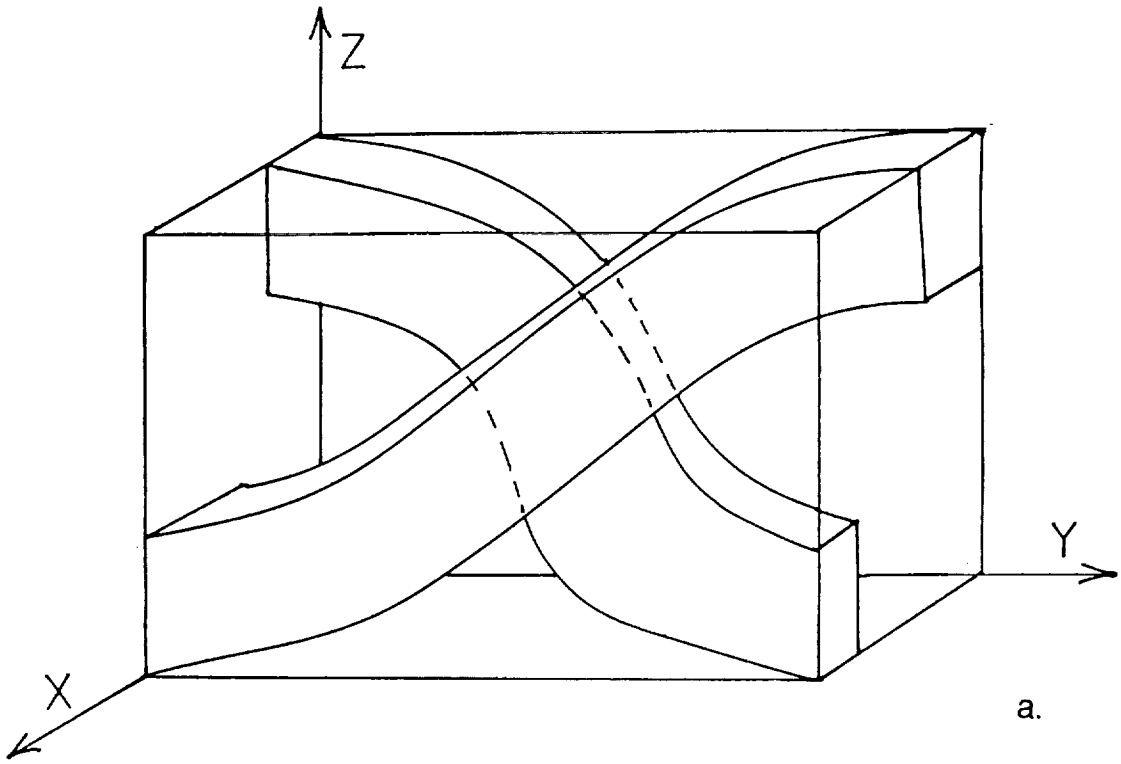

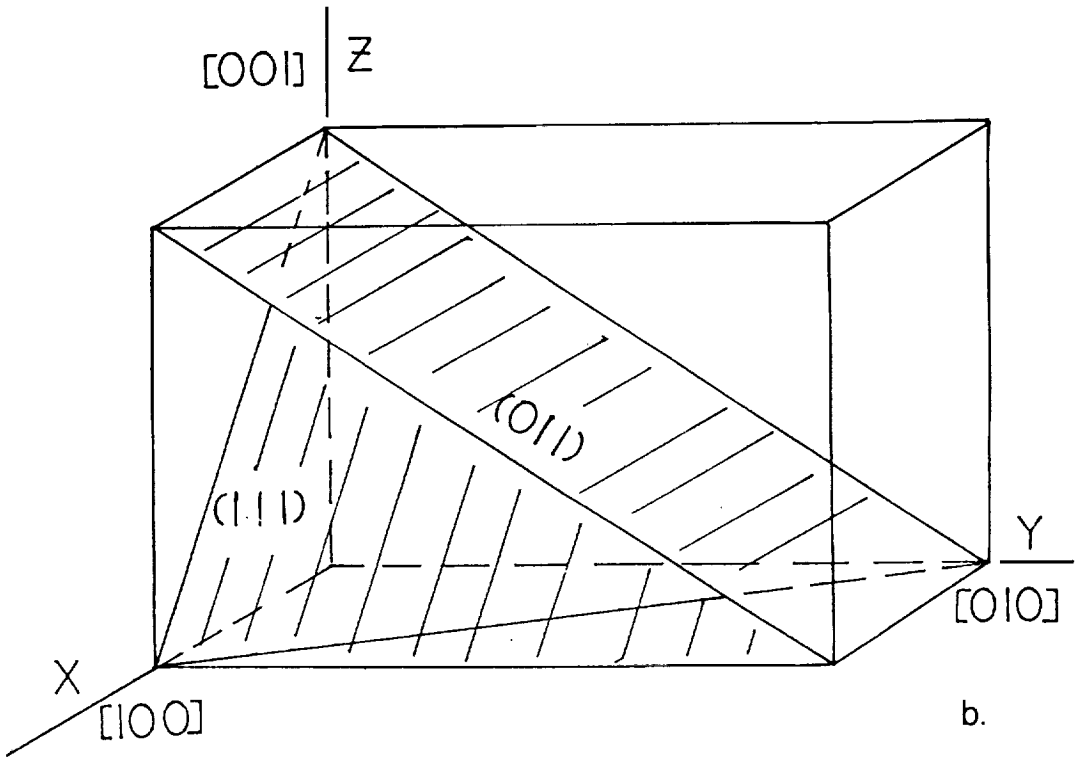

Figure 4. a- Unit Cell. b - Crystallographic Description of Same Pair.

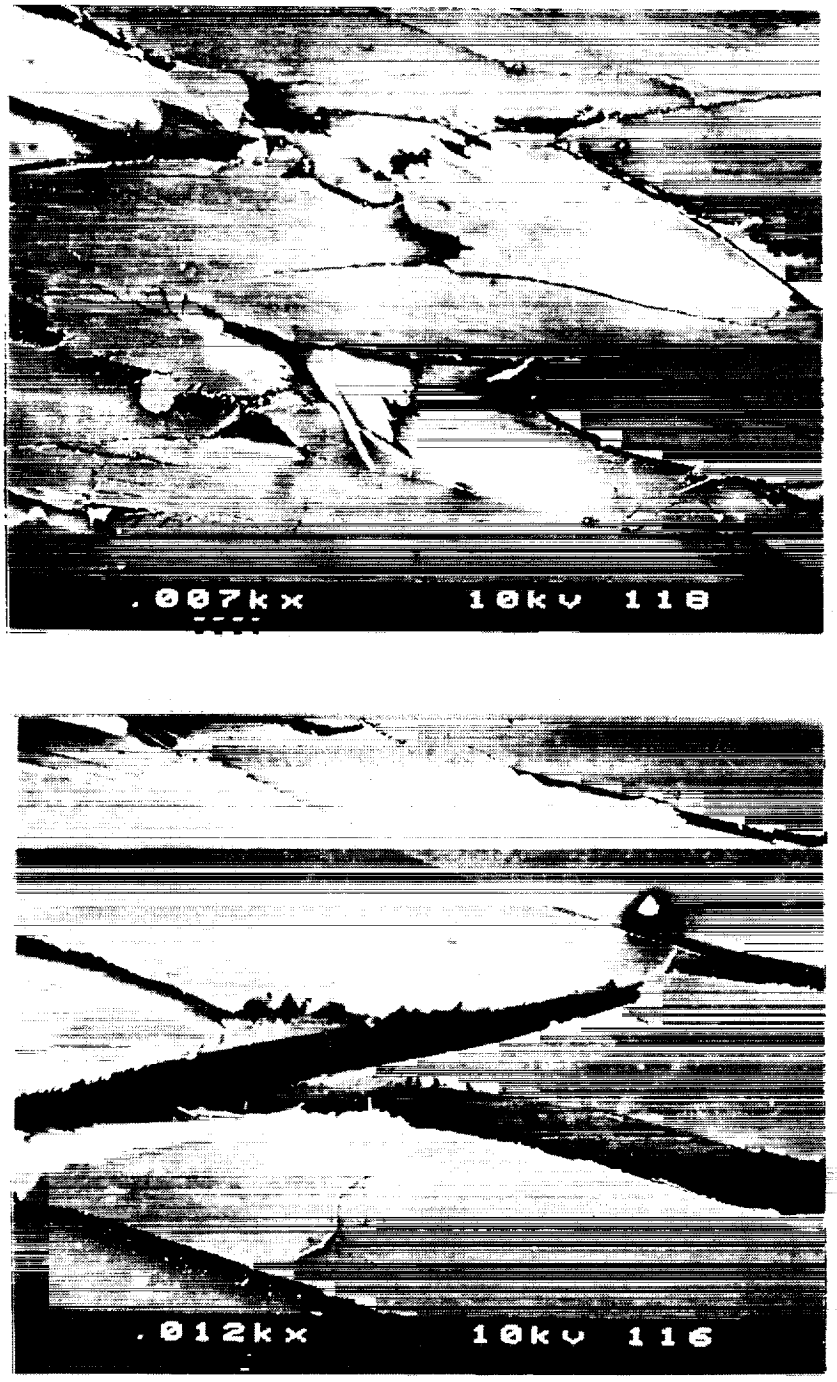

Figure 5. SEM Fractographs of Axial Compression Specimens. Surface is shown.

Figure 6. Notched E399-Type Specimen, Notched Perpendicular to Principal Braiding Direction.

Figure 7. Axially Compressed Tube

Figure 8. "T" Section Failed in 3-Point Bending

Improved Inhomogeneous Finite Elements for Fabric Reinforced Composite Mechanics Analysis

R. L. Foye
North Carolina A&T State University
Greensboro, NC

Lockheed Engineering & Sciences
Hampton, VA

Introduction

Inhomogeneous finite elements are an attractive alternative to homogeneous elements in the mechanical analysis of fabric reinforced composites (Figure 1). These elements greatly simplify the mesh generation problem created by the complex reinforcing geometry. However, this advantage has some drawbacks associated with it. Convergence, with diminishing element size, becomes less certain. Also, the computation of stresses within the various constituent materials of an element becomes a problem. This paper addresses both these concerns.

The convergence can be improved by replacing the inhomogeneous elements with special homogeneous elements whose properties are chosen to match the inhomogeneous element response to simple average strain states. One and two dimensional examples are considered. The three dimensional application is discussed without examples. The analysis also provides the basis for an approximate solution for the average stresses within each constituent material of each inhomogeneous element. This makes an approximate stress/failure analysis possible.

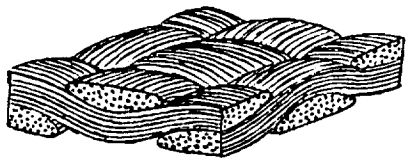

PLAIN WEAVE

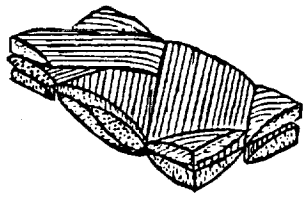

2 X 2 BRAID WITH STUFFER

FIGURE 1. FABRIC REINFORCED COMPOSITE MICROGEOMETRIES

The Analysis

The analysis uses the unit cell concept to create a boundary value problem that fully characterizes the reinforcing microgeometry. Division into subcells then establishes a finite element model of the unit cell and reduces the reinforcing complexity in each subcell to the point where average, subcell, constituent stress levels are meaningful. For example, consider the plain weave unit cell in Figure 2. Subcells that were adequate for stiffness analysis must be reduced in size to yield meaningful detailed stress information.

The individual subcell stiffness matrix, [k], can be obtained by numerical integration of the general finite element energy formula $[k] = \iiint B^T D B \, dvol$ where the matrix D contains only material property distribution functions and the matrix B contains only displacement mode shape derivatives (Ref. 1). Once a library of different subcell stiffness matrices has been created it remains to transform them into the global coordinates and assemble them into an overall stiffness matrix for the unit cell. The surface nodal forces and the average strains in each subcell, corresponding to each of the six independent strain states of 3-D elasticity, may then be solved. The surface nodal forces give the average stresses on the unit cell surfaces. The stiffness coefficients of the composite may then be computed. The convergence of this process is considered first. The subsequent computation of the constituent stresses is taken up later.

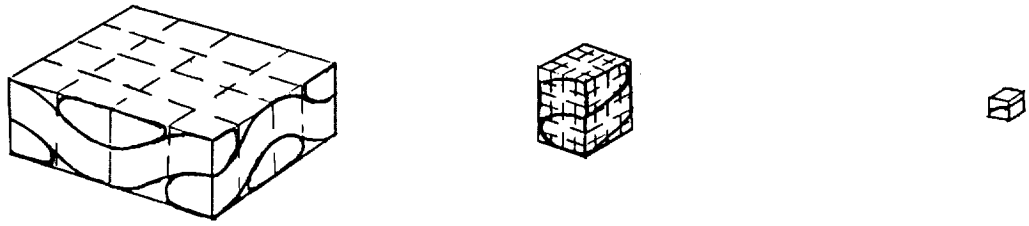

UNIT CELL | SUBCELL FOR STIFFNESS ANALYSIS | SUBCELL FOR STRESS ANALYSIS

FIGURE 2. DIVISIONS OF UNIT CELL

One Dimensional Example

The tension bar made from dissimilar materials (Figure 3) illustrates the convergence problems associated with inhomogenous elements and simple displacement mode shapes. If a finite element node coincides with the point of material discontinuity then the elements become homogeneous, the strain in each element becomes uniform, and the analysis converges abruptly to the true displacements. But, if the material discontinuity is always contained within some element, as in Figure 3, then the solution is approximate and the accuracy and convergence rate depend on the choice of assumed displacement mode shapes. For example, consider a linearly varying displacement mode shape within each element and an internal node placement at the 1/3 and 2/3 points along the bar. Each subsequent refinement divides each element into three equal segments. The middle element remains inhomogeneous as element size decreases. Figure 3 is a plot of bar elongation error as the element size diminishes. The load point displacement approaches the exact solution monotonically. Although rapid, this convergence is less satisfactory than that of the homogeneous element solution.

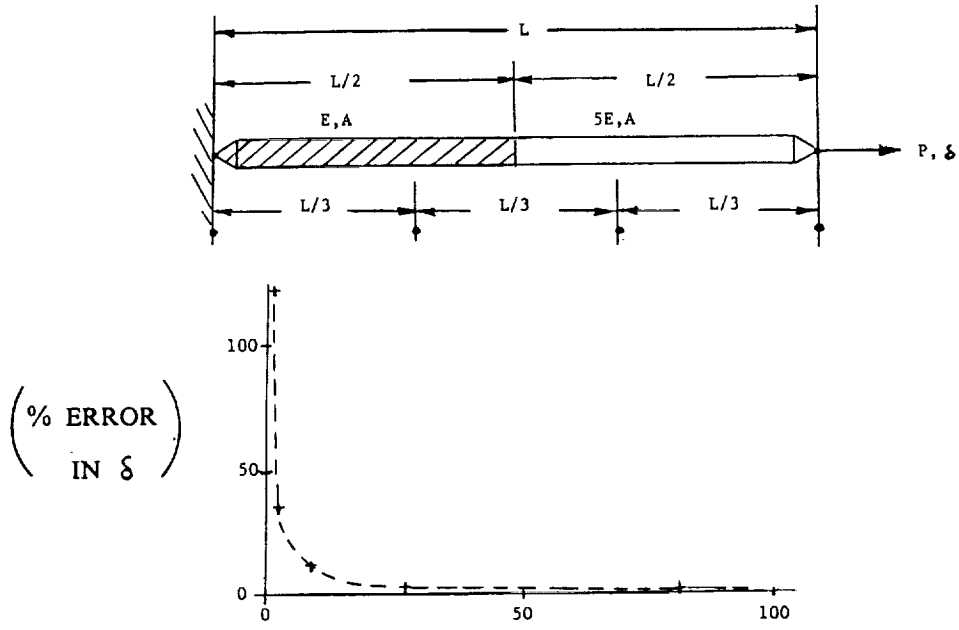

FIGURE 3. TENSION BAR PROBLEM

Improved Convergence

The convergence rate for the previous problem can be improved by using higher order displacement mode shapes (Ref. 2). It can also be improved by making a modification that overrides the source of error. The error source is the inability of the energy formulation, in combination with the linear displacement assumption, to distinguish between dissimilar material stiffnesses in series and parallel (Figure 4). The use of low order displacement modes is a presumption of parallel response when in reality the stiffnesses are functioning in series, in this particular application at least. The use of higher order modes would permit the analysis to make such a distinction. The same refinement can be attained by intervention of the analyst. Since the two materials in the center element are truly arranged in series, an effective modulus, E, of this element can be computed from the elementary series formulation $\frac{2}{E} = \frac{1}{E_L} + \frac{1}{E_R}$ where subscripts L, R designate left and right halves of the bar. The inhomogeneous center element can then be replaced by a homogeneous one with the modulus E. This correction leads to the immediate convergence of the deflection analysis. The logic in this argument seems trivial but as the dimension increases to two and three it becomes more complicated.

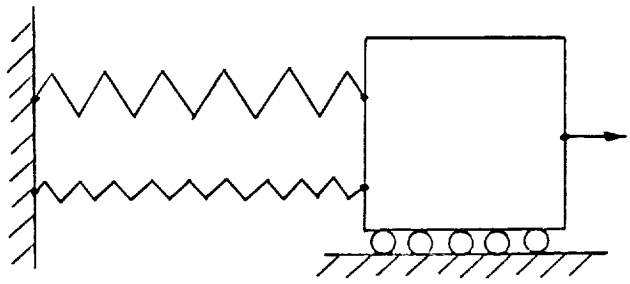

ELEMENTS IN PARALLEL

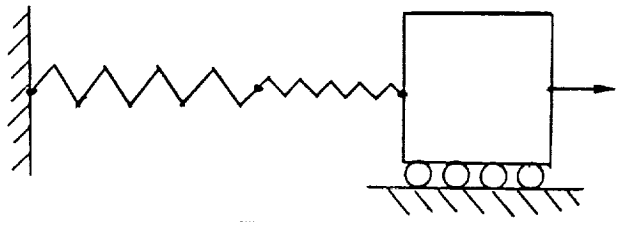

ELEMENTS IN SERIES

FIGURE 4. ELEMENTS IN SERIES AND PARALLEL

2-D Example

Figure 5 contains an example of a bimetallic composite in the form of bonded sheets of dissimilar materials. In the natural coordinates of the material the composite stiffnesses and internal stresses can be established from elementary mechanics. The results can be transformed into any other coordinates. In the coordinate system of Figure 5A the material can also be analyzed using inhomogeneous finite elements. A unit cell and a subcell division are shown in Figure 5B. Using the displacement modes usually associated with 8 node-isoparametric-brick elements (Ref. 1), generalized plane strain analysis, and the 32 node finite elements grid shown; the analysis overestimates the x and y moduli by over 20%. Refinement of the finite element grid leads to the composite moduli estimates of Figure 5C.

The convergence may be improved by recognizing how the reinforcing layers provide stiffness and then applying the appropriate rule of mixtures formulae while substituting homogeneous orthotropic elements in place of the inhomogeneous ones. Stiffnesses in parallel apply in the two principal reinforcing directions. Stiffnesses in series apply normal to the material boundaries. Figure 5C shows that this leads to abrupt convergence of the finite element sequence. The Appendix contains the relevant equations for this analysis.

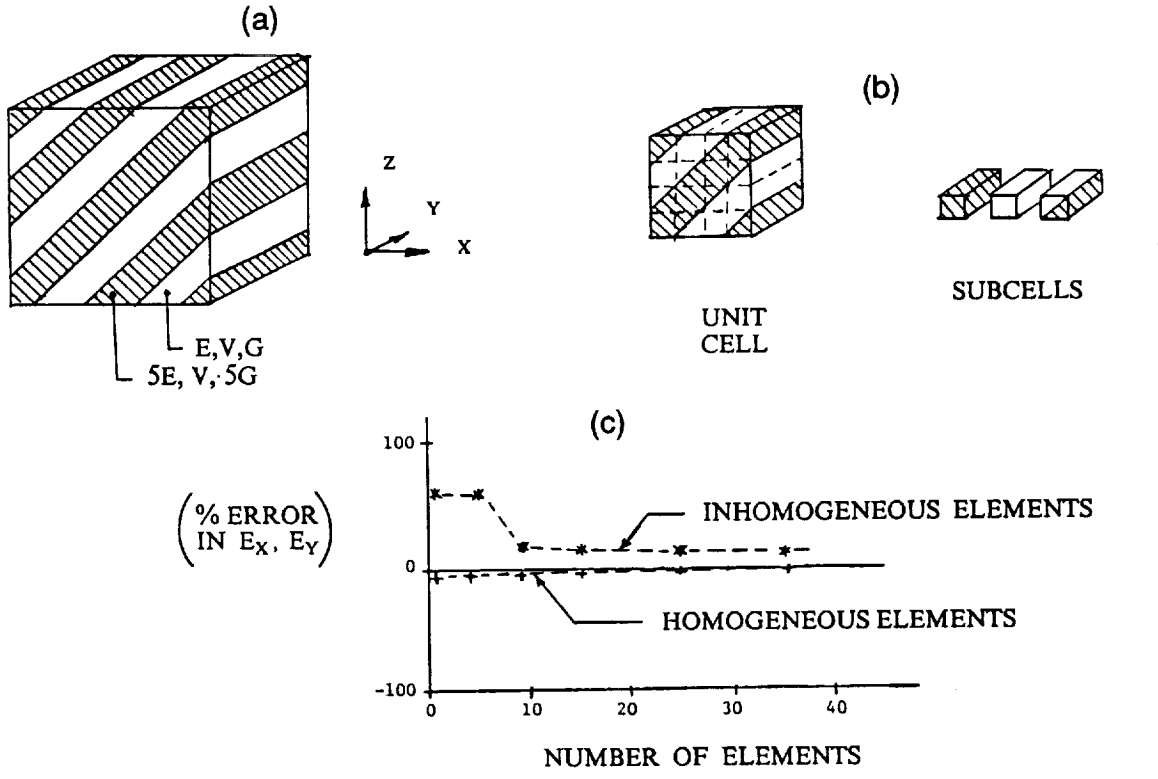

FIGURE 5. LAMINATED 2-D COMPOSITE MATERIAL

2-D Generalization

Consider generalizing the 2-D case to include more than two materials while restricting the material distribution within the subcell. Assume the material boundaries can be represented by a number of straight lines radiating from a common point within the subcell (Figure 6A). If additional lines are drawn from that point to each subcell corner node then each material will be contained in one or more homogeneous triangular finite elements. Corner displacements of the rectangular subcell are fixed by the applied strain case. Edge conditions must be approximated. The stresses within each material of the subcell can now be computed corresponding to each independent unit strain case. The nodal forces along the sides of the subcell are also available for calculating the mean stress/strain relations for the subcell. The subcell can then be considered homogeneous and anisotropic in the unit cell analysis.

If the common point lies outside the subcell boundaries then a similar analysis can be performed using some trapezoidal elements (Figure 6B). In either case full displacement continuity is not preserved between adjacent rectangular subcells.

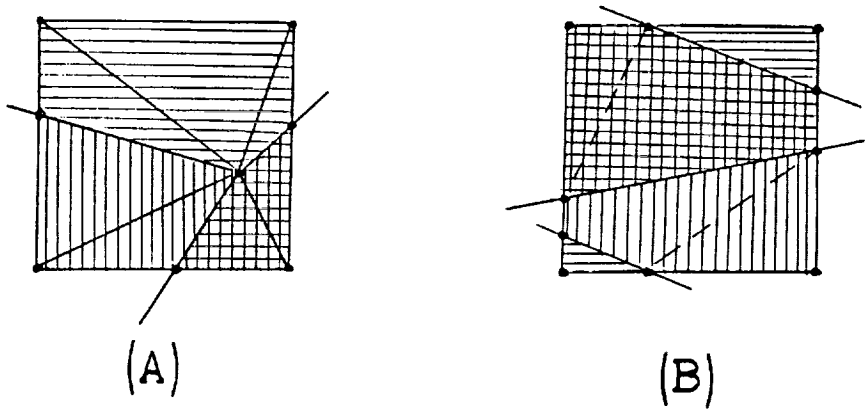

FIGURE 6. INHOMOGENEOUS/HOMOGENEOUS ELEMENT REPLACEMENT

Edge Boundary Conditions

The aforementioned boundary conditions on nodes created by the intersection of material boundaries and subcell edges are key points (Figure 7A). The assumptions used here are motivated by consideration of the special case where a material boundary and subcell edge cross at right angles (Figure 7B) and the surrounding material/loading arrangement is symmetric across the same subcell edge. Then the response will be symmetric. This implies zero tangential displacement along the material boundary (except for rigid motion) and zero nodal force normal to the material boundary.

The unit shear strain case (Figure 7C), relative to the same axes, represents antisymmetric loading with zero displacement normal to the material boundary (except for rigid motion) and zero nodal force component parallel to the material boundary.

For material boundaries which intersect subcell edges at angles other than 90° the true boundary conditions cannot be rationalized so easily. Nevertheless, it is assumed that the same displacement and force conditions remain as suitable approximations to the true conditions of equilibrium and compatibility across adjacent subcell boundaries.

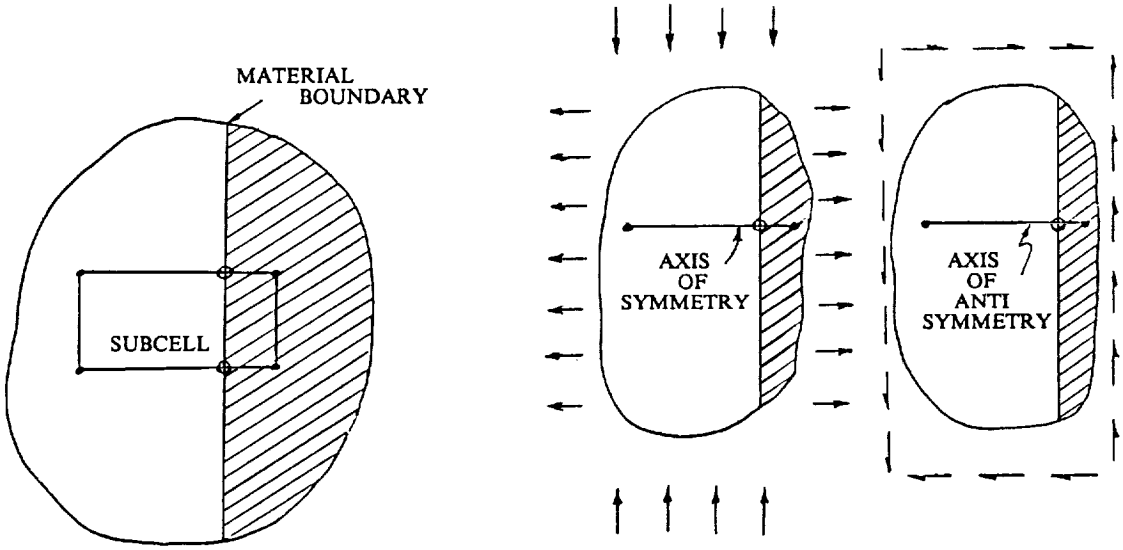

FIGURE 7. INTERFACE BOUNDARY CONDITIONS

3-D Analysis

To extend the analysis into three dimensions it is assumed that within any subcell of the rectangular 3-D array of subcells representing the unit cell, the dissimilar material boundaries consist of planes which intersect at a single straight line within the subcell (Figure 8). • Call this line the "common material axis". Consider the smallest sphere containing the subcell. A major circumference of the sphere exists which defines a plane which is normal to the common material axis and passes through the subcell centriod. By assuming the stresses do not vary along the common material axis the analysis reduces to a series of 2-D problems in the circumferential plane. Each 2-D problem resolves the displacements as a result of an applied unit strain with reference to the circumferential plane. The stresses within each wedge of dissimilar material may then be solved and the average stresses over any planar area within the subcell computed. These average stresses over the subcell surfaces permit the calculation of the equivalent anisotropic constants of the subcell. The boundary conditions at node points formed by the intersection of dissimilar material planes and subcell boundaries are established in the same way as in the 2-D case. Thus, inhomogeneous subcells are replaced by homogeneous ones in the unit cell analysis.

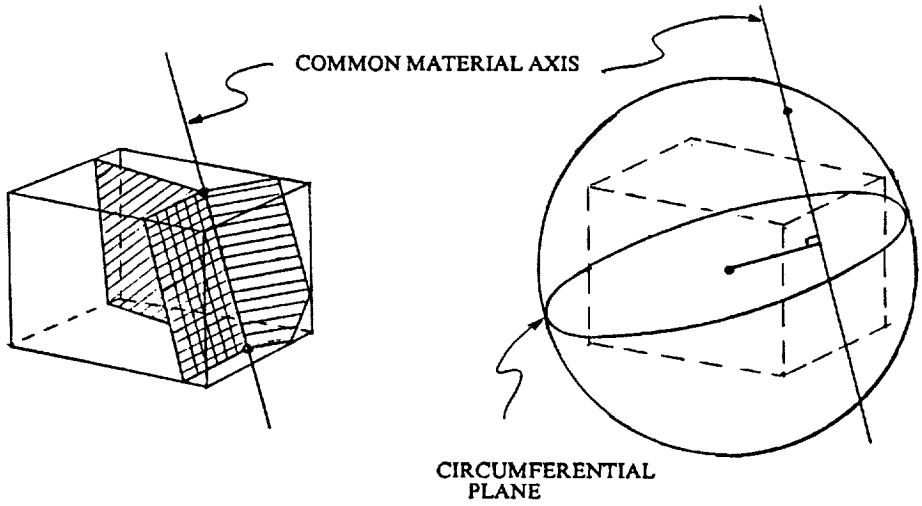

FIGURE 8. 3-D INHOMOGENEOUS SUBCELL GEOMETRY

Global-Local Analysis

It is likely that critical regions of high stress within a unit cell can be identified beforehand, making a complete stress analysis unnecessary. Certain subcells or portions of subcells will be of interest and can be isolated for detailed study through global-local analysis. This reduces the computational effort. For example, a crude model of a unit cell, based on a few subcells, can be used to obtain composite stiffnesses and define the displacements on the boundaries of a smaller volume of microstructure that contains a single subcell of further interest. A more refined grid may then be superposed on the smaller volume and more detailed stresses or displacements obtained for either a failure analysis or a more refined analysis of some smaller portion of that volume (Figure 9). Such a sequence of grid refinement may be expected to yield detailed finite element average stresses and strains in regions of tow bypass, tow contract, and sharp tow curvature. The problem of resolving these average element strains into average constituent strains and stresses will be considered next.

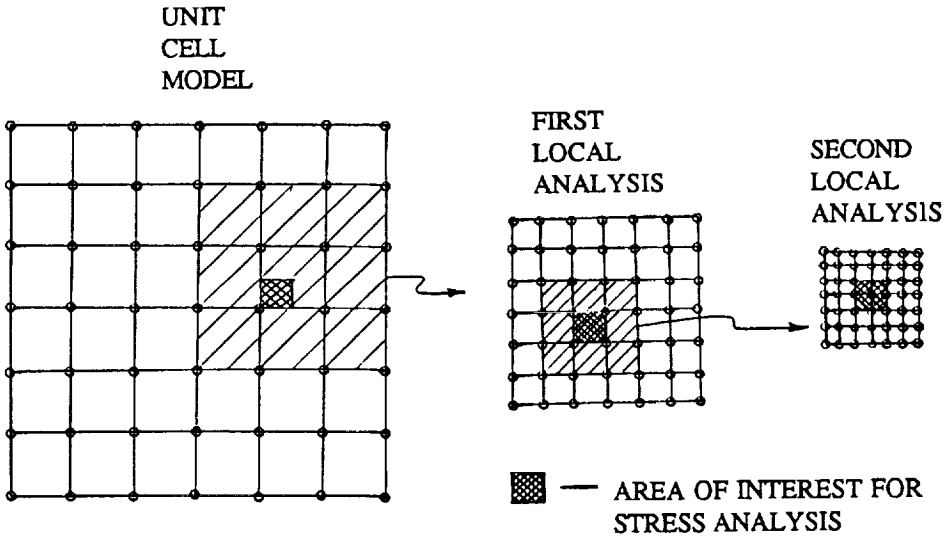

FIGURE 9. TYPICAL SEQUENCE OF INCREASING ANALYSIS DETAIL

Constituent Stresses

Returning to the one dimensional example, the determination of the stresses in the truly homogeneous elements of the tension bar is the same as in any finite element analysis. The strain is first computed from the displacements of the element nodes. The homogeneous, uniaxial stress/strain law of the material then leads to a stress calculation. For an inhomogeneous element the average strains are computed in the same way. Recourse to the stiffness in the series model that was used to compute the equivalent stiffness, E, also provides the basis for the constituent material stress calculation. The equations of strain compatibility and stress equilibrium plus the individual constituent material stress/strain relations are adequate in number for the stress calculations (Ref. 2).

In the general 2-D and 3-D cases the same mini-finite-element models that form a basis for equivalent stiffness calculations also provide a mechanism for backing out the constituent stresses (Figure 10). First, the element corner displacements, in conjunction with the displacement mode shapes establish internal displacements. Derivatives of the mode shapes establish detailed strains. The volume averages of these detailed strains establish the subcell average strains. Each average strain component, along with the mini-finite element model yields average strains in each constituent material. Constituent stress/strain laws then yield average stresses at the constituent material level.

SELECT A RECTANGULAR UNIT CELL

SUPERPOSE RECTANGULAR FINITE ELEMENT GRID ON UNIT CELL

REPLACE INHOMOGENEOUS ELEMENTS WITH MIMICKING HOMOGENEOUS ONES
(VIA MINI FINITE ELEMENT MODEL)

ANALYZE UNIT CELL FOR EACH OF THE SIX INDEPENDENT UNIT STRAIN CASES

COMPUTE COMPOSITE MODULI

COMPUTE UNIT CELL STRAINS FOR APPLIED LOAD CASES OF INTEREST

RATIO CONSTITUENT STRESSES IN EACH ELEMENT FROM UNIT STRAIN CASES TO APPLIED LOAD CASES

COMBINE CONSTITUENT STRESSES FOR THE APPLIED LOAD CASE STRAINS

FIGURE 10. STEPS IN STRESS ANALYSIS

Concluding Remarks

There is a need to do routine stress/failure analysis of fabric reinforced composite microstructures to provide additional confidence in critical applications and guide materials development. Conventional methods of 3-D stress analysis are time consuming to set up, run and interpret. A need exists for simpler methods of modeling these structures and analyzing the models. The principal difficulty is the discrete element mesh generation problem. Inhomogeneous finite elements are worth investigating for application to these problems because they eliminate the mesh generation problem. However, there are penalties associated with these elements. Their convergence rates can be slow compared to homogeneous elements. Also, there is no accepted method for obtaining detailed stresses in the constituent materials of each element. This paper shows that the convergence rate can be significantly improved by a simple device which substitutes homogeneous elements for the inhomogeneous ones. The device is shown to work well in simple one and two dimensional problems. However, demonstration of the application to more complex two and three dimensional problems remains to be done. Work is also progressing toward more realistic fabric microstructural geometries.

FABRIC MICROSTRUCTURAL ANALYSIS NEEDED

CONVENTIONAL (HOMOGENEOUS) FINITE ELEMENTS DIFFICULT TO APPLY TO FABRIC

SIMPLER METHODS/MODELS NEEDED

INHOMOGENEOUS ELEMENTS ATTRACTIVE ALTERNATIVE

SLOW CONVERGENCE PROBLEM CAN BE REMEDIED

CONSTITUENT MATERIAL STRESSES OBTAINABLE

ANALYSIS NOT PROVEN YET

WORK REMAINS TO BE DONE

FIGURE 11. CONCLUSIONS

List of References

1. Foye, R. L. "The Mechanics of Fabric Reinforced Composites", Fiber-Tex 1988, NASA Conference Publication 3038, 1989.

2. Dellinger, G. and Foye, R.L. "An Approximate Method of Stress Analysis for Fabric Reinforced Composites", Fiber-Tex 1989, NASA Conference Publication 3082, 1990.

3. Foye, R. L., The Transverse Poisson's Ratio Estimate for Unidirectional Composite Materials, Journal of Composite Materials, May. 1972.

Appendix

The rectangular inhomogeneous element of Figure 12 consists of two homogeneous isotropic materials (A and B). Parallel to the material boundary plane ($\bar{y}$ = o) the average Young's moduli ($E_{\bar{x}}$, $E_{\bar{z}}$) and Poisson's Ratios ($\upsilon_{\bar{x}\bar{y}}$, $\upsilon_{\bar{z}\bar{y}}$) can be approximated by the parallel Rule of Mixtures:

$$E_{\bar{x}} = E_{\bar{z}} = E_A v_A + E_B v_B \quad , \quad \upsilon_{\bar{x}\bar{y}} = \upsilon_{\bar{y}\bar{z}} = \upsilon_A v_A + \upsilon_B v_B$$

where v designates material volume fraction and subscripts A, B designate the material. The shear modulus ($G_{\bar{x}\bar{z}}$) can be approximated by the same rule

$$G_{\bar{x}\bar{z}} = G_A v_A + G_B v_B$$

Normal to the material boundary plane the average Young's modulus ($E_{\bar{y}}$) and shear modulus ($G_{\bar{x}\bar{y}}$) are given by the series Rule of Mixtures:

$$\frac{1}{E_{\bar{y}}} = \frac{v_A}{E_A} + \frac{v_B}{E_B} \quad , \quad \frac{1}{G_{\bar{x}\bar{y}}} = \frac{v_A}{G_A} + \frac{v_B}{G_B}$$

Considering $\bar{y}$ = o to be a plane of isotropy, the Poisson's Ratio ($\upsilon_{\bar{x}\bar{z}}$ or $\upsilon_{\bar{z}\bar{x}}$) in that plane can be approximated by (Ref. 3):

$$\upsilon_{\bar{x}\bar{z}} = \upsilon_{\bar{z}\bar{x}} = \frac{E_{\bar{z}}}{E_A}\left\{ \upsilon_A - (1-\upsilon_A)\left[\frac{E_B \upsilon_A - E_A \upsilon_B}{E_B(1-\upsilon_A) + E_A(1-\upsilon_B)R}\right]\right\} \quad \text{where } R = \frac{v_A}{v_B}$$

These equations are sufficient to support the construction of a homogeneous finite element stiffness matrix after the moduli are transformed into the global x,y,z coordinates.

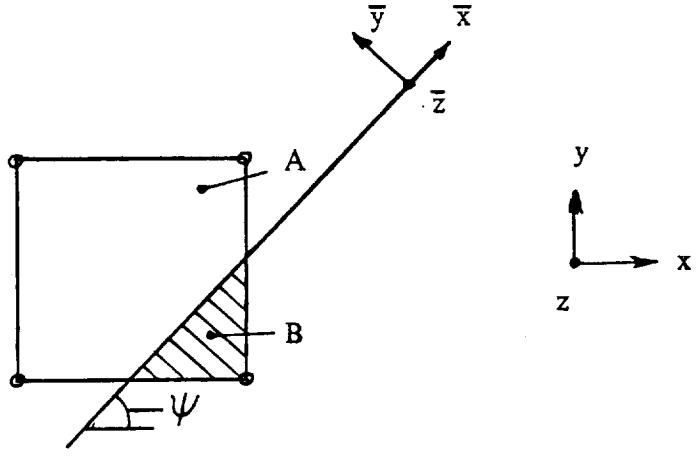

Figure 12: 2-D Analysis for Two Materials

REPORT DOCUMENTATION PAGE

Form Approved
OMB No. 0704-0188

1. AGENCY USE ONLY *(Leave blank)*	2. REPORT DATE	3. REPORT TYPE AND DATES COVERED
	October 1992	Conference Publication

4. TITLE AND SUBTITLE
FIBER-TEX 1991
The Fifth Conference on Advanced Engineering Fibers and Textile Structures for Composites

5. FUNDING NUMBERS
505-63-50-05

6. AUTHOR(S)
John D. Buckley, Editor

7. PERFORMING ORGANIZATION NAME(S) AND ADDRESS(ES)
NASA Langley Research Center
Hampton, VA 23681-0001

8. PERFORMING ORGANIZATION REPORT NUMBER
L-17173

9. SPONSORING/MONITORING AGENCY NAME(S) AND ADDRESS(ES)
National Aeronautics and Space Administration
Washington, DC 20546-0001

10. SPONSORING/MONITORING AGENCY REPORT NUMBER
NASA CP-3176

11. SUPPLEMENTARY NOTES
Co-sponsors: Department of Defense, Washington, DC; North Carolina State University, Raleigh, North Carolina; Clemson University, Clemson, South Carolina; Drexel University, Philadelphia, Pennsylvania.

12a. DISTRIBUTION/AVAILABILITY STATEMENT
Unclassified–Unlimited

Subject Category 24

12b. DISTRIBUTION CODE

13. ABSTRACT *(Maximum 200 words)*
This document is a compilation of papers presented at a joint NASA/North Carolina State University/DoD/ Clemson University/Drexel University conference on Fibers, Textile Technology, and Composites Structures held at the College of Textiles Building on Centennial Campus of North Carolina State University, Raleigh, North Carolina on October 15–17, 1991. Conference papers presented information on advanced engineering fibers, textile processes and structures, structural fabric production, mechanics and characteristics of woven composites, pultruded composites, and the latest requirements for the use of textiles in the production of composite materials and structures.

14. SUBJECT TERMS
Graphite fiber; Ceramic fibers; Fiber testing; 3-D braiding; Stitching; Automation; Towpreg; Thermoplastics; Aircraft

15. NUMBER OF PAGES
188

16. PRICE CODE
A09

17. SECURITY CLASSIFICATION OF REPORT	18. SECURITY CLASSIFICATION OF THIS PAGE	19. SECURITY CLASSIFICATION OF ABSTRACT	20. LIMITATION OF ABSTRACT
Unclassified	Unclassified	Unclassified	

NSN 7540-01-280-5500

Standard Form 298(Rev. 2-89)
Prescribed by ANSI Std. Z39-18
298-102

NASA-Langley, 1992